Doctoral theses at NTNU, 2024:84

Gianluca Tabella

Distributed Detection and Localization

Doctoral thesis

NTNU
Norwegian University of Science and Technology
Thesis for the Degree of
Philosophiae Doctor
Faculty of Information Technology and Electrical Engineering
Department of Electronic Systems

NTNU
Norwegian University of
Science and Technology

Gianluca Tabella

Distributed Detection and Localization

Thesis for the Degree of Philosophiae Doctor

Trondheim, April 2024

Norwegian University of Science and Technology
Faculty of Information Technology and Electrical Engineering
Department of Electronic Systems

NTNU
Norwegian University of Science and Technology

Thesis for the Degree of Philosophiae Doctor

Faculty of Information Technology and Electrical Engineering
Department of Electronic Systems

ISBN 978-82-326-7762-7 (printed ver.)
ISBN 978-82-326-7761-0 (electronic ver.)
ISSN 1503-8181 (printed ver.)
ISSN 2703-8084 (online ver.)

Doctoral theses at NTNU, 2024:84

Printed by NTNU Grafisk senter

Abstract

This thesis delves into the detection and localization aspects of distributed *Wireless Sensor Networks* (WSNs). Specifically, the research concentrates on WSNs in which sensors autonomously carry out detection tasks and transmit their decisions to a *fusion center* (FC). The FC's role is to make a comprehensive decision about the presence of a specific event of interest and estimate its potential location.

Given its broad significance, the thesis specializes in applying WSNs for industrial monitoring, particularly in the process and energy industry.

Three distinct approaches are explored in this thesis: (i) per-sample/batch detection, (ii) quickest detection, and (iii) sequential detection. Each framework proposes a set of detection and associated localization rules.

A primary objective of this work is to develop detection and localization strategies that leverage existing information about the monitored environment, bridging the gap between monitoring systems and the knowledge of the monitored system.

In the proposed per-sample/batch detection approach, sensors make localized binary decisions about the presence of an adverse event. The FC aggregates these decisions to provide a more reliable global binary decision. A comparative analysis is conducted between the *counting rule* and the newly proposed *modified Chair-Varshney rule*. Threshold design is facilitated through the maximization of Youden's Index. Upon detection, the FC offers an estimated position using four investigated localization algorithms: *maximum a-posteriori* localization, *minimum mean square error* localization, the *centroid-based algorithm*, and the newly proposed *modified centroid-based algorithm*.

Regarding the quickest detection approach, two architectures are introduced that capitalize on diverse network structures for quickly detecting and pinpointing faults

in industrial plants. Both incorporate a feedback mechanism transmitting parameters from higher to lower hierarchical levels. The first architecture, named *three-layer architecture*, involves multiple sensors overseeing a specific plant section, each independently conveying its local decisions to the FC. The FC gathers these local decisions spatially to generate a more comprehensive decision. Subsequently, a *post-processing center* (PPC) analyzes these global decisions over time, executing prompt detection and localization. In the second structure, named *two-layer architecture*, the FC engages in spatio-temporal aggregation to achieve swift detection, along with a potential estimation of the faulty component.

The sequential detection approach proposes a WSN where sensors perform local sequential detection and transmit decisions to the FC. Two variations of this algorithm, the *continuous sampling algorithm* (CSA) and the *decision-triggered sampling algorithm* (DTSA), each with a unique transmission and detection rule, are introduced. In the DTSA, the FC processes only those transmissions corresponding to local decisions. The CSA instead functions as a time-aware detector by processing every sensor's transmission, integrating the time of each transmission into the detection rule.

The per-sample/batch and quickest detection approaches and their localization methods are tested in an oil and gas scenario involving an oil spill within subsea production systems. Conversely, an industrial facility's carbon dioxide dispersion scenario tests the sequential detection approach.

System performance evaluation encompasses the receiver operating characteristic curve, decision delay, localization error, computational complexity, and communication costs.

Preface

This thesis is submitted to the Norwegian University of Science and Technology (NTNU) to partially fulfill the requirements for the degree of Doctor of Philosophy.

The doctoral work has been performed at the Department of Electronic Systems, NTNU, Trondheim, Norway, from January 2020 to November 2023.

The work has been conducted under the supervision of Professor Pierluigi Salvo Rossi from the Department of Electronic Systems, NTNU, and the co-supervision of Professor Nicola Paltrinieri from the Department of Mechanical and Industrial Engineering, NTNU, and Professor Domenico Ciuonzo from the Department of Electrical Engineering and Information Technologies, University of Naples "Federico II," Naples, Italy.

In 2022, part of the work was conducted at the Department of Electrical Engineering of Columbia University, New York (NY), USA, under the supervision of Professor Xiaodong Wang.

The members of the assessment committee are Professor Visa Koivunen from the Department of Information and Communications Engineering, Aalto University; Doctor Myrto Konstantinidou from the Institute of Nuclear & Radiological Sciences and Technology, Energy & Safety of NCSR Demokritos Demokritos, Athens, Greece; and Professor Geir Egil Dahle Øien from the Department of Electronic Systems, NTNU.

Acknowledgments

Pursuing the Ph.D. at NTNU has been among the hardest things I have ever done. At the same time, the amount of satisfaction, the knowledge I acquired, and the skills I developed during this journey cannot be described in a few sentences.

When I started this academic journey, I had just received my M.Sc. in chemical and process engineering and had very little knowledge of any of the things I went on to learn and do during these four years. As a chemical and process engineer, I went from learning the design of oil and gas equipment to learning how to design a detector whose task is to discriminate between two hypotheses. I have to admit that this transition has not been easy, but now I feel extremely lucky to be able to work with this mix of knowledge.

Being able to achieve all this would not have been possible without the support of the people around me. In particular, my family has always shown me love and never doubted that I could make it. Thanks, Mom, Dad, and Emanuela, for everything.

During these four years, my girlfriend Lisa has been next to me, and she has given me moral support and love and shown a level of patience that some future Ph.D. students should research. She was my most avid supporter. I likely would not have made it without you.

I want to express my gratitude to my academic advisor, Professor Pierluigi Salvo Rossi. After having him as a supervisor, I feel I could not have been luckier than that. With his knowledge, personality, support, and friendship, he helped me grow as a researcher and allowed me to fully take advantage of the world of possibilities given during doctoral studies. I must extend my gratitude to my co-supervisor, Professor Domenico Ciuonzo, for his valuable contributions to many of my publications. His insights, availability, and friendship have been essential during my work. I am

equally grateful to my co-supervisor, Professor Nicola Paltrinieri. Without him, I would not even be here, as he supervised my master's thesis when I came to NTNU for the first time. That thesis was my first experience with statistical signal processing and became the backbone of many of the works I published later.

I am also very thankful to Professor Xiaodong Wang for allowing me to be part of his lab at the Department of Electrical Engineering at Columbia University. It was an honor for me to spend almost one year with his group. His input and ideas helped me deliver quality research.

Many thanks also to my co-authors, Yuri Di Martino, Professor Yasin Yilmaz, and Professor Valerio Cozzani, for contributing to the realization of my research in different ways.

Also, many thanks to Andrey Kolmogorov, Thomas Bayes, Ronald Fisher, Abraham Wald, Jerzy Neyman, Egon Pearson, and many more for making my research much easier to carry out.

Working at NTNU was a great experience. Because of this, I want to thank the many people and friends I met there. Thanks to all of you.

In conclusion, completing this thesis has been a shared achievement, and I am sincerely thankful for the collective support that has shaped my academic and personal growth.

With gratitude,

Gianluca Tabella

Contents

List of Tables

List of Figures

Abbreviations and Symbols

Abbreviations

2LA	Two-Layer Architecture
3LA	Three-Layer Architecture
AAF	Amplitude Attenuation Function
ADD	Average Detection Delay
ATP	Average Transmission Period
AUC	Area Under the Curve
AWGN	Additive White Gaussian Noise
B&M	Britter & McQuaid Model
BLRT	Likelihood Ratio Test with Bayesian Marginalization
CBA	Centroid-Based Algorithm
CCDF	Complementary Cumulative Distribution Function
CDF	Cumulative Distribution Function
CMA	Cumulative Moving Average
CMEC	Center of the Minimum Enclosing Circle
CMER	Center of the Minimum Enclosing Rectangle

CO_2	Carbon Dioxide
CR	Counting Rule
CRLB	Cramér-Rao Lower Bound
CSA	Continuous Sampling Algorithm
CVR	Chair-Varshney Rule
DRMF	Dynamic Risk Management Framework
DTSA	Decision-Triggered Sampling Algorithm
EOS	Equation of State
FC	Fusion Center
FI	Fisher Information
FPSO	Floating Production Storage and Offloading
G-CUSUM	Generalized CUSUM
GLRT	Generalized Likelihood Ratio Test
GSPRT	Generalized Sequential Probability Ratio Test
i.i.d.	Independent and Identically Distributed
IoT	Internet of Things
LDS	Leak Detection System
LMPT	Locally Most Powerful Test
LOC	Loss-Of-Containment
LOD	Locally-Optimum Detection
LRT	Likelihood Ratio Test
MAP	Maximum A-Posteriori
MCBA	Modified Centroid-Based Algorithm
MCVR	Modified Chair-Varshney Rule
MIMO	Multiple-Input and Multiple-Output

ML	Maximum Likelihood
MLE	Maximum Likelihood Estimator
MMSE	Minimum Mean Square Error
OOK	On-Off Keying
PDF	Probability Density Function
PMF	Probability Mass Function
PPC	Post-Processing Center
RMSE	Root Mean Square Error
ROC	Receiver Operating Characteristic
ROV	Remotely Operated Vehicle
SNR	Signal-to-Noise Ratio
SPAR	Single Point Anchor Reservoir
SPRT	Sequential Probability Ratio Test
SPS	Subsea Production System
TLP	Tension-Leg Platform
UMP	Uniformly Most Powerful
WSN	Wireless Sensor Network

Symbols

α	Seawater absorption coefficient
$\boldsymbol{\mathcal{D}}[n]$	Collection of FC's binary decisions since last inspection (at nth instant)
$\boldsymbol{\theta}$	Position of the event of interest
$\boldsymbol{\theta}_m$	Position of the mth item
$\boldsymbol{d}[n]$	Vector of local binary decisions (at nth instant)

$\boldsymbol{T}_m[j]$	Collection of the mth item's failure times up to and including the jth failure
$\boldsymbol{x}_k$	Position vector of the generic kth sensor
Δt	Sampling interval
ℓ_{ref}	Reference length
ℓ_m^n	Likelihood-ratio of sensors' decisions in 2LA with respect to the failure of the mth item (at nth instant)
γ^*	Global detection threshold
γ_k	kth sensor's detection threshold
$\gamma_k[n]$	kth sensor's detection threshold (at nth instant)
λ_m	Failure rate of mth item
Λ_n^k	kth sensor's test statistic (at nth instant)
Λ_n^{BLRT}	BLRT test statistic with binary inputs (at nth instant)
Λ_n^{CR}	CR test statistic (at nth instant)
Λ_n^{CSA}	CSA test statistic (at nth instant)
Λ_n^{CVR}	CVR test statistic (at nth instant)
Λ_n^{DTSA}	DTSA test statistic (at nth instant)
Λ_n^{GLRT}	GLRT test statistic with binary inputs (at nth instant)
Λ_n^{MCVR}	MCVR test statistic (at nth instant)
$\lambda_{m,0}$	Literature estimate of λ_m
$\mathcal{C}[n]$	G-CUSUM test statistic with binary inputs (at nth instant)
$\mathcal{C}_m[n]$	G-CUSUM test statistic with binary inputs with respect to the mth item (at nth instant)
$\mathcal{D}[n]$	FC's binary decision in 3LA (at nth instant)
$\mathcal{D}_{ij}^*$	FC's expected value of time to declare $\mathcal{H}_i$ when $\mathcal{H}_j$ is true ($\mathcal{H}_X$ stands for any hypothesis)

$\mathcal{D}_{ij}^{k}$	kth sensor's expected value of time to declare $\mathcal{H}_i$ when $\mathcal{H}_j$ is true ($\mathcal{H}_X$ stands for any hypothesis)
$\mathcal{H}[n]$	System's state variable (at nth instant)
$\mathcal{H}_0$	Null hypothesis
$\mathcal{H}_1$	Alternative hypothesis
$\mathcal{H}_m[n]$	mth item's state variable (at nth instant)
$\mathcal{L}_\theta\big(\tau_k\big[n_m^k\big], a_k[n]\big)$	Time-aware likelihood-ratio of kth sensor' transmission value $\tau_k[n_m^k]$ in CSA (parametrized by θ)
$\mathcal{L}_\theta\big(\tau_k\big[n_m^k\big]\big)$	Likelihood-ratio of kth sensor' transmission value $\tau_k[n_m^k]$ in DTSA (parametrized by θ)
$\mathcal{L}_m^n$	Likelihood-ratio of FC' decisions in 3LA with respect to the failure of the mth item (at nth instant)
$\mathcal{M}_n^k$	kth sensor's count of local decisions up to the nth instant
$\mathcal{P}_1$	Probability of occurrence (probability of faulty state)
$\mathcal{P}_C^k$	kth sensor's overall probability of correct rejection
$\mathcal{P}_C^{(k,i)}$	kth sensor's (ith-)instant probability of correct rejection
$\mathcal{P}_D^k(s_k)$	kth sensor's overall probability of detection (parameterized by s_k)
$\mathcal{P}_D^{(k,i)}(s_k)$	kth sensor's (ith-)instant probability of detection (parameterized by s_k)
$\mathcal{P}_D^{(k,m)}$	kth sensor's probability of detection with respect of the mth item
$\mathcal{P}_D^{(k,m)}[n]$	kth sensor's probability of detection with respect of the mth item (at nth instant)
$\mathcal{P}_F^k$	kth sensor's overall probability of false alarm
$\mathcal{P}_F^k[n]$	kth sensor's probability of false alarm (at nth instant)
$\mathcal{P}_F^{(k,i)}$	kth sensor's (ith-)instant probability of false alarm

$\mathcal{P}_M^k(s_k)$	kth sensor's overall probability of miss-detection (parameterized by s_k)
$\mathcal{P}_M^{(k,i)}(s_k)$	kth sensor's (ith-)instant probability of miss-detection (parameterized by s_k)
$\mathcal{P}_{10}$	Global probability of false alarm (for 3LA and 2LA)
$\mathcal{R}^{\mathrm{FC}}[n]$	Posterior probability of system failure in 2LA (at nth instant)
$\mathcal{R}^{\mathrm{PPC}}[n]$	Posterior probability of system failure in 3LA (at nth instant)
$\mathcal{R}_m^{\mathrm{FC}}[n]$	Posterior probability of mth item failure in 2LA (at nth instant)
$\mathcal{R}_m^{\mathrm{PPC}}[n]$	Posterior probability of mth item failure in 3LA (at nth instant)
$\mathcal{S}_m[n]$	Count of failures of the mth item (at nth instant)
$\mathcal{T}^*$	FC's decision deadline
$\mathcal{T}_k$	kth sensor's decision deadline
$\mathrm{AUC}(\mathcal{D}_{X1}^*)$	AUC of the curve Q_F vs. $\mathcal{D}_{X1}^*$
$\mathrm{P_{atm}}$	Atmospheric pressure
$\mathrm{P_{op}}$	Operating pressure
$\mathrm{SNR_{ref}}$	Reference SNR
T_0	Release temperature
$\mathrm{T_{atm}}$	Atmospheric temperature
$\mathrm{T_{op}}$	Operating temperature
$\mu_{w,k}$	Mean of $w_k[n]$
ν_m	Variance of the literature estimate of $\lambda_{m,0}$
$\overline{\mathcal{P}_D^k}$	kth sensor's mean probability of detection
$\overline{Q_D}$	FC's mean probability of detection
ψ	Wind direction (angle)
ρ_0	Release density

ρ_{air}	Density of the air
$\sigma^2_{\xi,m}$	Variance of $\xi_{m,k}[n]$
$\sigma^2_{w,k}$	Variance of $w_k[n]$
$\tau_k[n]$	kth sensor's transmission value (at nth instant)
τ_n	Amount of time passed since the last inspection (at nth instant)
$\varepsilon_{m,j}$	Detection delay with respect to the mth item's jth failure
φ_m	Stationary prior probability of failure of mth item
$\varphi_m[n]$	Dynamic prior probability of failure of mth item
$\widehat{\boldsymbol{\theta}}$	Estimate of the position of the event of interest
$\widehat{\lambda}_m[n]$	Most recent estimate of λ_m (at nth instant)
$\widehat{\mathcal{H}}$	Global binary decision
$\widehat{\mathcal{H}}[n]$	Estimate of the system's state (at nth instant)
$\widehat{c}_{k,n}$	kth sensor's estimate of c_k (at nth instant)
$\xi_{m,k}[n]$	kth sensor's signal fluctuation with respect to the failure of the mth item (at nth instant)
$a_k[n]$	kth sensor's number of instant passed since the last decision (at nth instant)
c_0	Release concentration
c_k	Gas molar fraction at the generic kth sensor
d_0	Release diameter
$d_k[n]$	kth sensor's binary decision (at nth instant)
$F[n]$	System's failure function (at nth instant)
$F_m[n]$	mth item's failure function (at nth instant)
$g(\boldsymbol{x}_k, \boldsymbol{\theta}_m)$	AAF as a function of $\boldsymbol{x}_k$ and $\boldsymbol{\theta}_m$
I	Intensity of the event of interest

J	Youden's index
k_{sc}	Spreading coefficient
n^*	FC's stopping time
n_m^k	kth sensor's mth stopping time
Q_D^m	Global probability of detection with respect of the mth item
$Q_D^m[n]$	Global probability of detection with respect of the mth item (at nth instant)
Q_F	Global probability of false alarm
$Q_F[n]$	Global probability of false alarm (at nth instant)
$s_k(\cdot)$	Effect of $\mathcal{H}_1$ on $y_k[n]$ ($s_k^n(\cdot)$ highlights possible time dependency)
$T_{m,j}$	Time spent by the mth item between the $(j-1)$th and jth failure
$T_{m,j}^*$	Sum of $T_{m,j}$ and $\varepsilon_{m,j}$
u	Wind speed
V	Release volumetric flow rate
$w_k[n]$	kth sensor's measurement noise (at nth instant)
$y_k[n]$	kth sensor's measured signal (at nth instant)

Chapter 1

Introduction

Wireless Sensor Networks (WSNs) have witnessed remarkable growth in recent decades, primarily driven by the proliferation of cost-effective and environmentally friendly sensor devices used for monitoring applications [1]. This expansion can be attributed to significant advancements in sensor technology, wireless communication protocols, and the rise of the *Internet of Things* (IoT) [2]. WSNs play a pivotal role within the IoT, seamlessly connecting the physical and digital realms by providing real-time data for various inference tasks [3].

One focal point in WSNs is the *detection* and *localization* of events, particularly concerning safety-critical systems. These tasks can be broadly defined as follows:

- *Detection:* This involves identifying the presence or absence of a specific event or hypothesis, often in the presence of noise or uncertainty.
- *Localization:* This is the process of determining the precise position or location of an object of interest, typically achieved through point estimation or M-ary detection techniques, often in noisy or uncertain conditions.

For an overview of inference and learning from data, the reader should refer to the [4–6].

Industries such as process, energy, and manufacturing have a vested interest in these areas, where a single equipment failure can jeopardize worker safety and environmental well-being. Such failures often result in substantial environmental and societal costs and significant financial losses due to unplanned shutdowns [7]. A typical critical event in this context is the *loss-of-containment* (LOC) which is defined as follows:

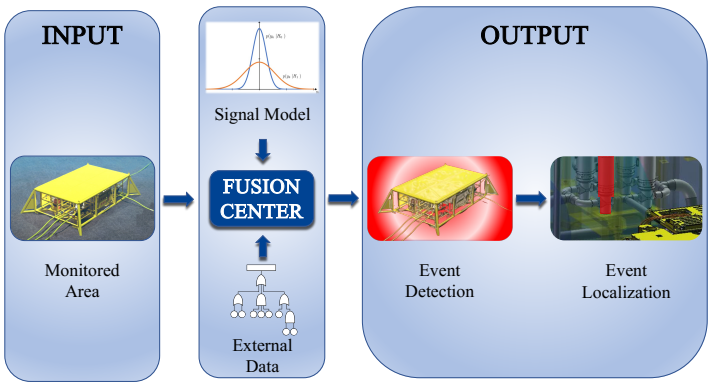

Figure 1.1: Diagram of an industrial monitoring system designed for detection and localization.

"*[LOC is an] unplanned or uncontrolled release of any material, fire, explosion, and toxic hazards. LOC is a type of event. An unplanned or uncontrolled release is a LOC, irrespective of whether the material is released into the environment, into secondary containment, or into other primary containment, not intended to contain the material released under normal operating conditions.*" [8]

In light of these challenges, the global critical infrastructure protection market has reached a valuation of USD 132 billion, with forecasts indicating a steady compound annual growth rate of 3.4% through 2030, and IoT technologies are poised to play a pivotal role [9].

To enhance the efficiency of WSNs and prolong their lifespan while minimizing monitoring costs, sensors are frequently engineered to transmit binary decisions to a *fusion center* (FC). The FC's function is to aggregate local decisions and generate a global decision regarding the occurrence of an event, such as a fault in the monitored plant [10, 11]. When an undesired event is detected, the FC triggers an alarm, facilitating timely responses like emergency plant maintenance to mitigate the consequences. A schematic representation of such a setup is shown in Figure 1.1.

The use of WSNs for event detection, particularly in industrial applications, has attracted significant research attention, with a specific focus on underwater settings [12, 13]. Underwater environments pose unique challenges in detecting equipment failures resulting in a LOC, especially when inspections are prohibitively costly, such as subsea plants [14].

Another significant challenge lies in detecting uncooperative sources, such as the

LOC of gases in the process industry. To address stringent bandwidth and energy constraints while ensuring the longevity of IoT nodes, there has been a growing emphasis on adopting binary sensors for detecting gases in safety-critical systems, as highlighted in prior research [15, 16].

Moreover, beyond industrial applications, WSNs are gaining momentum in security, counter-terrorism, and defense [17]. Concurrently, in the context of Industry 4.0, WSNs play a pivotal role in ensuring safety and environmental protection [18].

Modern monitoring systems rely on many sensors to surveil specific areas of interest. These sensors commonly employ a per-sample or batch detection approach, identifying events after processing a fixed number of samples. In such a configuration, each sensor is tasked with event identification, and an inspection is triggered when a sensor raises an alarm.

The current state-of-the-art industrial monitoring systems unveil several challenges and promising avenues for improvement. These challenges encompass issues such as a notable likelihood of errors, including false alarms and miss-detections. However, they also present opportunities for enhancing system efficiency and reliability.

1.1 State of the Art

The initial significant contribution to the field of *batch* data fusion in distributed WSN for event detection came from the groundbreaking work in [19]. Over time, interest in distributed WSNs, where sensors transmit binary decisions to a FC to reduce communication and processing costs, has grown [20].

Several notable contributions have emerged to address bath detection problems. In [21, 22], fusion rules like the *Chair-Varshney rule* (CVR) and the *counting rule* (CR) were proposed, addressing local sensor-based detection. Optimality considerations concerning the Neyman–Pearson criterion have been researched in [23]. In [24], sub-optimal heuristic fusion rules were introduced, such as the Equal Gain Combining Fusion Statistic and the Maximum Ratio Combining Fusion Statistic. Meanwhile, in [25], the Ordering-Based CR is investigated to improve the performances of its traditional counterpart. Several pieces of research have also been conducted to enhance the energy efficiency of the WSN as well as design frameworks for data transmission and routing among sensors and between the sensor and the FC [26–29].

Additionally, in [30], a comparison was presented between a WSN employing a FC that receives binary decisions and performs a *locally most powerful test* (LMPT) and the same network where the FC executes the LMPT after receiving raw local

measurements, particularly in scenarios with weak signals.

The work in [31, 32] introduced the Rao Test, showcasing the asymptotically equivalent performance of the CR compared to the *generalized likelihood ratio test* (GLRT).

Moreover, [33] presented a set of fusion rules based on GLRT, Bayesian frameworks, the *locally-optimum detection* (LOD) framework, and hybrid approaches. The issue of detection in WSNs was further investigated using *multiple-input multiple-output* (MIMO) architectures, where sensors transmit local binary decisions to an FC, focusing on the performance of the communication channel between sensors and the FC [34–36].

In the context of WSNs with a single FC and 1-bit local decisions, the problem of target localization has been extensively studied, resulting in various localization algorithms. Many of these methods have a statistical foundation, as described in [33]. Unfortunately, most of these methods have high computational complexity and may not be adaptable to specific conditions. Statistical-based methods often require precise knowledge of the signal's statistical model, which may not always be available.

Consequently, several heuristic strategies have been developed. These are known for their low computational complexity and ease of implementation, requiring less knowledge of the signal's statistical model. Some popular heuristic localization methods, like the centroid method, are introduced in [37]. Variations of the centroid method have been proposed, such as range-based methods as in [38, 39], which utilize additional information to calculate centroid weights. Other heuristic localization methods include the *center of the minimum enclosing rectangle* (CMER) [37], an extension introducing the Steiner center to remove coordinate system dependency [40], and the *center of the minimum enclosing circle* (CMEC) [41]. Additionally, [37] highlights the effectiveness of CMEC in noise-free settings with a unitary probability of detection in the target's proximity.

An essential aspect of WSNs with FC is the design of quantizers. In [42], the local quantization problem is addressed for Bayesian estimation of location parameters, considering both conditionally unbiased and efficient estimators with conditionally independent observations, as well as scenarios with bit rate constraints and conditionally dependent observations. In [43], quantization for tracking moving targets is discussed, proposing a method for dynamically updating local thresholds, striking a balance between maximum *Fisher information* (FI) and the minimum sum of sensor transmission probabilities.

The quantization issue has been explored within distributed detection, especially to

establish optimal quantization strategies [44]. In [45], quantizers were explicitly crafted for a WSN executing a Generalized LOD test (from Davies' framework) for detecting a target with an unknown position and emitted power. These quantizers were devised using an asymptotically optimal approach.

Similarly, in [46], the optimal quantizer for a deterministic signal in a WSN with an imperfect reporting channel and a FC performing a GLRT was explored. In [30], the resulting quantizer was derived by maximizing the FI. Furthermore, [47] derived the binary asymmetric quantizer by minimizing the maximum *Cramér-Rao lower bound* (CRLB).

The problem of *online detection* via *quickest detection* framework is still an open research field nowadays. An overview of the main results of the quickest detection framework can be found in [48–50].

Peculiar characteristics and challenges for the problem of quickest detection, especially in industrial settings, are: (i) the finite spatial extent of the event being monitored; (ii) the fault location is unknown; (iii) each fault may be more or less probable depending on the reliability of the item responsible for it; (iv) efficient detection algorithms should be conceived to detect such events as quickly as possible while keeping false alarms under control; (v) detection approaches should be coupled with (or better, include) localization procedures to identify the faulty item.

In the context of challenges (i) and (ii), various algorithms have been proposed in the literature for detecting spatially localized events at unknown locations (such as radiation releases, anomalous parameter fields, or non-cooperative targets) via distributed WSNs. Initial attempts involve the straightforward application [51, 52] or adaptations/extensions [53] (e.g., by using ordering schemes according to most informative sensors) of the sub-optimal CR. Notably, the plain CR has recently found application in the specific domain of subsea oil spill detection [54]. Regrettably, these rules do not consider the *limited extent* and *unknown location* of the detected phenomenon by design. This results in *diminished detection performance*.

Conversely, recent years have witnessed the emergence of a range of fusion rules designed for the explicit detection of spatially localized events with unknown locations through distributed WSNs [11, 33, 55]. To tackle this challenge, these approaches have harnessed methodologies such as the GLRT, Bayesian techniques, generalized score tests, or hybrid variations. While *primarily focused on detecting non-cooperative targets*, these algorithms can be adapted to address challenges (i), (ii), and (v). However, it is essential to note that the fusion methods mentioned are fundamentally designed in a batch fashion (or overlook temporal dependencies) and fail to target the rapid onset of faults, thus not fully addressing challenge

(iv). Recent advancements in this domain have made strides in mitigating the constraints associated with batch design [56, 57]. Nevertheless, these proposals cannot promptly detect events as they occur, which is crucial in addressing the quickest detection problem.

Furthermore, to the best of the author's understanding, *no approach has effectively integrated data regarding the dependability of the system being monitored when developing the detection algorithm*, i.e., challenge (iii). Vital data, encompassing critical items' positions, failure rates, and failure models, represent valuable prior information that may be seamlessly substantiated within a Bayesian approach.

Sequential detection, also known as *sequential analysis* or *sequential hypothesis testing*, was popularized by Wald with the *sequential probability ratio test* (SPRT). A thorough overview of sequential detection can be found in several references, including [58–60]. Although sequential detection in WSNs has been explored in recent years, it remains an ongoing area of research. [61] proposed an architecture where sensors and the FC perform sequential detection, with sensors transmitting their local decisions to the FC. This setup demonstrated performance asymptotically equivalent to the centralized counterpart under certain conditions. [62] presented a higher-performance alternative based on the assumption that the observed signal is a sampled version of a continuous stochastic process with continuous paths. Recent research has focused on alternative tests to SPRT for WSNs, as exact knowledge of the signal's distribution function in the alternative hypothesis is often unavailable. A *generalized sequential probability ratio test* (GSPRT) was investigated for this purpose in [63].

In the realm of cognitive radio, distributed sequential detection strategies have become widely employed for spectrum sensing [64–68]. In particular, [69] applied the distributed sequential detection paradigm to develop spectrum sensing schemes for cognitive radio networks, exploring quantization strategies. Practical considerations such as imperfect reporting channels and the need for reduced energy consumption were addressed in subsequent works [70, 71].

Truncated versions of sequential tests have been explored to limit decision time and prevent excessively long durations. A thorough exploration of truncated tests can be found in [60]. Truncation was initially explored for SPRT and GSPRT in [72] and has more recently been adopted in combination with other tests [56, 57, 73, 74].

This thesis primarily focuses on WSNs characterized by hierarchical structures. In these networks, the lowest layer, represented by the sensors, is responsible for sensing the surrounding environment and transmitting data autonomously to the higher layer(s). This setup contrasts with fully decentralized WSNs, where the FC

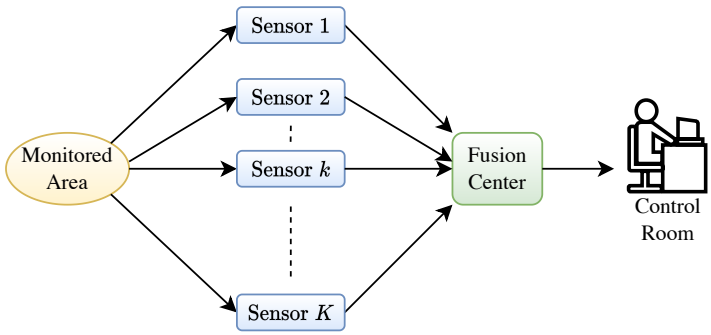

Figure 1.2: Basic structure of a distributed WSN.

is absent, and inference tasks are achieved through consensus strategies. Relevant literature about such setups can be found in [75, 76].

1.2 Scope and Objective

This thesis focuses on detecting critical events and, whenever possible, estimating their precise location, specifically emphasizing industrial settings. The research aims to develop distributed WSN architectures and associated data processing algorithms, leveraging statistical signal processing and data fusion methodologies (see Figure 1.2 for a schematic representation).

In particular, the research is guided by the following objectives:

O1 Design WSN architectures organized into hierarchical layers, following the principles of both the edge-cloud and edge-fog-cloud paradigms. These hierarchical structures allocate increasing computational complexity to nodes ascending through the layers.

O2 Introduce a statistical-based approach that empowers users to apply the proposed algorithms effectively, even in scenarios with limited previously collected data. This is particularly valuable when dealing with rare events, where data-driven methods often fall short. This approach ensures the practicality and versatility of the methods across a wide range of operational conditions.

O3 Integrate domain-specific knowledge into the design of detection and localization rules. By leveraging expertise in the relevant field, the aim is to enhance the performance and accuracy of the proposed detection and localization system, making it more adaptive to the unique characteristics of the specific industrial environment.

1.3 Contributions and Publications

The work presented in this thesis addresses the objectives **O1**, **O2**, and **O3** reported in Section 1.2 and spans three main contributions, each focusing on different categories of signal processing techniques for detection and localization.

In general, the following steps have been used to form the methodology adopted in this thesis:

1. Identifying the problem, examining its current challenges, and assessing the societal requirements related to the topic.
2. Conducting a comprehensive review of the state of the art in the field.
3. Formulating the problem mathematically, which involves characterizing the signals and modeling the monitored system appropriately.
4. Developing suitable algorithms for implementation within WSNs, ensuring that these algorithms align with the objectives mentioned in Section 1.2.
5. Analyzing the computational complexity of the developed algorithms to ensure their practical feasibility.
6. Selecting relevant metrics for evaluating the detection and localization algorithms.
7. Implementing relevant case studies to test the proposed architectures in practical settings.
8. Presenting the results obtained through simulation and analytical derivations when applicable.

1.3.1 Thesis Contributions

The three main contributions of the thesis, each focusing on different signal processing techniques for detection and localization, are here outlined: (**C1**) per-sample/batch detection, (**C2**) quickest detection, and (**C3**) sequential detection.

In the context of the thesis, each of the three main contributions is associated with a key publication. In particular, the work in contribution **C1** is primarily detailed in publication **P3**, which involves per-sample/batch detection and localization. **C2** is developed in **P5** which focuses on the quickest detection and localization framework. **C3** is explored in **P8** which deals with sequential analysis.

Section 1.3.2 gives the complete list of publications.

Each of these publications contributes to advancing the field of statistical data processing in the context of industrial WSNs, offering innovative architectural designs tailored for specific applications and addressing the thesis's outlined objectives.

The three contributions are summarized as follows.

C1 Per-Sample Detection and Localization: This contribution addresses the use of per-sample detection approaches in distributed WSNs for detecting and localizing unwanted events in industrial plants, with a case study on oil leakages from the *subsea production system* (SPS) of the Goliat FPSO [77].[1]

This contribution aims at satisfying the objective **O2** by implementing variations and modifications of well-known statistical detection and localization procedures, lowering their computational complexity.

This work has been carried out within publications **P1**, **P2**, and **P3**. The contributions can be summarized as follows:

- Various optimization criteria for the selection of the detection thresholds were studied both for the sensors and the FC with a focus on three objective functions, namely the *Youden's Index*, the *Closest-to-(0,1)*, and the *Concordance Probability*.
- At a local level, the detection is carried out via optimal test statistics, while at the FC level, two fusion rules are used: the widely recognized CR is a familiar concept, alongside the newly introduced *modified Chair-Varshney rule* (MVCR). While maintaining the computational complexity of the CR, the MVCR offers increased flexibility and the potential for improved performance.
- The proposed localization methods are divided into two primary categories: heuristic and statistical approaches. Within the heuristic methods, there is the *centroid-based algorithm* (CBA), and a novel approach called the *modified centroid-based algorithm* (MCBA). The MCBA, as a modification of the former, eliminates the constraint that the event must be situated within the smallest convex volume encompassing all sensors while maintaining the same algorithm's complexity. On the statistical side, two Bayesian algorithms are introduced: a *maximum a-posteriori* (MAP) estimator and a *minimum mean square error* (MMSE) estimator. These leverage the failure rates of the monitored plant's components to establish prior probabilities for component faults. All these algorithms are engineered for enhanced performance while containing their inherent complexity.

[1] FPSO is the acronym for *floating production storage and offloading* unit.

This contribution reduces the disparity between recent advancements in distributed data fusion and their practical implementation in industrial settings. It introduces innovative energy-efficient fusion rules explicitly designed for detection and localization in the process and energy industry. These rules consider the reliability of components, thereby introducing a significant advancement by connecting the existing knowledge within the industry with the capabilities offered by contemporary information fusion techniques. Such research on applied distributed batch data processing extends the contributions outlined in Section 1.1.

C2 Quickest Detection and Localization: Building upon the oil and gas case study from **C1**, this contribution introduces a quickest detection approach in distributed WSNs. To satisfy objective **O3**, the quickest detection approach is here enhanced by its combination within a Bayesian framework, which aims at providing optimal detection and localization system via the exploitation of reliability data regarding the monitored environment. Moreover, satisfying objective **O1** is a pillar of this research as two architectures with different numbers of layers are proposed.

The abovementioned is found in publications **P4** and **P5**. Hence, the contributions are the following:

- Two spatio-temporal sensor fusion approaches are presented. These WSN architectures carry out quickest detection and localization of faults within a system. Specifically, the sensors observe the status of various equipment components and communicate their decisions to *two their immediate superior hierarchical layer*. Moreover, the highest hierarchical unit continuously transmits updated parameters to the lower layers for improved performance.
- The *three-layer architecture* (3LA) aligns to an edge-fog-cloud [78] paradigm and is composed of a FC which performs spatial aggregation and an optimal per-sample decision. A *post-processing center* (PPC) subsequently processes these decisions over time. The PPC is responsible for identifying system faults based on a Bayesian approach and takes advantage of time-varying statistical distributions influenced by the reliability data of system components.
- The *two-layer architecture* (2LA) aligns to an edge-cloud paradigm and is composed of a FC only, which performs a joint spatio-temporal aggregation in a Bayesian quickest detection fashion.

This study builds upon the findings of **C1**, which focused on developing Bayesian methods for distributed quickest fault detection and localization

within the process and energy sectors. Given the ongoing evolution of quickest detection methods, this research expands upon the insights presented in Section 1.1 by introducing two novel multi-layer architectures tailored to leverage fault models. Employing a Bayesian framework enables the utilization of reliability data to introduce spatio-temporal biases into the inferential processes. Moreover, this approach, combined with an energy-efficient multi-layer architecture, represents a significant advancement beyond current state-of-the-art methodologies.

C3 Sequential Detection and Localization: This contribution proposes a sequential hypothesis testing approach for detection in industrial settings. In **C2**, objective **O3** has been addressed by incorporating reliability data regarding the monitored components into the detector, resulting in a Bayesian approach. In **C3**, on the other hand, the domain knowledge is incorporated by exploiting the knowledge of the mathematical model that describes the signal dispersion in space, therefore improving the likelihood of the measured signals. To properly evaluate the benefits of using the integration of the dispersion model within the design of the detection and localization algorithm, the *Bayesian* approach is here dropped in favor of a *classical* approach.[2] Due to particular risks related to the LOC of heavy gas, the case study of *carbon dioxide* (CO_2) is here taken into consideration. The work in **P8** focuses on the detection task. However, some localization algorithms have been compared in a batch detection scenario in **P6** and **P7**.

This research is found in publications **P6**, **P7**, and **P8**. The contributions can be summarized as follows:

- Modeling the release of CO_2 by employing analytical relationships derived from the well-established empirical model by *Britter & McQuaid* (B&M). This approach eliminates the need for manual inspection of a nomogram.
- Integrating the gas dispersion model and external measurements from weather stations (e.g., wind measurements) into the design of the FC forms the basis of this study.
- Introduction of a fully-batch algorithm with a fixed sample size at sensors and FC.

[2] In the Bayesian framework, the detection and estimation tasks are performed on *events* and *random variables*, respectively. On the other hand, in the classical framework, the same tasks are performed on *hypotheses* and *deterministic parameters*, respectively. Note that hybrid approaches are often employed.

- Introduction of the *decision-triggered sampling algorithm* (DTSA) as the first proposed sequential method. This involves the FC sampling the sensors' transmission only when local decisions are made.
- Introduction of the *continuous sampling algorithm* (CSA) as the second proposed sequential method. In the CSA, the FC continuously monitors sensor transmissions, incorporating a *time-aware* algorithm that updates a test statistic based on transmission values and time elapsed since the last sensors' decision at each instant.

This contribution greatly extends the state of the art in industrial monitoring via distributed sequential detection described in Section 1.1. First, developing a set of gas detection algorithms able to integrate the empirical model of gas dispersion and real-time input from a weather station is beyond the current state of the art. Also, in the case of the CSA, a new time-aware data processing method is proposed (whose application goes well beyond such application), which improves the system's accuracy and detection delay performance.

1.3.2 List of Publications

The list of publications resulting from the author's research includes seven published papers and one currently under review and is reported below. These publications cover various topics of signal processing and data fusion, addressing different aspects of detection and localization in industrial settings.

P1 [79] G. Tabella, N. Paltrinieri, V. Cozzani, and P. Salvo Rossi, "Subsea Oil Spill Risk Management Based on Sensor Networks," *Chemical Engineering Transactions*, vol. 82, pp. 199–204, Oct. 2020;

P2 [80] G. Tabella, N. Paltrinieri, V. Cozzani, and P. Salvo Rossi, "Data Fusion for Subsea Oil Spill Detection Through Wireless Sensor Networks," presented at *IEEE Sensors 2020*, Rotterdam, The Netherlands, Oct. 2020;

P3 [81] G. Tabella, N. Paltrinieri, V. Cozzani, and P. Salvo Rossi, "Wireless Sensor Networks for Detection and Localization of Subsea Oil Leakages," *IEEE Sensors Journal*, vol. 21, no. 9, pp. 10890–10904, 1 May 2021;

P4 [82] G. Tabella, D. Ciuonzo, N. Paltrinieri, and P. Salvo Rossi, "Spatio-Temporal Decision Fusion for Quickest Fault Detection Within Industrial Plants: The Oil and Gas Scenario," presented at the *IEEE 24th International Conference on Information Fusion*, Sun City, South Africa, Nov. 2021;

P5 [83] G. Tabella, D. Ciuonzo, N. Paltrinieri, and P. Salvo Rossi, "Bayesian Fault Detection and Localization Through Wireless Sensor Networks in Industrial Plants," *IEEE Internet of Things Journal*, 2024. in press;

P6 [84] G. Tabella, Y. Di Martino, D. Ciuonzo, N. Paltrinieri, X. Wang, and P. Salvo Rossi, "Decision Fusion for Carbon Dioxide Release Detection from Pressure Relief Devices," presented at the *12th IEEE Sensor Array and Multichannel Signal Processing*, Trondheim, Norway, Jun. 2022, pp. 46–50;

P7 [85] G. Tabella, Y. Di Martino, D. Ciuonzo, N. Paltrinieri, X. Wang, and P. Salvo Rossi, "Sensor Fusion for Detection and Localization of Carbon Dioxide Releases for Industry 4.0," presented at the *IEEE 25th International Conference on Information Fusion*, Linköping, Sweden, Jul. 2022;

P8 [86] G. Tabella, D. Ciuonzo, Y. Yilmaz, X. Wang, and P. Salvo Rossi, "Time-Aware Distributed Sequential Detection of Gas Dispersion via Wireless Sensor Networks," *IEEE Transactions on Signal and Information Processing over Networks*, vol. 9, pp. 721-735.

1.4 Thesis Outline

The remainder of the thesis is organized as follows.

Chapter 2 overviews the proposed detection and localization frameworks, including the per-sample/batch approach, quickest detection approach, and sequential analysis, and introduces the proposed methods.

Chapter 3 focuses on two specific scenarios of interest: oil leakages in SPSs and CO_2 dispersions. This chapter includes detailed signal characterizations of these scenarios and presents results through mathematical analysis and simulations.

Finally, Chapter 4 concludes the thesis and discusses potential further research directions.

The remaining part of this thesis is dedicated to the articles that form the basis of the dissertation.

1.5 Mathematical Notation

Lowercase (respectively uppercase) bold letters represent column vectors (respectively matrices); $|\cdot|$ and $[\cdot]^{\mathrm{T}}$ denote the Euclidean norm and transpose operators, respectively; $\widehat{a}$ is an estimation of a; $\mathbb{E}(\cdot)$ represents the expectation; $\mathbb{P}(\cdot)$ and $p(\cdot)$ indicate the *probability mass functions* (PMFs) and *probability density functions*

(PDFs), while $\mathbb{P}(\cdot|\cdot)$ and $p(\cdot|\cdot)$ represent their corresponding conditional counterparts; particularly, $\mathbb{E}_i(\cdot)$, $\mathbb{P}_i(\cdot)$, and $p_i(\cdot)$ indicate the expectation, the PMF, and PDF, respectively, under the hypothesis $\mathcal{H}_i$; $F_a(\cdot)$ is the *cumulative distribution function* (CDF) of the variable a; $\mathcal{U}(a, b)$ indicates a continuous uniform distribution with a minimum value of a and a maximum value of b; $\mathcal{N}(\boldsymbol{\mu}, \boldsymbol{\Sigma})$ represents a multivariate Gaussian distribution with a mean of $\boldsymbol{\mu}$ and a covariance matrix of $\boldsymbol{\Sigma}$; $\mathrm{Exp}(\lambda)$ denotes an exponential distribution with a rate of λ; $\mathrm{Gamma}(\alpha, \beta)$ indicates a Gamma distribution with a shape of α and a rate of β; $\mathcal{Q}(\cdot)$ is the *complementary cumulative distribution function* (CCDF) of the standard normal distribution; a^+ represents the positive part of the real number a; the symbol $\sim$ signifies "distributed as;" finally, $\mathcal{O}(\cdot)$ represents the big O notation.

Chapter 2

Detection and Localization via Wireless Sensor Networks

This chapter offers a comprehensive overview of the three detection frameworks proposed in this thesis: per-sample/batch detection, quickest detection, and sequential detection, as well as their associated localization algorithms and an analysis of their computational complexity.

In particular, Section 2.1 focuses on per-sample and batch detection, presenting the widely recognized CR, the newly introduced MCVR, and related localization methods such as the well-established CBA and the newly proposed MCBA. Additionally, it discusses the utilization of MAP and MMSE localization procedures.

Section 2.2 introduces the framework of quickest detection, highlighting the newly proposed 3LA and 2LA along with their associated MAP localization algorithms.

Finally, Section 2.3 delves into the topic of sequential detection, providing insights into the newly developed DTSA and CSA.

The typical WSN architecture throughout the thesis consists of K sensors and one FC. The sensors individually sense their surrounding environment to detect the absence ($\mathcal{H}_0$) or presence ($\mathcal{H}_1$) of the event of interest.[1]

The kth sensor (where $k = 1, 2, \ldots, K$) performs a test on the received signal y_k and makes a local decision $d_k = i \in \{0, 1\}$, if $\mathcal{H}_i$ is declared. Generally speaking,

[1]The analysis of the optimal sampling frequency is never considered in the present work.

the local task consists of performing detection on the following signal:

$$\begin{cases} \mathcal{H}_0: & y_k = w_k \\ \mathcal{H}_1: & y_k = s_k(\boldsymbol{x}_k, \boldsymbol{\theta}) + w_k \end{cases}, \tag{2.1}$$

in which w_k denotes the noise contribution and $s_k(\boldsymbol{x}_k, \boldsymbol{\theta})$ is the effect on the measured signal given by the presence of the event of interest. The contribution $s_k(\boldsymbol{x}_k, \boldsymbol{\theta})$ depends, among other variables and parameters, on the position of the event of interest indicated with the vector $\boldsymbol{\theta}$ and the position of the kth sensor shown with the vector $\boldsymbol{x}_k$. Such a dependency is exploited when addressing the localization task.

Furthermore, apart from its spectral efficiency, the system demonstrates exceptional energy efficiency when utilizing *on-off keying* (OOK) modulation for communication between the sensor and the FC, as only 1-bit communication is needed on the reporting channel.

The local decisions are gathered and processed by the FC, which has the task of performing the detection task using the local decisions as primary inputs.

The global decision is $\widehat{\mathcal{H}} = i \in \{0, 1\}$, if $\mathcal{H}_i$ is declared. Specifically, when $\widehat{\mathcal{H}} = \mathcal{H}_1$, the FC provides, via an appropriate localization algorithm, an estimate of the position of the detected event denoted with the vector $\widehat{\boldsymbol{\theta}}$.

The framework mentioned above is common to the proposed methods during the work, with specific differences that will be brought to the reader's attention. Such differences, despite the efforts to keep them at a minimum, are present as the three approaches formalize the problem statement in three different mathematical ways.

2.1 Per-Sample and Batch Detection

Batch detection is one of the most common detection frameworks. It is particularly suitable for offline data processing to establish the hypothesis under which the collected measurements have been generated.

In particular, assuming N measurements are collected $\boldsymbol{y} \triangleq \begin{bmatrix} y[1] & \cdots & y[N] \end{bmatrix}^{\mathrm{T}}$, the problem is reduced to designing a decision rule of the form:

$$f(\boldsymbol{y}) \underset{\widehat{\mathcal{H}}=\mathcal{H}_0}{\overset{\widehat{\mathcal{H}}=\mathcal{H}_1}{\gtrless}} \gamma\,, \tag{2.2}$$

where $f(\boldsymbol{y})$ and γ is a test statistic function of the N measurements and a test threshold (respectively) that need to be appositely decided in the detector's design stage.

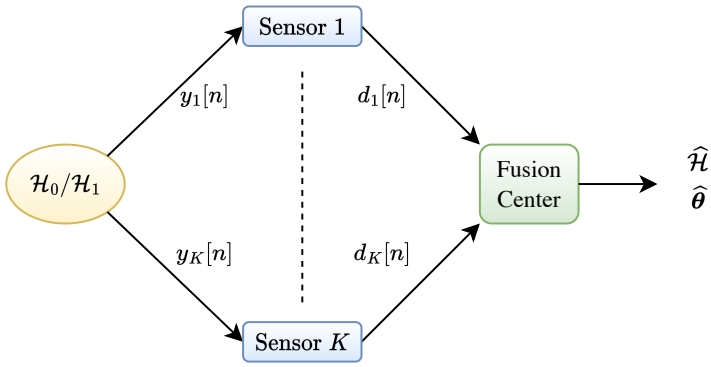

Figure 2.1: Wireless Sensor Network scheme for batch/per-sample detection and localization.

Such a framework can be adapted for online detection by performing subsequent batch detection procedures.

A critical step during the design of a batch detector is the choice of N (i.e., the amount of sample collected between two decisions). In particular, we talk about *per-sample detection* when $N = 1$. If this technique were used for online detection, a decision would be taken after every collected measurement based solely on that specific measurement.

Generally speaking, batch detection for online applications does not constitute an optimal approach. However, it might be desirable for a series of reasons:

- Ease of implementation – This framework is well-known with various available tests in both classical (based on the Neyman-Pearson theorem) and Bayesian (based on minimization of the Bayes risk) approaches.

- Lack of optimal alternatives – Generally speaking, the goal of achieving optimal solutions when designing an online detector is still an open research field, also due to the difficulty surrounding the ability to know the statistical distribution of the signal in both the null and alternative hypothesis. For this reason, detectors might often rely on repeated batch detection procedures for such applications.

- Ease of analysis – It is easier to analyze the performances of batch detectors as they are based on known and well-established mathematical theories.

2.1.1 System Model

The proposed architecture for the distributed WSN (refer to Figure 2.1) consists of K sensors and one FC. The sensors are tasked with detecting the presence ($\mathcal{H}_1$) or absence ($\mathcal{H}_0$) of a specific adverse event.

At the nth discrete time, the kth sensor individually conducts a test on the received signal $y_k[n]$ and makes a local decision $d_k[n] = i$ if $\mathcal{H}_i$ is declared. The vector of local decisions is denoted as $\boldsymbol{d}[n] = \begin{bmatrix} d_1[n] & \cdots & d_K[n] \end{bmatrix}^{\mathrm{T}}$. These local decisions are then collected and processed at the FC to arrive at a global decision $\widehat{\mathcal{H}} = i$ if $\mathcal{H}_i$ is declared.

Suppose the global decision is $\widehat{\mathcal{H}} = \mathcal{H}_1$. In that case, the FC executes a localization algorithm to estimate the event's position. Such an estimate is denoted as $\widehat{\boldsymbol{\theta}}$.

In industrial contexts, it is often possible to locate items and mechanical parts having higher failure rates, making them more prone to failure and being responsible for an adverse event. The position of the mth item is here denoted with $\boldsymbol{\theta}_m$, with $m = 1, \ldots, M$.

For the sake of simplicity, it is assumed that the component failures are statistically independent. The *static prior probability of item failure* with respect to the mth item is denoted with φ_m and is the following:

$$\varphi_m \triangleq \mathbb{P}_1(\boldsymbol{\theta} = \boldsymbol{\theta}_m) = \frac{\lambda_m}{\sum_{m=1}^{M} \lambda_m} , \tag{2.3}$$

where λ_m is the failure rate of the mth item.

2.1.2 Signal Model

During the nth discrete time, the kth sensor measures a signal $y_k[n]$. Depending on the corresponding hypothesis, the signal is defined as follows:

$$\begin{cases} \mathcal{H}_0 : & y_k[n] = w_k[n] \\ \mathcal{H}_1 | m : & y_k[n] = s_k^n(\boldsymbol{x}_k, \boldsymbol{\theta}_m) + w_k[n] \end{cases} , \tag{2.4}$$

where $s_k^n(\boldsymbol{x}_k, \boldsymbol{\theta}_m)$ represents the contribution at the kth sensor on the measured signal given by the presence of the event of interest in correspondence of the mth item and $w_k[n]$ represents the measurement noise. $s_k^n(\boldsymbol{x}_k, \boldsymbol{\theta}_m)$ is a function of the location of the kth sensor ($\boldsymbol{x}_k$) and the position of the mth item ($\boldsymbol{\theta}_m$) and can be either a deterministic parameter or a random variable. $s_k^n(\boldsymbol{x}_k, \boldsymbol{\theta}_m)$ and $w_k[n]$ are assumed statistically independent thanks to the spatial separation of the sensors.

2.1.3 Local Detection

At the nth instant, the kth sensor computes a statistic Λ_n^k and performs a test on it aimed at making a local decision $d_k[n]$ [87]:

$$\Lambda_n^k \underset{d_k[n]=0}{\overset{d_k[n]=1}{\gtrless}} \gamma_k \ , \tag{2.5}$$

where γ_k is the local threshold. The local performances of this test, in terms of *local probability of false alarm* ($\mathcal{P}_F^k$) and *local probability of detection* with respect to the mth item ($\mathcal{P}_D^{(k,m)}$), are defined as follows:

$$\mathcal{P}_F^k \triangleq \mathbb{P}_0(d_k[n]=1) = \mathbb{P}_0\Big(\Lambda_n^k \geq \gamma_k\Big) \ , \tag{2.6}$$

$$\mathcal{P}_D^{(k,m)} \triangleq \mathbb{P}_1(d_k[n]=1|\boldsymbol{\theta}=\boldsymbol{\theta}_m) = \mathbb{P}_1\Big(\Lambda_n^k \geq \gamma_k \Big| \boldsymbol{\theta}=\boldsymbol{\theta}_m\Big) \ . \tag{2.7}$$

2.1.4 Counting Rule and Modified Chair Varshney Rule

The FC assesses the presence of the event of interest based on a test statistic (Λ) depending on the local decisions $d_k[n]$'s after these are transmitted by the sensors:

$$\widehat{\mathcal{H}} = \begin{cases} \mathcal{H}_0 \, , & \Lambda < \gamma^* \\ \mathcal{H}_1 \, , & \Lambda \geq \gamma^* \end{cases} \ , \tag{2.8}$$

where γ^* is the global threshold.

The *uniformly most powerful* (UMP) test for this application is the CVR reported below:

$$\Lambda_n^{\text{CVR}} \triangleq \sum_{k=1}^{K} \left[d_k[n] \ln\left(\frac{\mathcal{P}_D^k}{\mathcal{P}_F^k}\right) + (1-d_k[n]) \ln\left(\frac{1-\mathcal{P}_D^k}{1-\mathcal{P}_F^k}\right)\right] \ , \tag{2.9}$$

with $\mathcal{P}_D^k \triangleq \mathbb{P}_1(d_k[n]=1)$.

The CVR is obtained as a result of the *likelihood ratio test* (LRT) [19]. Regrettably, the CVR cannot be employed in its current form as it necessitates knowledge of the probabilities of detection, denoted as $\mathcal{P}_D^k$.

One possibility to overcome this issue is to refer to mean performances, i.e.:

$$\overline{\mathcal{P}_D^k} \triangleq \sum_{m=1}^{M} \varphi_m \mathcal{P}_D^{(k,m)} \ . \tag{2.10}$$

Two different low-complexity fusion rules are considered for computing the test statistic at the FC: (i) the CR and (ii) the MCVR.

More specifically, the corresponding test statistics are computed as follows:

$$\Lambda_n^{\mathrm{CR}} \triangleq \sum_{k=1}^{K} d_k[n] \;, \tag{2.11}$$

$$\Lambda_n^{\mathrm{MCVR}} \triangleq \sum_{k=1}^{K} \left[d_k[n] \ln\left(\frac{\overline{\mathcal{P}_D^k}}{\mathcal{P}_F^k}\right) + (1-d_k[n]) \ln\left(\frac{1-\overline{\mathcal{P}_D^k}}{1-\mathcal{P}_F^k}\right)\right] . \tag{2.12}$$

The MCVR here proposed replaces the values of $\mathcal{P}_D^k$'s used in the CVR with the corresponding values $\overline{\mathcal{P}_D^k}$'s shown in Equation (2.10).

The performance of the system for each fusion rule is characterized in terms of *global probability of detection* with respect to the failure of the mth item ($Q_D^{(m)}$) and *global probability of false alarm* (Q_F).

$$\begin{aligned} Q_D^{(m)} &\triangleq \mathbb{P}_1\Big(\widehat{\mathcal{H}} = \mathcal{H}_1 \Big| \boldsymbol{\theta} = \boldsymbol{\theta}_m\Big) = \mathbb{P}_1(\Lambda \geq \gamma^* | \boldsymbol{\theta} = \boldsymbol{\theta}_m) \\ &= \sum_{\boldsymbol{d}:\Lambda(\boldsymbol{d})\geq\gamma^*} \prod_{k=1}^{K} \left[\left(\mathcal{P}_D^{(k,m)}\right)^{d_k} \left(1-\mathcal{P}_D^{(k,m)}\right)^{1-d_k}\right] , \end{aligned} \tag{2.13}$$

$$\begin{aligned} Q_F &\triangleq \mathbb{P}_0\Big(\widehat{\mathcal{H}} = \mathcal{H}_1\Big) = \mathbb{P}_0(\Lambda \geq \gamma^*) \\ &= \sum_{\boldsymbol{d}:\,\Lambda(\boldsymbol{d})\geq\gamma^*} \prod_{k=1}^{K} \left[\left(\mathcal{P}_F^{k}\right)^{d_k} \left(1-\mathcal{P}_F^{k}\right)^{1-d_k}\right] , \end{aligned} \tag{2.14}$$

where Λ is any fusion rule performed by the FC.

2.1.5 Other Fusion Rules

Other rules can be used to fuse the local decisions coming from the sensors. In this thesis, the LRT with *Bayesian marginalization* (BLRT) and the GLRT have also been explored. These tests have the following forms:

$$\Lambda_n^{\mathrm{BLRT}} \triangleq \sum_{m=1}^{M} \left\{ \varphi_m \prod_{k=1}^{K} \left[\left(\frac{\mathcal{P}_D^{(k,m)}}{\mathcal{P}_F^k}\right)^{d_k[n]} \left(\frac{1-\mathcal{P}_D^{(k,m)}}{1-\mathcal{P}_F^k}\right)^{1-d_k[n]}\right]\right\} , \tag{2.15}$$

$$\Lambda_n^{\mathrm{GLRT}} \triangleq \max_m \sum_{k=1}^{K} \left[d_k[n] \ln\left(\frac{\mathcal{P}_D^{(k,m)}}{\mathcal{P}_F^k}\right) + (1-d_k[n]) \ln\left(\frac{1-\mathcal{P}_D^{(k,m)}}{1-\mathcal{P}_F^k}\right)\right] . \tag{2.16}$$

The calculation of system performances follows the same procedure reported in Equations (2.13) and (2.14).

2.1.6 Localization Algorithms

Let us assume that, at instant $n = 1$, the FC declares $\widehat{\mathcal{H}} = \mathcal{H}_1$: in such a scenario, the system provides an estimate of its position. In practical scenarios, the location of an unwanted event remains unknown until inspection is performed.

In this work, four different algorithms are presented: (i) CBA, (ii) MCBA, (iii) MAP localization, and (iv) MMSE localization.

Centroid-Based Algorithm

The algorithm relies on the following steps:

1. At time n, obtain the centroid of the sensors reporting $d_k[n] = 1$:

$$\boldsymbol{x}^{(\mathrm{c})}[n] = \frac{\sum_{k=1}^{K} d_k[n]\boldsymbol{x}_k}{\sum_{k=1}^{K} d_k[n]} \,. \tag{2.17}$$

2. Compute the *cumulative moving average* (CMA) of the centroid positions:

$$\overline{\boldsymbol{x}^{(\mathrm{c})}}[n] = \begin{cases} \boldsymbol{x}^{(\mathrm{c})}[1]\,, & n = 1 \\ \overline{\boldsymbol{x}^{(\mathrm{c})}}[n-1] + \frac{\boldsymbol{x}^{(\mathrm{c})}[n] - \overline{\boldsymbol{x}^{(\mathrm{c})}}[n-1]}{n}\,, & n > 1 \end{cases} . \tag{2.18}$$

3. Assuming that N measurements are allowed to be collected between the declaration of the presence of an adverse event and the declaration of $\widehat{\boldsymbol{\theta}}$, the final result is obtained by minimizing the distance between the positions of the items and the CMA of the centroid:

$$\widehat{m} = \arg\min_{m} \left\| \overline{\boldsymbol{x}^{(\mathrm{c})}}[N] - \boldsymbol{\theta}_m \right\| , \tag{2.19}$$

$$\widehat{\boldsymbol{\theta}} = \boldsymbol{\theta}_{\widehat{m}} \,. \tag{2.20}$$

Modified Centroid-Based Algorithm

This algorithm is introduced because the CBA is unable to localize events caused by items positioned outside the smallest convex volume encompassing all K sensors. This limitation is addressed through a modification of Equation (2.17). The heuristic consists of accounting for the antipodal point with respect to a point reflection, with

the centroid being the point of inversion, for each sensor declaring $d_k[n] = 0$. First, it is necessary to define $\boldsymbol{z}$ as the centroid of all sensors:

$$\boldsymbol{z} = \frac{1}{K} \sum_{k=1}^{K} \boldsymbol{x}_k \ . \tag{2.21}$$

Given that this term remains constant over time, there is no need to repeat this step. Subsequently, the modified centroid, which considers both the active sensors (via their actual positions) and inactive sensors (via antipodal positions), is determined:

$$\boldsymbol{x}^{(\mathrm{mc})}[n] = 2\boldsymbol{x}^{(\mathrm{c})}[n] - \boldsymbol{z} \ . \tag{2.22}$$

Including the antipodal positions enables the FC to localize events beyond the perimeter of the sensors. It is possible to perform this algorithm by substituting Equation (2.17) in Step 1 of the CBA with Equation (2.22).

Maximum A-Posteriori Localization

The following Bayesian estimator is proposed in order to exploit the knowledge of the values of φ_m's:

1. For each item, compute the log-likelihood with respect to the failure of the mth item of the decision vector at the nth discrete-time as $\boldsymbol{d}[n]$:

$$\begin{aligned} &\ln \mathbb{P}_1(\boldsymbol{d}[n] | \boldsymbol{\theta} = \boldsymbol{\theta}_m) \\ &= \sum_{k=1}^{K} \left[d_k[n] \ln \mathcal{P}_D^{(k,m)} + (1 - d_k[n]) \ln \left(1 - \mathcal{P}_D^{(k,m)} \right) \right] . \end{aligned} \tag{2.23}$$

2. For each item, calculate the joint probability of the decision vectors up to the current discrete time using the updating formula in Equation (2.24). This formula exploits the conditional independence of sensor decisions in both space and time:

$$\begin{aligned} &\ln \mathbb{P}_1(\boldsymbol{d}[n], \ldots, \boldsymbol{d}[1], \boldsymbol{\theta} = \boldsymbol{\theta}_m) \\ &= \begin{cases} \ln \mathbb{P}_1(\boldsymbol{d}[1] | \boldsymbol{\theta} = \boldsymbol{\theta}_m) + \ln \varphi_m \, , & n = 1 \\ \ln \mathbb{P}_1(\boldsymbol{d}[n] | \boldsymbol{\theta} = \boldsymbol{\theta}_m) + \ln \mathbb{P}_1(\boldsymbol{d}[n-1], \ldots, \boldsymbol{d}[1], \boldsymbol{\theta} = \boldsymbol{\theta}_m) \, , & n > 1 \end{cases} . \end{aligned} \tag{2.24}$$

3. Assuming that N measurements are allowed to be collected between the declaration of the presence of an adverse event and the declaration of $\widehat{\boldsymbol{\theta}}$, the final result is obtained through joint probability maximization:

$$\widehat{m} = \arg\max_{m} \ln \mathbb{P}_1(\boldsymbol{d}[1], \ldots, \boldsymbol{d}[N], \boldsymbol{\theta} = \boldsymbol{\theta}_m) \ , \tag{2.25}$$

$$\widehat{\boldsymbol{\theta}} = \boldsymbol{\theta}_{\widehat{m}} \ . \tag{2.26}$$

Note that fixing $\varphi_1 = \ldots = \varphi_M = 1$ (therefore treating φ_m's as *improper priors*) turns the algorithm into a *maximum likelihood estimator* (MLE).

Minimum Mean Square Error Localization

For compactness, let us introduce the following definition:

$$\alpha_m[n] \triangleq \mathbb{P}_1(\boldsymbol{d}[n], \ldots, \boldsymbol{d}[1], \boldsymbol{\theta} = \boldsymbol{\theta}_m) \,. \tag{2.27}$$

1. For each item, compute the likelihood of the decision vector at the nth discrete time, denoted as $\boldsymbol{d}[n]$, given that the event is located at the mth item. This calculation involves exploiting the conditional independence of sensor decisions in space:

$$\mathbb{P}_1(\boldsymbol{d}[n]|\boldsymbol{\theta} = \boldsymbol{\theta}_m) = \prod_{k=1}^{K} \left[\left(\mathcal{P}_D^{(k,m)} \right)^{d_k[n]} \left(1 - \mathcal{P}_D^{(k,m)} \right)^{1-d_k[n]} \right] . \tag{2.28}$$

2. Obtain the geometric mean of all the probabilities $\mathbb{P}_1(\boldsymbol{d}[n]|\boldsymbol{\theta} = \boldsymbol{\theta}_m)$'s:

$$c[n] = \sqrt[M]{\prod_{m=1}^{M} \mathbb{P}_1(\boldsymbol{d}[n]|\boldsymbol{\theta} = \boldsymbol{\theta}_m)} \,. \tag{2.29}$$

3. For each item, compute the scaled version of the joint probability $\alpha_m[n]$ via the following updating formula:

$$\tilde{\alpha}_m[n] = \begin{cases} \varphi_m \,, & n = 0 \\ c[n]^{-1} \mathbb{P}_1(\boldsymbol{d}[n]|\boldsymbol{\theta} = \boldsymbol{\theta}_m) \tilde{\alpha}_m[n-1] \,, & n > 0 \end{cases} . \tag{2.30}$$

4. Calculate the expected value of the posterior probability of the event position given the vectors of decisions up to the current discrete time:

$$\boldsymbol{x}^{(\mathrm{MMSE})}[n] = \mathbb{E}_1(\boldsymbol{\theta}|\boldsymbol{d}[n], \ldots, \boldsymbol{d}[1]) = \frac{\sum_{m=1}^{M} \tilde{\alpha}_m[n] \boldsymbol{\theta}_m}{\sum_{m=1}^{M} \tilde{\alpha}_m[n]} \,. \tag{2.31}$$

5. Assuming that N measurements are allowed to be collected between the declaration of the presence of an adverse event and the declaration of $\widehat{\boldsymbol{\theta}}$, the final result is obtained via distance minimization between the positions of the items and the result of Equation (2.31):

$$\widehat{m} = \arg\min_{m} \left\| \boldsymbol{x}^{(\mathrm{MMSE})}[N] - \boldsymbol{\theta}_m \right\| \,, \tag{2.32}$$

$$\widehat{\boldsymbol{\theta}} = \boldsymbol{\theta}_{\widehat{m}} \,. \tag{2.33}$$

Table 2.1: Computational complexity of the per-sample/batch detection and localization algorithms.

Task	Algorithm	Complexity
Detection	CR	$\mathcal{O}(K)$
	MCVR	$\mathcal{O}(K)$
	BLRT	$\mathcal{O}(KM)$
	GLRT	$\mathcal{O}(KM)$
Localization	CBA	$\mathcal{O}(K+M)$
	MCBA	$\mathcal{O}(K+M)$
	MAP	$\mathcal{O}(KM)$
	MMSE	$\mathcal{O}(KM)$

2.1.7 Computational Complexity

In Table 2.1, the computational complexity of all introduced fusion rules and the localization rules is reported.

It is shown that the proposed MCVR has the same amount of computational complexity as the CR, which is known for being a low-complexity fusion rule.

Table 2.1 also compares the computational complexity of the proposed localization algorithms, showing that the heuristic methods have the advantage of a reduced computational complexity than the statistical-based methods.

2.2 Quickest Detection

Quickest detection is a framework that finds its main application within online time-series analysis.

This framework assumes that the collected measurements initially belong to the null hypothesis $\mathcal{H}_0$. At a moment in time, they will belong to the alternative hypothesis $\mathcal{H}_1$. Note that in this section, the null hypothesis $\mathcal{H}_0$ that indicates the absence of an event of interest is denoted with $\mathcal{H}[n]=0$, while the alternative hypothesis $\mathcal{H}_1$ indicating the presence of an event of interest is denoted with $\mathcal{H}[n]=1$, therefore turning $\mathcal{H}_0/\mathcal{H}_1$ into a binary variable function of time.

The goal is to rapidly identify such a change in the signal model, exploiting the change in its statistical distribution. Specifically, assuming n measurements $\boldsymbol{y}[n] \triangleq$

$\begin{bmatrix} y[1] & \cdots & y[n] \end{bmatrix}^{\mathrm{T}}$ have been collected, the goal is to detect whether there has been a change in the signal model at any instant in the interval $[1, n]$. If such a change has not been detected, this procedure will be repeated after collecting the $(n+1)$th sample, where now the task is to detect the possible change in the signal model at any instant in the interval $[1, n+1]$.

In particular, at a generic instant n, the problem consists of designing a decision rule of the form:

$$f(\boldsymbol{y}[n]) \underset{\widehat{\mathcal{H}}[n]=0}{\overset{\widehat{\mathcal{H}}[n]=1}{\gtrless}} \gamma \,, \tag{2.34}$$

where $f(\boldsymbol{y}[n])$ and γ are a test statistic function of the $\boldsymbol{y}[n]$ and a test threshold (respectively) to be designed. Note that, depending on the decision rule, it might be possible to even estimate the discrete time point $n_0 \in [1, n]$ such that $\mathcal{H}[n_0 - 1] = 0$ and $\mathcal{H}[n_0] = 1$.

Unlike the batch detection case, relying on an optimal detection rule in both classical and Bayesian frameworks is impossible.

While the Bayesian approach can rely on a set of decision rules to achieve optimality, various algorithms exist that satisfy different optimality criteria within the classical framework. Such criteria have been created to compensate for the impracticality of finding a UMP test.

Quickest detection is the approach that ought to be employed when designing an online detector. However, this approach comes with disadvantages:

- Need for recursive form – At any given instant n, the detection rule should remain a function of all the measurements collected within $[1, n]$. However, this process requires increased memory and processing power as n increases, with the likely result of making the detection procedure computationally unfeasible. Many of the quickest detection rules can be performed recursively to achieve the same result at a reduced computational cost. This means finding a function h, such that $f(\boldsymbol{y}[n]) = h(y[n], h(\boldsymbol{y}[n-1]))$. However, this is not always possible, especially when the problem deviates from the ideal case of fully known distributions in the two hypotheses. When relying on the convenience of a recursive form is impossible, it is often necessary to resort to sub-optimal options.

- Frequent lack of optimality – As stated regarding the classical framework, obtaining a UMP test is impossible. Therefore, other optimality criteria are used (often based on *minimax* rules). Such optimality criteria are likely

less meaningful for industrial applications compared to the more intuitive concepts of the UMP test and Bayesian detection.

- Difficulty of analysis – It is common for quickest detection rules to carry a certain degree of complexity, making assessing their performances often unfeasible through analytical means.

2.2.1 System Model

As in Section 2.1, the plant is conceptualized as a system comprising M items. Here, each item's state at discrete-time n is represented by the following state variable:

$$\mathcal{H}_m[n] = \begin{cases} 0\,, & m\text{th item is } \textbf{operational} \\ 1\,, & m\text{th item is } \textbf{faulty} \end{cases}, \tag{2.35}$$

where *operational* indicates that the item is functioning as intended with no immediate action required, while *faulty* signifies that the item requires maintenance. On the other hand, the state variable at discrete-time n for the *whole system* is defined as:

$$\mathcal{H}[n] = 1 - \prod_{m=1}^{M} (1 - \mathcal{H}_m[n]) = \begin{cases} 0\,, & \textbf{operational} \text{ system} \\ 1\,, & \textbf{faulty} \text{ system} \end{cases}, \tag{2.36}$$

implying *independent failures and a series system*. An item retains a faulty state until maintenance is carried out. In the present work, when an item becomes faulty, the sensors that monitor the system measure a signal with a different statistical distribution. After detecting such a shift in the distribution, an inspection is carried out to evaluate the whole system, and maintenance is executed on faulty items.

The operational life of the generic mth item is modeled as a *homogeneous Poisson process* characterized by its failure rate λ_m (see Figure 2.2).

In these modeling, $T_{m,j}$ represents the amount of time the mth item spends in the operational state between the $(j-1)$th and the jth generic failures. It follows that $T_{m,j} \sim \text{Exp}(\lambda_m)$. Furthermore, $T^*_{m,j} \triangleq T_{m,j} + \varepsilon_{m,j}$ where $\varepsilon_{m,j}$ represents the *detection delay*. At instant n, τ_n is the amount of time elapsed since the most recent inspection. A consequence of the failure model is the derivation of the *failure function* for the mth item:

$$F_m[n] = \mathbb{P}(\mathcal{H}_m[n] = 1) = 1 - e^{-\lambda_m \tau_n}\,. \tag{2.37}$$

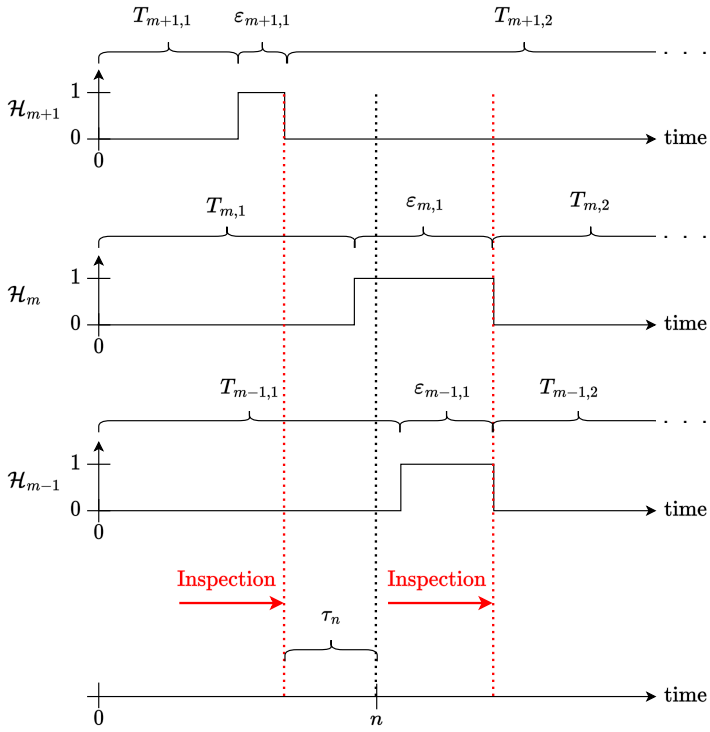

Figure 2.2: Failure model (excluding inspection and maintenance periods).

Subsequently, the failure function for the entire system is determined:

$$F[n] = \mathbb{P}(\mathcal{H}[n] = 1) = 1 - \prod_{m=1}^{M} (1 - F_m[n]) \approx \sum_{m=1}^{M} F_m[n] \, . \tag{2.38}$$

Such an approximation (henceforth called *rare events approximation*) is used when the items constituting the system have sufficiently low values of $F_m[n]$'s resulting in their products becoming negligible [88].

Furthermore, Equation (2.38) suggests the occurrence of *disjoint failures*. This implies that at any given instant n, *at most* one item will be faulty. The rare event approximation allows the definition of a *dynamic prior probability of item failure* for the mth item labeled as $\varphi_m[n]$:

$$\varphi_m[n] \triangleq \mathbb{P}(\mathcal{H}_m[n] = 1 | \mathcal{H}[n] = 1) \approx \frac{\mathbb{P}(\mathcal{H}_m[n] = 1)}{\mathbb{P}(\mathcal{H}[n] = 1)} = \frac{F_m[n]}{F[n]} \, . \tag{2.39}$$

In this work, the WSN collects measurements via the sensors with a sampling

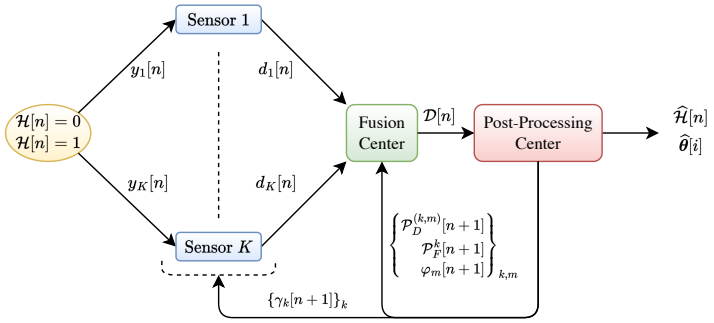

(a) Three-Layer Architecture.

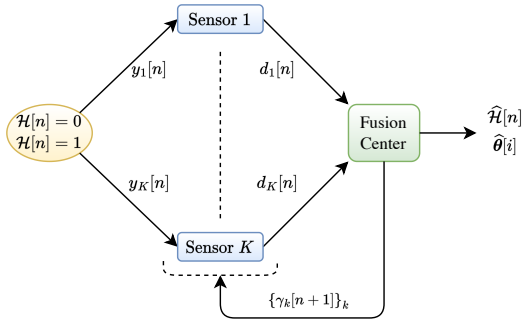

(b) Two-Layer Architecture.

Figure 2.3: Proposed Wireless Sensor Network scheme for quickest detection and localization.

interval of Δt, while n_0 indicates the first discrete-time instant that follows the last inspection.

Two fusion architectures are presented here. The first (3LA) uses an *edge-fog-cloud* approach where the network can be separated into three hierarchical layers with growing computational power as we approach the cloud layer (see Figure 2.3(a)). In contrast, the second (2LA) uses two hierarchical layers, i.e., an *edge-cloud approach* (see Figure 2.3(b)). Both architectures are equipped with a feedback system transmitting updated parameters from the cloud layer to the lower layers.

The proposed WSN architectures comprise a set of K sensors responsible for monitoring the area of interest, aiming to identify if the system is in an operational ($\mathcal{H}[n]=0$) or a faulty state ($\mathcal{H}[n]=1$) at a given discrete-time n. The generic kth sensor performs a per-sample detection of the signal $y_k[n]$. It does so by comparing a statistic derived from the measured signal to a time-dependent threshold $\gamma_k[n]$. A local decision is indicted with $d_k[n]=i$ when the sensor declares $\mathcal{H}[n]=i$.

2.2.2 Signal Model

The signal model is analogous to the one introduced in Section 2.1.2. However, it needs to be adapted to the new mathematical model used to represent failures in the system.

The expression for the received signal $y_k[n]$ at the kth sensor during the nth discrete-time point is then rewritten as follows:

$$y_k[n] = \sum_{m=1}^{M} \mathcal{H}_m[n] s_k^n(\boldsymbol{x}_k, \boldsymbol{\theta}_m) + w_k[n] \ , \tag{2.40}$$

where the variables composing the signal have been defined when discussing Equation (2.4) In particular, when $\mathcal{H}[n] = 0$, we have $\sum_{m=1}^{M} \mathcal{H}_m[n] = 0$, whereas when $\mathcal{H}[n] = 1$, we have $\sum_{m=1}^{M} \mathcal{H}_m[n] \geq 1$.

Note that the rare event approximation introduced in Equation (2.38) hinders the possibility of modeling more than one faulty item at a given time.

2.2.3 Local Detection

This section describes the local detector that is common to both proposed architectures.

The optimal test is a BLRT on $y_k[n]$. Here, the unknown location of the faulty item is marginalized using the dynamic prior probability of item failure from Equation (2.39). Precisely, at the nth instant, the kth sensor performs a *maximum likelihood* (ML) detection:

$$\frac{p(y_k[n]|\mathcal{H}[n]=1)}{p(y_k[n]|\mathcal{H}[n]=0)} = \frac{\sum_{m=1}^{M} \varphi_m[n]\, p(y_k[n]|\mathcal{H}_m[n]=1)}{p(y_k[n]|\mathcal{H}[n]=0)} \underset{d_k[n]=0}{\overset{d_k[n]=1}{\gtrless}} 1 \ . \tag{2.41}$$

Since Equation (2.41) requires the parameters $\varphi_m[n]$'s and has a computational complexity of $\mathcal{O}(M)$, we convert it into an equivalent, but computationally simpler test Λ_n^k:

$$\Lambda_n^k \underset{d_k[n]=0}{\overset{d_k[n]=1}{\gtrless}} \gamma_k[n] \ , \tag{2.42}$$

where the only time-varying parameter is $\gamma_k[n]$ which is transmitted by the highest layer. Such a test will have a $\mathcal{O}(1)$.

The performances of the test in Equation (2.42), in terms of probability of detection ($\mathcal{P}_D^{(k,m)}[n]$) associated with the failure of the mth item and probability of false alarm ($\mathcal{P}_F^k[n]$), are the following:

$$\mathcal{P}_F^k[n] \triangleq \mathbb{P}(d_k[n]=1|\mathcal{H}[n]=0) = \mathbb{P}\Big(\Lambda_n^k \geq \gamma_k[n]\Big|\mathcal{H}[n]=0\Big)\,, \tag{2.43}$$

$$\mathcal{P}_D^{(k,m)}[n] \triangleq \mathbb{P}(d_k[n]=1|\mathcal{H}_m[n]=1) = \mathbb{P}\Big(\Lambda_n^k \geq \gamma_k[n]\Big|\mathcal{H}_m[n]=1\Big)\,. \tag{2.44}$$

2.2.4 Three-Layer Architecture

The first WSN is the 3LA, consisting of one FC and one PPC. In this setup, the vector of local decisions $\boldsymbol{d}[n] = \begin{bmatrix} d_1[n] & \cdots & d_K[n] \end{bmatrix}^{\mathrm{T}}$ is gathered and processed at the FC for a decision $\mathcal{D}[n]=i$ if $\mathcal{H}[n]=i$ is declared.

The FC performs a ML detection based on Equation (2.40), without assuming prior knowledge about the probabilities of events $\mathcal{H}[n]=0$ and $\mathcal{H}[n]=1$. On the other hand, the PPC collects $\boldsymbol{\mathcal{D}}[n] = \begin{bmatrix} \mathcal{D}[n_0] & \cdots & \mathcal{D}[n] \end{bmatrix}^{\mathrm{T}}$ and incorporates information from the failure model as well as the signal model defined in Equation (2.40). The PPC makes a final decision $\widehat{\mathcal{H}}[n]$ through a *Bayesian posterior detection*, with $\widehat{\mathcal{H}}[n]=1$ triggering inspection operations. Moreover, in the case of $\widehat{\mathcal{H}}[n]=1$, the PPC computes the estimated position of the faulty item $\widehat{\boldsymbol{\theta}}[i] = \boldsymbol{\theta}_{\widehat{m}[i]}$, where i indicates the number of times an alarm has been raised, up to instant n. Additionally, the PPC is responsible for ongoing communication with the sensors, providing them with updated values for their individual time-dependent thresholds and calculating and transmitting to the FC some time-dependent parameters necessary to perform the global detection task.

Fusion Center Detection

In the proposed 3LA, the FC, at the nth instant, performs a ML detection, whose task is to fuse the components of $\boldsymbol{d}[n]$ into a single decision $\mathcal{D}[n]$:

$$\Lambda_n^{\mathrm{BLRT}} \underset{\mathcal{D}[n]=0}{\overset{\mathcal{D}[n]=1}{\gtrless}} 1\,, \tag{2.45}$$

where $\Lambda_n^{\mathrm{BLRT}}$ differs from the analogous in Equation (2.15) due to the presence of the feedback system. This feedback allows Equation (2.45) to exploit time-dependent parameters such as $\varphi_m[n]$'s, $\mathcal{P}_D^{(k,m)}[n]$'s, $\mathcal{P}_F^k[n]$'s. The values of these parameters are sent to the FC by the PPC.

For this case, the (FC) time-dependent *probability of detection* ($Q_D^{(m)}[n]$) associated with the failure of the mth item and the time-dependent *probability of false*

alarm ($Q_F[n]$) at the nth instant can be computed. These are calculated using Equations (2.13) and (2.14) where the values of $\Lambda(\boldsymbol{d})$, $\mathcal{P}_D^{(k,m)}$'s, and $\mathcal{P}_F^k$'s are substituted with those of $\Lambda_n^{\text{BLRT}}(\boldsymbol{d})$, $\mathcal{P}_D^{(k,m)}[n]$'s, and $\mathcal{P}_F^k[n]$'s, respectively.

Post-Processing Center Detection

The primary responsibility of the PPC is to receive $\mathcal{D}[n]$ and determine if an alarm should be triggered. In contrast to local and FC detection, the PPC incorporates the failure model and utilizes all $\mathcal{D}[j]$ values, where $j = n_0, \ldots, n$, to enact a robust quickest fault detection strategy. For this task, the PPC acts as a *posterior detector* performing a test on $\mathcal{R}^{\text{PPC}}[n] \triangleq \mathbb{P}(\mathcal{H}[n] = 1|\boldsymbol{\mathcal{D}}[n])$, exploiting Equation (2.38) which leads to the following test:

$$\mathcal{R}^{\text{PPC}}[n] = \sum_{m=1}^{M} \mathcal{R}_m^{\text{PPC}}[n] \underset{\widehat{\mathcal{H}}[n]=0}{\overset{\widehat{\mathcal{H}}[n]=1}{\gtrless}} \gamma^* \,. \tag{2.46}$$

The calculation of $\mathcal{R}_m^{\text{PPC}}[n]$ can be expressed recursively via the following equation:

$$\begin{aligned} \mathcal{R}_m^{\text{PPC}}[n] &\triangleq \mathbb{P}(\mathcal{H}_m[n] = 1|\boldsymbol{\mathcal{D}}[n]) \qquad (2.47)\\ &= \begin{cases} \left[1 + \frac{1}{\mathcal{L}_m^{n_0}}\left(\frac{1}{1-e^{-\widehat{\lambda}_m[n_0]\Delta t}} - 1\right)\right]^{-1}, & \text{if } n = n_0 \\ \left[1 + \frac{1}{\mathcal{L}_m^{n}}\left(\frac{1}{1-e^{-\widehat{\lambda}_m[n]\Delta t}(1-\mathcal{R}_m^{\text{PPC}}[n-1])} - 1\right)\right]^{-1}, & \text{if } n > n_0 \end{cases}, \end{aligned}$$

where

$$\mathcal{L}_m^n \triangleq \frac{\mathbb{P}(\mathcal{D}[n]|\mathcal{H}_m[n] = 1)}{\mathbb{P}(\mathcal{D}[n]|\mathcal{H}[n] = 0)} = \left(\frac{Q_D^{(m)}[n]}{Q_F[n]}\right)^{\mathcal{D}[n]} \left(\frac{1 - Q_D^{(m)}[n]}{1 - Q_F[n]}\right)^{1-\mathcal{D}[n]} . \tag{2.48}$$

Equation (2.47) requires the storage of only the M values of $\mathcal{R}_m^{\text{PPC}}[n-1]$'s and the value of $\mathcal{D}[n]$, instead of the $(n - n_0 + 1)$ values contained in $\boldsymbol{\mathcal{D}}[n]$.

Moreover, Equation (2.47) uses $\widehat{\lambda}_m[n]$ since failure rates are considered random variables whose realization must be estimated. The description of this task is given later.

Post-Processing Center Localization

When $\widehat{\mathcal{H}}[n] = 1$, the PPC localizes the faulty item for the generic ith time by selecting the index m that maximizes the posterior probability of item failure $\mathcal{R}_m^{\text{PPC}}[n]$ resulting in the following MAP estimator:

$$\widehat{m}[i] = \arg\max_m \mathcal{R}_m^{\text{PPC}}[n] \,, \tag{2.49}$$

$$\widehat{\boldsymbol{\theta}}[i] = \boldsymbol{\theta}_{\widehat{m}[i]} \,. \tag{2.50}$$

Post-Processing Center Failure Rate Estimation

The exact failure rate of the generic mth item often remains unknown. However, literature may frequently offer an estimate (referred to here as $\lambda_{m,0}$) along with its associated variance (referred to as ν_m). Nevertheless, literature data is often derived from limited experiments on items that may not be identical to those in the system (or under the same operating conditions). Consequently, the PPC treats each λ_m as a random variable in this context.

Specifically, when the PPC raises an alarm, an inspection is conducted to assess the system's status. If the mth item's jth failure is confirmed, it becomes feasible to update the estimate of λ_m using $T_{m,j} \approx T^*_{m,j}$.

Utilizing the vector $\boldsymbol{T}_m[j] \triangleq \begin{bmatrix} T_{m,1} & \cdots & T_{m,j} \end{bmatrix}^{\mathrm{T}}$, the PPC calculates the following MMSE Estimator for the mth item:

$$\widehat{\lambda}_{m,j} = \mathbb{E}(\lambda_m | \boldsymbol{T}_m[j]) = \frac{\alpha_{m,j}}{\beta_{m,j}} \,. \tag{2.51}$$

Given that $T_{m,j} \sim \mathrm{Exp}(\lambda_m)$, the Gamma distribution is chosen to model λ_m as it is the *conjugate prior* of the Exponential distribution (see [89]): $\lambda_m \sim \mathrm{Gamma}(\alpha_{m,0}, \beta_{m,0})$. It becomes apparent that $\lambda_m | \boldsymbol{T}_m[j] \sim \mathrm{Gamma}(\alpha_{m,j}, \beta_{m,j})$, with the Gamma parameters calculated recursively by the PPC as $\alpha_{m,j} = (\alpha_{m,j-1} + 1)$ and $\beta_{m,j} = (\beta_{m,j-1} + T_{m,j})$. Here, $\alpha_{m,0} \triangleq (\lambda^2_{m,0}/\nu_m)$ and $\beta_{m,0} \triangleq (\lambda_{m,0}/\nu_m)$ are computed using literature values.

At any given discrete-time n, the most recent estimate of λ_m usable for inference purposes corresponds to $\widehat{\lambda}_{m,\mathcal{S}_m[n-1]}$, where $\mathcal{S}_m[n-1]$ denotes the count of failures for the mth item reported up to discrete-time $(n-1)$. This estimate will be referred to as $\widehat{\lambda}_m[n]$.

Post-Processing Center Parameters Calculation and Transmission

The last step of the PPC at instant n consists of obtaining the values of $\varphi_m[n+1]$'s exploiting $\widehat{\lambda}_m[n+1]$'s. Next, it computes and delivers the values of the local thresholds $\gamma_k[n+1]$'s to the respective sensors.

Once produced the thresholds, the PPC calculates the values of $\mathcal{P}_D^{(k,m)}[n+1]$'s and $\mathcal{P}_F^k[n+1]$'s and sends them to the FC alongside the values of $\varphi_m[n+1]$'s. This will allow the FC to evaluate $\Lambda^{\mathrm{BLRT}}_{n+1}$.

In the final step, the PPC computes the values of $Q_D^{(m)}[n+1]$'s to be used by the PPC itself in the recursive computation of $\mathcal{R}^{\mathrm{PPC}}[n+1]$.

2.2.5 Two-Layer Architecture

In this second architecture, the FC collects $\boldsymbol{d}[n_0], \ldots, \boldsymbol{d}[n]$ and directly performs a *Bayesian posterior detection*, therefore incorporating the functions of the PPC within the FC itself. Consequently, it becomes the FC's task to provide the estimated position of the faulty item and transmit updated local thresholds to the respective sensors.

Fusion Center Detection

Upon receiving $\boldsymbol{d}[n]$, the FC establishes whether an alarm should be raised. As with the PPC, the FC now utilizes all $\boldsymbol{d}[j]$ values, where $j = n_0, \ldots, n$, to perform a test on $\mathcal{R}^{\mathrm{FC}}[n] \triangleq \mathbb{P}(\mathcal{H}[n] = 1 | \boldsymbol{d}[n], \ldots, \boldsymbol{d}[n_0])$:

$$\mathcal{R}^{\mathrm{FC}}[n] = \sum_{m=1}^{M} \mathcal{R}_m^{\mathrm{FC}}[n] \underset{\widehat{\mathcal{H}}[n]=0}{\overset{\widehat{\mathcal{H}}[n]=1}{\gtrless}} \gamma^* \, . \tag{2.52}$$

Also here, $\mathcal{R}_m^{\mathrm{FC}}[n]$ can be expressed recursively via the following equation:

$$\begin{aligned} \mathcal{R}_m^{\mathrm{FC}}[n] &\triangleq \mathbb{P}(\mathcal{H}_m[n] = 1 | \boldsymbol{d}[n], \ldots, \boldsymbol{d}[n_0]) \qquad (2.53) \\ &= \begin{cases} \left[1 + \left(\prod_{k=1}^{K} \ell_{m,k}^{n_0} \right)^{-1} \left(\frac{1}{1 - e^{-\widehat{\lambda}_m[n_0]\Delta t}} - 1 \right) \right]^{-1}, & \text{if } n = n_0 \\ \left[1 + \left(\prod_{k=1}^{K} \ell_{m,k}^{n} \right)^{-1} \left(\frac{1}{1 - e^{-\widehat{\lambda}_m[n]\Delta t}(1 - \mathcal{R}_m^{\mathrm{FC}}[n-1])} - 1 \right) \right]^{-1}, & \text{if } n > n_0 \end{cases}, \end{aligned}$$

where

$$\ell_{m,k}^{n} \triangleq \frac{\mathbb{P}(d_k[n] | \mathcal{H}_m[n] = 1)}{\mathbb{P}(d_k[n] | \mathcal{H}[n] = 0)} = \left(\frac{\mathcal{P}_D^{(k,m)}[n]}{\mathcal{P}_F^{k}[n]} \right)^{d_k[n]} \left(\frac{1 - \mathcal{P}_D^{(k,m)}[n]}{1 - \mathcal{P}_F^{k}[n]} \right)^{1 - d_k[n]} . \tag{2.54}$$

Equation (2.53) allows the FC, at the nth instant, to store only the M values of $\mathcal{R}_m^{\mathrm{FC}}[n-1]$'s and the vector $\boldsymbol{d}[n]$.

Fusion Center Localization

Analogously to the 3LA, the FC can provide an estimate of the faulty item by maximizing the posterior probability of item failure to raise the ith alarm if $\widehat{\mathcal{H}}[n] = 1$, resulting in the following MAP estimator:

$$\widehat{m}[i] = \arg\max_{m} \mathcal{R}_m^{\mathrm{FC}}[n] \, , \tag{2.55}$$

$$\widehat{\boldsymbol{\theta}}[i] = \boldsymbol{\theta}_{\widehat{m}[i]} \, . \tag{2.56}$$

Fusion Center Failure Rate Estimation

As in the 3LA, the FC provides an updated estimate of the failure rates λ_m's by treating them as random variables. At each discrete-time n, $\widehat{\lambda}_m[n]$ indicates the most recent estimate of λ_m obtained by discrete-time $(n-1)$.

Fusion Center Parameters Calculation and Transmission

In the process's final stage, the FC updates the estimates of the failure rates and subsequently computes the values of $\varphi_m[n+1]$'s. Following this, it calculates and transmits the values of $\gamma_k[n+1]$'s to the respective sensors.

After obtaining the thresholds, the FC calculates the values of $\mathcal{P}_D^{(k,m)}[n+1]$'s and $\mathcal{P}_F^k[n+1]$'s that are needed for the computation of $\mathcal{R}^{\text{FC}}[n+1]$.

2.2.6 Other Rules: CUSUM

The following is the description of the CUSUM algorithm adapted to be performed by the FC upon collecting the sensors' local decisions in time.

The CUSUM procedure has the following form:

$$\max_{n_0 \le j \le n} \ln \frac{\mathbb{P}(\boldsymbol{d}[n], \ldots, \boldsymbol{d}[j] | \mathcal{H}[j] = 1)}{\mathbb{P}(\boldsymbol{d}[n], \ldots, \boldsymbol{d}[j] | \mathcal{H}[j] = 0)} \underset{\widehat{\mathcal{H}}[n]=0}{\overset{\widehat{\mathcal{H}}[n]=1}{\gtrless}} \gamma^* \,. \tag{2.57}$$

Equation (2.57) implicitly estimates the instant corresponding to the system-state change via ML estimation. However, Equation (2.57) uses the system's state variable $\mathcal{H}[n]$, posing the problem that the only available likelihoods are with respect to the failure of the individual items, and have been illustrated in Equation (2.43) and (2.44). Due to the finite number of items M, we can use the *generalized CUSUM* (G-CUSUM) algorithm to address this issue. The following is the G-CUSUM rule:

$$\begin{aligned} \mathcal{C}[n] &\triangleq \max_{n_0 \le j \le n} \ln \frac{\max\limits_m \mathbb{P}(\boldsymbol{d}[n], \ldots, \boldsymbol{d}[j] | \mathcal{H}_m[j] = 1)}{\mathbb{P}(\boldsymbol{d}[n], \ldots, \boldsymbol{d}[j] | \mathcal{H}[j] = 0)} \\ &= \max_m \max_{n_0 \le j \le n} \ln \frac{\mathbb{P}(\boldsymbol{d}[n], \ldots, \boldsymbol{d}[j] | \mathcal{H}_m[j] = 1)}{\mathbb{P}(\boldsymbol{d}[n], \ldots, \boldsymbol{d}[j] | \mathcal{H}[j] = 0)} = \max_m \mathcal{C}_m[n] \underset{\widehat{\mathcal{H}}[n]=0}{\overset{\widehat{\mathcal{H}}[n]=1}{\gtrless}} \gamma^* \,, \end{aligned} \tag{2.58}$$

which is equivalent to a joint estimation (via ML) of the failure instant and the faulty item. $\mathcal{C}_m[n]$ can be expressed with a recursive form starting from its definition and

exploiting the independence of the sensor's decision in time:

$$\mathcal{C}_m[n] = \begin{cases} \sum_{k=1}^{K} \ln(\ell_{m,k}(d_k[n_0])), & \text{if } n = n_0 \\ (\mathcal{C}_m[n-1])^+ + \sum_{k=1}^{K} \ln(\ell_{m,k}(d_k[n])), & \text{if } n > n_0 \end{cases} . \tag{2.59}$$

Also for the case of the G-CUSUM, if $\widehat{\mathcal{H}}[n] = 1$, a localization procedure is readily available for the ith alarm. Such a procedure is the following MLE:

$$\widehat{m}[i] = \arg\max_m \mathcal{C}_m[n] \ , \tag{2.60}$$

$$\widehat{\boldsymbol{\theta}}[i] = \boldsymbol{\theta}_{\widehat{m}[i]} \ . \tag{2.61}$$

2.2.7 Computational Complexity

Table 2.2 shows the computational complexity of the tasks performed in all previously outlined architectures.

All the architectures share the same edge-layer design in which each sensor performs a local test at each discrete instant. Specifically, it was possible to lower the computational complexity of the local tests from $\mathcal{O}(M)$ to $\mathcal{O}(1)$, as previously shown in Equation 2.42. The complexity of finding $\gamma_k[n+1]$'s is not reported here as it depends on the mathematical form of the BLRT and the used root-finding technique. Therefore, it will be reported in Chapter 3 when the architectures are applied to practical use cases.

2.3 Sequential Detection

Sequential detection is an adaptation of batch detection with the further goal of optimizing its online use.

In other words, while batch detection requires the collection of N samples before performing the detection task, with N being fixed and predetermined, in sequential detection, the sampling is performed until the decision statistic leaves a predetermined interval, therefore removing the need to establish a fixed sample size.

In many cases, it is desirable to choose a test statistic $f(\boldsymbol{y}[n])$ such that:

$$\mathbb{E}_0(f(\boldsymbol{y}[n+1])) < \mathbb{E}_0(f(\boldsymbol{y}[n])) < 0 < \mathbb{E}_1(f(\boldsymbol{y}[n])) < \mathbb{E}_1(f(\boldsymbol{y}[n+1])) \ , \tag{2.62}$$

for each n.

Table 2.2: Computational complexity of the quickest detection architectures.

Architecture	Layer	Task	Complexity
3LA	FC	Detection	$\mathcal{O}(KM)$
	PPC	Detection (incl. localization)	$\mathcal{O}(M)$
		Failure Rates Update	$\mathcal{O}(1)$ *per item*
		$\varphi_m[n+1]$'s Calculation	$\mathcal{O}(M)$
		$\gamma_k[n+1]$'s Calculation	–
		$\mathcal{P}_F^k[n+1]$'s Calculation	$\mathcal{O}(K)$
		$\mathcal{P}_D^{(k,m)}[n+1]$'s Calculation	$\mathcal{O}(KM)$
		$Q_F[n+1]$ Calculation	$\mathcal{O}(2^K)$
		$Q_D^{(m)}[n+1]$'s Calculation	$\mathcal{O}(2^K M)$
2LA	FC	Detection (incl. localization)	$\mathcal{O}(KM)$
		Failure Rates Update	$\mathcal{O}(1)$ *per item*
		$\varphi_m[n+1]$'s Calculation	$\mathcal{O}(M)$
		$\gamma_k[n+1]$'s Calculation	–
		$\mathcal{P}_F^k[n+1]$'s Calculation	$\mathcal{O}(K)$
		$\mathcal{P}_D^{(k,m)}[n+1]$'s Calculation	$\mathcal{O}(KM)$
G-CUSUM	FC	Detection (incl. localization)	$\mathcal{O}(KM)$

This allows the creation of a detection rule having the following form:

$$\widehat{\mathcal{H}} = \begin{cases} \mathcal{H}_1 \text{ (stop collecting samples)}, & \text{if } f(\boldsymbol{y}[n]) \geq \gamma_+ \\ \mathcal{H}_0 \text{ (stop collecting samples)}, & \text{if } f(\boldsymbol{y}[n]) \leq \gamma_- \\ \text{collect } (n+1)\text{th sample}, & \text{otherwise} \end{cases}, \tag{2.63}$$

with $\gamma_+ \in \mathbb{R}^+$ and $\gamma_- \in \mathbb{R}^-$ denoting an upper and lower threshold, respectively. This is the case when the SPRT is used for *independent and identically distributed* (i.i.d.) samples: $f(\boldsymbol{y}[n]) = \sum_{i=1}^{n} \ln\left(p_1(y[i])/p_0(y[i])\right)$.

However, this has two main drawbacks: (i) even if it was possible to find a statistic $f(y[n])$ satisfying Equation (2.62), this could result in a high number of collected samples before reaching a decision; (ii) Equation (2.62) might not be satisfied with any feasible statistic.

The introduction of a time deadline $\mathcal{T}$ is a common technique to fix such issues: if no decision has been taken after collecting $\mathcal{T}$, then $\mathcal{H}_0$ is declared.

In some cases, the available test statistic is such that it can only satisfy the following condition:

$$0 < \mathbb{E}_0(f(\boldsymbol{y}[n])) < \mathbb{E}_1(f(\boldsymbol{y}[n]))\ , \tag{2.64}$$

for any n. This is the case for one-sided tests.

In the case of one-sided tests, the problem is further simplified as no lower threshold is needed. In such a case, collecting $\mathcal{T}$ samples without ever declaring $\mathcal{H}_1$ becomes the only way to declare $\mathcal{H}_0$.

This sequential approach, equipped with a time deadline and stripped of a lower threshold, is what is explored in this thesis as it is compatible with most scenarios and can be expressed as follows:

$$\widehat{\mathcal{H}} = \begin{cases} \mathcal{H}_1 \text{ (stop collecting samples)}\,, & \text{if } f(\boldsymbol{y}[n]) \geq \gamma \\ \mathcal{H}_0 \text{ (stop collecting samples)}\,, & \text{if } f(\boldsymbol{y}[n]) < \gamma \text{ and } n = \mathcal{T}\ . \\ \text{collect } (n+1)\text{th sample}\,, & \text{otherwise} \end{cases} \tag{2.65}$$

As in the case of batch detection, this framework can be adapted for online detection by performing subsequent sequential detection procedures.

Sequential detection for online detection applications, generally speaking, does not constitute an optimal approach. However, it might be desirable for a series of reasons:

- Ease of implementation – As in batch detection, this framework is well-known with tests of either the classical or the Bayesian approaches.
- Improved Performances – In the case of perfect knowledge of the statistical distribution of the measurements in both hypotheses, it is proven that the SPRT can perform faster decisions with unaltered performances compared to the LRT. For this reason, repeated SPRT might be preferred over repeated LRT in the case of online detection applications due to the criticality of ensuring quick detections.

2.3.1 System Model

The scenario entails a distributed WSN comprising K sensors assigned to determine the global absence ($\mathcal{H}_0$) or presence ($\mathcal{H}_1$) of a specific event in the monitored

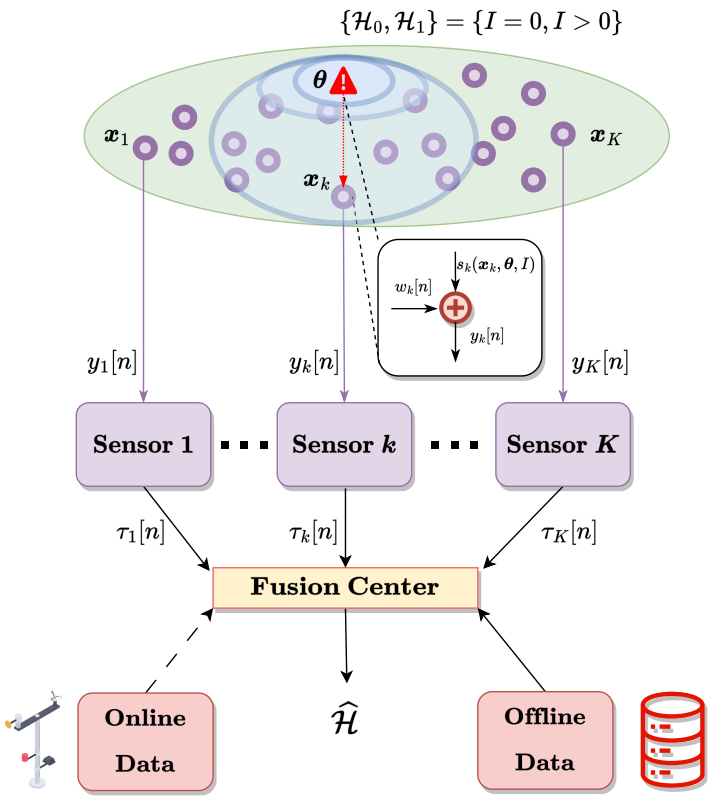

Figure 2.4: Proposed Wireless Sensor Network scheme for sequential detection.

environment, as illustrated in Figure 2.4. The event is characterized by its position $\boldsymbol{\theta}$ and intensity I. For the kth sensor, the location and measurement at the nth time are represented by $\boldsymbol{x}_k$ and $y_k[n]$, respectively.

Each sensor conducts a sequential test on the mentioned signal, evaluating the local absence ($\mathcal{H}_0$) or presence ($\mathcal{H}_1$) of the event. The sensors assume identical sampling frequencies and perfect synchronization. A sensor initiates a new detection process until the FC makes a global decision. This setup enables the FC to receive multiple decisions from a single sensor. The global decision integrates real-time external data (e.g., meteorological data) and offline data (e.g., the model of signal attenuation in space) to enhance accuracy.

Two novel architectures are presented: (i) DTSA and (ii) the CSA. In these proposed algorithms, sensors and the FC adopt sequential detection techniques to minimize decision delays compared to conventional batch approaches.

In the DTSA, each sensor transmits a *transmission value* $\tau_k[n] = 1$ (respectively $\tau_k[n] = -1$) to the FC when declaring $\mathcal{H}_1$ (respectively $\mathcal{H}_0$), and $\tau_k[n] = 0$ when the sensor has not made a decision yet. No physical communication is transmitted to the FC when $\tau_k[n] = 0$. At each time instant n, the FC tests $\{\tau_k[n] : |\tau_k[n]| = 1\}_k$ and makes a global decision $\widehat{\mathcal{H}} \in \{\mathcal{H}_0, \mathcal{H}_1\}$.

On the other hand, in the CSA, each sensor sends a bit $\tau_k[n] = 1$ (respectively $\tau_k[n] = 0$) to the FC upon local declaration of $\mathcal{H}_1$ (respectively $\mathcal{H}_0$ or when the sensor is has not made a decision yet). Furthermore, at each time instant n, the FC sequentially tests the transmission values $\{\tau_k[n], a_k[n]\}_k$, where $a_k[n]$ represents the number of instants passed since the last decision made by the kth sensor.

2.3.2 Signal Model

The model of the measurements $y_k[n]$ is the following:

$$\begin{cases} \mathcal{H}_0 : & y_k[n] = w_k[n] \\ \mathcal{H}_1 : & y_k[n] = s_k(\boldsymbol{x}_k, \boldsymbol{\theta}, I) + w_k[n] \end{cases}. \tag{2.66}$$

Equation (2.66) is similar to Equation (2.4) with the difference that in this work, the focus shifts from the exploitation of the knowledge of the failure model to the exploitation of the knowledge of the signal propagation model resulting in the *unknown* deterministic and constant parameter $s_k > 0$. This results in dropping the Bayesian approach and focusing on a more accurate characterization of the signal model.

In this study, we assume that the measurements gathered by the same sensor, denoted as $\{y_k[n]\}_n$, are i.i.d., while measurements collected by different sensors, represented as $\{y_k[n]\}_k$, are assumed to be independent and have distributions that depend on $\{s_k\}_k$. While this simplification may deviate from real-world complexities, assuming null space and time correlation in modeling $\{w_k[n]\}_{n,k}$ can be justified by ensuring adequate spatial separation between sensors and a sufficiently low sampling frequency [33, 90].

2.3.3 Local Detection

Every sensor conducts sequential detection on the hypotheses outlined in Equation (2.66). The GSPRT statistic is calculated, wherein the log-likelihood ratio's parameter s_k is substituted with its MLE. At time n, the resulting one-sided test statistic is denoted as Λ_n^k. Denoting γ_k as a local threshold, the time at which the sensor takes the mth decision with n_m^k, and $\mathcal{T}_k$ as a local decision deadline, the mth stopping time is therefore the following:

$$n_m^k \triangleq \min\left\{\inf\left\{n > n_{m-1}^k : \Lambda_n^k - \Lambda_{n_{m-1}^k}^k \geq \gamma_k\right\}, n_{m-1}^k + \mathcal{T}_k\right\}, \tag{2.67}$$

with $n_0^k = 0$ and $\Lambda_0^k = 0$. Next, the decision rule is as follows:

$$d_m^k \triangleq \begin{cases} \mathcal{H}_1\,, & \text{if } \Lambda_n^k - \Lambda_{n_{m-1}^k}^k \geq \gamma_k \\ \mathcal{H}_0\,, & \text{otherwise} \end{cases} . \tag{2.68}$$

Instant Local Performances

The following are the kth sensor's *instant probability of false alarm* $\mathcal{P}_F^{(k,i)}$ and *instant probability of detection* $\mathcal{P}_D^{(k,i)}(s_k)$ for the arbitrary mth decision across each time instant $\left\{n_{m-1}^k + i\right\}_{i=1}^{\mathcal{T}_k}$:

$$\begin{aligned} \mathcal{P}_F^{(k,i)} &\triangleq \mathbb{P}_0\Big(d_m^k = \mathcal{H}_1, n_m^k - n_{m-1}^k = i\Big) \\ &= \mathbb{P}_0\Big(\Big\{\Lambda_n^k < \gamma_k\Big\}_{n<i}, \Lambda_i^k \geq \gamma_k\Big)\,, \end{aligned} \tag{2.69}$$

$$\begin{aligned} \mathcal{P}_D^{(k,i)}(s_k) &\triangleq \mathbb{P}_1\Big(d_m^k = \mathcal{H}_1, n_m^k - n_{m-1}^k = i; s_k\Big) \\ &= \mathbb{P}_1\Big(\Big\{\Lambda_n^k < \gamma_k\Big\}_{n<i}, \Lambda_i^k \geq \gamma_k; s_k\Big)\,. \end{aligned} \tag{2.70}$$

Moreover, the *instant probability of correct rejection* ($\mathcal{P}_C^{(k,i)}$) and the *instant probability of miss-detection* ($\mathcal{P}_M^{(k,i)}(s_k)$) is:

$$\mathcal{P}_C^{(k,i)} \triangleq \mathbb{P}_0\Big(d_m^k = \mathcal{H}_0, n_m^k - n_{m-1}^k = i\Big) = 1 - \sum_{j=1}^{i} \mathcal{P}_F^{(k,j)}\,, \tag{2.71}$$

$$\mathcal{P}_M^{(k,i)}(s_k) \triangleq \mathbb{P}_1\Big(d_m^k = \mathcal{H}_0, n_m^k - n_{m-1}^k = i; s_k\Big) = 1 - \sum_{j=1}^{i} \mathcal{P}_D^{(k,j)}(s_k)\,. \tag{2.72}$$

Hence, the values of $\mathcal{P}_C^{(k,i)}$ and $\mathcal{P}_M^{(k,i)}$ are obtained using the previously shown probabilities.

Overall Local Performances

The *overall probabilities of false alarm* ($\mathcal{P}_F^k$), *detection* ($\mathcal{P}_D^k(s_k)$), *correct rejection* ($\mathcal{P}_C^k$), and *miss-detection* ($\mathcal{P}_M^k(s_k)$) at the kth sensor are:

$$\mathcal{P}_F^k \triangleq \mathbb{P}_0\Big(d_m^k = \mathcal{H}_1\Big) = \sum_{i=1}^{\mathcal{T}_k} \mathcal{P}_F^{(k,i)}\,, \tag{2.73}$$

$$\mathcal{P}_D^k(s_k) \triangleq \mathbb{P}_1\Big(d_m^k = \mathcal{H}_1; s_k\Big) = \sum_{i=1}^{\mathcal{T}_k} \mathcal{P}_D^{(k,i)}(s_k)\,, \tag{2.74}$$

$$\mathcal{P}_C^k \triangleq \mathbb{P}_0\Big(d_m^k = \mathcal{H}_0\Big) = \mathcal{P}_C^{(k,\mathcal{T}_k)} \,, \tag{2.75}$$

$$\mathcal{P}_M^k(s_k) \triangleq \mathbb{P}_1\Big(d_m^k = \mathcal{H}_0; s_k\Big) = \mathcal{P}_M^{(k,\mathcal{T}_k)}(s_k) \,. \tag{2.76}$$

Local Decision Delays

As the local detection algorithm operates sequentially, it enables the evaluation of the average time needed to make a decision. We use $\mathcal{D}_{1j}^k$ to denote the expected delay for the kth sensor to declare $\mathcal{H}_1$ when $\mathcal{H}_j$ is true. Similarly, $\mathcal{D}_{0X}^k$ signifies the expected delay for the kth sensor to declare $\mathcal{H}_0$ regardless of the true hypothesis:

$$\mathcal{D}_{10}^k \triangleq \mathbb{E}_0\Big(n_m^k - n_{m-1}^k \Big| d_m^k = \mathcal{H}_1\Big) = \frac{1}{\mathcal{P}_F^k} \sum_{i=1}^{\mathcal{T}_k} i\, \mathcal{P}_F^{(k,i)} \,, \tag{2.77}$$

$$\mathcal{D}_{11}^k(s_k) \triangleq \mathbb{E}_1\Big(n_m^k - n_{m-1}^k \Big| d_m^k = \mathcal{H}_1; s_k\Big) = \frac{1}{\mathcal{P}_D^k(s_k)} \sum_{i=1}^{\mathcal{T}_k} i\, \mathcal{P}_D^{(k,i)}(s_k) \,, \tag{2.78}$$

$$\mathcal{D}_{0X}^k \triangleq \mathbb{E}\Big(t_m^k - t_{m-1}^k \Big| d_m^k = \mathcal{H}_0\Big) = \mathcal{T}_k \,. \tag{2.79}$$

Furthermore, one can articulate the anticipated duration $\mathcal{D}_{Xj}^k$ required by the kth sensor to reach any decision when $\mathcal{H}_j$ is true:

$$\begin{aligned} \mathcal{D}_{X0}^k &\triangleq \mathbb{E}_0\Big(t_m^k - t_{m-1}^k\Big) \\ &= \mathcal{D}_{10}^k \mathcal{P}_F^k + \mathcal{T}_k \mathcal{P}_C^k = \mathcal{T}_k - \sum_{i=1}^{\mathcal{T}_k} (\mathcal{T}_k - i) \mathcal{P}_F^{(k,i)} \,, \end{aligned} \tag{2.80}$$

$$\begin{aligned} \mathcal{D}_{X1}^k(s_k) &\triangleq \mathbb{E}_1\Big(t_m^k - t_{m-1}^k; s_k\Big) \\ &= \mathcal{D}_{11}^k(s_k) \mathcal{P}_D^k(s_k) + \mathcal{T}_k \mathcal{P}_M^k(s_k) = \mathcal{T}_k - \sum_{i=1}^{\mathcal{T}_k} (\mathcal{T}_k - i) \mathcal{P}_D^{(k,i)}(s_k) \,. \end{aligned} \tag{2.81}$$

2.3.4 Global Detection

In this section, we outline two sequential detection approaches for FC: (i) the DTSA, wherein the FC generates a test statistic relying solely on the received local decisions, and (ii) the CSA, an innovative algorithm where the FC calculates a test statistic at moments when the sensors make decisions and also at instances when the sensors have not yet reached a decision (knowledge of the sampling period for each sensor is essential).

Decision-Triggered Sampling Algorithm

In this algorithm, the FC iteratively updates a test statistic following a local decision made by the sensors. The transmission rule encapsulates the detection status of the sensors:

$$\tau_k[n] \triangleq \begin{cases} +1\,, & \text{if } \exists\, m : n = n_m^k \ \wedge\ d_m^k = \mathcal{H}_1 \\ -1\,, & \text{if } \exists\, m : n = n_m^k \ \wedge\ d_m^k = \mathcal{H}_0\ , \\ 0\,, & \text{otherwise} \end{cases} \tag{2.82}$$

where $\tau_k[n] = 0$ indicates the absence of a physical transmission from the sensor to FC. This transmission rule translates into a test statistic performed on the decision-triggered transmissions $\{\tau_k[n] : |\tau_k[n]| = 1\}_{n,k}$. In a manner akin to the configuration of the local detectors, the involvement of the unknown parameters $\boldsymbol{\theta}$ and I in the hypothesis $\mathcal{H}_1$ necessitates the utilization of a GSPRT statistic denoted here as $\Lambda_n^{\mathrm{DTSA}}$. Similarly, a predefined time limit $\mathcal{T}^*$ is employed. If the FC has not declared $\mathcal{H}_1$ by this limit, $\mathcal{H}_0$ is automatically asserted, resulting in the formulation of the subsequent stopping rule and decision rule:

$$n^* \triangleq \min\{\inf\{n : \Lambda_n^{\mathrm{DTSA}} \geq \gamma^*\}, \mathcal{T}^*\}\,, \tag{2.83}$$

$$\widehat{\mathcal{H}} \triangleq \begin{cases} \mathcal{H}_1\,, & \text{if } \Lambda_{n^*}^{\mathrm{DTSA}} \geq \gamma^* \\ \mathcal{H}_0\,, & \text{otherwise} \end{cases}\ . \tag{2.84}$$

At every instance n, for computing $\Lambda_n^{\mathrm{DTSA}}$, the FC is required to retrieve the stopping times n_m^k and, recursively, determine the count of local decisions made by the kth sensor up to time n (denoted as $\mathcal{M}_n^k$), considering all k:

$$n_m^k = \inf\Big\{n > n_{m-1}^k : |\tau_k[n]| = 1\Big\}\,, \quad n_0^k = 0\,. \tag{2.85}$$

$$\mathcal{M}_n^k = \mathcal{M}_{n-1}^k + |\tau_k[n]|\,, \quad \mathcal{M}_0^k = 0\,. \tag{2.86}$$

The subsequent stage involves the FC calculating the GSPRT statistic $\Lambda_n^{\mathrm{DTSA}}$:

$$\Lambda_n^{\mathrm{DTSA}} \triangleq \max_{\boldsymbol{\theta},I}\left\{\sum_{k=1}^{K}\sum_{m=1}^{\mathcal{M}_n^k} \mathcal{L}_{\boldsymbol{\theta},I}\Big(\tau_k\Big[n_m^k\Big]\Big)\right\}. \tag{2.87}$$

The term $\mathcal{L}_{\boldsymbol{\theta},I}\big(\tau_k\big[n_m^k\big]\big)$ can be obtained via the following:

$$\mathcal{L}_{\boldsymbol{\theta},I}\Big(\tau_k\Big[n_m^k\Big]\Big) \triangleq \begin{cases} \ln\frac{\mathcal{P}_D^k(s_k(\boldsymbol{x}_k,\boldsymbol{\theta},I))}{\mathcal{P}_F^k}\,, & \text{if } \tau_k\big[n_m^k\big] = +1 \\ \ln\frac{\mathcal{P}_M^k(s_k(\boldsymbol{x}_k,\boldsymbol{\theta},I))}{\mathcal{P}_C^k}\,, & \text{if } \tau_k\big[n_m^k\big] = -1 \end{cases}\ . \tag{2.88}$$

Continuous Sampling Algorithm

Under this arrangement, the kth sensor transmits a physical message to the FC solely upon declaring $\mathcal{H}_1$. Therefore, we can express the following transmission rule at each instance n:

$$\tau_k[n] \triangleq \begin{cases} 1\,, & \text{if } \exists\, m : n = n_m^k \ \wedge\ d_m^k = \mathcal{H}_1 \\ 0\,, & \text{otherwise} \end{cases}, \tag{2.89}$$

where $\tau_k[n]$ is the *transmission value*, with $\tau_k[n] = 0$ indicating the absence of a physical transmission.

Simultaneously, the FC continually updates a statistic based on the received transmission values $\{\tau_k[n]\}_{k,n}$. The awareness of the sampling period for each sensor allows this ongoing sampling, even when $\tau_k[n] = 0$. The rationale behind using the identical transmission value $\tau_k[n] = 0$ to signify both the absence of a decision and a negative decision stems from the deterministic nature of the time taken by a sensor to declare $\mathcal{H}_0$ (equal to $\mathcal{T}_k$). This deterministic nature allows for a clear distinction between the two scenarios.

Similar to the previously proposed framework, we implement a truncated GSPRT, denoting its statistic as Λ_n^{CSA}, along with a predefined time limit $\mathcal{T}^*$. This approach leads to the subsequent formulation of the stopping rule and decision rule:

$$n^* \triangleq \min\{\inf\{n : \Lambda_n^{\mathrm{CSA}} \geq \gamma^*\}, \mathcal{T}^*\}\,, \tag{2.90}$$

$$\widehat{\mathcal{H}} \triangleq \begin{cases} \mathcal{H}_1\,, & \text{if } \Lambda_{n^*}^{\mathrm{CSA}} \geq \gamma^* \\ \mathcal{H}_0\,, & \text{otherwise} \end{cases}. \tag{2.91}$$

For each time step n, computing Λ_n^{CSA} entails the FC sequentially determining, for each sensor, whether the received transmission value $\tau_k[n]$ aligns with a local decision or not, and extracting the current delay $a_k[n]$:

$$n_m^k = \min\Big\{\inf\Big\{n > n_{m-1}^k : \tau_k[n] = 1\Big\}, n_{m-1}^k + \mathcal{T}_k\Big\}\,, \tag{2.92}$$

$$\mathcal{M}_n^k = \begin{cases} \mathcal{M}_{n-1}^k + 1\,, & \text{if } n = n^k_{\mathcal{M}_{n-1}^k} + 1 \\ \mathcal{M}_{n-1}^k\,, & \text{otherwise} \end{cases}, \tag{2.93}$$

$$a_k[n] = \begin{cases} 1\,, & \text{if } n = n^k_{\mathcal{M}_{n-1}^k} + 1 \\ a_k[n-1] + 1\,, & \text{otherwise} \end{cases}, \tag{2.94}$$

where $\mathcal{M}_n^k$ now represents the count of local decisions made by the kth sensor at instant n, *including* the one presently being taken, where $n_0^k = 0$ and $\mathcal{M}_0^k = 0$. The

subsequent stage involves the FC calculating the GSPRT statistic Λ_n^{CSA}:

$$\Lambda_n^{\mathrm{CSA}} \triangleq \max_{\boldsymbol{\theta},I} \left\{ \sum_{k=1}^{K} \sum_{m=1}^{\mathcal{M}_n^k} \mathcal{L}_{\boldsymbol{\theta},I}\Big(\tau_k\Big[\min\Big\{n, n_m^k\Big\}\Big], a_k\Big[\min\Big\{n, n_m^k\Big\}\Big]\Big) \right\} . \quad (2.95)$$

The generic value of $\mathcal{L}_{\boldsymbol{\theta},I}(\tau_k[n], a_k[n])$ can be expressed via the following:

$$\mathcal{L}_{\boldsymbol{\theta},I}(\tau_k[n], a_k[n]) \triangleq \begin{cases} \ln \frac{\mathcal{P}_D^{(k,a_k[n])}(s_k(\boldsymbol{x}_k,\boldsymbol{\theta},I))}{\mathcal{P}_F^{(k,a_k[n])}}, & \text{if } \tau_k[n]=1 \\ \ln \frac{\mathcal{P}_M^{(k,a_k[n])}(s_k(\boldsymbol{x}_k,\boldsymbol{\theta},I))}{\mathcal{P}_C^{(k,a_k[n])}}, & \text{if } \tau_k[n]=0 \end{cases} . \quad (2.96)$$

2.3.5 Computational Complexity and Communication Costs

In both algorithms, the central task of the FC is to obtain the log-likelihood ratios of observations and ascertain the maximum with respect to the unknown parameters. As the computational demands escalate with finer grids during the online computation of log-likelihood ratios, we posit a preliminary offline stage preceding online detection. In this phase, log-likelihood ratios are pre-computed for each grid point and transmitted to the FC.

Both algorithms instruct the FC regarding the timing and methodology of updating the decision statistic. When an update is necessitated, the computational complexity is equal across the algorithms, with this being $\mathcal{O}(K \cdot |\mathrm{grid}(\boldsymbol{\theta})| \cdot |\mathrm{grid}(I)|)$. The primary computational divergence lies in the frequency of these updates, which is more frequent when employing the CSA.

Each architecture is configured with a unique blend of decision rule and transmission rule at the sensor level, resulting in a distinctive *average transmission period* (ATP) for physical communications from *each sensor* to the FC for each presented architecture:

$$\mathrm{ATP}_{\mathrm{CSA}} \triangleq \mathbb{E}\left(n_b^k - n_a^k \middle| \sum_{n=n_a^k}^{n_b^k} \tau_k[n] = 2 \right) = \begin{cases} \frac{\mathcal{D}_{X0}^k}{\mathcal{P}_F^k}, & \text{if } \mathcal{H}_0 \text{ is true} \\ \frac{\mathcal{D}_{X1}^k(s_k)}{\mathcal{P}_D^k(s_k)}, & \text{if } \mathcal{H}_1 \text{ is true} \end{cases} , \quad (2.97)$$

$$\mathrm{ATP}_{\mathrm{DTSA}} \triangleq \mathbb{E}\Big(n_m^k - n_{m-1}^k\Big) = \begin{cases} \mathcal{D}_{X0}^k, & \text{if } \mathcal{H}_0 \text{ is true} \\ \mathcal{D}_{X1}^k(s_k), & \text{if } \mathcal{H}_1 \text{ is true} \end{cases} . \quad (2.98)$$

It is evident that $\mathrm{ATP}_{\mathrm{CSA}} \geq \mathrm{ATP}_{\mathrm{DTSA}}$. This directly arises from the absence of physical communication when a sensor opts for $\mathcal{H}_0$ in the CSA architecture.

Chapter 3

Use Cases

This chapter explores the effectiveness of the previously suggested solutions through two distinct use cases.

In Section 3.1, we evaluate the architectures proposed in Sections 2.1 and 2.2 in the context of a simulated subsea oil spill in a SPS. The second case, discussed in Section 3.2, focuses on testing the architectures from Section 2.3 in a hypothetical scenario of CO_2 dispersion within an outdoor industrial complex.

3.1 Oil Spill in Subsea Production Systems

Over recent decades, significant strides have been made in the oil and gas industry's offshore resource exploitation technologies. These advancements enable extracting offshore resources once deemed inaccessible or economically unviable. An illustration of this progress is the adoption of SPSs, connectable to various offshore platforms like fixed platforms, FPSOs, *single point anchor reservoir* (SPAR) platforms, *tension-leg platforms* (TLPs), semi-submersible platforms, or even directly to the shore. However, the latter is less common [91].

SPSs involve relocating equipment to the seabed, including the transfer of *christmas trees* (referred to as *subsea trees* in this context, distinct from *surface trees* on traditional platforms). A single platform can host multiple subsea trees through SPSs. Typically, the outlet streams of adjacent subsea trees connect to a *manifold* via pipes called *jumpers*. Manifolds mix flows before transferring them topside via *production risers* (occasionally, subsea preliminary treatments like separation occur). Various SPS components sometimes consolidate into a *template*. Operators topside can control the SPS using *umbilicals*, bundles of tubes, and conductors for functions such as control fluid transfer, chemical delivery, powering subsea

components, and sensor data collection. Bai Y. and Bai Q. provide an in-depth description of an SPS [92].

This approach enables oil extraction in deep waters, extending beyond fixed platforms' reach, offering versatile field exploitation [93]. However, SPS usage increases seabed components, heightening vulnerability to failures. Detecting spills in deep waters becomes more challenging, leading to delayed production shutdowns and risking worker safety and the environment. Locating a seabed spill is complex, requiring costly inspections by *remotely operated vehicles* (ROVs) [14]. Swift leak detection and localization are crucial to minimize economic losses, necessitating a *leak detection system* (LDS) capable of promptly identifying and locating oil leaks.

An LDS's effectiveness depends on integration into a risk management framework exploiting knowledge about the SPS, achievable with the *dynamic risk management framework* (DRMF). The DRMF, integrating external experience and early warnings, enhances awareness of risks associated with unknown events. It involves *horizon screening*, *hazard identification*, *risk assessment*, and *decision/action*, requiring iterative updates for adaptability [94–97]. From this perspective, an LDS is an early warning subsystem guiding actions like plant shutdowns within a decision-support system.

Current leak detection technologies use internal methods based on process variable measurements and external methods with sensors monitoring the SPS's environment. These sensors, already present in several offshore fields [98, 99], adhere to strict quality standards [100].

A distinctive feature of underwater leaks is the associated acoustic signal, detectable through passive acoustic sensors [101, 102]. Unlike capacitive sensors requiring direct contact with leaking fluid, passive acoustic sensors offer a broader detection range, easy installation, and are cost-effective. However, passive acoustic sensors are susceptible to measurement noise, challenging the detection of smaller leaks [98–100].

Given these characteristics, a promising approach is LDS deployment based on acoustic sensors functioning as WSN nodes. While WSNs for leak detection are prevalent in monitoring oil and gas pipelines [103–105], recent research has extended to using WSNs for SPS monitoring, emphasizing benefits, particularly in the context of DRMF [54, 106, 107].

3.1.1 Signal Model

Using the general expression shown in Equation (2.40), it is possible to formulate the signal model of $y_k[n]$ captured by the kth underwater hydrophone situated in

the proximity of an item potentially being the source of underwater oil leakage:

$$y_k[n] = \sum_{m=1}^{M} \mathcal{H}_m[n]\xi_{m,k}[n]g(\boldsymbol{x}_k, \boldsymbol{\theta}_m) + w_k[n] \ , \tag{3.1}$$

where $\xi_{m,k}[n] \sim \mathcal{N}(0, \sigma^2_{\xi,m})$ and $w_k[n] \sim \mathcal{N}(0, \sigma^2_{w,k})$ represent the fluctuation of the emitted sound pressure produced by the leakage at a reference length (l_{ref}) and the *additive white Gaussian noise* (AWGN), respectively. $\xi_{m,k}[n]$ and $w_k[n]$ are assumed statistically independent thanks to the spatial separation of the sensors with *known* values of $\sigma^2_{\xi,m}$ and $\sigma^2_{w,k}$, $\forall m, k$ [33]. $g(\boldsymbol{x}_k, \boldsymbol{\theta}_m)$ represents the *amplitude attenuation function* (AAF) depending on the distance between the kth sensor and the leak caused by the failure of the mth item.

This, and the rare event approximation, allow one to express the statistical behavior of the measured signal as follows:

$$\begin{cases} y_k[n]|\mathcal{H}[n] = 0 \sim \mathcal{N}\Big(0, \sigma^2_{w,k}\Big) \\ y_k[n]|\mathcal{H}_m[n] = 1 \sim \mathcal{N}\Big(0, \sigma^2_{\xi,m}\, g^2(\boldsymbol{x}_k, \boldsymbol{\theta}_m) + \sigma^2_{w,k}\Big) \end{cases} . \tag{3.2}$$

The following is used to obtain the AAF [108]:

$$g(\boldsymbol{x}_k, \boldsymbol{\theta}_m) \triangleq \sqrt{\left(\frac{l_{\text{ref}}}{\|\boldsymbol{x}_k - \boldsymbol{\theta}_m\|}\right)^{k_{\text{sc}}} 10^{(l_{\text{ref}} - \|\boldsymbol{x}_k - \boldsymbol{\theta}_m\|)\alpha 10^{-4}}} \ , \tag{3.3}$$

where α is the seawater absorption coefficient in dB/km k_{sc} is the dimensionless spreading coefficient.

The *Francois & Garrison Equation* reported below is chosen for the calculation of α as it is among the best-performing equations available with one of the highest ranges of validity [109–111]. The value of the underwater speed of sound is obtained using the updated *Chen & Millero Equation* because of the wide range of applicability [111–114]. The detailed method is reported in [81].

3.1.2 Local Detection

Each sensor computes a LRT statistic Λ^k_n tests it. This LRT is computed as it is UMP and takes a local decision $d_k[n]$ [87]:

The resulting local ML detection test is the following:

$$\sum_{m=1}^{M} \Big(\varphi_m[n]\, a_{m,k}\, e^{b_{m,k}\, y^2_k[n]}\Big) \underset{d_k[n]=0}{\overset{d_k[n]=1}{\gtrless}} 1 \ , \tag{3.4}$$

where

$$a_{m,k} \triangleq \sqrt{\frac{\sigma_{w,k}^2}{\sigma_{\xi,m}^2\, g^2(\boldsymbol{x}_k, \boldsymbol{\theta}_m) + \sigma_{w,k}^2}} \,, \tag{3.5}$$

$$b_{m,k} \triangleq \frac{1}{2}\left(\frac{1}{\sigma_{w,k}^2} - \frac{1}{\sigma_{\xi,m}^2\, g^2(\boldsymbol{x}_k, \boldsymbol{\theta}_m) + \sigma_{w,k}^2}\right) . \tag{3.6}$$

Using the Karlin-Rubin Theorem, the test in Equation (3.4) is replaced with the following equivalent energy test [115]:

$$\Lambda_n^k = y_k^2[n] \underset{d_k[n]=0}{\overset{d_k[n]=1}{\gtrless}} \gamma_k[n] \,. \tag{3.7}$$

This equals to the determination of the value of $\gamma_k[n]$ that solves the following:

$$\sum_{m=1}^{M} \left(\varphi_m[n] a_{m,k} e^{b_{m,k}\gamma_k[n]}\right) = 1 \,. \tag{3.8}$$

The left-hand side exhibits smoothness, convexity, and increases with $\gamma_k[n]$. Consequently, convergence is assured, starting from any initial value $\gamma_k^{(0)}[n]$ when employing the *Newton-Raphson method* [116]:

$$\gamma_k^{(q+1)}[n] = \gamma_k^{(q)}[n] - \frac{\sum_{m=1}^{M} \left(\varphi_m[n] a_{m,k} e^{b_{m,k}\gamma_k^{(q)}[n]}\right) - 1}{\sum_{m=1}^{M} \left(\varphi_m[n] a_{m,k} b_{m,k} e^{b_{m,k}\gamma_k^{(q)}[n]}\right)} \,, \tag{3.9}$$

where q denotes the iteration index. This case shows that the computational complexity of finding the value of $\gamma_k[n]$ is $\mathcal{O}(M)$ per iteration per sensor.

The performances of the energy test in Equation (3.7) are [87]:

$$\mathcal{P}_D^{(k,m)}[n] = 2\mathcal{Q}\left(\sqrt{\frac{\gamma_k[n]}{\sigma_{\xi,m}^2\, g^2(\boldsymbol{x}_k, \boldsymbol{\theta}_m) + \sigma_{w,k}^2}}\right) , \tag{3.10}$$

$$\mathcal{P}_F^k[n] = 2\mathcal{Q}\left(\sqrt{\frac{\gamma_k[n]}{\sigma_{w,k}^2}}\right) . \tag{3.11}$$

3.1.3 Simulation Setup

The Goliat FPSO, situated in the Norwegian Barents Sea, stands as the world's northernmost offshore platform for oil production. Due to its placement in an

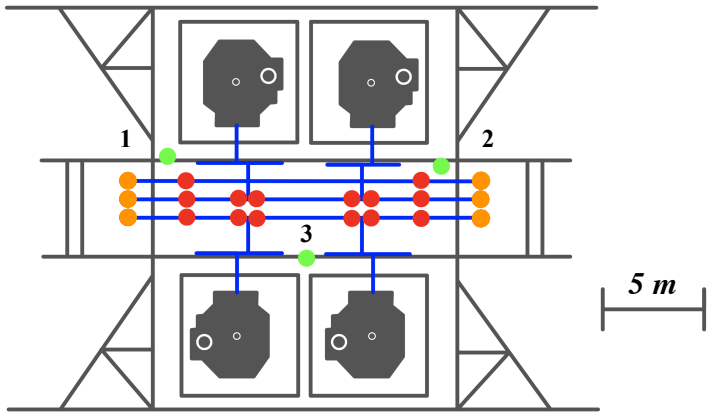

Figure 3.1: Goliat's template: the structural components are represented in gray, the manifold in blue, the sensors in green, the valves in red, and the connectors in orange.

environmentally sensitive region, the platform adheres to stringent regulations, particularly those concerning oil spills [100]. The FPSO employs a SPS with eight subsea templates supporting twenty-two wells, including twelve production wells, seven water injectors, and three gas injectors. Each template features a manifold and four well slots, as illustrated in Figure 3.1. The LDS monitoring each template combines internal and external sensors, with the internal sensors primarily serving process monitoring purposes. The external LDS comprises one capacitive sensor above each subsea tree, while three passive acoustic sensors are strategically placed to monitor the manifold [77, 117]. For this study, it is assumed that items and sensors are positioned at the same height.

Twenty critical items have been recognized within the SPS. Such components correspond to fourteen valves and six connectors. The reliability data of these categories of items are reported in Table 3.1, where literature values were sourced from the *OREDA Handbook* [118]. Sensors and critical items are highlighted in Figure 3.1 where it can be seen that 6 (respectively 14) critical items are inside (respectively outside) the sensors' perimeter.

The methodologies for detection and localization described in Sections 2.1 and 2.2 are applied here.

The simulations have been carried out using MATLAB. The parameters used for the case study are found in Table 3.2.

Table 3.1: Literature failure rates of components in subsea manifolds.

Item Category	$\lambda_{m,0}$ (in yr^{-1})	ν_m (in yr^{-2})
Valve, process isolation	7.3000×10^{-3}	7.0715×10^{-5}
Connector	9.5812×10^{-4}	2.4649×10^{-6}

Table 3.2: Parameters used to simulate a leak scenario.

Parameter	Value	Note / Reference
Reference Frequency	2.5 kHz	[102]
Water Temperature	3.8 °C	[119]
Water Salinity	35 ‰	[119]
Depth	350 m	[117]
pH	8	[120]
k_{sc}	1.5	[108]
l_{ref}	1 m	–
$\sigma^2_{w,k}$	1	$\forall k$

3.1.4 Per-Sample and Batch Detection and Localization

In order to better analyze the results, two different *signal-to-noise ratios* (SNRs) are simulated: $\text{SNR}_{\text{ref}} \triangleq \sigma^2_{\xi,m}/\sigma^2_{w,k} \in \{10\,\text{dB}, 15\,\text{dB}\}, \forall m, k$. When evaluating the per-sample and batch algorithms, the failure rates are assumed to be equal among all items, so that $\varphi_1 = \ldots = \varphi_M$.

The values for Q_F and Q_D were determined through numerical simulation, involving 10^8 Monte Carlo runs evenly split between scenarios $\mathcal{H}_0$ and $\mathcal{H}_1$. The assessment of localization performance was conducted via numerical simulation. In these simulations, the FC executed both the CR and the MCVR methods, with detection thresholds determined by maximizing the Youden's Index (J) [121]. For the threshold selection at the local level, we have:

$$\gamma_k = \arg\max_{\gamma} J(\gamma) = \arg\max_{\gamma} \left\{ \overline{\mathcal{P}_D^k}(\gamma) - \mathcal{P}_F^k(\gamma) \right\}, \tag{3.12}$$

where γ_k, $\overline{\mathcal{P}_D^k}$, and $\mathcal{P}_F^k$ are replaced with γ^*, $\overline{Q_D} \triangleq \sum_{m=1}^{M} \varphi_m Q_D^{(m)}$, and Q_F when

Table 3.3: Leak detection performances at the sensors.

$\mathrm{SNR}_{\mathrm{ref}}$	Sensor (k)	SNR_k	γ_k	$\overline{\mathcal{P}_D^k}(\gamma_k)$	$\mathcal{P}_F^k(\gamma_k)$	$J(\gamma_k)$
10 dB	1	-0.63 dB	1.4402	0.3540	0.2301	0.1238
	2	0.39 dB	1.5204	0.3563	0.2176	0.1388
	3	-1.61 dB	1.3189	0.3701	0.2508	0.1193
15 dB	1	4.37 dB	1.7916	0.4230	0.1807	0.2422
	2	5.39 dB	1.8820	0.4293	0.1701	0.2592
	3	3.39 dB	1.6887	0.4460	0.1938	0.2522

tuning the FC's global threshold.

The localization performances are assessed in terms of variation of the *root mean square error* (RMSE) with respect to the number of instants (N) since the leakage was detected.

Local Detection Results

In Table 3.3, the tuning outcomes following the maximization of J are presented, emphasizing how a higher value of $\mathrm{SNR}_k \triangleq \mathrm{SNR}_{\mathrm{ref}} \sum_{m=1}^{M} \varphi_m g^2(\boldsymbol{x}_k, \boldsymbol{\theta}_m)$ results in a higher threshold γ_k. The distribution of operating points in the *receiver operating characteristic* (ROC) space is depicted in Figure 3.2, revealing that the averaging procedure in Equation (2.10) yields three similar ROC curves, leading to comparable operating points. This consistency is expected given the similar values of SNR_k observed in this case study.

Global Detection Results

Figure 3.3 visually presents the ROC curves of the LDS where the CR and MCVR are compared against the CVR, serving as the upper benchmark (allowing the use of Equation (2.9)). The impact of $\mathrm{SNR}_{\mathrm{ref}}$ on overall performance is evident.

Except for instances where $\overline{Q_D} = Q_F = 0$ or $\overline{Q_D} = Q_F = 1$, the CR exhibits three possible operating points while the MCVR has seven. This emphasizes that the MCVR, with its broader spectrum of operating points, is more adaptable to diverse design requirements than the CR.

Table 3.4 represents the operating points resulting from threshold optimization procedures at the FC. The CR and MCVR demonstrate lower values of the maximum

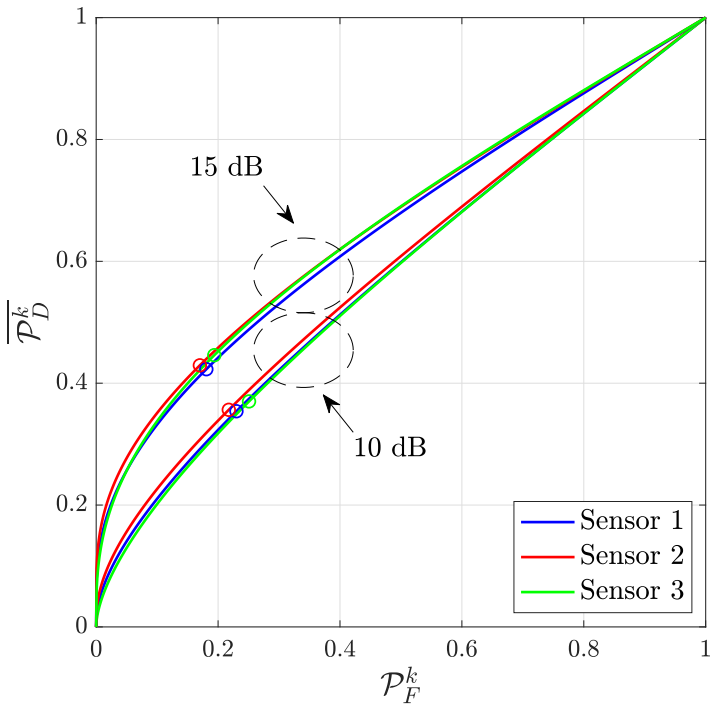

Figure 3.2: Local ROC curves highlighting the operating points.

J than the CVR. Interestingly, for $\mathrm{SNR}_{\mathrm{ref}} = 15\,\mathrm{dB}$, the optimal operating points from the two fusion rules are very similar. However, for $\mathrm{SNR}_{\mathrm{ref}} = 10\,\mathrm{dB}$, the optimization points differ, and the MCVR point lacks a close counterpart in the CR. Furthermore, the optimization point from the MCVR tends to be closer (in terms of $\overline{Q_D}$ and Q_F) to the one from the CVR. This underscores how, while maintaining the same complexity as the CR, the MCVR provides greater flexibility to the LDS and may enable superior results.

Localization Results

Figures 3.4, 3.5, 3.6, and 3.7 depict the outcomes of the four proposed localization techniques for both fusion rules (CR and MCVR). Additionally, the CRLB is presented for an estimator aligned with a perfect detector ($\overline{Q_D} = 1$, $Q_F = 0$), making it independent of the fusion rule and only varies based on the value of $\mathrm{SNR}_{\mathrm{ref}}$. It is essential to note that this lower bound is purely theoretical and cannot be achieved in practice, even with the CVR, as illustrated in Figure 3.3.

The distinction in performance between a leakage located inside or outside the sensor perimeter is also emphasized in the figures. The simulations incorporate the

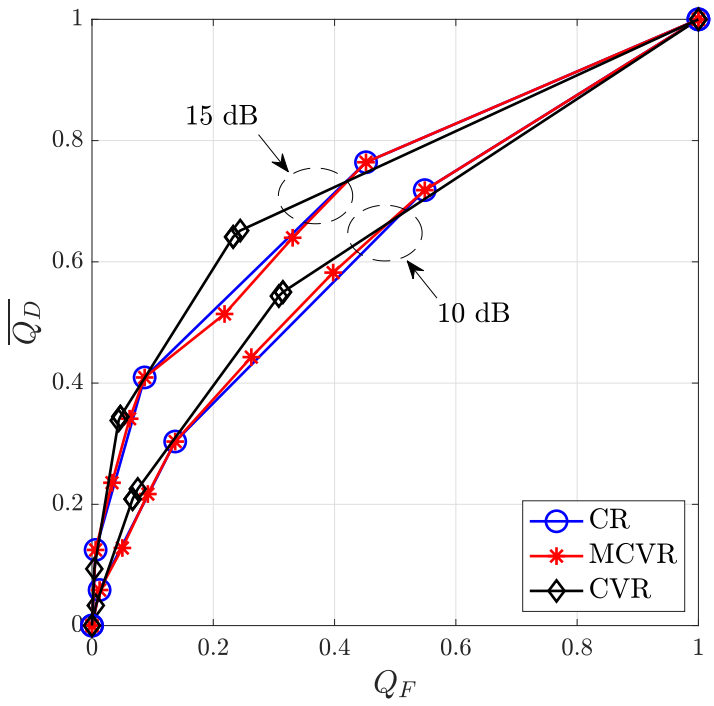

Figure 3.3: Global ROC curves.

Table 3.4: Leak detection performances at the FC.

SNR_{ref}	Fusion Rule	γ^*	$\overline{Q_D}(\gamma^*)$	$Q_F(\gamma^*)$	$J(\gamma^*)$
10 dB	CR	1	0.7183	0.5487	0.1696
	CVR	0.0849	0.5435	0.3081	0.2354
	MCVR	0.0650	0.5823	0.3977	0.1846
15 dB	CR	2	0.4093	0.0868	0.3225
	CVR	0.1411	0.6411	0.2328	0.4083
	MCVR	1.3584	0.4092	0.0869	0.3224

local and global thresholds from Table 3.3 and Table 3.4.

The choice of fusion rule (CR or MCVR) has little impact on the performance of the localization procedures. The CBA is the least effective, particularly in

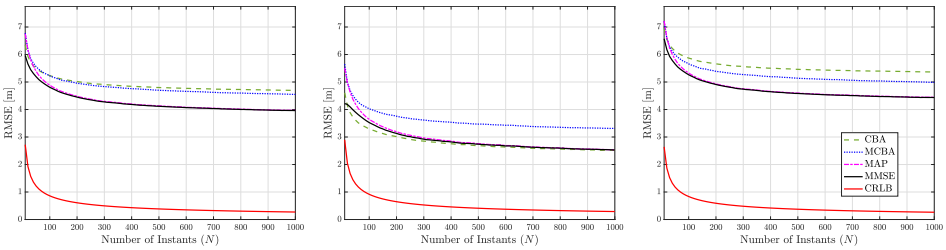

(a) All items. **(b)** Items inside sensor perimeter. **(c)** Items outside sensor perimeter.

Figure 3.4: Localization performances with CR and $\mathrm{SNR}_{\mathrm{ref}} = 10\,\mathrm{dB}$.

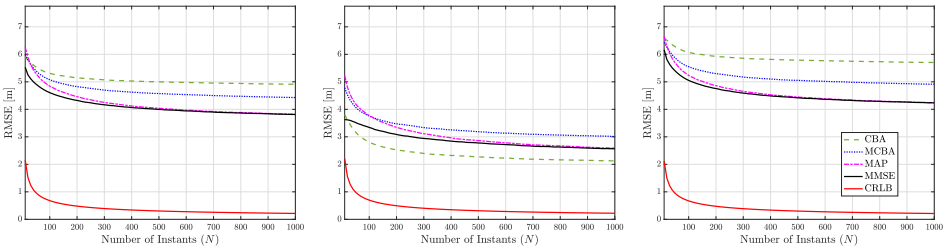

(a) All items. **(b)** Items inside sensor perimeter. **(c)** Items outside sensor perimeter.

Figure 3.5: Localization performances with CR and $\mathrm{SNR}_{\mathrm{ref}} = 15\,\mathrm{dB}$.

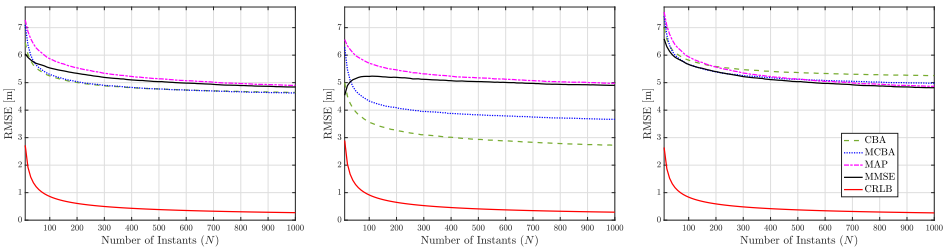

(a) All items. **(b)** Items inside sensor perimeter. **(c)** Items outside sensor perimeter.

Figure 3.6: Localization performances with MCVR and $\mathrm{SNR}_{\mathrm{ref}} = 10\,\mathrm{dB}$.

localizing leakages outside the sensor perimeter. In contrast, the MCBA addresses this limitation, and numerical simulations affirm its effectiveness without requiring additional computational resources. Notably, the CBA excels in cases where leakages are inside the sensor perimeter but performs poorly otherwise.

Both considered statistical approaches exhibit superior performance compared to

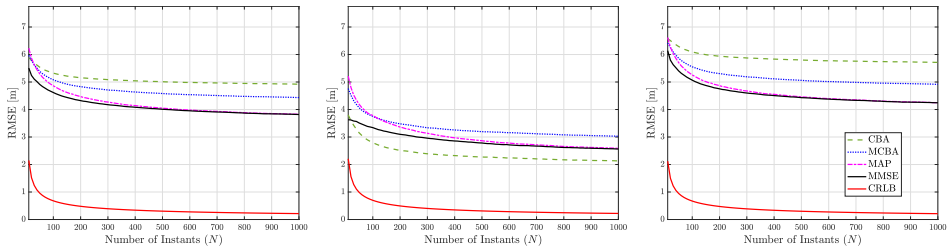

(a) All items.

(b) Items inside sensor perimeter.

(c) Items outside sensor perimeter.

Figure 3.7: Localization performances with MCVR and $\mathrm{SNR}_{\mathrm{ref}} = 15\,\mathrm{dB}$.

previous heuristic methods, albeit at a higher computational cost. Specifically, MAP and MMSE demonstrate similar behaviors, with the latter slightly outperforming the former at low values of N.

It is essential to note that the trade-off between probabilities of detection and false alarm at the detection stage is addressed in this work through the maximization of J. However, the detection probability is more critical from a localization standpoint, as increased detection probability leads to enhanced localization performance. This consideration is crucial when comparing performance across different $\mathrm{SNR}_{\mathrm{ref}}$ values, which may correspond to distinct operation points on the ROC curve. The design of the overall parameter configuration, considering both detection and localization performance, is not explicitly addressed in this work.

3.1.5 Quickest Detection and Localization

The proposed 3LA is compared with a WSN performing a BLRT analogous to Equation (2.45) with varying global thresholds. Such a configuration is here named *Shewhart chart*. This choice is because the 3LA is designed to be installed over an existing architecture where a FC makes the final decision via the Shewhart chart by adding a PPC and a feedback system. The 2LA is instead compared with a WSN performing detection and localization via the G-CUSUM. The architectures used for comparison reasons lack a feedback system. The Shewhart and G-CUSUM charts use the stationary prior probabilities of item failure seen in Equation (2.3), where the values of λ_m's are substituted by $\lambda_{m,0}$'s from Table 3.1 as the former are unknown.

The numerical results were derived via simulation consisting of 200 Monte Carlo runs.[1] In these simulations, each run emulated the operational lifespan of the platform fixed here at 15 years [122], neglecting inspection and maintenance times.

[1] Each set of 200 runs was performed for various γ^* values to generate the performance curves.

Moreover, the value of $\Delta t = 15$ min, and $\mathrm{SNR}_{\mathrm{ref}} \in \{0\ \mathrm{dB}, 5\ \mathrm{dB}, 10\ \mathrm{dB}\}$ are used. At each run, a new set of realizations of the M Poisson processes and their corresponding failure rates was generated, with λ_m values drawn from a Gamma distribution using central moments from Table 3.1.

In order to summarize the main detection results, it is necessary to introduce the following metrics:

$$\mathcal{P}_{10} \triangleq \mathbb{P}\left(\widehat{\mathcal{H}}[n] = 1 \middle| \mathcal{H}[n] = 0\right), \tag{3.13}$$

$$\mathcal{P}_{1} \triangleq \mathbb{P}(\mathcal{H}[n] = 1), \tag{3.14}$$

$$\mathrm{ADD} \triangleq \frac{\mathbb{E}(\varepsilon_{m,j})}{\Delta t}, \tag{3.15}$$

where $\mathcal{P}_{10}$ is the *probability of false alarm*, $\mathcal{P}_1$ is the *probability of faulty state*, and ADD is the *average detection delay*. The localization performances are evaluated using the RMSE between the estimated position of the leak and its actual location. Figures 3.8, 3.9, and 3.10 show the previously introduced metrics as $\mathcal{P}_{10}$ varies, at different values of $\mathrm{SNR}_{\mathrm{ref}}$. Higher values (respectively lower values) of $\mathcal{P}_{10}$ can be obtained by decreasing (respectively increasing) the threshold γ^* in the highest architectural layer.

Detection Results

By looking at Figures 3.8(a), 3.9(a), and 3.10(a), it is immediately visible how ADD greatly decreases as the $\mathrm{SNR}_{\mathrm{ref}}$ increases regardless of the employed architecture, once $\mathcal{P}_{10}$ is fixed. In particular, the ADD shows a decreasing trend with respect to $\mathcal{P}_{10}$ as a consequence of the lowering of γ^*, with $\mathrm{ADD} \to 0$ as $\mathcal{P}_{10} \to 1$, for all the methods. Specifically, for low values of $\mathcal{P}_{10}$, the proposed 2LA shows the lowest values of ADD among the four. The Shewhart chart is unable to operate at $\mathcal{P}_{10} < 10^{-2}$ due to missing temporal integration in the FC. Such a limitation is overcome by using the PPC as in the proposed 3LA, showing performances equivalent to the Shewhart chart with the further benefit of being able to work at $\mathcal{P}_{10} < 10^{-2}$. Moreover, at low $\mathrm{SNR}_{\mathrm{ref}}$, the 3LA tends to perform slightly better than the G-CUSUM chart, highlighting the benefits of a Bayesian approach, especially at low $\mathrm{SNR}_{\mathrm{ref}}$.

These performance trends are also observed when evaluating $\mathcal{P}_1$, representing the fraction of time the system spends in a faulty state. Figures 3.8(b), 3.9(b), and 3.10(b) show a similarity in behavior between the ADD and $\mathcal{P}_1$, as we vary $\mathcal{P}_{10}$. This shows the trade-off between a low $\mathcal{P}_{10}$ and a low $\mathcal{P}_1$, which must be addressed when choosing the proper threshold γ^*. As it is desirable to work at low values of $\mathcal{P}_{10}$, it is vital to select an architecture that can limit the effect of having a higher

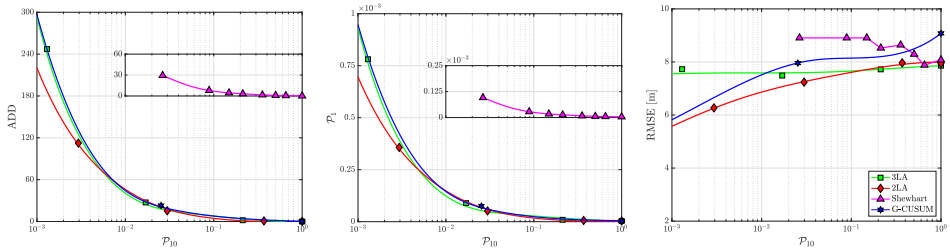

(a) $\mathcal{P}_{10}$ vs. ADD. **(b)** $\mathcal{P}_{10}$ vs. $\mathcal{P}_1$. **(c)** $\mathcal{P}_{10}$ vs. RMSE.

Figure 3.8: Performance curves at $\mathrm{SNR}_{\mathrm{ref}} = 0\,\mathrm{dB}$, $\forall m, k$.

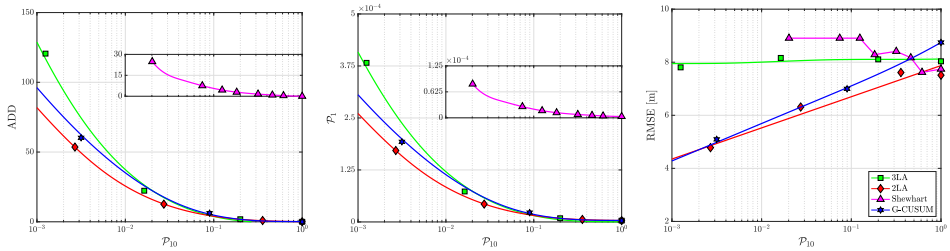

(a) $\mathcal{P}_{10}$ vs. ADD. **(b)** $\mathcal{P}_{10}$ vs. $\mathcal{P}_1$. **(c)** $\mathcal{P}_{10}$ vs. RMSE.

Figure 3.9: Performance curves at $\mathrm{SNR}_{\mathrm{ref}} = 5\,\mathrm{dB}$, $\forall m, k$.

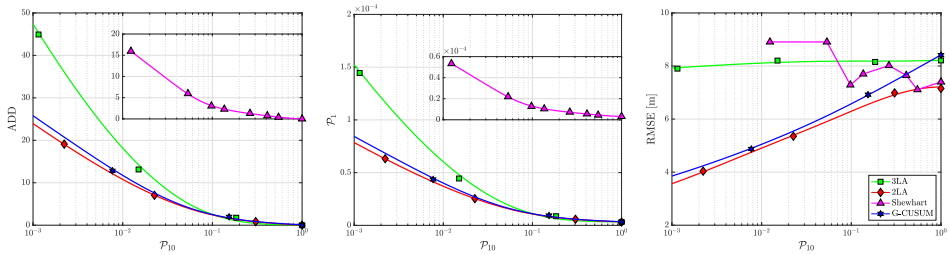

(a) $\mathcal{P}_{10}$ vs. ADD. **(b)** $\mathcal{P}_{10}$ vs. $\mathcal{P}_1$. **(c)** $\mathcal{P}_{10}$ vs. RMSE.

Figure 3.10: Performance curves at $\mathrm{SNR}_{\mathrm{ref}} = 10\,\mathrm{dB}$, $\forall m, k$.

threshold on $\mathcal{P}_1$. Because of the abovementioned issue, it is easy to see that the 2LA provides an excellent solution by reaching the lowest values of $\mathcal{P}_1$, given a fixed $\mathcal{P}_{10}$.

Localization Results

The localization results displayed in Figures 3.8(c), 3.9(c), and 3.10(c) show that, for the case of the 2LA and the G-CUSUM chart, as we lower $\mathcal{P}_{10}$, we simultaneously lower the localization RMSE causing a trade-off between localization accuracy and a quick detection. The explanation for this behavior is that raising the detection

threshold has the double effect of increasing the ADD, which simultaneously means that the highest hierarchical layer can collect more inputs, therefore improving the identification of the faulty item.

This does not apply to the Shewhart chart and the 3LA: the RMSE observed when employing the Shewhart chart does not have a monotonic behavior (as well as not being able to operate at $\mathcal{P}_{10} < 10^{-2}$), while the 3LA, as we lower $\mathcal{P}_{10}$, has a virtually null localization improvement. The behavior associated with the Shewhart chart is given by the nature of its localization algorithm, which produces estimates using only the last vector of local decisions as an input. Such a lack of time aggregation prevents the localization algorithm from updating its estimate as new local decisions are collected over time, which would cause the RMSE to decrease together with $\mathcal{P}_{10}$, like in the case of the 2LA and the G-CUSUM chart. Interestingly, we observe that in the Shewhart chart, as $\mathcal{P}_{10}$ decreases, the behavior of the RMSE reaches its maximum value when $\mathcal{P}_{10}$ reaches its minimum. In fact, for a system performing detection and localization without time aggregation, there exists a trade-off between a low $\mathcal{P}_{10}$ and localization RMSE. This is because a lower value of $\mathcal{P}_{10}$ means that the threshold required to trigger an alarm must be increased with a consequent effect of triggering alarms only when a higher number of sensors sends a positive detection. However, a low threshold can compromise the ability of the system to localize the faulty item, as there is a loss of correlation between the position of the faulty item and the particular configuration of the activated sensors. The 3LA (like the Shewhart chart) does not provide effective results in localization RMSE, confirming its primary purpose of being a way to lower the probability of false alarm of the Shewhart chart. Unlike the Shewhart chart, the 3LA performs a time aggregation in its highest hierarchical layer (the PPC), creating more stability in the behavior of the localization RMSE, as $\mathcal{P}_{10}$ changes. However, such time aggregation is performed on the FC's decisions over time that do not contain any spatial information regarding the sensors that contributed to such decisions.

This problem is addressed by the 2LA and the G-CUSUM chart, where the FC performs both time and spatial aggregation of the sensors' local decisions over time. As in the discussion of the detection performances, we notice how the 2LA outperforms the rest of the architectures in terms of localization RMSE.

3.2 Carbon Dioxide Dispersion in Industrial Plants

This application scenario pertains to monitoring CO_2 dispersion through a WSN comprising concentration sensors.

Existing research predominantly relies on a Gaussian plume point source model

based on diffusion/advection processes or the direct application of Fick's laws of diffusion. This approach, often unsuitable for realistic industrial systems, has been employed in studies addressing the dispersion of biochemical moving sources [123, 124], the localization of atmospheric pollutants [125], and the release of light gases [126]. In dealing with the uncertain prior, a study on CO_2 dispersion incorporated importance sampling along with the progressive correction technique [127], while innovative methods, such as those leveraging neural networks for plume tracking [128], focus on dispersion characterization rather than the detection task itself.

In contrast, CO_2 is a heavy gas with diverse applications in domestic and industrial settings [129]. Detecting heavy gases is a critical challenge due to their unique dispersion behavior of tending to spread close to the ground. This dispersion poses risks of asphyxiation by displacing air and reducing oxygen concentrations [130].

Within this context, the associated inference challenges revolve around the early sequential detection of uncooperative sources, as exemplified in a LOC scenario. In industrial settings, quickly and accurately identifying such critical events is paramount.

Complicating matters further is the natural presence of CO_2 in the atmosphere, which can significantly impair detector performance. Notably, many existing studies concentrate on gases uncommon in the atmosphere, resulting in heightened SNRs.

3.2.1 System Model

The scenario consists of a WSN tasked to assess the *global* absence ($\mathcal{H}_0$) or presence ($\mathcal{H}_1$) of a CO_2 dispersion within the monitored environment (see Figure 2.4). A dispersion is characterized by its position $\boldsymbol{\theta}$ and volumetric flow rate V (in Section 2.3, the generic intensity variable I was used). The global decision exploits the integration of real-time weather data as well as the dispersion model of the gas.

3.2.2 Signal Model

The statistical model of the measured gas concentration $y_k[n]$, depending on the corresponding hypothesis, is the following:

$$\begin{cases} \mathcal{H}_0: & y_k[n] = w_k[n] \\ \mathcal{H}_1: & y_k[n] = c_k + w_k[n] \end{cases}, \tag{3.16}$$

where $w_k[n] \sim \mathcal{N}\left(\mu_{w,k}, \sigma^2_{w,k}\right)$ represents the gas concentration present in normal operating conditions in the surrounding of the kth sensor [131], where $\mu_{w,k}$ and $\sigma^2_{w,k}$ are *known*. Also, $c_k \geq 0$ is the observed excess gas concentration resulting from dispersion.

In this work, the measurements collected by the same sensor $\{y_k[n]\}_n$ are assumed to be i.i.d., while the measurements collected by different sensors $\{y_k[n]\}_k$ are independent. Hence, the distribution of $y_k[n]$ is:

$$\begin{cases} \mathcal{H}_0: & y_k[n] \sim \mathcal{N}\left(\mu_{w,k}, \sigma^2_{w,k}\right) \\ \mathcal{H}_1: & y_k[n] \sim \mathcal{N}\left(\mu_{w,k} + c_k, \sigma^2_{w,k}\right) \end{cases} . \tag{3.17}$$

The heavy gas dispersion model here is based on the B&M model for continuous releases [132–137]. More specifically, the following map is provided:

$$c_k = c_k(\boldsymbol{x}_k, \boldsymbol{\theta}, \mathrm{T}_0, \rho_0, c_0, V, d_0, \mathrm{T}_{\mathrm{atm}}, \rho_{\mathrm{air}}, u, \psi) \ , \tag{3.18}$$

where T_0, ρ_0, c_0, and V are the temperature, density, concentration, and volumetric flow rate (respectively) of the gas at release condition from the source, whose diameter is denoted with d_0; $\mathrm{T}_{\mathrm{atm}}$ is the atmospheric temperature; ρ_{air} is the density of air at $\mathrm{T}_{\mathrm{atm}}$; finally u and ψ are the wind speed at the height of 10 meters and its direction (respectively).[2] $\mathrm{T}_{\mathrm{atm}}$, ρ_{air}, u, and ψ are *known* thanks to the integration of real-time weather measurements. A detailed description of the method is given in [85].

3.2.3 Local Detection

Each sensor engages in sequential detection based on the hypotheses presented in Equation (3.17). In this process, we calculate the GSPRT statistic, where the parameter c_k is substituted with its MLE $\widehat{c}_{k,n} \triangleq \frac{1}{n}\sum_{i=1}^{n} y_k[i] - \mu_{w,k}$. This results in Λ_n^k having the following form:

$$\Lambda_n^k \triangleq \sum_{i=1}^{n} (y_k[i] - \mu_{w,k}) \ . \tag{3.19}$$

By examining Equations (3.17) and (3.19), one can find:

$$\begin{cases} \mathcal{H}_0: & \Lambda_i^k \sim \mathcal{N}\left(0, i\sigma^2_{w,k}\right) \\ \mathcal{H}_1: & \Lambda_i^k \sim \mathcal{N}\left(ic_k, i\sigma^2_{w,k}\right) \end{cases} . \tag{3.20}$$

The local instant performances at the kth sensor $\mathcal{P}_F^{(k,i)}$ and $\mathcal{P}_D^{(k,i)}(c_k)$ for the generic mth decision with respect to this use case are the following:

$$\mathcal{P}_F^{(k,i)} \triangleq \mathbb{P}_0\left(d_m^k = \mathcal{H}_1, n_m^k - n_{m-1}^k = i\right)$$

[2] Wind blowing from north: 0° (360°), east: 90°, south: 180°, west: 270°.

$$= \mathbb{P}_0\Big(\Big\{\Lambda_n^k < \gamma_k\Big\}_{n<i}, \Lambda_n^k \geq \gamma_k\Big) = \mathbb{P}_0\Big(\boldsymbol{z}_i^k \leq \mathbf{0}\Big)\,, \tag{3.21}$$

$$\mathcal{P}_D^{(k,i)}(c_k) \triangleq \mathbb{P}_1\Big(\Big\{\Lambda_n^k < \gamma_k\Big\}_{n<i}, \Lambda_i^k \geq \gamma_k; c_k\Big) = \mathbb{P}_1\Big(\boldsymbol{z}_i^k \leq \mathbf{0}\Big)\,, \tag{3.22}$$

with $\boldsymbol{z}_i^k \overset{\mathcal{H}_j}{\sim} \mathcal{N}\Big(\boldsymbol{\mu}^j_{\boldsymbol{z}_i^k}, \boldsymbol{\Sigma}_{\boldsymbol{z}_i^k}\Big)$. Specifically:

$$\boldsymbol{z}_i^k \triangleq \begin{bmatrix} \Lambda_1^k - \gamma_k \\ \vdots \\ \Lambda_{i-1}^k - \gamma_k \\ -\Lambda_i^k + \gamma_k \end{bmatrix},\ \boldsymbol{\mu}^0_{\boldsymbol{z}_i^k} \triangleq \begin{bmatrix} -\gamma_k \\ \vdots \\ -\gamma_k \\ \gamma_k \end{bmatrix},\ \boldsymbol{\mu}^1_{\boldsymbol{z}_i^k} \triangleq \begin{bmatrix} c_k - \gamma_k \\ \vdots \\ (i-1)c_k - \gamma_k \\ -ic_k + \gamma_k \end{bmatrix},$$

$$\boldsymbol{\Sigma}_{\boldsymbol{z}_i^k} \triangleq \begin{bmatrix} \sigma^2_{w,k} & \sigma^2_{w,k} & \cdots & \sigma^2_{w,k} & -\sigma^2_{w,k} \\ \sigma^2_{w,k} & 2\sigma^2_{w,k} & \cdots & 2\sigma^2_{w,k} & -2\sigma^2_{w,k} \\ \vdots & \vdots & \ddots & \vdots & \vdots \\ \sigma^2_{w,k} & 2\sigma^2_{w,k} & \cdots & (i-1)\sigma^2_{w,k} & -(i-1)\sigma^2_{w,k} \\ -\sigma^2_{w,k} & -2\sigma^2_{w,k} & \cdots & -(i-1)\sigma^2_{w,k} & i\sigma^2_{w,k} \end{bmatrix}. \tag{3.23}$$

The values of $\mathcal{P}_C^{(k,i)}$ and $\mathcal{P}_M^{(k,i)}$ are obtained from previously calculated probabilities as seen from Equations (2.71) and (2.72). Nonetheless, the direct calculation of $\mathcal{P}_C^{(k,i)}$ and $\mathcal{P}_M^{(k,i)}(c_k)$ is here included:

$$\begin{aligned} \mathcal{P}_C^{(k,i)} &\triangleq \mathbb{P}_0\left(\left\{\Lambda_n^k < \gamma_k\right\}_{n\leq i}\right) = \mathbb{P}_0\Big(\boldsymbol{v}_i^k \leq \mathbf{0}\Big)\,, \\ \mathcal{P}_M^{(k,i)}(c_k) &\triangleq \mathbb{P}_1\left(\left\{\Lambda_n^k < \gamma_k\right\}_{n\leq i}; c_k\right) = \mathbb{P}_1\Big(\boldsymbol{v}_i^k \leq \mathbf{0}\Big)\,, \end{aligned} \tag{3.24}$$

with $\boldsymbol{v}_i^k \overset{\mathcal{H}_j}{\sim} \mathcal{N}\Big(\boldsymbol{\mu}^j_{\boldsymbol{v}_i^k}, \boldsymbol{\Sigma}_{\boldsymbol{v}_i^k}\Big)$. Specifically:

$$\boldsymbol{v}_i^k \triangleq \begin{bmatrix} \Lambda_1^k - \gamma_k \\ \vdots \\ \Lambda_i^k - \gamma_k \end{bmatrix},\ \boldsymbol{\mu}^0_{\boldsymbol{v}_i^k} \triangleq \begin{bmatrix} -\gamma_k \\ \vdots \\ -\gamma_k \end{bmatrix},\ \boldsymbol{\mu}^1_{\boldsymbol{v}_i^k} \triangleq \begin{bmatrix} c_k - \gamma_k \\ \vdots \\ (i-1)c_k - \gamma_k \\ ic_k - \gamma_k \end{bmatrix},$$

$$\boldsymbol{\Sigma}_{\boldsymbol{v}_i^k} \triangleq \begin{bmatrix} \sigma^2_{w,k} & \sigma^2_{w,k} & \sigma^2_{w,k} & \cdots & \sigma^2_{w,k} \\ \sigma^2_{w,k} & 2\sigma^2_{w,k} & 2\sigma^2_{w,k} & \cdots & 2\sigma^2_{w,k} \\ \sigma^2_{w,k} & 2\sigma^2_{w,k} & 3\sigma^2_{w,k} & \cdots & 3\sigma^2_{w,k} \\ \vdots & \vdots & \vdots & \ddots & \vdots \\ \sigma^2_{w,k} & 2\sigma^2_{w,k} & 3\sigma^2_{w,k} & \cdots & i\sigma^2_{w,k} \end{bmatrix}. \tag{3.25}$$

3.2.4 Results

The considered scenario models the dispersion of *saturated* CO_2.

The impact of small values of d_0 on the parameter c_k is typically negligible, allowing us to consider it as known and equal to zero. This simplification significantly reduces the computational complexity of the algorithms.

The presented results are obtained from simulations conducted within a monitored square area with sides measuring 100 meters, featuring evenly spaced sensors, as depicted in Figure 3.11. The simulated scenarios cover various network sizes $K \in \{9, 16\}$ for both *low flow rate* and *high flow rate* dispersions.

The results for each combination are derived from numerical simulations comprising 10^5 Monte Carlo runs, evenly distributed between scenarios $\mathcal{H}_0$ and $\mathcal{H}_1$ using MATLAB. In each run, parameters such as wind direction (ψ), wind speed (u), dispersion position ($\boldsymbol{\theta}$), flow rate (V), and dispersion diameter (d_0) are generated according to specific distributions.

Table 3.5 provides the values or distribution boundaries of the parameters, while the specifications of the parameter grids necessary for offline data preparation are outlined in Table 3.6.

The DTSA and the CSA are juxtaposed against a batch variant of the DTSA, where each sensor and the FC render a decision after a fixed number of measurements. To facilitate a straightforward comparison among the presented architectures throughout the remainder of the work, we presume that the deadlines $\mathcal{T}_k$'s (and $\mathcal{T}^*$) utilized in the DTSA and the CSA have values identical to the sample sizes at the sensor level (and FC level) employed in the batch algorithm.

Figure 3.12 displays the ROC *surfaces* of the kth sensor in the context of a batch detector (Figure 3.12(a)) and two sequential detectors (Figures 3.12(b) and 3.12(c)). The probability of detection strongly depends on c_k, given a fixed probability of false alarm. In terms of the *area under the curve* AUC, as $c_k \to 0$, $\mathrm{AUC} \to 0.5$, and as $c_k \to \infty$, $\mathrm{AUC} \to 1$, regardless of the chosen approach.

The figure also highlights the decision delays in the two approaches as the probability of false alarm and c_k undergo variations. Figure 3.12(a) showcases a constant decision delay equal to $\mathcal{T}_k$, while the other surfaces depict changes in $\mathcal{D}_{11}^k$ and $\mathcal{D}_{X1}^k$. Notably, as $\mathcal{P}_F^k \to 1$, $\left(\mathcal{D}_{11}^k, \mathcal{D}_{X1}^k\right) \to (1, 1)$, and as $\mathcal{P}_F^k \to 0$, $\left(\mathcal{D}_{11}^k, \mathcal{D}_{X1}^k\right) \to (\mathcal{T}_k, \mathcal{T}_k)$ due to the truncation preventing the delays from diverging to infinity.

The comparison between a batch and a sequential detector is facilitated in Fig-

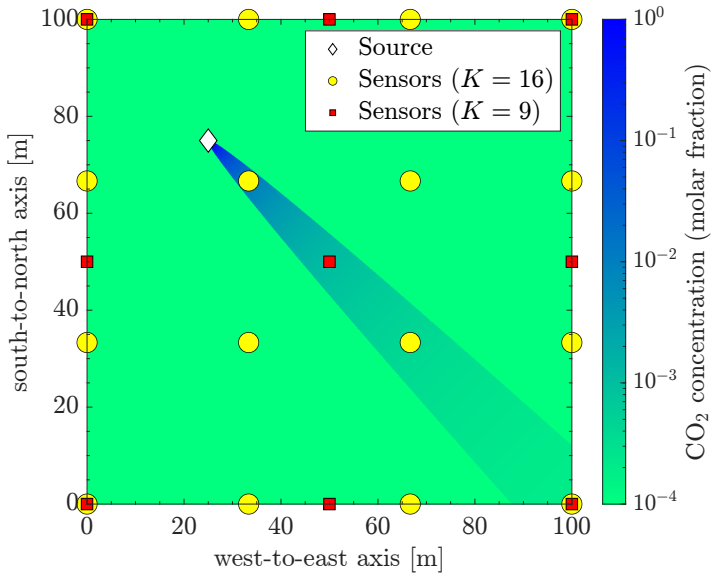

(a) Low flow rate: $V = 0.05\,\mathrm{m}^3/\mathrm{s}$ (maximum value).

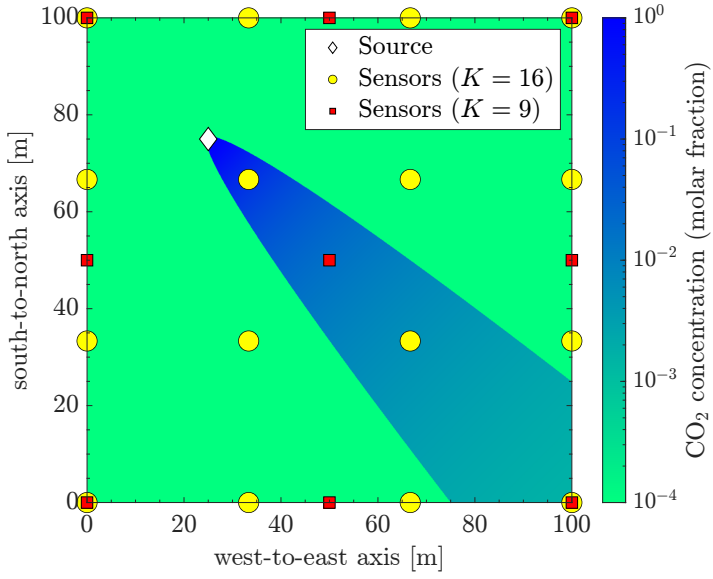

(b) High flow rate: $V = 0.5\,\mathrm{m}^3/\mathrm{s}$ (maximum value).

Figure 3.11: Mean concentration in a $\mathcal{H}_1$ scenario at different values of V with $\boldsymbol{\theta} = [25\,\mathrm{m}\ 75\,\mathrm{m}]^\mathrm{T}$, $\psi = 315°$, $d_0 = 0.1\,\mathrm{m}$, and $u = 5\,\mathrm{m/s}$.

ure 3.13. Figure 3.13(a) displays three sets of ROC curves and indicates a negligible

Table 3.5: Parameters used to simulate a gas dispersion scenario.

Parameter	Value / Distribution	Notes
θ_1 and θ_2	$\mathcal{U}(0, 100)$ m	uniform in monitored area
c_0	1	$c_0 = 10^6$ ppm
$\mathrm{T_{op}}$	253 K	[138]
$\mathrm{P_{op}}$	19.8 bar	saturation pressure at $\mathrm{T_{op}}$
$\mathrm{T_0}$	219 K	*Soave-Redlich-Kwong* EOS [139]
$\mathrm{P_{atm}}$	1.01 bar	–
ρ_0	2.48 kg/m^3	*Soave-Redlich-Kwong* EOS [139]
$\mathrm{T_{atm}}$	293 K	–
ρ_{air}	1.20 kg/m^3	–
u	$\mathcal{U}(0, 10)$ m/s	–
ψ	$\mathcal{U}(0, 2\pi)$	–
V	$\mathcal{U}(0, 0.05)$ m^3/s	low flow rate dispersion
V	$\mathcal{U}(0.4, 0.5)$ m^3/s	high flow rate dispersion
d_0	$\mathcal{U}(0, 0.2)$ m	–
$\mu_{w,k}$	400 ppm	$\forall k$
$\sigma_{w,k}$	200 ppm	$\forall k$
$\mathcal{T}_k$	4	$\forall k$
$\mathcal{P}_F^k$	0.05	$\forall k$
γ_k	693 ppm	$\forall k$, DTSA and CSA
γ_k	658 ppm	$\forall k$, Batch

difference in performance between the two approaches. Likewise, Figure 3.13(b) illustrates that once $\mathcal{P}_F^k$ is fixed, the value of $\mathcal{T}_k$ needed to achieve a desired value of $\mathcal{P}_D^k$ is similar in both batch and sequential approaches. Thus, the differences in detection accuracy between the batch and sequential approaches are negligible. The distinctive advantage of the sequential approach is illustrated in Figure 3.13(c). Here, the sequential decision delay $\mathcal{D}_{X1}^k$ consistently outperforms the batch decision time $\mathcal{T}_k$. This underscores the critical insight that when the probability of false alarm is held constant, employing a sequential approach allows a sensor to achieve detection with a noticeably reduced decision delay compared to a batch approach while maintaining a nearly identical probability of detection.

Figure 3.14 depicts the values of ATP across the various architectures as a function of the probability of occurrence $\mathcal{P}_1 \triangleq \mathbb{P}(\mathcal{H}_1)$. Upon examining the plot, it

Table 3.6: Parameters used for grid construction.

Parameter	Grid Limits	Grid Interval
θ_1 and θ_2	$[0, 100]$ m	1 m
V (low flow rate)	$[0, 0.05]$ m^3/s	$1/60$ m^3/s
V (medium flow rate)	$(0.05, 0.4)$ m^3/s	$60/7$ m^3/s
V (high flow rate)	$[0.4, 0.5]$ m^3/s	$1/30$ m^3/s
u	$[0.5, 10]$ m/s	0.5 m/s
ψ	$[0, 2\pi)$	$\pi/8$

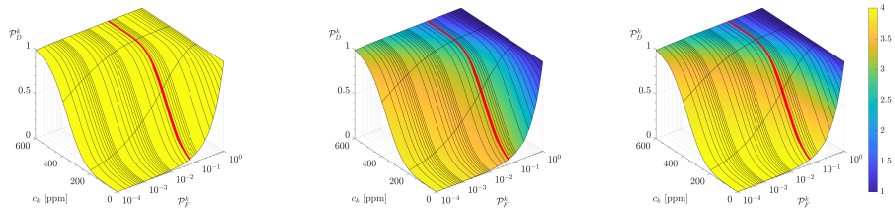

(a) Batch detector (colorbar shows $\mathcal{T}_k$). **(b)** Sequential detector (colorbar shows $\mathcal{D}_{11}^k$). **(c)** Sequential detector (colorbar shows $\mathcal{D}_{X1}^k$).

Figure 3.12: ROC surfaces of local detectors using batch and sequential approach (red line indicates performances at $\mathcal{P}_F^k = 0.05$).

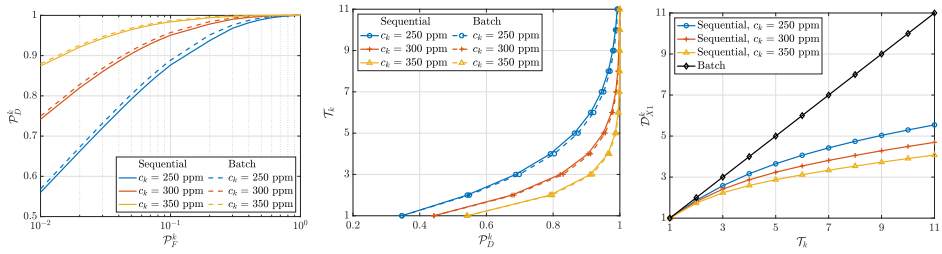

(a) ROC curves of the sensors. **(b)** $\mathcal{P}_D^k$ vs. $\mathcal{T}_k$, with $\mathcal{P}_F^k = 0.05$. **(c)** $\mathcal{T}_k$ vs. $\mathcal{D}_{X1}^k$, with $\mathcal{P}_F^k = 0.05$.

Figure 3.13: Detection performances of the sensor.

is evident that both $\mathrm{ATP}_{\mathrm{CSA}}$ and $\mathrm{ATP}_{\mathrm{DTSA}}$ exhibit an increase as $\mathcal{P}_1$ decreases. However, while $\mathrm{ATP}_{\mathrm{DTSA}}$ is capped by an upper bound represented by $\mathrm{ATP}_{\mathrm{Batch}}$, the relationship between $\mathrm{ATP}_{\mathrm{CSA}}$ and $\mathrm{ATP}_{\mathrm{Batch}}$ varies depending on $\mathcal{P}_1$ and c_k.

In the extreme scenario where $\mathcal{P}_1 = 1$ (corresponding to $\mathcal{H}_1$) or $\mathcal{P}_1 = 0$ (cor-

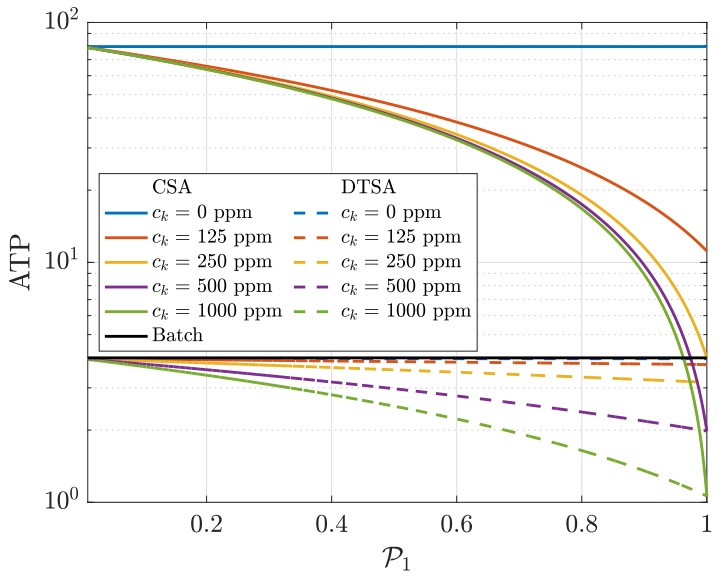

Figure 3.14: Average Transmission Period vs. Probability of Occurrence.

responding to $\mathcal{H}_0$), the ATP values exhibit clear distinct behaviors. Under $\mathcal{H}_1$, $\mathrm{ATP}_{\mathrm{CSA}}$ tends to rise for lower values of c_k, eventually surpassing $\mathrm{ATP}_{\mathrm{Batch}}$. In $\mathcal{H}_0$, $\mathrm{ATP}_{\mathrm{CSA}}$ remains significantly higher than $\mathrm{ATP}_{\mathrm{Batch}}$, irrespective of c_k. Consequently, when the reasonable assumption of low $\mathcal{P}_1$ holds, $\mathrm{ATP}_{\mathrm{CSA}}$ demonstrates an enhancement in reducing communication costs.

Let us examine the performance of the FC across the four mentioned configurations concerning the *global probability of false alarm* $Q_F \triangleq \mathbb{P}_0\left(\widehat{\mathcal{H}} = \mathcal{H}_1\right)$, *global probability of detection* $Q_D \triangleq \mathbb{P}_1\left(\widehat{\mathcal{H}} = \mathcal{H}_1\right)$, and *global decision delay* (in $\mathcal{H}_1$) defined as $\mathcal{D}^*_{X1} \triangleq \mathbb{E}_1(t^*)$ for the CSA and the DTSA and equal to $\mathcal{D}^*_{X1} \triangleq \mathcal{T}^*$ for the batch algorithm.

Figures 3.15 and 3.16 showcase the ROC curves and curves where $\mathcal{D}_{X1}$ is displayed as a function of Q_F. Various points on the curve are obtained by applying different values of the global threshold γ^* to the FC's detection rule. The presented results correspond to $\mathcal{T}^* \in \{4, 12\}$ (chosen as multiples of $\mathcal{T}_k$). The corresponding AUC values are detailed in Table 3.7 (including $\mathcal{T}^* = 8$).

Parallel to the AUC of the ROC curve, we define $\mathrm{AUC}(\mathcal{D}^*_{X1}) \triangleq \int_0^1 \mathcal{D}^*_{X1}(Q_F)\,\mathrm{d}Q_F$ to facilitate the discussion in Figures 3.15(c) and 3.16(c). This metric represents the mean value of $\mathcal{D}^*_{X1}$ over the domain of Q_F, with its values reported in Table 3.8.

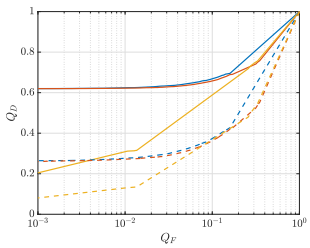

(a) ROC curves, $\mathcal{T}^* = 4$, $K = 9$.

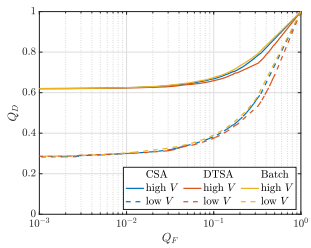

(b) ROC curves, $\mathcal{T}^* = 12$, $K = 9$.

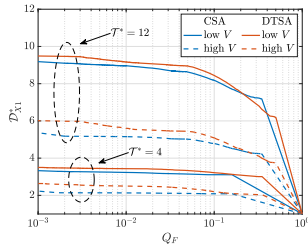

(c) Decision delay curves, $K = 9$.

Figure 3.15: ROC curves and decision delay curves, $K = 9$.

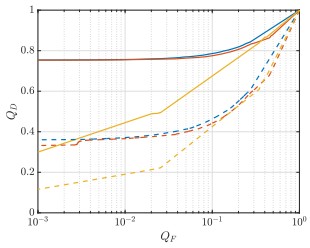

(a) ROC curves, $\mathcal{T}^* = 4$, $K = 16$.

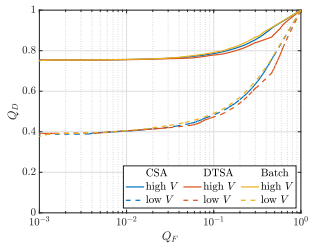

(b) ROC curves, $\mathcal{T}^* = 12$, $K = 16$.

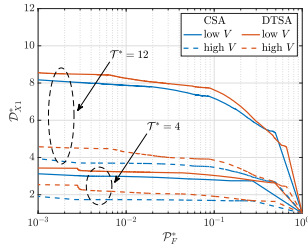

(c) Decision delay curves, $K = 16$.

Figure 3.16: ROC curves and decision delay curves, $K = 16$.

Table 3.7: AUC in the simulated detection configurations.

K	Method	$\mathcal{T}^* = 4$ low V	$\mathcal{T}^* = 4$ high V	$\mathcal{T}^* = 8$ low V	$\mathcal{T}^* = 8$ high V	$\mathcal{T}^* = 12$ low V	$\mathcal{T}^* = 12$ high V
9	CSA	**0.6556**	**0.8173**	0.6672	**0.8252**	0.6754	0.8313
	DTSA	0.6509	0.8121	0.6593	0.8169	0.6654	0.8208
	Batch	0.6307	0.7710	**0.6686**	0.8251	**0.6781**	**0.8343**
16	CSA	**0.7183**	**0.8878**	**0.7343**	**0.8945**	0.7428	0.8988
	DTSA	0.7047	0.8786	0.7157	0.8822	0.7221	0.8848
	Batch	0.6724	0.8294	0.7320	0.8911	**0.7444**	**0.9010**

The ROC curves demonstrate that augmenting the number of sensors enhances Q_D regardless of the algorithm employed. This improvement can be ascribed to two key factors: Firstly, a more significant number of sensors supplies the FC with more information, facilitating better discrimination between hypotheses. Secondly, given the anisotropic nature of gas dispersions, more sensors heightens the likelihood

Table 3.8: $\mathrm{AUC}(\mathcal{D}^*_{X1})$ in the simulated configurations.

K	Method	$\mathcal{T}^* = 4$ low V	$\mathcal{T}^* = 4$ high V	$\mathcal{T}^* = 8$ low V	$\mathcal{T}^* = 8$ high V	$\mathcal{T}^* = 12$ low V	$\mathcal{T}^* = 12$ high V
9	CSA	**2.2263**	**1.6320**	**3.8154**	**2.4724**	**5.3837**	**3.2943**
	DTSA	2.4062	1.7448	3.9661	2.5883	5.5021	3.4148
	Batch	4	4	8	8	12	12
16	CSA	**2.1243**	**1.4326**	**3.4569**	**1.9629**	**4.7146**	**2.4609**
	DTSA	2.3249	1.5427	3.6606	2.0990	4.9415	2.6321
	Batch	4	4	8	8	12	12

of multiple sensors being in contact with the gas plume. This, in turn, increases the chances of more sensors detecting $c_k > 0$ and contributes to non-random local detections.

Another notable observation is the elevated value of Q_D with an increased flow rate V. This phenomenon arises because an increase in V leads to a higher c_k for sensors already situated in the gas plume and more sensors experiencing $c_k > 0$.

In Table 3.7, there is a discernible increase in AUC with higher values of $\mathcal{T}^*$. At $\mathcal{T}^* = 4$, the presented values indicate $\mathrm{AUC}_{\mathrm{CSA}} > \mathrm{AUC}_{\mathrm{DTSA}} > \mathrm{AUC}_{\mathrm{Batch}}$, with a marginal difference in AUC (averaged among the four configurations) between the CSA and the batch algorithm. This trend shifts at $\mathcal{T}^* = 12$, reflecting a convergence in AUC values, with the batch algorithm exhibiting the highest values. Nevertheless, the average AUC difference between the CSA and the batch algorithm remains negligible.

Additional analysis uncovers that the anisotropic behavior of gas dispersions plays a role in the negligible differences in performance observed with higher values of $\mathcal{T}^*$. In scenarios where none of the sensors experience $c_k > 0$, each sensor (and the FC) operates as a random detector, irrespective of the specific value of $\mathcal{T}^*$.

However, the advantages in terms of $\mathcal{D}^*_{X1}$ become evident as K and V increase, as illustrated in Figures 3.15(c) and 3.16(c). While converging values of AUC are achieved by increasing $\mathcal{T}^*$, the difference in $\mathrm{AUC}(\mathcal{D}^*_{X1})$ is further accentuated in favor of the sequential algorithms, particularly the CSA.

Table 3.8 distinctly demonstrates that $\mathrm{AUC}(\mathcal{D}^*_{X1})_{\mathrm{CSA}} > \mathrm{AUC}(\mathcal{D}^*_{X1})_{\mathrm{DTSA}} > \mathrm{AUC}(\mathcal{D}^*_{X1})_{\mathrm{Batch}}$ for all configurations and values of $\mathcal{T}^*$. This is attributed to the fact that in the CSA and the DTSA, $\mathcal{D}^*_{X1}$ grows at a slower rate than $\mathcal{T}^*$, unlike

in the batch algorithm where the growth is identical.

Figures 3.15 and 3.16 vividly depict how the choice of the threshold γ^* impacts performance. Reducing γ^* leads to a simultaneous increase in Q_D and a decrease in $\mathcal{D}^*_{X1}$, but it comes at the expense of an elevated value of Q_F. Nevertheless, the curves demonstrate that both the CSA and the DTSA manage to sustain lower Q_F while maintaining stable levels of Q_D and $\mathcal{D}^*_{X1}$, particularly at lower values of $\mathcal{T}^*$.

Chapter 4

Conclusions and Future Directions

This research explored the detection and localization aspects of WSNs in the context of industrial monitoring. Three distinct approaches, namely per-sample/batch detection, quickest detection, and sequential detection, were investigated to develop strategies that bridge the gap between current sensor fusion strategies and a monitoring system taking advantage of the knowledge of the monitored system.

In the per-sample/batch detection approach, the comparative analysis between the CR and the MCVR demonstrated the latter's effectiveness as this provides more flexibility. The proposed localization algorithms showed that the heuristic methods can provide satisfactory results (especially in the MCBA case) and significantly lower the localization task's computational complexity.

The quickest detection approach introduced two architectures, the 3LA and the 2LA, leveraging diverse network structures for quickest fault detection in industrial plants. These architectures demonstrated the benefits of employing a Bayesian approach when information regarding the reliability of the monitored items is available. The 2LA, in particular, showcased the potential of spatio-temporal aggregation to reduce the detection time and improve the faulty components' localization accuracy.

The sequential detection approach proposed a WSN where sensors perform local sequential detection and transmit decisions to the FC. The DTSA and the CSA were introduced, and the evaluation in a CO_2 dispersion scenario in an industrial facility highlighted the effectiveness of these algorithms in addressing sequential detection challenges with respect to a batch approach. In particular, the CSA showed promising results in both detection performances and communication costs.

This research makes significant contributions to the field of WSNs for industrial monitoring. The proposed approaches and associated localization methods provide robust frameworks for timely and accurate event detection.

The findings have practical implications for designing and implementing WSNs in industrial settings. The developed strategies enhance monitoring systems' overall efficiency and reliability, facilitating quicker responses to adverse events and potentially minimizing the impact on industrial processes.

Future works include: (a) considering more complex failure models when employing Bayesian strategies; (b) the reduction of complexity via more efficient techniques for the calculation of high-complexity tasks (e.g., threshold selection, exact calculation of FC performances, and likelihood maximization); (c) modeling errors in communication channels between the sensors and the FC; (d) a more accurate statistical representation of the signal measured by the sensors; (e) development of algorithms that account for noisy dispersion models; (f) integration of hybrid machine learning approaches for improved detection and localization.

Bibliography

[1] J. C. Lopez-Ardao, R. F. Rodriguez-Rubio, A. Suarez-Gonzalez, M. Rodriguez-Perez, and M. E. Sousa-Vieira, "Current trends on green wireless sensor networks," *Sensors*, vol. 21, no. 13, p. 4281, 2021.

[2] K. Rose, S. Eldridge, and L. Chapin, "The Internet of Things: An overview," *The Internet Society (ISOC)*, vol. 80, pp. 1–50, 2015.

[3] S. He, K. Shi, C. Liu, B. Guo, J. Chen, and Z. Shi, "Collaborative sensing in Internet of Things: A comprehensive survey," *IEEE Communications Surveys & Tutorials*, vol. 24, no. 3, pp. 1435–1474, 2022.

[4] A. H. Sayed, *Inference and Learning from Data – Volume 1: Foundations*. Cambridge, UK: Cambridge University Press, 2022.

[5] A. H. Sayed, *Inference and Learning from Data – Volume 2: Inference*. Cambridge, UK: Cambridge University Press, 2022.

[6] A. H. Sayed, *Inference and Learning from Data – Volume 3: Learning*. Cambridge, UK: Cambridge University Press, 2022.

[7] T. Sahoo, *Process Plants – Shutdown and Turnaround Management*. Boca Raton (FL), USA: Taylor & Francis Group, 2014.

[8] M. Clay, M. Kidd, A. Gale, T. Boardman, J. Murphy, T. Wynn, S. Naylor, and J. Ellwood, "Understanding loss of containment of non-radiological chemotoxic materials in the civil nuclear and process industries," *Process Safety and Environmental Protection*, vol. 136, pp. 203–213, 2020.

[9] Market Research Future, "Market Research Report," 2023.

[10] M. A. Al-Jarrah, M. A. Yaseen, A. Al-Dweik, O. Dobre, and E. Alsusa, "Decision fusion for IoT-based wireless sensor networks," *IEEE Internet of Things Journal*, vol. 7, no. 2, pp. 1313–1326, 2019.

[11] D. Ciuonzo, P. Salvo Rossi, and P. K. Varshney, "Distributed detection in wireless sensor networks under multiplicative fading via generalized score tests," *IEEE Internet of Things Journal*, vol. 8, no. 11, pp. 9059–9071, 2021.

[12] N. Paltrinieri, G. Landucci, and P. Salvo Rossi, "Real-Time Data for Risk Assessment in the Offshore Oil and Gas Industry," in *International Conference on Offshore Mechanics and Arctic Engineering (OMAE)*, 2017.

[13] Y. Song, "Underwater Acoustic Sensor Networks With Cost Efficiency for Internet of Underwater Things," *IEEE Transactions on Industrial Electronics*, vol. 68, no. 2, pp. 1707–1716, 2021.

[14] C. Mai, S. Pedersen, L. Hansen, K. L. Jepsen, and Z. Yang, "Subsea infrastructure inspection: A review study," in *International Conference on Underwater System Technology: Theory and Applications (USYS)*, pp. 71–76, 2016.

[15] B. Ristic, A. Gunatilaka, and R. Gailis, "Localisation of a source of hazardous substance dispersion using binary measurements," *Atmospheric Environment*, vol. 142, pp. 114–119, 2016.

[16] D. D. Selvaratnam, I. Shames, D. V. Dimarogonas, J. H. Manton, and B. Ristic, "Co-operative estimation for source localisation using binary sensors," in *56th IEEE Annual Conference on Decision and Control (CDC)*, pp. 1572–1577, 2017.

[17] R. Abielmona, R. Falcon, N. Zincir-Heywood, and H. A. Abbass, eds., *Recent Advances in Computational Intelligence in Defense and Security*. (Studies in Computational Intelligence), Cham, Switzerland: Springer, 2016.

[18] L. Da Xu, W. He, and S. Li, "Internet of things in industries: A survey," *IEEE Transactions on Industrial Informatics*, vol. 10, no. 4, pp. 2233–2243, 2014.

[19] P. K. Varshney, *Distributed Detection and Data Fusion*. New York (NY), USA: Springer-Verlag, 1997.

[20] A. Shoari, G. Mateos, and A. Seyedi, "Analysis of target localization with ideal binary detectors via likelihood function smoothing," *IEEE Signal Processing Letters*, vol. 23, pp. 737–741, May 2016.

[21] Z. Chair and P. K. Varshney, "Optimal data fusion in multiple sensor detection systems," *IEEE Transactions on Aerospace and Electronic Systems*, vol. AES-22, pp. 98–101, Jan. 1986.

[22] R. Niu, P. K. Varshney, and Q. Cheng, "Distributed detection in a large wireless sensor network," *Information Fusion*, p. 15, 2006.

[23] Q. Yan and R. Blum, "Distributed signal detection under the Neyman-Pearson criterion," *IEEE Transactions on Information Theory*, vol. 47, pp. 1368–1377, May 2001.

[24] B. Chen, R. Jiang, T. Kasetkasem, and P. Varshney, "Channel aware decision fusion in wireless sensor networks," *IEEE Transactions on Signal Processing*, vol. 52, pp. 3454–3458, Dec. 2004.

[25] N. Sriranga, K. G. Nagananda, R. S. Blum, A. Saucan, and P. K. Varshney, "Energy-efficient decision fusion for distributed detection in wireless sensor networks," in *IEEE 21st International Conference on Information Fusion (FUSION)*, pp. 1541–1547, IEEE, July 2018.

[26] Y. Yang, R. S. Blum, and B. M. Sadler, "Distributed energy-efficient scheduling for radar signal detection in sensor networks," in *IEEE Radar Conference (RADAR)*, pp. 1094–1099, IEEE, 2010.

[27] Y. Yang, R. Blum, and B. Sadler, "A distributed and energy-efficient framework for Neyman-Pearson detection of fluctuating signals in large-scale sensor networks," *IEEE Journal on Selected Areas in Communications*, vol. 28, pp. 1149–1158, Sept. 2010.

[28] N. Sriranga, K. G. Nagananda, and R. S. Blum, "Shared channel ordered transmissions for energy-efficient distributed signal detection," *IEEE Communications Letters*, vol. 23, pp. 96–99, Jan. 2019.

[29] Y. Yang, R. Blum, and B. Sadler, "Energy-efficient routing for signal detection in wireless sensor networks," *IEEE Transactions on Signal Processing*, vol. 57, pp. 2050–2063, June 2009.

[30] X. Wang, G. Li, and P. K. Varshney, "Distributed detection of weak signals from one-bit measurements under observation model uncertainties," *IEEE Signal Processing Letters*, vol. 26, pp. 415–419, Mar. 2019.

[31] D. Ciuonzo, G. Papa, G. Romano, P. Salvo Rossi, and P. Willett, "One-bit decentralized detection with a rao test for multisensor fusion," *IEEE Signal Processing Letters*, vol. 20, pp. 861–864, Sept. 2013.

[32] D. Ciuonzo, P. Salvo Rossi, and P. Willett, "Generalized rao test for decentralized detection of an uncooperative target," *IEEE Signal Processing Letters*, vol. 24, pp. 678–682, May 2017.

[33] D. Ciuonzo and P. Salvo Rossi, "Distributed detection of a non-cooperative target via generalized locally-optimum approaches," *Information Fusion*, vol. 36, pp. 261–274, 2017.

[34] D. Ciuonzo, G. Romano, and P. Salvo Rossi, "Channel-aware decision fusion in distributed MIMO wireless sensor networks: Decode-and-fuse vs. decode-then-fuse," *IEEE Transactions on Wireless Communications*, vol. 11, no. 8, pp. 2976–2985, 2012.

[35] P. Salvo Rossi, D. Ciuonzo, T. Ekman, and H. Dong, "Energy detection for MIMO decision fusion in underwater sensor networks," *IEEE Sensors Journal*, vol. 15, no. 3, pp. 1630–1640, 2015.

[36] P. S. Rossi, D. Ciuonzo, K. Kansanen, and T. Ekman, "Performance analysis of energy detection for MIMO decision fusion in wireless sensor networks over arbitrary fading channels," *IEEE Transactions on Wireless Communications*, vol. 15, no. 11, pp. 7794–7806, 2016.

[37] A. Shoari and A. Seyedi, "Localization of an uncooperative target with binary observations," in *2010 IEEE 11th International Workshop on Signal Processing Advances in Wireless Communications (SPAWC)*, (Marrakech, Morocco), pp. 1–5, June 2010.

[38] J. Zhao, Q. Zhao, Z. Li, and Y. Liu, "An improved weighted centroid localization algorithm based on difference of estimated distances for wireless sensor networks," *Telecommunication Systems*, vol. 53, pp. 25–31, May 2013.

[39] Q. Dong and X. Xu, "A novel weighted centroid localization algorithm based on RSSI for an outdoor environment," *Journal of Communications*, vol. 9, no. 3, pp. 279–285, 2014.

[40] S. Durocher and D. Kirkpatrick, "The Steiner centre of a set of points: Stability, eccentricity, and applications to mobile facility locations," *International Journal of Computational Geometry and Applications*, vol. 16, pp. 345–371, Aug. 2006.

[41] Q. Zhou, X. Li, and Y. Xu, "Smallest enclosing circle based localization approach for wireless sensor networks," in *2009 WRI International Conference on Communications and Mobile Computing*, (Kunming, Yunnan, China), pp. 61–65, IEEE, Jan. 2009.

[42] A. Vempaty, H. He, B. Chen, and P. K. Varshney, "On quantizer design for distributed bayesian estimation in sensor networks," *IEEE Transactions on Signal Processing*, vol. 62, pp. 5359–5369, Oct. 2014.

[43] A. Kose and E. Masazade, "A multiobjective optimization approach for adaptive binary quantizer design for target tracking in wireless sensor networks," in *2015 IEEE International Conference on Multisensor Fusion and Integration for Intelligent Systems (MFI)*, (San Diego (CA), USA), pp. 31–36, Sept. 2015.

[44] J. Hu and R. Blum, "On the optimality of finite-level quantizations for distributed signal detection," *IEEE Transactions on Information Theory*, vol. 47, pp. 1665–1671, May 2001.

[45] D. Ciuonzo and P. Salvo Rossi, "Quantizer design for generalized locally optimum detectors in wireless sensor networks," *IEEE Wireless Communications Letters*, vol. 7, pp. 162–165, Apr. 2018.

[46] J. Fang, Y. Liu, H. Li, and S. Li, "One-bit quantizer design for multisensor GLRT fusion," *IEEE Signal Processing Letters*, vol. 20, pp. 257–260, Mar. 2013.

[47] S. Kar, H. Chen, and P. K. Varshney, "Optimal identical binary quantizer design for distributed estimation," *IEEE Transactions on Signal Processing*, vol. 60, pp. 3896–3901, July 2012.

[48] L. Xie, S. Zou, Y. Xie, and V. V. Veeravalli, "Sequential (quickest) change detection: Classical results and new directions," *IEEE Journal on Selected Areas in Information Theory*, vol. 2, no. 2, pp. 494–514, 2021.

[49] H. V. Poor and O. Hadjiliadis, *Quickest Detection*. Cambridge, UK: Cambridge University Press, 2008.

[50] A. Tartakovsky, I. Nikiforov, and M. Basseville, *Sequential Analysis: Hypothesis Testing and Changepoint Detection*. Monographs on Statistics and Applied Probability, Boca Raton (FL), USA: Chapman & Hall/CRC, 2014.

[51] R. Niu and P. K. Varshney, "Performance analysis of distributed detection in a random sensor field," *IEEE Transactions on Signal Processing*, vol. 56, no. 1, pp. 339–349, 2007.

[52] S. Sen, N. S. V. Rao, C. Q. Wu, M. L. Berry, K. M. Grieme, R. R. Brooks, and G. Cordone, "Performance analysis of Wald-statistic based network detection methods for radiation sources," in *19th International Conference on Information Fusion (FUSION)*, pp. 820–827, 2016.

[53] N. Sriranga, K. G. Nagananda, R. S. Blum, A. Saucan, and P. K. Varshney, "Energy-efficient decision fusion for distributed detection in wireless sensor networks," in *21st International Conference on Information Fusion (FUSION)*, pp. 1541–1547, 2018.

[54] M. Bucelli, I. B. Utne, P. Salvo Rossi, and N. Paltrinieri, "A system engineering approach to subsea spill risk management," *Safety Science*, vol. 123, 2020.

[55] A. Shoari and A. Seyedi, "Detection of a non-cooperative transmitter in Rayleigh fading with binary observations," in *IEEE Military Communications Conference (MILCOM)*, pp. 1–5, 2012.

[56] L. Hu, J. Zhang, X. Wang, S. Wang, and E. Zhang, "Decentralized truncated one-sided sequential detection of a noncooperative moving target," *IEEE Signal Processing Letters*, vol. 25, no. 10, pp. 1490–1494, 2018.

[57] X. Cheng, D. Ciuonzo, P. Salvo Rossi, X. Wang, and W. Wang, "Multi-bit & sequential decentralized detection of a noncooperative moving target through a generalized Rao test," *IEEE Transactions on Signal and Information Processing over Networks*, vol. 7, pp. 740–753, 2021.

[58] H. Poor, *An Introduction to Signal Detection and Estimation*. (Springer Texts in Electrical Engineering), New York (NY), USA: Springer, 2 ed., 2013.

[59] A. Wald, *Sequential Analysis*. (Wiley publication in mathematical statistics), New York (NY), USA: J. Wiley & sons, Incorporated, 1947.

[60] D. Siegmund, *Sequential Analysis: Tests and Confidence Intervals*. (Springer Series in Statistics), New York (NY), USA: Springer, 1985.

[61] Y. Mei, "Asymptotic optimality theory for decentralized sequential hypothesis testing in sensor networks," *IEEE Transactions on Information Theory*, vol. 54, no. 5, pp. 2072–2089, 2008.

[62] G. Fellouris and G. V. Moustakides, "Decentralized sequential hypothesis testing using asynchronous communication," *IEEE Transactions on Information Theory*, vol. 57, no. 1, pp. 534–548, 2011.

[63] S. Li, X. Li, X. Wang, and J. Liu, "Decentralized sequential composite hypothesis test based on one-bit communication," *IEEE Transactions on Information Theory*, vol. 63, no. 6, pp. 3405–3424, 2017.

[64] Z. Li, S. Cheng, F. Gao, and Y.-C. Liang, "Sequential detection for cognitive radio with multiple primary transmit power levels," *IEEE Transactions on Communications*, vol. 65, pp. 2769–2780, July 2017.

[65] Q. Zou, S. Zheng, and A. H. Sayed, "Cooperative sensing via sequential detection," *IEEE Transactions on Signal Processing*, vol. 58, pp. 6266–6283, Dec. 2010.

[66] S.-J. Kim and G. B. Giannakis, "Sequential and cooperative sensing for multi-channel cognitive radios," *IEEE Transactions on Signal Processing*, vol. 58, pp. 4239–4253, Aug. 2010.

[67] S. Chaudhari, V. Koivunen, and H. Poor, "Autocorrelation-based decentralized sequential detection of ofdm signals in cognitive radios," *IEEE Transactions on Signal Processing*, vol. 57, pp. 2690–2700, July 2009.

[68] S. Chaudhari, J. Lunden, and V. Koivunen, "Effects of quantization and channel errors on sequential detection in cognitive radios," in *2012 46th Annual Conference on Information Sciences and Systems (CISS)*, (Princeton (NJ), USA), pp. 1–6, Mar. 2012.

[69] Y. Yilmaz, G. V. Moustakides, and X. Wang, "Cooperative sequential spectrum sensing based on level-triggered sampling," *IEEE Transactions on Signal Processing*, vol. 60, pp. 4509–4524, Sept. 2012.

[70] Y. Yilmaz, G. V. Moustakides, and X. Wang, "Channel-aware decentralized detection via level-triggered sampling," *IEEE Transactions on Signal Processing*, vol. 61, no. 2, pp. 300–315, 2013.

[71] Y. Yilmaz and X. Wang, "Sequential distributed detection in energy-constrained wireless sensor networks," *IEEE Transactions on Signal Processing*, vol. 62, no. 12, pp. 3180–3193, 2014.

[72] S. Tantaratana and H. Poor, "Asymptotic efficiencies of truncated sequential tests," *IEEE Transactions on Information Theory*, vol. 28, no. 6, pp. 911–923, 1982.

[73] M. Guerriero, V. Pozdnyakov, J. Glaz, and P. Willett, "A repeated significance test with applications to sequential detection in sensor networks," *IEEE Transactions on Signal Processing*, vol. 58, no. 7, pp. 3426–3435, 2010.

[74] P. Khanduri, D. Pastor, V. Sharma, and P. K. Varshney, "Truncated sequential non-parametric hypothesis testing based on random distortion testing," *IEEE Transactions on Signal Processing*, vol. 67, no. 15, pp. 4027–4042, 2019.

[75] A. H. Sayed, "Adaptation, learning, and optimization over networks," *Foundations and Trends® in Machine Learning*, vol. 7, no. 4–5, pp. 311–801, 2014.

[76] A. H. Sayed, "Diffusion adaptation over networks," in *Array and Statistical Signal Processing* (A. M. Zoubir, M. Viberg, R. Chellappa, and S. Theodoridis, eds.), vol. 3 of *Academic Press Library in Signal Processing*, Elsevier, 2014.

[77] E. Røsby, "Goliat development project – Subsea leak detection design," 2011.

[78] J. Pan and J. McElhannon, "Future edge cloud and edge computing for internet of things applications," *IEEE Internet of Things Journal*, vol. 5, no. 1, pp. 439–449, 2017.

[79] G. Tabella, N. Paltrinieri, V. Cozzani, and P. Salvo Rossi, "Subsea oil spill risk management based on sensor networks," *Chemical Engineering Transactions*, vol. 82, pp. 199–204, Oct. 2020.

[80] G. Tabella, N. Paltrinieri, V. Cozzani, and P. Salvo Rossi, "Data fusion for subsea oil spill detection through wireless sensor networks," in *Proceedings of IEEE Sensors*, 2020.

[81] G. Tabella, N. Paltrinieri, V. Cozzani, and P. Salvo Rossi, "Wireless sensor networks for detection and localization of subsea oil leakages," *IEEE Sensors Journal*, vol. 21, no. 9, pp. 10890–10904, 2021.

[82] G. Tabella, D. Ciuonzo, N. Paltrinieri, and P. Salvo Rossi, "Spatio-temporal decision fusion for quickest fault detection within industrial plants: The oil and gas scenario," in *IEEE 24th International Conference on Information Fusion (FUSION)*, 2021.

[83] G. Tabella, D. Ciuonzo, N. Paltrinieri, and P. Salvo Rossi, "Bayesian fault detection and localization through wireless sensor networks in industrial plants," *IEEE Internet of Things Journal*, 2024. in press.

[84] G. Tabella, Y. Di Martino, D. Ciuonzo, N. Paltrinieri, X. Wang, and P. Salvo Rossi, "Decision fusion for carbon dioxide release detection from pressure relief devices," in *IEEE 12th Sensor Array and Multichannel Signal Processing Workshop (SAM)*, pp. 46–50, 2022.

[85] G. Tabella, Y. Di Martino, D. Ciuonzo, N. Paltrinieri, X. Wang, and P. Salvo Rossi, "Sensor fusion for detection and localization of carbon dioxide releases for Industry 4.0," in *IEEE 25th International Conference on Information Fusion (FUSION)*, 2022.

[86] G. Tabella, D. Ciuonzo, Y. Yilmaz, X. Wang, and P. Salvo Rossi, "Time-aware distributed sequential detection of gas dispersion via wireless sensor networks," *IEEE Transactions on Signal and Information Processing over Networks*, vol. 9, pp. 721–735, 2023.

[87] S. Kay, *Fundamentals of Statistical Signal Processing: Detection theory*. Prentice Hall Signal Processing Series, Upper Saddle River (NJ), USA: Prentice-Hall PTR, 1 ed., 1998.

[88] M. Rausand and A. Høyland, *System reliability theory: models, statistical methods, and applications*. (Wiley series in probability and statistics), Hoboken (NJ), USA: Wiley-Interscience, 2 ed., 2004.

[89] M. Rausand and S. Haugen, *Risk Assessment: Theory, Methods, and Applications*. Hoboken (NJ), USA: John Wiley & Sons, 1 ed., 2011.

[90] A. D'Costa, V. Ramachandran, and A. M. Sayeed, "Distributed classification of gaussian space-time sources in wireless sensor networks," *IEEE Journal on Selected Areas in Communications*, vol. 22, no. 6, pp. 1026–1036, 2004.

[91] H. Fang and M. Duan, *Offshore Operation Facilities: Equipment and Procedures*. Elsevier Science, 2014.

[92] Y. Bai and Q. Bai, *Subsea Engineering Handbook*. Houston (TX), USA: Elsevier, 2012.

[93] F. Pallavicini, "Developement of offshore fields," in *Encyclopaedia of Hydrocarbons Volume 1 – Exploration, Production and Transport*, ch. 5.2, pp. 609–628, Rome, Italy: Treccani, 2005.

[94] N. Paltrinieri, F. Khan, P. Amyotte, and V. Cozzani, "Dynamic approach to risk management: Application to the Hoeganaes metal dust accidents," *Process Safety and Environmental Protection*, vol. 92, pp. 669–679, Nov. 2014.

[95] V. Villa, N. Paltrinieri, F. Khan, and V. Cozzani, "Towards dynamic risk analysis: A review of the risk assessment approach and its limitations in the chemical process industry," *Safety Science*, vol. 89, pp. 77–93, Nov. 2016.

[96] T. Grøtan and N. Paltrinieri, "Dynamic risk management in the perspective of a resilient system," in *Dynamic Risk Analysis in the Chemical and Petroleum Industry*, pp. 245–257, Elsevier, 2016.

[97] N. Paltrinieri, L. Comfort, and G. Reniers, "Learning about risk: Machine learning for risk assessment," *Safety Science*, vol. 118, pp. 475–486, 2019.

[98] M. A. Adegboye, W. K. Fung, and A. Karnik, "Recent advances in pipeline monitoring and oil leakage detection technologies: Principles and approaches," *Sensors*, vol. 19, no. 11, 2019.

[99] U. Baroudi, A. A. Al-Roubaiey, and A. Devendiran, "Pipeline leak detection systems and data fusion: A survey," *IEEE Access*, vol. 7, pp. 97426–97439, 2019.

[100] DNV-GL, "Recommended practice RP-F302 offshore leak detection," Apr. 2016.

[101] H. Fuchs and R. Riehle, "Ten years of experience with leak detection by acoustic signal analysis," *Applied Acoustics*, vol. 33, no. 1, pp. 1–19, 1991.

[102] E. G. Eckert, J. W. Maresca, R. W. Hillger, and J. J. Yezzi, "Location of leaks in pressurized petroleum pipelines by means of passive-acoustic sensing methods," in *Leak Detection for Underground Storage Tanks* (P. Durgin and T. Young, eds.), pp. 53–69, West Conshohocken (PA), USA: ASTM International, 1993.

[103] J. Li, C. Wang, Q. Zheng, and Z. Qian, "Leakage localization for long distance pipeline based on compressive sensing," *IEEE Sensors Journal*, vol. 19, no. 16, pp. 6795–6801, 2019.

[104] M. Meribout, "A wireless sensor network-based infrastructure for real-time and online pipeline inspection," *IEEE Sensors Journal*, vol. 11, no. 11, pp. 2966–2972, 2011.

[105] T. R. Sheltami, A. Bala, and E. M. Shakshuki, "Wireless sensor networks for leak detection in pipelines: a survey," *Journal of Ambient Intelligence and Humanized Computing*, vol. 7, pp. 347–356, June 2016.

[106] N. Paltrinieri, G. Landucci, and P. Salvo Rossi, "An integrated approach to support the dynamic risk assessment of complex industrial accidents," *Chemical Engineering Transactions*, vol. 77, pp. 265–270, 2019.

[107] M. R. Akhondi, A. Talevski, S. Carlsen, and S. Petersen, "Applications of wireless sensor networks in the oil, gas and resources industries," in *2010 24th IEEE International Conference on Advanced Information Networking and Applications*, (Perth, Australia), pp. 941–948, 2010.

[108] M. Stojanovic, "On the relationship between capacity and distance in an underwater acoustic communication channel," in *Proceedings of the 1st ACM international workshop on Underwater networks – WUWNet '06*, ACM Press, 2006.

[109] R. E. Francois and G. R. Garrison, "Sound absorption based on ocean measurements: Part I: Pure water and magnesium sulfate contributions," *Journal of the Acoustical Society of America*, vol. 72, no. 3, pp. 896–907, 1982.

[110] R. E. Francois and G. R. Garrison, "Sound absorption based on ocean measurements: Part II: Boric acid contribution and equation for total absorption," *Journal of the Acoustical Society of America*, vol. 72, no. 6, pp. 1879–1890, 1982.

[111] P. C. Etter, *Underwater Acoustic Modeling and Simulation*. Boca Raton (FL), USA: CRC Press, 5 ed., 2018.

[112] C. Chen and F. J. Millero, "Speed of sound in seawater at high pressures," *Journal of the Acoustical Society of America*, vol. 62, no. 5, pp. 1129–1135, 1977.

[113] F. J. Millero and X. Li, "Comments on 'on equations for the speed of sound in seawater' [J. Acoust. Soc. Am. 93, 255–275 (1993)]," *Journal of the Acoustical Society of America*, vol. 95, no. 5, pp. 2757–2759, 1994.

[114] G. S. K. Wong and S. Zhu, "Speed of sound in seawater as a function of salinity, temperature, and pressure," *Journal of the Acoustical Society of America*, vol. 97, no. 3, pp. 1732–1736, 1995.

[115] G. Casella and R. L. Berger, *Statistical Inference*. Pacific Grove (CA), USA: Thomson Learning, 2 ed., 2002.

[116] D. Kincaid and W. Cheney, *Numerical Analysis: Mathematics of Scientific Computing*. Providence (RI), USA: American Mathematical Society, 3 ed., 2002.

[117] E. Bjørnbom, "Goliat – Leak detection and monitoring from template to satellite," 2011.

[118] SINTEF, *OREDA Offshore Reliability Data Handbook*. OREDA Participants, 4 ed., 2002.

[119] Institute of Marine Research, "Mareano," 2021.

[120] A. A. Vetrov and E. A. Romankevich, *Carbon Cycle in the Russian Arctic Seas*. Berlin, Germany: Springer, 2004.

[121] W. J. Youden, "Index for rating diagnostic tests," *Cancer*, vol. 3, pp. 32–35, 1950.

[122] Vår Energi, "Goliat Barrier Status Panel," 2016.

[123] T. Zhao and A. Nehorai, "Detecting and estimating biochemical dispersion of a moving source in a semi-infinite medium," *IEEE Transactions on Signal Processing*, vol. 54, no. 6, pp. 2213–2225, 2006.

[124] S. Aldalahmeh, M. Ghogho, and A. Swami, "Fast distributed detection, localization, and estimation of a diffusive target in wireless sensor networks," in *7th IEEE International Symposium on Wireless Communication Systems (ISWCS)*, pp. 882–886, 2010.

[125] B. Ristic, A. Gunatilaka, and R. Gailis, "Achievable accuracy in Gaussian plume parameter estimation using a network of binary sensors," *Information Fusion*, vol. 25, pp. 42–48, 2015.

[126] S. Vijayakumaran, Y. Levinbook, and T. F. Wong, "Maximum likelihood localization of a diffusive point source using binary observations," *IEEE Transactions on Signal Processing*, vol. 55, no. 2, pp. 665–676, 2007.

[127] A. Gunatilaka, B. Ristic, A. Skvortsov, and M. Morelande, "Parameter estimation of a continuous chemical plume source," in *11th IEEE International Conference on Information Fusion (FUSION)*, pp. 1–8, 2008.

[128] J. Shi, W. Xie, J. Li, X. Zhang, X. Huang, A. S. Usmani, F. Khan, and G. Chen, "Real-time plume tracking using transfer learning approach," *Computers & Chemical Engineering*, vol. 172, p. 108172, 2023.

[129] Y. Di Martino, S. E. Duque, G. Reniers, and V. Cozzani, "Making the chemical and process industries more sustainable: Innovative decision-making framework to incorporate technological and non-technological inherently safer design (ISD) opportunities," *Journal of Cleaner Production*, vol. 296, p. 126421, 2021.

[130] P. Harper, *Assessment of the major hazard potential of carbon dioxide (CO_2)*. UK: Health and Safety Executive, 2011.

[131] Y. Liu, Z. Pang, M. Karlsson, and S. Gong, "Anomaly detection based on machine learning in iot-based vertical plant wall for indoor climate control," *Building and Environment*, vol. 183, p. 107212, 2020.

[132] R. E. Britter and J. McQuaid, *Workbook on the dispersion of dense gases*. UK: Health and Safety Executive, 1988.

[133] S. Hanna, "Britter and McQuaid (B&M) 1988 workbook nomograms for dense gas modeling applied to the Jack Rabbit II chlorine release trials," *Atmospheric Environment*, vol. 232, p. 117539, 2020.

[134] TNO, *Yellow Book – Methods for the calculation of physical effects due to releases of hazardous materials (liquids and gases)*. The Hague, The Netherlands: The Committee for the Prevention of Disasters by Hazardous Materials, 2005.

[135] S. Mannan, *Lees' Loss Prevention in the Process Industries*. Oxford, UK: Butterworth-Heinemann, 4 ed., 2012.

[136] CCPS, *Guidelines for Consequence Analysis of Chemical Releases*. Hoboken (NJ), USA: John Wiley & Sons, 1 ed., 1999.

[137] D. A. Crowl and J. F. Louvar, *Chemical Process Safety: Fundamentals with Applications*. London, UK: Pearson Education, 4 ed., 2019.

[138] NIST, "Thermophysical Properties of Carbon dioxide," 2023.

[139] J. M. Smith, H. C. Van Ness, M. M. Abbott, and M. T. Swihart, *Introduction to Chemical Engineering Thermodynamics*. New York (NY), USA: McGraw-Hill Education, 8 ed., 2018.

Paper 1

Subsea Oil Spill Risk Management Based on Sensor Networks

G. Tabella, N. Paltrinieri, V. Cozzani, and P. Salvo Rossi

Chemical Engineering Transactions, vol. 82, pp. 199–204, Oct. 2020.

CHEMICAL ENGINEERING TRANSACTIONS
VOL. 82, 2020
A publication of AIDIC
The Italian Association of Chemical Engineering
Online at www.cetjournal.it
Guest Editors: Bruno Fabiano, Valerio Cozzani, Genserik Reniers

ISBN 978-88-95608-80-8; **ISSN** 2283-9216

Subsea Oil Spill Risk Management Based on Sensor Networks

Gianluca Tabella[a,*], Nicola Paltrinieri[b], Valerio Cozzani[c], Pierluigi Salvo Rossi[a]

[a]Department of Electronic Systems, NTNU Norwegian University of Science and Technology, Norway
[b]Department of Mechanical and Industrial Engineering, NTNU Norwegian University of Science and Technology, Norway
[c]Department of Civil, Chemical, Environmental, and Materials Engineering, University of Bologna, Italy
gianluca.tabella@ntnu.no

The use of Wireless Sensor Networks (WSNs) in support of Dynamic Risk Assessment regarding oil spills still lacks a proper integration. WSNs enable prompt responses to such emergencies through an appropriate inspection, thus avoiding possible larger disasters. This work proposes a methodology for the setup of a WSN as a Leak Detection System in which a Fusion Center collects sensors' binary decisions and provides a more reliable decision about the presence/absence of a leak. The detection rules are based on statistical signal processing techniques, and the choice of the optimal thresholds is made through the optimization of three objective functions tailored to the Oil&Gas industry. Detection performances are assessed in terms of the Receiver Operating Characteristic (ROC) curve. The case study is the Goliat FPSO, a production platform located in the Barents Sea, and related requirements dictated by Norwegian authorities to prevent oil spills. The considered WSN monitors the subsea manifolds through passive acoustic sensors.

1. Introduction

Oil spills are known to cause a highly negative impact on the safety of offshore workers, the environment, and productivity. The early detection of a spill is crucial to limit its potential consequences. A Leak Detection System (LDS) is reliable if it can provide a high rate of correct detections ensuring a limited rate of false alarms, thus avoiding unnecessary production shutdowns and costly Remotely Operated Vehicles (ROV) inspections. Different technologies, among which the use of passive acoustic sensors, are nowadays available and are used to monitor the external underwater environment and the process conditions (Adegboye et al., 2019; Baroudi et al., 2019). Passive acoustic sensors have shown a high level of accuracy enabling the possibility to localize the spill source. This can be done without the need to install the sensors near the leaking component (which is a limitation of many other LDSs). Also, this technology can detect all hydrocarbon fluids. Acoustic sensors are easy to install and are appropriate for retrofitting. These properties make this LDS among the most used. The importance of a reliable LDS creates the need for a framework that integrates it into the Dynamic Risk Assessment (DRA). This is possible as the use of a distributed Wireless Sensor Network (WSN) can provide real-time monitoring of the subsea environment increasing the level of knowledge on the system allowing a more accurate DRA (Paltrinieri et al., 2014, 2019a). So far, the application of WSNs in the Oil&Gas industry has only been introduced (Paltrinieri et al., 2019b). This work gives a methodology for the setup of passive acoustic sensors in a WSN used for monitoring subsea templates and discusses its performances.

2. Signal Model

The WSN aims at detecting possible oil spills, so the problem is formalized as a binary hypothesis testing with the null hypothesis H_0 corresponding to a non-spill scenario, and the alternative hypothesis H_1 corresponding to a spill scenario. For the generic kth sensor, the two following different signal models are assumed for each hypothesis:

$$\begin{cases} H_1: & y_k = \xi \cdot AAF(\boldsymbol{x}_k, \boldsymbol{x}_T) + w_k \\ H_0: & y_k = w_k \end{cases} \quad \Rightarrow \quad \begin{cases} H_1: & y_k \sim \mathcal{N}(0,\ AAF^2(\boldsymbol{x}_k, \boldsymbol{x}_T) \cdot \sigma_s^2 + \sigma_w^2) \\ H_0: & y_k \sim \mathcal{N}(0,\ \sigma_w^2) \end{cases} \tag{1}$$

where:

y_k is the signal (sound pressure) received at the kth sensor where $k = 1,2,\dots,K$;

$\xi \sim \mathcal{N}(0,\ \sigma_s^2)$ is a Gaussian random variable representing the emitted signal caused by the spill;

$w_k \sim \mathcal{N}(0,\ \sigma_w^2)$ is Additive White Gaussian Noise having the same power σ_w^2 for any sensor;

$AAF(\boldsymbol{x}_k, \boldsymbol{x}_T)$ is the Amplitude Attenuation Function (AAF) which only depends on the distance between the position $\boldsymbol{x}_k$ (kth sensor position) and $\boldsymbol{x}_T$ (leak position).

The AAF is treated deterministically and represents the loss of the acoustic intensity level and accounts for seawater absorption and geometrical spreading (Stojanovic, 2006):

$$10\log AAF^2(\boldsymbol{x}_k, \boldsymbol{x}_T) = -\alpha \cdot 10^{-3}(\|\boldsymbol{x}_k - \boldsymbol{x}_T\| - \ell_{\mathrm{ref}}) - k_{\mathrm{sc}} \cdot 10\log\left(\frac{\|\boldsymbol{x}_k - \boldsymbol{x}_T\|}{\ell_{\mathrm{ref}}}\right) \tag{2}$$

From which, the AAF can be obtained:

$$AAF(\boldsymbol{x}_k, \boldsymbol{x}_T) = \sqrt{\left(\frac{\ell_{\mathrm{ref}}}{\|\boldsymbol{x}_k - \boldsymbol{x}_T\|}\right)^{k_{\mathrm{sc}}} 10^{\left[\frac{\alpha}{10^4}(\ell_{\mathrm{ref}} - \|\boldsymbol{x}_k - \boldsymbol{x}_T\|)\right]}} \tag{3}$$

where α is the seawater absorption coefficient in $\mathrm{dB/km}$, $\|\boldsymbol{x}_k - \boldsymbol{x}_T\|$ and ℓ_{ref} (reference length) are in meters, and k_{sc} is the spreading coefficient. The absorption coefficient α is obtained using the Francois & Garrison equation (Francois and Garrison, 1982a, 1982b). The speed of sound (required by Francois & Garrison) is obtained using the updated Chen & Millero equation (Wong and Zhu, 1995).

3. Wireless Sensor Network Model

The modeled WSN is made of K passive acoustic sensors monitoring the external environment (as shown in Figure 1). The kth sensor, with a given sampling frequency, senses the received signal amplitude y_k and sends to a Fusion Center (FC) its binary local decision d_k on whether the sensed amplitude is caused by a spill. The choice of local binary decision is due to the energy constraints imposed by the use of a WSN (Shoari et al., 2016), such constraint will also reduce operating costs as only one bit is transmitted when a spill is detected. Finally, the FC takes a global decision $\hat{H}$ on the occurrence of the spill based on the received d_k's.

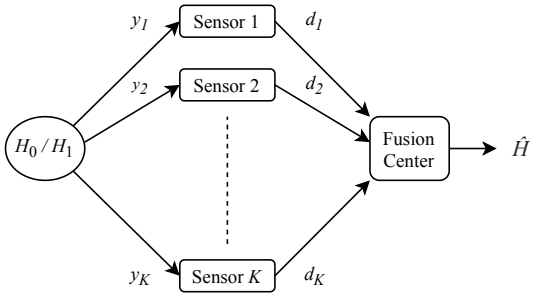

Figure 1: Wireless Sensor Network Model

4. Detection Rules

Each sensor performs an Energy Test, which is Uniformly Most Powerful for this application, where the signal energy y_k^2 is compared to a threshold λ_k to assess its decision (Ciuonzo and Salvo Rossi, 2017):

$$d_k = \begin{cases} 1, & y_k^2 \geq \lambda_k \\ 0, & y_k^2 < \lambda_k \end{cases} \tag{4}$$

As the statistics of the received signal is known, the Local Probability of Detection ($P_{d,k}$) and Local Probability of False Alarm ($P_{f,k}$) for the kth sensor can be defined as follows:

$$P_{d,k} = \Pr\left(y_k^2 \geq \lambda_k \middle| H_1\right) = 2Q\left(\sqrt{\frac{\lambda_k}{AAF^2(\boldsymbol{x_k}, \boldsymbol{x_T}) \cdot \sigma_s^2 + \sigma_w^2}}\right) \tag{5}$$

$$P_{f,k} = \Pr\left(y_k^2 \geq \lambda_k \middle| H_0\right) = 2Q\left(\sqrt{\frac{\lambda_k}{\sigma_w^2}}\right) \tag{6}$$

where $Q(x)$ is the complementary cumulative distribution function of the standard normal random variable:

$$Q(x) = \frac{1}{2\pi}\int_x^\infty \exp\left(-\frac{t^2}{2}\right)dt \tag{7}$$

The proposed method assumes the Signal-to-Noise Ratio $SNR_T = \sigma_s^2/\sigma_w^2$ at ℓ_{ref} from the source to be known. The Counting Rule is used as Fusion Rule by the FC because of its simplicity which suits the constraint of low processing costs. This rule uses the local decisions d_k as an input and has the following form:

$$\widehat{H} = \begin{cases} H_1, & \sum_{k=1}^{K} d_k \geq \Lambda \\ H_0, & \sum_{k=1}^{K} d_k < \Lambda \end{cases} \tag{8}$$

This indicates that the FC counts the number of sensors detecting the spill and compares it to a threshold Λ. In case the sum is equal or higher than the threshold, the FC sends an alarm.

5. Threshold Selection

Three different optimality criteria based on the Receiver Operating Characteristic (ROC) curve will be analyzed (Liu, 2012):

Youden Index (J):

$$\lambda^* = \arg\max_{\lambda} J(\lambda) = \arg\max_{\lambda}\left\{P_d(\lambda) - P_f(\lambda)\right\} \tag{9}$$

Closest-to-(0,1) (ER):

$$\lambda^* = \arg\min_{\lambda} ER(\lambda) = \arg\min_{\lambda}\sqrt{\left(1 - P_d(\lambda)\right)^2 + P_f(\lambda)^2} \tag{10}$$

Concordance Probability (CZ):

$$\lambda^* = \arg\max_{\lambda} CZ(\lambda) = \arg\max_{\lambda}\left\{P_d(\lambda) \cdot \left(1 - P_f(\lambda)\right)\right\} \tag{11}$$

These definitions are applicable both for the sensors and the FC with the appropriate substitutions (λ is λ_k and Λ; P_d is $P_{d,k}$ and Q_d; P_f is $P_{f,k}$ and Q_f; λ^* is λ_k^* and Λ^*). The selection of the optimal threshold λ_k^* for the kth sensor is carried out through a grid search where one optimal value is found for each one of the criteria. More specifically, the metrics in the optimality criteria are computed referring to average performances with respect to the hotspot positions $\boldsymbol{h}_m$, where $m = 1,2,\ldots,M$. This is necessary as the Probabilities of Detection (both local and global) depend on the leak position. The hotspots are those components of the subsea production system that, in case of failure, would be the source of a spill. Also, it is assumed that the selected hotspots have the same failure rate and their spills cause signals having the same power σ_s^2. Therefore:

$$\begin{cases} \overline{P_{d,k}} = \dfrac{1}{M}\sum_{m=1}^{M} P_{d,k,m} & \xrightarrow{\text{optimize objective function}} \quad \lambda_k^* \\ \overline{P_{f,k}} = P_{f,k} \end{cases} \tag{12}$$

where, for the kth sensor, λ_k^* is the chosen local threshold (using one of the criteria), $\overline{P_{d,k}}$ and $\overline{P_{f,k}}$ are its average performances and $P_{d,k,m}$ is $P_{d,k}$ when the leak source is the mth hotspot by using $AAF(\boldsymbol{x_k}, \boldsymbol{h}_m)$.

The choice of the optimal threshold at the FC follows the local threshold choice and uses the same procedure:

$$\begin{cases} \overline{Q_d} = \dfrac{1}{M}\sum_{m=1}^{M} Q_{d,m} & \xrightarrow{\text{optimize objective function}} \quad \Lambda^* \\ \overline{Q_f} = Q_f \end{cases} \tag{13}$$

where Λ^* is the chosen global threshold. $Q_d = \Pr\left(\widehat{H} = H_1 \middle| H_1\right)$ and $Q_f = \Pr\left(\widehat{H} = H_1 \middle| H_0\right)$ are the values of Global Probability of Detection and Global Probability of False Alarm, where m means that the mth hotspot is

modeled as the leak source, and the bar denotes the average probability. $Q_{d,m}$ and Q_f are obtained via Monte Carlo Simulation requiring the simulation of the local decisions using the previously chosen local thresholds.

6. Case Study – Goliat FPSO

The Goliat FPSO is an offshore platform located in the Norwegian Barents Sea equipped with a multi-template Subsea Production System. Each template can host up to four wellheads and the manifold. The latter is monitored by three passive acoustic sensors to detect the presence of an oil spill (Bjørnbom, 2011; Røsby, 2011). For an overview of the subsea equipment, the reader could refer to the specific literature (Bai and Bai, 2012).

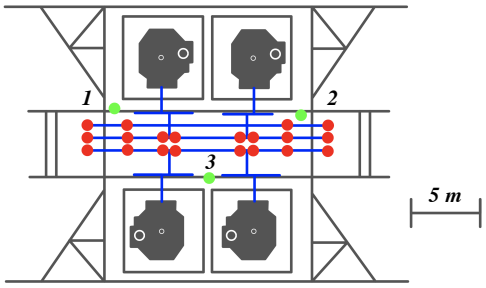

Figure 2: Scheme of Goliat's subsea template: the grey elements are the structure and the Christmas Trees, the blue lines are the main streamlines, the green dots are the sensors, and the red dots are the hotspots

20 hotspots (connections and valves) were recognized in the manifold. Hotspots and sensors are assumed to be at the same height. The following parameters are used for this case study:

Table 1: Parameters used to simulate the spill's sound emission and its Amplitude Attenuation Function

Parameter	Value	Note
$SNR_T = \sigma_s^2/\sigma_w^2$	13 dB	$\ell_{\text{ref}} = 1$ m
Noise Variance σ_w^2	1	Normalized
Reference Frequency	2.5 kHz	(Eckert et al., 1993), used for AAF
Temperature	3.8 ℃	(Institute of Marine Research, 2020), used for AAF
Salinity	3.5 ‰	(Institute of Marine Research, 2020), used for AAF
Depth	350 m	(Bjørnbom, 2011), used for AAF
pH	8	(Vetrov and Romankevich, 2004), used for AAF
Spreading Coefficient k_{sc}	1.5	(Stojanovic, 2006)

7. Results

The values of $SNR_k = AAF^2(\boldsymbol{x}_k, \boldsymbol{h}_m) \cdot \sigma_s^2/\sigma_w^2$ averaged among all hotspots show a mean attenuation of 90.28 % and are the following:

Table 2: Averaged Signal-to-Noise Ratio at the sensors

Sensor 1	Sensor 2	Sensor 3
2.4 dB	3.4 dB	1.4 dB

At sensor-level (Table 3 and Figure 3), the optimization of J results in local thresholds with values distant from those obtained optimizing ER or CZ which tend to be similar. When J is used, in fact, the thresholds are oriented towards smaller values of $P_{d,k}$ and $P_{f,k}$. The values of Area Under the Curve (AUC) of the averaged ROC curves among the three sensors have a standard deviation equal to $4 \cdot 10^{-3}$, this justifies the similar average performances among the sensors when tuned using the same objective function.

Table 3: Local threshold selection's results

Sensor	Value of Optimized Function	Threshold	$\overline{P_{d,k}}$	$\overline{P_{f,k}}$
1	$J = 0.1896$	1.6380	0.3902	0.2006
	$ER = 0.5886$	0.7919	0.5451	0.3735
	$CZ = 0.3417$	0.8427	0.5328	0.3586
2	$J = 0.2064$	1.7268	0.3952	0.1888
	$ER = 0.5785$	0.8271	0.5496	0.3631
	$CZ = 0.3504$	0.8896	0.5354	0.3456
3	$J = 0.1923$	1.5169	0.4104	0.2181
	$ER = 0.5845$	0.7947	0.5497	0.3727
	$CZ = 0.3450$	0.8435	0.5378	0.3584

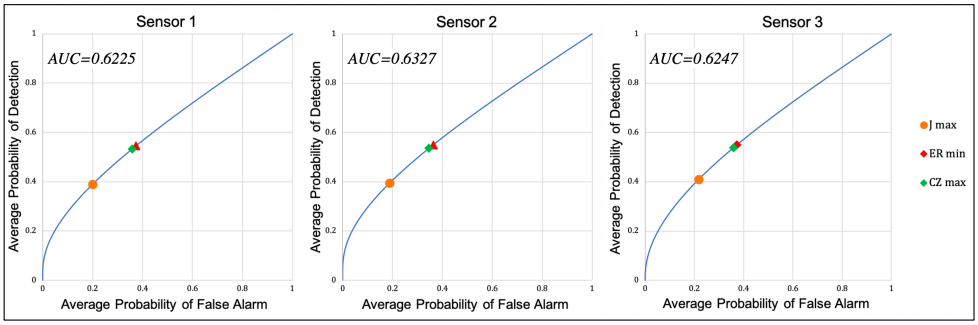

Figure 3: Averaged local ROC curves displaying the optimal points according to the different applied criteria

At FC-level, results were obtained with 10^8 Monte Carlo runs (Table 4 and Figure 4). The performance at a given threshold varies according to the objective function used for the sensors. When sensors are tuned using J, the optimal global threshold is divided between the value 1 if ER and CZ are optimized, and 2 if J is optimized. When sensors are tuned using ER or CZ, the optimal global threshold is always 2 using any optimization criterion. The highest value of AUC at the FC is obtained when sensors are tuned using J.

Table 4: Global threshold selection's results

Function used for Sensors	Value of Optimized Function	Threshold	$\overline{Q_d}$	$\overline{Q_f}$
Youden Index (J)	$J = 0.2546$	2	0.3608	0.1062
	$ER = 0.5553;\ CZ = 0.3774$	1	0.7442	0.4928
Closest-to-(0,1) (ER)	$J = 0.2562;\ ER = 0.5334;\ CZ = 0.3905$	2	0.5652	0.3090
Concordance Probability (CZ)	$J = 0.2598;\ ER = 0.5363;\ CZ = 0.3899$	2	0.5472	0.2875

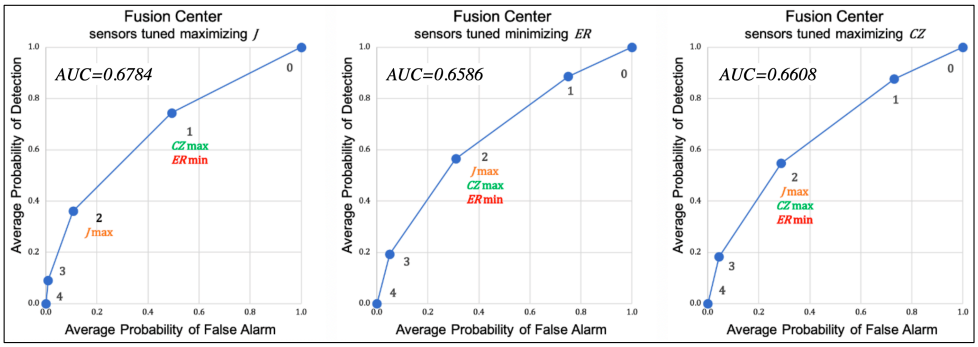

Figure 4: Averaged global ROC curves displaying the optimal points according to the different applied criteria

8. Conclusions

It is clear how the choice of the objective function at sensor-level is fundamental to determine the performances at FC-level for a given global threshold. The case study showed how tuning the sensors using the Youden Index increases the global AUC and orients the performances towards lower values of false alarm rate of the LDS, which may be preferable to avoid shutdowns. The optimal global thresholds show a similar behavior on the ROC space if compared to the results obtained when computing the optimal local thresholds. However, the tendency of the Youden Index to generate thresholds having a lower probability of detection and false alarm with respect to those generated by the other two indexes is less evident at FC-level since only $K + 2$ points can be placed on the ROC space. The three objective functions can also be adapted and corrected using coefficients to fit specific applications and requirements. The proposed methodology shows how important the number of sensors and their positioning can be and how the network performances heavily rely on the signal model. For this reason, more information regarding the statistical properties of the signal and other contributions that influence the AAF should be integrated if available. These factors can be signal perturbations, interferences, ambient noise, and oceanic phenomena (currents, tides, internal waves, etc.). This work is a step towards the integration of subsea monitoring using WSNs with Risk Assessment techniques necessary to localize the hotspots and to select the most appropriate objective function.

References

Adegboye, M.A., Fung, W.K., Karnik, A., 2019. Recent Advances in Pipeline Monitoring and Oil Leakage Detection Technologies: Principles and Approaches. Sensors 19.

Bai, Y., Bai, Q., 2012. Subsea Engineering Handbook, 1st ed. Gulf Professional Publishing, Houston, TX.

Baroudi, U., Al-Roubaiey, A.A., Devendiran, A., 2019. Pipeline Leak Detection Systems and Data Fusion: A Survey. IEEE Access 7, 97426–97439.

Bjørnbom, E., 2011. Goliat – Leak detection and monitoring from template to satellite. URL <https://www.norskoljeoggass.no/globalassets/dokumenter/drift/presentasjonerarrangementer/subsea-leak-detection--2011/4.-enino_n1862090_v1_eni_presentation_-_olf_seminar_-_subsea_leak_detection_-_03_november_2011.pdf> (accessed 6.6.20).

Ciuonzo, D., Salvo Rossi, P., 2017. Distributed detection of a non-cooperative target via generalized locally-optimum approaches. Inf. Fusion 36, 261–274.

Eckert, E.G., Maresca, J.W., Hillger, R.W., Yezzi, J.J., 1993. Location of Leaks in Pressurized Petroleum Pipelines by Means of Passive-Acoustic Sensing Methods, in: Durgin, P., Young, T. (Eds.), Leak Detection for Underground Storage Tanks. ASTM International, West Conshohocken, PA, pp. 53–69.

Francois, R.E., Garrison, G.R., 1982a. Sound absorption based on ocean measurements: Part I: Pure water and magnesium sulfate contributions. J. Acoust. Soc. Am. 72, 896–907.

Francois, R.E., Garrison, G.R., 1982b. Sound absorption based on ocean measurements. Part II: Boric acid contribution and equation for total absorption. J. Acoust. Soc. Am. 72, 1879–1890.

Institute of Marine Research, 2020. Mareano. URL <http://www.mareano.no/kart> (accessed 6.6.20).

Liu, X., 2012. Classification accuracy and cut point selection. Stat. Med. 31, 2676–2686.

Paltrinieri, N., Comfort, L., Reniers, G., 2019a. Learning about risk: Machine learning for risk assessment. Saf. Sci. 118, 475–486.

Paltrinieri, N., Landucci, G., Salvo Rossi, P., 2019b. An Integrated Approach to Support the Dynamic Risk Assessment of Complex Industrial Accidents. Chem. Eng. Trans. 77, 265–270.

Paltrinieri, N., Scarponi, G.E., Khan, F., Hauge, S., 2014. Addressing dynamic risk in the petroleum industry by means of innovative analysis solutions. Chem. Eng. Trans. 36, 451–456.

Røsby, E., 2011. Goliat development project - Subsea leak detection design. URL <https://www.norskoljeoggass.no/globalassets/dokumenter/drift/presentasjonerarrangementer/subsea-leak-detection--2011/15.-goliat-development-project_subsea_leak_detection_3_nov_2011_elling-rosby.pdf> (accessed 6.6.20).

Shoari, A., Mateos, G., Seyedi, A., 2016. Analysis of Target Localization With Ideal Binary Detectors via Likelihood Function Smoothing. IEEE Signal Process. Lett. 23, 737–741.

Stojanovic, M., 2006. On the relationship between capacity and distance in an underwater acoustic communication channel, in: Proceedings of the 1st ACM International Workshop on Underwater Networks - WUWNet '06. ACM Press, New York, NY, pp. 41–47.

Vetrov, A., Romankevich, E., 2004. Carbon Cycle in the Russian Arctic Seas, 1st ed. Springer, Berlin, Germany.

Wong, G.S.K., Zhu, S., 1995. Speed of sound in seawater as a function of salinity, temperature, and pressure. J. Acoust. Soc. Am. 97, 1732–1736.

Paper 2

Data Fusion for Subsea Oil Spill Detection Through Wireless Sensor Networks

G. Tabella, N. Paltrinieri, V. Cozzani, and P. Salvo Rossi

presented at *IEEE Sensors 2020*, Rotterdam, The Netherlands, Oct. 2020.

Data Fusion for Subsea Oil Spill Detection Through Wireless Sensor Networks

Gianluca Tabella*, Nicola Paltrinieri†, Valerio Cozzani‡, Pierluigi Salvo Rossi*
*Dept. Electronic Systems, Norwegian University of Science and Technology, 7491 Trondheim, Norway
†Dept. Mechanical and Industrial Engineering, Norwegian University of Science and Technology, 7491 Trondheim, Norway
‡Dept. Civil, Chemical, Environmental and Materials Engineering, University of Bologna, 40131 Bologna, Italy
Email: gianluca.tabella@ntnu.no; nicola.paltrinieri@ntnu.no; valerio.cozzani@unibo.it; salvorossi@ieee.org

***Abstract*—This work studies the impact of Wireless Sensor Networks (WSNs) for oil spill detection in subsea Oil&Gas applications. The case study is the Goliat FPSO where one WSN with passive acoustic sensors is assumed to be installed on each subsea template to monitor the manifold. Sensors take local binary decisions regarding the presence/absence of a spill by performing an energy test. A Fusion Center (FC) collects such local decisions and provides a more reliable global binary decision. The Counting Rule (CR) and a modified Chair-Varshney Rule (MCVR) are compared. An objective function derived from the Receiver Operating Characteristic (ROC) is used for threshold design. The considered methodology requires the knowledge of the involved subsea production system, in particular of its hotspots whose failure could cause an oil spill.**

***Index Terms*—Data fusion, leak detection, oil spill, subsea production system, wireless sensor network**

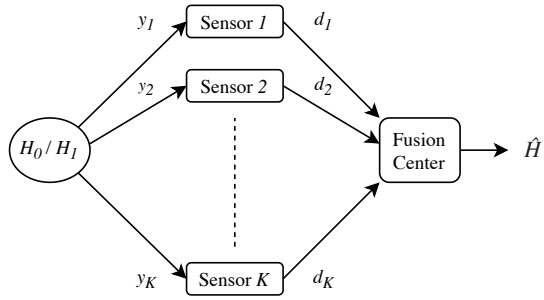

Fig. 1. Wireless Sensor Network

I. Introduction

The Oil&Gas industry over the last few decades has developed new technologies for the exploitation of offshore resources that were once technologically inaccessible or economically unfeasible. One of these is the use of Subsea Production Systems (SPS) which can be connected to a close fixed platform, a floating system, or directly to the shore. This allows the oil extraction in deep waters which are normally out of range of standard fixed platforms, as well as exploiting fields more efficiently due to the versatility of such systems [1]. On the other hand, one of the disadvantages related to this technology is that the presence of a SPS in deep water makes the detection of oil spills less effective resulting in delayed production shutdowns with a consequent risk for workers' safety and the environment. For this reason, the presence of a Leak Detection System (LDS) able to quickly detect oil spills is of critical importance.

Current technologies rely on both internal methods (based on measurements of process variables) and external methods (monitoring the SPS's surrounding environment). More specifically, an underwater oil spill is known to cause an acoustic signal that can be sensed via passive acoustic sensors [2], [3]. Although the use of WSNs for leak detection has been considered mainly in the monitoring of Oil&Gas pipelines [4], [5], recent works have focused on monitoring of a SPS through a WSN [6]–[8]. This work investigates the use of Wireless Sensor Networks (WSNs) as an external method for leakage detection and illustrates results on a realistic case-study based on the Goliat FPSO. This approach has the advantage of being able to detect (and eventually localize) oil spills with a small number of sensors and limited power consumption.

The remainder of the paper is organized as follows. Sec. II provides a system overview, including assumptions related to signals characterizations. Data processing for leak detection is described in Sec. III, which includes local detection at sensor location and global detection at the Fusion Center (FC). Numerical results on the considered case study are presented in Sec. IV in terms of Receiver Operating Characteristic (ROC). Finally, conclusions and further works are addressed in Sec. V.

II. System Model

A. Wireless Sensor Network Model

The proposed WSN architecture (see Fig. 1) is made of K acoustic sensors[1] used to detect the presence ($\mathcal{H}_1$) or absence ($\mathcal{H}_0$) of an oil spill. The kth sensor (where $k = 1, \ldots, K$) individually performs a test on the received amplitude y_k and takes a local decision $d_k = i \in \{0, 1\}$ if $\mathcal{H}_i$ is declared. The local decisions are collected and combined at the FC for a global decision $\widehat{\mathcal{H}} \in \{\mathcal{H}_0, \mathcal{H}_1\}$. Such a system is extremely energy efficient when On-Off Keying is considered for decision reporting from the sensors to the FC.

[1]Sound pressure is sensed. Analysis concerning the sampling frequency is not treated in the present work.

B. Signal Model

The model of the received signal at the kth sensor, depending on the corresponding hypothesis (presence/absence of a leakage), is the following:

$$\begin{cases} \mathcal{H}_0: & y_k = w_k \\ \mathcal{H}_1: & y_k = \xi \cdot g(\boldsymbol{x}_k, \boldsymbol{x}_T) + w_k \end{cases} , \tag{1}$$

where $\xi \sim \mathcal{N}(0,\, \sigma_s^2)$ and $w_k \sim \mathcal{N}(0,\, \sigma_{w,k}^2)$ are independent Gaussian random variables representing the emitted sound pressure produced by the leakage at a reference length (ℓ_{ref}) and the Additive White Gaussian Noise (AWGN) at the kth sensor, respectively. Also, $g(\boldsymbol{x}_k, \boldsymbol{x}_T)$ is the Amplitude Attenuation Function (AAF) depending on the distance between the kth sensor and the leakage, whose positions are denoted $\boldsymbol{x}_k$ and $\boldsymbol{x}_T$, respectively. The signal power σ_s^2 and the noise power $\sigma_{w,k}^2$ are assumed to be known (for all K sensors). The AAF, here treated as the contribution of the sea-water absorption and the geometrical spreading, has the following form:

$$g^2(\boldsymbol{x}_k, \boldsymbol{x}_T) = \left(\frac{\ell_{\text{ref}}}{\|\boldsymbol{x}_k - \boldsymbol{x}_T\|} \right)^{k_{\text{sc}}} 10^{(\ell_{\text{ref}} - \|\boldsymbol{x}_k - \boldsymbol{x}_T\|)\alpha 10^{-4}} , \tag{2}$$

where ℓ_{ref} and $\|\boldsymbol{x}_k - \boldsymbol{x}_T\|$ are measured in meters, the seawater absorption coefficient α is measured in dB/km, and k_{sc} is the spreading coefficient. It can be noticed that if $\ell_{\text{ref}} = \|\boldsymbol{x}_k - \boldsymbol{x}_T\|$, then $g(\boldsymbol{x}_k, \boldsymbol{x}_T) = 1$.

III. Leak Detection

A. Local Detection

Given Eq. (1), the *uniformly most powerful* test [9] to be performed by the kth sensor is the energy test [10]:

$$d_k = \begin{cases} 0, & y_k^2 < \tau_k \\ 1, & y_k^2 \geq \tau_k \end{cases} , \tag{3}$$

where τ_k is a local threshold. The local performances, in terms of probability of detection and probability of false alarm, of this test are defined and computed as follows:

$$P_{d,k} = \Pr(y_k^2 \geq \tau_k | \mathcal{H}_1) = 2\mathcal{Q}\left(\sqrt{\frac{\tau_k}{g^2(\boldsymbol{x}_k, \boldsymbol{x}_T)\sigma_s^2 + \sigma_{w,k}^2}} \right) , \tag{4}$$

$$P_{f,k} = \Pr(y_k^2 \geq \tau_k | \mathcal{H}_0) = 2\mathcal{Q}\left(\sqrt{\frac{\tau_k}{\sigma_{w,k}^2}} \right) , \tag{5}$$

where $Q(\cdot)$ is the complementary cumulative distribution function of the standard normal random variable. However, since the leakage position is unknown, Eq. (4) cannot be used directly. One possibility to overcome the issue is to refer to average performances with respect to the SPS's hotspots[2] and their positions $\boldsymbol{h}_m$ (where $m = 1, \ldots, M$), i.e.

$$\overline{P_{d,k}} = \frac{1}{M} \sum_{m=1}^{M} P_{d,k,m} , \quad \overline{P_{f,k}} = P_{f,k} , \tag{6}$$

[2]The hotspots are those components within the SPS that could be the source of a spill in case of failure.

where $P_{d,k,m}$ is obtained replacing $\boldsymbol{x}_T$ with $\boldsymbol{h}_m$ in Eq. (4). By using the arithmetic mean, Eq. (6) assumes that the hotspots have equal failure rates and that their leakages would cause signals having equal power σ_s^2.

We define the reference Signal-to-Noise ratio (SNR) and the sensing SNR at the kth sensor respectively as

$$\Gamma_{\text{ref},k} = \frac{\sigma_s^2}{\sigma_{w,k}^2} , \quad \Gamma_k = \frac{\Gamma_{\text{ref},k}}{M} \sum_{m=1}^{M} g^2(\boldsymbol{x}_k, \boldsymbol{h}_m) . \tag{7}$$

B. Global Detection

The FC assesses the presence of a leakage based on a test statistic (Λ) depending on the local decisions d_k:

$$\widehat{\mathcal{H}} = \begin{cases} \mathcal{H}_0, & \Lambda < T \\ \mathcal{H}_1, & \Lambda \geq T \end{cases} , \tag{8}$$

where T is a global threshold.

Two different fusion rules are considered for computing the test statistic at the FC: (i) the Counting Rule (CR), and (ii) a modified version of the Chair-Varshney Rule (MCVR). MCVR is adapted to work using the mean performances in Eq. (6). More specifically, the corresponding test statistics are computed as follows:

$$\Lambda_{\text{CR}} = \sum_{k=1}^{K} d_k , \tag{9}$$

$$\Lambda_{\text{MCVR}} = \sum_{k=1}^{K} \left[d_k \ln\left(\frac{\overline{P_{d,k}}}{\overline{P_{f,k}}} \right) + (1 - d_k) \ln\left(\frac{1 - \overline{P_{d,k}}}{1 - \overline{P_{f,k}}} \right) \right] . \tag{10}$$

Global system performances for each fusion rule are expressed in terms of *Global Probability of Detection* and *Global Probability of False Alarm* at the FC, defined as $Q_d = \Pr(\Lambda \geq T | \mathcal{H}_1)$ and $Q_f = \Pr(\Lambda \geq T | \mathcal{H}_0)$, respectively. It is worth noticing that Q_d will depend on the position of the leakage, then the same approach used in the previous section for local performances is considered:

$$\overline{Q_d} = \frac{1}{M} \sum_{m=1}^{M} Q_{d,m} , \quad \overline{Q_f} = Q_f . \tag{11}$$

C. Threshold Selection

Local thresholds τ_k are hyper-parameters that ideally should be optimized based on the global performance. Such a task does not exhibit an easy solution, then sub-optimal solutions are usually considered. Here we consider to select the thresholds based on the optimization of the Youden Index (J) [11]:

$$\tau^* = \arg\max_{\tau} J(\tau) = \arg\max_{\tau} \{P_d(\tau) - P_f(\tau)\} . \tag{12}$$

In Eq. (12), the variables τ, P_d, and P_f are replaced with τ_k, $\overline{P_{d,k}}$, and $\overline{P_{f,k}}$ (respectively T, $\overline{Q_{d,k}}$, and $\overline{Q_{f,k}}$) when tuning the sensors (respectively the FC).

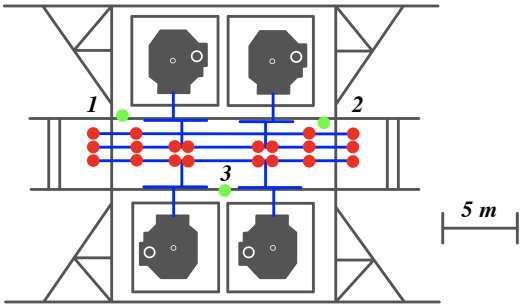

Fig. 2. Goliat's subsea template: the grey elements are the structure and the Christmas Trees, the blue lines are the main streamlines, the green dots are the sensors, and the red dots are the hotspots

IV. Case Study (Goliat FPSO)

The Goliat FPSO is a production platform located in the Norwegian Barents Sea relying on eight subsea templates. Each template has its manifold monitored by three passive acoustic sensors as part of the external LDS [12], [13]. Twenty hotspots (corresponding to the main valves and connections) have been highlighted in Fig. 2. Hotspots and sensors are assumed to be at the same height.

Numerical performances have been obtained via simulation with 10^8 Monte Carlo runs using the software MATLAB. The parameters used for the case study can be found in Table I. The seawater absorption coefficient α in Eq. (2) has been computed using *Francois & Garrison equation* [14], [15], where the underwater speed of sound was obtained using the *updated Chen & Millero equation* [16]. Table II shows the average SNR for each sensor in case of $\Gamma_{\text{ref}} = 13.0$ dB and $\Gamma_{\text{ref}} = 14.8$ dB.

Fig. 3 shows the ROC curves of the LDS in the two SNR cases comparing the two fusion rules. It is apparent how both CR and MCVR perform almost similar in the considered case. The reason is the symmetrical topology of the considered case study. Asymmetrical setups would show the advantage of MCVR over CR. Also, it is worth noticing that the ROC of the MCVR exhibits more flexibility than the CR in terms of global performance since a larger number of possible thresholds is admitted (7 vs. 3 in the specific case study). Also, Table III shows the maximum Youden Index and the corresponding global probabilities of detection and false alarm, to highlights the incremental improvement of MCVR with respect to CR.

V. Conclusions

This work investigated the use of Wireless Sensor Networks (WSNs) for subsea oil spill detection, using Goliat FPSO as a case study. Local sensors' decisions are collected at the FC, where CR and MCVR are considered for data fusion. ROC performances have been obtained through realistic numerical simulations, showing the potential benefit of the considered approach. Future works will include a more extended analysis on the local and global threshold selection as well as the localization of the subsea component responsible for the spill which is crucial for quicker and more efficient maintenance.

TABLE I
Parameters used to simulate a leak scenario

Parameter	Value	Note / Reference
Reference Frequency	2.5 kHz	[17]
Temperature	3.8 °C	[18]
Salinity	3.5 %	[18]
Depth	350 m	[12]
pH	8	[19]
Spreading Coeff. (k_{sc})	1.5	[20]
Ref. Length (ℓ_{ref})	1 m	–
Noise Variance (σ_w^2)	1	$\sigma_w^2 = \sigma_{w,k}^2 \ \forall k$
Γ_{ref}	13.0 dB; 14.8 dB	$\Gamma_{\text{ref}} = \Gamma_{\text{ref},k} \ \forall k$

TABLE II
Average SNR at the different sensors

Γ_{ref}	Γ_1	Γ_2	Γ_3
13.0 dB	2.4 dB	3.4 dB	1.4 dB
14.8 dB	4.1 dB	5.2 dB	3.2 dB

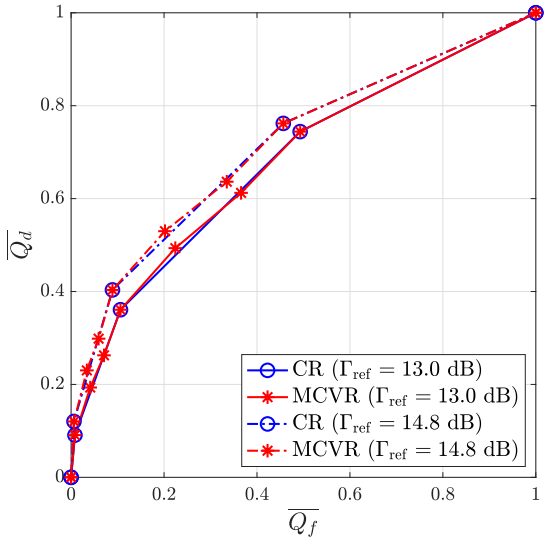

Fig. 3. ROC curves at the Fusion Center

TABLE III
Leak Detection System Performances

Γ_{ref}	Fusion Rule	$J(\Lambda^*)$	$\overline{Q_d(\Lambda^*)}$	$\overline{Q_f(\Lambda^*)}$
13.0 dB	MCVR	0.269	0.493	0.224
	CR	0.255	0.361	0.106
14.8 dB	MCVR	0.328	0.530	0.202
	CR	0.314	0.403	0.089

REFERENCES

[1] F. Pallavicini, "Developement of offshore fields," in *Encyclopaedia of Hydrocarbons Volume 1 - Exploration, Production and Transport*. Rome, Italy: Treccani, 2005, ch. 5.2, pp. 609–628.

[2] M. A. Adegboye, W. K. Fung, and A. Karnik, "Recent Advances in Pipeline Monitoring and Oil Leakage Detection Technologies: Principles and Approaches," *Sensors*, vol. 19, no. 11, 2019.

[3] U. Baroudi, A. A. Al-Roubaiey, and A. Devendiran, "Pipeline Leak Detection Systems and Data Fusion: A Survey," *IEEE Access*, vol. 7, pp. 97 426–97 439, 2019.

[4] J. Li, C. Wang, Q. Zheng, and Z. Qian, "Leakage Localization for Long Distance Pipeline Based on Compressive Sensing," *IEEE Sensors Journal*, vol. 19, no. 16, pp. 6795–6801, 2019.

[5] M. Meribout, "A Wireless Sensor Network-Based Infrastructure for Real-Time and Online Pipeline Inspection," *IEEE Sensors Journal*, vol. 11, no. 11, pp. 2966–2972, 2011.

[6] N. Paltrinieri, G. Landucci, and P. Salvo Rossi, "An Integrated Approach to Support the Dynamic Risk Assessment of Complex Industrial Accidents," *Chemical Engineering Transactions*, vol. 77, pp. 265–270, 2019.

[7] M. Bucelli, I. B. Utne, P. Salvo Rossi, and N. Paltrinieri, "A system engineering approach to subsea spill risk management," *Safety Science*, vol. 123, 2020.

[8] M. R. Akhondi, A. Talevski, S. Carlsen, and S. Petersen, "Applications of Wireless Sensor Networks in the Oil, Gas and Resources Industries," in *2010 24th IEEE International Conference on Advanced Information Networking and Applications*. Perth, Australia: IEEE, 2010, pp. 941–948.

[9] S. Kay, *Fundamentals of Statistical Signal Processing: Detection theory*, 1st ed., ser. Prentice Hall Signal Processing Series. Upper Saddle River, NJ: Prentice-Hall PTR, 1998.

[10] D. Ciuonzo and P. Salvo Rossi, "Distributed detection of a non-cooperative target via generalized locally-optimum approaches," *Information Fusion*, vol. 36, pp. 261–274, 2017.

[11] W. J. Youden, "Index for rating diagnostic tests," *Cancer*, vol. 3, pp. 32–35, 1950.

[12] E. Bjørnbom, "Goliat – Leak detection and monitoring from template to satellite," 2011.

[13] E. Røsby, "Goliat development project - Subsea leak detection design," 2011.

[14] R. E. Francois and G. R. Garrison, "Sound absorption based on ocean measurements: Part I: Pure water and magnesium sulfate contributions," *The Journal of the Acoustical Society of America*, vol. 72, no. 3, pp. 896–907, 1982.

[15] ——, "Sound absorption based on ocean measurements. Part II: Boric acid contribution and equation for total absorption," *The Journal of the Acoustical Society of America*, vol. 72, no. 6, pp. 1879–1890, Dec. 1982.

[16] G. S. K. Wong and S. Zhu, "Speed of sound in seawater as a function of salinity, temperature, and pressure," *The Journal of the Acoustical Society of America*, vol. 97, no. 3, pp. 1732–1736, 1995.

[17] E. G. Eckert, J. W. Maresca, R. W. Hillger, and J. J. Yezzi, "Location of Leaks in Pressurized Petroleum Pipelines by Means of Passive-Acoustic Sensing Methods," in *Leak Detection for Underground Storage Tanks*, P. Durgin and T. Young, Eds. West Conshohocken, PA: ASTM International, 1993, pp. 53–69.

[18] Institute of Marine Research, "Mareano," Available at http://www.mareano.no/kart (2020/06/06).

[19] A. Vetrov and E. Romankevich, *Carbon Cycle in the Russian Arctic Seas*, 1st ed. Berlin, Germany: Springer, 2004.

[20] M. Stojanovic, "On the relationship between capacity and distance in an underwater acoustic communication channel," in *Proceedings of the 1st ACM international workshop on Underwater networks - WUWNet '06*. New York, NY: ACM Press, 2006, pp. 41–47.

Paper 3

Wireless Sensor Networks for Detection and Localization of Subsea Oil Leakages

G. Tabella, N. Paltrinieri, V. Cozzani, and P. Salvo Rossi

IEEE Sensors Journal, vol. 21, no. 9, pp. 10890–10904, 1 May 2021.

Wireless Sensor Networks for Detection and Localization of Subsea Oil Leakages

Gianluca Tabella, *Graduate Student Member, IEEE*, Nicola Paltrinieri, Valerio Cozzani and Pierluigi Salvo Rossi, *Senior Member, IEEE*

***Abstract*— This work studies the impact of Wireless Sensor Networks (WSNs) for oil spill detection and localization in Subsea Production Systems. The case study is the Goliat FPSO, with a realistic assumption about the presence of a WSN built upon the existing passive acoustic sensors installed on each subsea template to monitor the manifold. The sensors take local binary decisions regarding the presence/absence of a spill by performing an energy test. A Fusion Center (FC) collects such local decisions and provides a more reliable global binary decision. The Counting Rule (CR) and a modified Chair-Varshney Rule (MCVR) are compared. An objective function based on the Receiver Operating Characteristic (ROC) is used for threshold design. The FC, in case of a spill detection, provides an estimated position of the leak source. Four localization algorithms are explored: *Maximum A-Posteriori* (MAP) estimation, *Minimum Mean Square Error* (MMSE) estimation, and two heuristic centroid-based algorithms. Detection and localization performances are assessed in comparison to the (position) Clairvoyant Chair-Varshney Rule (CVR) and to the Cramér-Rao Lower Bound (CRLB), respectively. The considered framework requires the prior knowledge of the involved subsea production system in terms of components that in case of failure would cause a leakage and their corresponding failure rates.**

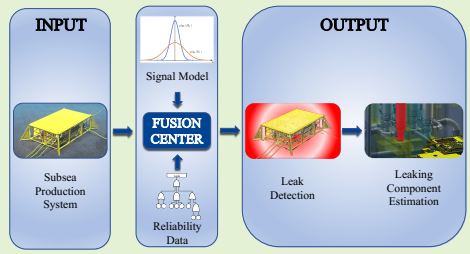

***Index Terms*— Data Fusion, leak detection, leak localization, oil spill, subsea production system, wireless sensor network**

I. Introduction

THE Oil&Gas industry over the last few decades has developed new technologies for the exploitation of offshore resources previously technologically inaccessible or economically unfeasible. A relevant example is the use of Subsea Production Systems (SPS) connected to a close fixed platform, a floating system such as Floating Production Storage and Offloading (FPSO) Unit, Single Point Anchor Reservoir (SPAR) platform, Tension-Leg Platform (TLP), a Semi-submersible platform, or directly to the shore (less common option) [1].

This research is a part of BRU21 – NTNU Research and Innovation Program on Digital and Automation Solutions for the Oil and Gas Industry (www.ntnu.edu/bru21).

Part of this work has been presented to the conference IEEE SENSORS 2020, Rotterdam, The Netherlands, October 2020.

G. Tabella is with the Department of Electronic Systems, Norwegian University of Science and Technology, 7491 Trondheim, Norway (e-mail: gianluca.tabella@ntnu.no).

P. Salvo Rossi is with the Department of Electronic Systems, Norwegian University of Science and Technology, 7491 Trondheim, Norway, and with the Department of Gas Technology, SINTEF Energy Research, Norway (e-mail: salvorossi@ieee.org).

N. Paltrinieri is with the Department of Mechanical and Industrial Engineering, Norwegian University of Science and Technology, 7491 Trondheim, Norway (e-mail: nicola.paltrinieri@ntnu.no).

V. Cozzani is with the Department of Civil, Chemical, Environmental and Materials Engineering, University of Bologna, 40131 Bologna, Italy (e-mail: valerio.cozzani@unibo.it).

SPSs are solutions that move part of the equipment on the seabed, in particular they transfer the *Christmas trees* (which are named *subsea trees* in this specific configuration in opposition to the *surface trees* present on traditional production platforms). A SPS allows a single platform to be equipped with several subsea trees. Usually the outlet streams of a group of neighboring subsea trees are connected to a *manifold* using pipes called *jumpers*. Manifolds are used to mix flows in a single stream before being transferred topside through *production risers* (some preliminary treatment like separation can be occasionally performed subsea). Sometimes multiple components of the SPS are gathered together in a single structure called *template*. The topside operators can control the SPS using *umbilicals*, which are bundles of flexible tubes and electrical conductors necessary for the transfer of the control fluid (necessary for the hydraulic control system), the transfer of chemicals (e.g. corrosion inhibitors, wax inhibitors, etc.), the powering of the subsea electrical components, and the collection of the information coming from the sensors. A description of a SPS has been given by Bai Y. and Bai Q. [2].

This solution allows for oil extraction in deep waters, which is normally out of range for fixed platforms, and provides more effective field exploitation due to its versatility [3]. On the other hand, having a SPS means to have a greater number of components located on the seabed that can be subject to

failure. In case a spill occurs, in fact, there is an increased difficulty to detect it as this will be happening in deep waters, which results in delayed production shutdowns with a consequent risk for workers' safety and the environment. Furthermore, having a spill originated on the seabed makes its localization more complex as a visual inspection is clearly not possible forcing costly inspections performed by Remotely Operated Vehicles (ROVs) [4]. Reducing the inspection time by having an estimated leak position can be vital to reduce the economic loss. For this reason, the presence of a Leak Detection System (LDS) capable to quickly detect and localize oil leakages is of paramount importance.

It is important to mention that the effectiveness of a LDS lies also in the quality of its integration into a risk management framework so that the increased level of knowledge on the SPS can be fully exploited. A proper integration can be obtained when the *Dynamic Risk Management Framework* (DRMF) is employed. The DRMF is a process open to external experience and early warnings allowing the integration of unknown information. Increased awareness of risks related to unknown events may lead to a learning and understanding phase (based on *monitoring* and *review* of accumulated information). *Horizon screening*, *hazard identification*, *assessment*, and final *decision/action* are the steps required by the DRMF to exhaustively evaluate the risks associated with known potential accident scenarios. Iterative updates are necessary to employ the DRMF as an adaptive process [5]–[8]. From this perspective, a LDS represents an early warning subsystem, part of a decision-support system related to actions such as plant shutdown and maintenance.

A. Related Work

Current technologies for leak detection rely on both internal methods based on measurements of process variables (e.g. flow rate and pressure) and external methods where sensors monitor the SPS's surrounding environment. Their characteristics have been extensively studied and most of these sensors are already in place in several offshore fields [9], [10] and their use is subject to strict quality standards [11]. A key feature of leakages is their associated acoustic signal that can be sensed via passive acoustic sensors [12], [13]. Unlike other technologies (e.g. capacitive sensors) that need to be in direct contact with the leaking fluid, passive acoustic sensors exhibit a much broader detection range. Also, their installation is easy and cost-effective as opposed to fiber optic cables. However, passive acoustic sensors are extremely sensitive to measurement noise with consequent difficulty in detecting smaller leaks [9]–[11]. The above-mentioned characteristics suggest the use of LDS based on acoustic sensors working as nodes of a WSN. Although the use of WSNs for leak detection purposes has been considered mainly in the monitoring of Oil&Gas pipelines [14]–[16], some recent works have focused on the monitoring of a SPS through WSNs showing its benefits, especially from the point of view of the DRMF [17]–[19].

The field of data fusion in distributed WSN for event detection has its first big contribution from the initial work in [20]. Overtime, there has been a growing interest in distributed WSN where the sensors transmit binary decisions to a Fusion Center (FC) as this lowers communications and processing costs [21]. The following is a list of the main contributions for such kind of detection problem. In [22], [23] some fusion rules such as the Chair-Varshney Rule (CVR) and the Counting Rule (CR) have been proposed addressing also the problem of the detection performed locally by the sensors. In [24] a sub-optimal and a heuristic fusion rule, respectively called Maximum Ratio Combining Fusion Statistic and Equal Gain Combining Fusion Statistic, are proposed. [25] shows, in the case of weak signal, a comparison between a WSN with a FC receiving binary decisions that performs a Locally Most Powerful Test (LMPT) and the same network where the FC performs the LMPT after receiving the raw local measurements. In [26], [27] the Rao Test is proposed showing the asymptotically equivalent performances of this CR with respect to the Generalized Likelihood Ratio Test (GLRT). In [28] a set of fusion rules based on the GLRT, the Bayesian frameworks and hybrid approaches are shown; the work then proposes some fusion rules based on the Locally-Optimum Detection (LOD) framework; the paper also gives a basis for the localization of the target. The detection problem in WSN has also been approached proposing Multiple-Input Multiple-Output (MIMO) architectures with sensors sending local binary decisions to a FC where the focus is on the performance of the communication channel between sensors and FC [29]–[31].

The target localization problem in WSN with one FC and 1-bit local decisions has been studied in various works and several localization algorithms have been proposed. Many methods having a statistical basis can be found in [28]. Unfortunately, many of these methods have high computational complexity and have not been adapted or simplified to work in specific conditions like the one examined in this work. Statistical-based methods often require precise information on the statistical model of the signal which in many cases may not be available. As a consequence, several heuristic strategies have been developed that have the advantage of often having low computational complexity and easy implementation and requiring little knowledge on the statistical model of the signal. The most popular heuristic models are here reported. In [32] the centroid method is introduced showing great simplicity; this method has been subject to many variations to improve its performances reducing the ease of implementation and increasing the required knowledge on the statistical model of the signal turning it into range-based methods as in [33], [34], where the additional knowledge is used to create weights for the centroid calculation. Other popular range-free heuristic localization methods are the Center of the Minimum Enclosing Rectangle (CMER) [32] including its extension where the Steiner center is introduced to remove the dependency on the chosen coordinate system of the CMER [35], and the Center of the Minimum Enclosing Circle (CMEC) [36]. Moreover, [32] shows the validity of the CMEC when sensors operate in noise-free settings with a unitary probability of detection in the proximity of the target.

An important aspect regarding WSNs with FC receiving 1-bit local decisions is the quantizer design. In [37] the

local quantization problem is addressed for the problem of Bayesian estimation of location parameter in the case of a conditionally unbiased and efficient estimator with conditionally independent observations. The study is also extended to a scenario when the WSN is under a bit rate constraint and when the observations are conditionally dependent. In [38] the quantization task is treated for the problem of tracking moving targets showing a method for updating dynamically the local thresholds via Multiobjective Optimization Problem resulting in a trade-off solution between maximum Fisher Information and minimum sum of sensor transmission probabilities. The problem has also been treated for the detection task: in [39] the quantizers have been designed for a WSN performing a Generalized LOD (from Davies' framework) test for detection of a target whose position and emitted power is unknown; in this scenario the quantizers are designed using a semi-theoretical asymptotically optimal approach. In [40] it is shown the optimal quantizer in case of a deterministic signal and a WSN with imperfect reporting channel and a FC performing a GLRT concluding that the optimal threshold should be set to zero at all nodes. In [25] the case resulting quantizer was obtained through maximization of the Fisher Information. In [41] the binary asymmetric quantizer is obtained minimizing the maximum Cramér-Rao Lower Bound (CRLB) quantizer.

In general, the problem of the quantizer design has been mainly treated separately for the detection and estimation problem so that no optimal quantization strategy has been proposed so far to jointly maximize detection and parameter estimation performances.

B. Contribution and Paper Organization

This work investigates the use of a WSN made of passive acoustic sensors as an external LDS proposing two different methodologies for leak detection and four algorithms for leak localization and illustrates results on a realistic case-study based on the Goliat FPSO and represents a continuation and extension of the previous work on this topic [42], [43]. The underwater sensors transmit to the FC their decision regarding the presence or absence of a leakage assuming an On-Off Keying (OOK) modulation. The FC fuses the local decision and takes a global decision and, in the case that a leak is detected, estimates its position.

The detection is treated at sensor level showing the optimal test statistics to be performed locally, and at a global level, showing two fusion rules: the well-known CR, and a newly proposed modified version of the CVR (MCVR). The threshold selection is based on the optimization of an objective function and exploits the knowledge of the failure rates of the components of the SPS.

The analyzed localization methods can be divided into heuristic and Bayesian methods. The heuristic methods consist of a centroid-based algorithm, and a newly proposed modified centroid-based algorithm representing an alteration of the first methods which extends the localization area without altering the complexity of the algorithm. The two proposed Bayesian algorithms are a *Maximum A-Posteriori* (MAP) estimator and a *Minimum Mean Square Error* (MMSE) estimator which are adapted to work in the current framework: they use the information of the failure rates of the components of the SPS to build the prior probabilities for these components being the leak source.

The present work shows some new advances in the field of process monitoring:

- The entire work is based on the knowledge and integration of reliability data of the SPS into the design and configuration of the LDS;
- The proposed algorithms are built keeping low computational complexity, and ease of implementation;
- The newly proposed MCVR offers, without altering the computational complexity of the CR, more flexibility and the possibility of better results;
- The modified centroid-based method for localization, without altering the computational complexity of the centroid-based method, removes the limitation imposed by a centroid of being located inside the smallest convex volume inscribing all the sensors;
- The proposed Bayesian localization algorithms are designed for increased performances keeping contained their complexity and can further exploit the knowledge of some reliability data of the SPS.

The remainder of the paper is organized as follows. Sec. II provides a system overview, focusing on the network architecture, the signal model (including assumptions related to signals characterizations), and the necessary knowledge on the SPS. Data processing for leak detection is described in Sec. III, which includes local detection at sensor location and global detection at the FC, plus a description of the methodology for the selection of the thresholds. Sec. IV shows the necessary steps of four proposed algorithms for leak localization. Numerical results on the considered case study are presented in Sec. V in terms of Receiver Operating Characteristic (ROC) for the detection and Root Mean Square Error (RMSE) for the localization. Finally, conclusions and further works are addressed in Sec. VI.

C. Notation

Upper-case bold letters denote matrices and lower-case bold letters denote column vectors; $(\cdot)^T$, and $\|\cdot\|$ denote transpose and Euclidean norm operators, respectively; $\hat{a}$ and $\mathbb{E}(a)$ denote an estimate and the expectation of the random variable a, respectively; $\Pr(\cdot)$ and $p(\cdot)$ denote probability mass functions (pmfs) and probability density functions (pdfs), while $\Pr(\cdot|\cdot)$ and $p(\cdot|\cdot)$ their corresponding conditional counterparts; $\mathcal{N}(\mu, \sigma^2)$ denotes a Gaussian distribution with mean μ and variance σ^2; $\mathcal{Q}(\cdot)$ is the complementary cumulative distribution function (ccdf) of the standard normal distribution; $\mathcal{B}(p)$ denotes a Bernoulli distribution with mean p and variance $p(1-p)$; the symbol $\sim$ means "distributed as"; $\delta(\cdot)$ is the Dirac delta function; $\binom{n}{k} = \frac{n!}{k!(n-k)!}$ denotes the binomial coefficient; finally $\mathcal{O}(\cdot)$ denotes the big O notation.

II. System Model

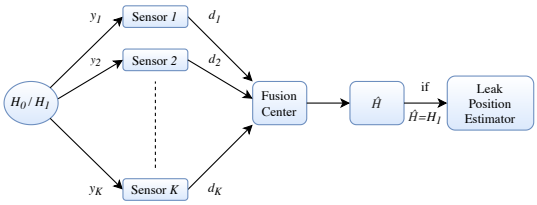

Fig. 1: Distributed Wireless Sensor Network

A. Distributed Wireless Sensor Network Architecture

The proposed distributed WSN architecture (see Fig. 1) is made of K passive acoustic sensors and one FC. The sensors sense sound pressure to detect the presence ($\mathcal{H}_1$) or absence ($\mathcal{H}_0$) of an oil spill[1]. The kth sensor (where $k = 1, 2, \ldots, K$) individually performs a test on the received signal y_k and takes a local decision $d_k = i \in \{0, 1\}$ if $\mathcal{H}_i$ is declared. The vector of local decisions $\boldsymbol{d} = \begin{bmatrix} d_1 & \ldots & d_K \end{bmatrix}^T$ is collected and processed at the FC for a global decision $\widehat{\mathcal{H}} \in \{\mathcal{H}_0, \mathcal{H}_1\}$. If $\widehat{\mathcal{H}} = \mathcal{H}_1$, the FC executes a localization algorithm to estimate the leak position. In addition to be spectrally-efficient, as only 1-bit communication is required on the reporting channel between the sensor and the FC, such a system is extremely energy efficient when OOK is employed for communicating the local decisions.

B. Signal Model

The model of the received sound pressure $y_k[n]$ at the kth sensor during the nth discrete time, depending on the corresponding hypothesis (absence/presence of a leakage), is the following:

$$\begin{cases} \mathcal{H}_0: & y_k[n] = w_k[n] \\ \mathcal{H}_1: & y_k[n] = \xi\ g(\boldsymbol{s}_k, \boldsymbol{\theta}) + w_k[n] \end{cases}, \tag{1}$$

where $\xi \sim \mathcal{N}(0, \sigma_\xi^2)$ and $w_k[n] \sim \mathcal{N}(0, \sigma_w^2)$ represent the emitted sound pressure produced by the leakage at a reference length (ℓ_{ref}) and the Additive White Gaussian Noise (AWGN), respectively. $w_k[n]$ and ξ are assumed both statistically independent due to the spatial separation of the sensors. The signal power σ_ξ^2 and the noise power σ_w^2 are assumed to be known, where σ_w^2 is assumed equal for all sensors. Also, $g(\boldsymbol{s}_k, \boldsymbol{\theta})$ represents the Amplitude Attenuation Function (AAF) depending on the distance between the kth sensor and the leak, whose positions are denoted $\boldsymbol{s}_k$ and $\boldsymbol{\theta}$, respectively. Here the AAF is treated as the contribution of the seawater absorption and the geometrical spreading and has the following form:

$$g(\boldsymbol{s}_k, \boldsymbol{\theta}) = \sqrt{\left(\frac{\ell_{\text{ref}}}{\|\boldsymbol{s}_k - \boldsymbol{\theta}\|}\right)^{k_{\text{sc}}} 10^{(\ell_{\text{ref}} - \|\boldsymbol{s}_k - \boldsymbol{\theta}\|)\alpha 10^{-4}}}, \tag{2}$$

where ℓ_{ref} and $\|\boldsymbol{s}_k - \boldsymbol{\theta}\|$ are measured in meters, the seawater absorption coefficient α is measured in [dB/km], and k_{sc} is the spreading coefficient. It can be noticed that if $\|\boldsymbol{s}_k - \boldsymbol{\theta}\| = \ell_{\text{ref}}$, then $g(\boldsymbol{s}_k, \boldsymbol{\theta}) = 1$. Any additional phenomenon influencing the attenuation can only be modeled if the environmental conditions and the design of the SPS are precisely known. The seawater absorption coefficient α can be computed using several methods, e.g. *Thorp equation* [44], *Schulkin & Marsh equation* [45], *Fisher & Simmons equation* [46], *Ainslie & McColm equation* [47], and *Francois & Garrison equation* [48], [49]. The *Francois & Garrison equation*, reported in Appendix I is chosen in this work as it is one of the most performing equations available with one of the highest range of validity [50]. This equation depends on several variables such as salinity, reference frequency, temperature, depth, pH, and speed of sound. The underwater speed of sound, unlike the other variables, is often not available in form of experimental data, therefore it needs to be calculated numerically using one of the several equations available, e.g. *Medwin equation* [51], *Mackenzie equation* [52], *Del Grosso equation* [53], and *Chen & Millero equation* [54], [55]. In this work we choose to use the *Chen & Millero equation* with updated coefficients [56] due to its wide range of applicability [50]. This equation depends on variables such as salinity, temperature, and pressure (which can be obtained when depth and average seawater density are known) and is reported in Appendix II.

[1]The analysis related to the sampling frequency is not considered in the present work.

C. Subsea Production System

The SPS, as any plant, presents pieces of equipment and mechanical parts having higher failure rates which makes them more likely to cause a leakage. In this work, such components will be referred to as *hotspots*, and the position of the mth hotspot will be denoted $\boldsymbol{h}_m$ (where $m = 1, 2, \ldots, M$). We assume that the component failures are statistically independent and we denote φ_m the conditional probability (given the hypothesis $\mathcal{H}_1$) that a failure happens at the mth hotspot, which can be expressed as

$$\varphi_m = \Pr(\boldsymbol{\theta} = \boldsymbol{h}_m | \mathcal{H}_1) = \frac{f_m}{\sum_{m=1}^{M} f_m}, \tag{3}$$

where f_m is the failure rate of the mth hotspot.

III. Leak Detection

A. Local Detection

Given Eq. (1), the *uniformly most powerful* test [57] to be performed by the kth sensor at the generic nth instant is the energy test [28]:

$$d_k[n] = \begin{cases} 0, & y_k^2[n] < \tau_k \\ 1, & y_k^2[n] \geq \tau_k \end{cases}, \tag{4}$$

where τ_k is a local threshold. The local performances, in terms of probability of detection and probability of false alarm, of

this test are defined and computed as follows:

$$P_{D,k} = \Pr(y_k^2[n] \geq \tau_k | \mathcal{H}_1) = 2\mathcal{Q}\left(\sqrt{\frac{\tau_k}{\sigma_\xi^2 g^2(\boldsymbol{s}_k, \boldsymbol{\theta}) + \sigma_w^2}}\right) , \tag{5}$$

$$P_{F,k} = \Pr(y_k^2[n] \geq \tau_k | \mathcal{H}_0) = 2\mathcal{Q}\left(\sqrt{\frac{\tau_k}{\sigma_w^2}}\right) . \tag{6}$$

However, since the leakage position is unknown, Eq. (5) cannot be used directly. One possibility to overcome this issue is to refer to average performances with respect to the SPS's hotspots, i.e.

$$\overline{P_{D,k}} = \sum_{m=1}^{M} \varphi_m P_{D,k,m} , \tag{7}$$

where $P_{D,k,m}$ is obtained replacing $\boldsymbol{\theta}$ with $\boldsymbol{h}_m$ in Eq. (5), with the implicit assumption that leakages generated in the different hotspots produce signals with equal power σ_ξ^2.

We define the reference Signal-to-Noise ratio (SNR) and the average sensing SNR at the kth sensor respectively as

$$\Gamma_{\text{ref}} = \frac{\sigma_\xi^2}{\sigma_w^2} , \quad \Gamma_k = \Gamma_{\text{ref}} \sum_{m=1}^{M} \varphi_m g^2(\boldsymbol{s}_k, \boldsymbol{h}_m) . \tag{8}$$

B. Global Detection

The FC assesses the presence of a leakage based on a test statistic (Λ) depending on the local decisions d_k (in this subsection we omit the dependence on n to keep notation short):

$$\widehat{\mathcal{H}} = \begin{cases} \mathcal{H}_0, & \Lambda < \tau_o \\ \mathcal{H}_1, & \Lambda \geq \tau_o \end{cases} , \tag{9}$$

where τ_o is a global threshold.

Three different fusion rules are considered for computing the test statistic at the FC: (i) the CR, (ii) the CVR, and (iii) the MCVR.

More specifically, the corresponding test statistics are computed as follows:

$$\Lambda_{\text{CR}} = \sum_{k=1}^{K} d_k , \tag{10}$$

$$\Lambda_{\text{CVR}} = \sum_{k=1}^{K} \left[d_k \ln\left(\frac{P_{D,k}}{P_{F,k}}\right) + (1-d_k) \ln\left(\frac{1-P_{D,k}}{1-P_{F,k}}\right)\right] , \tag{11}$$

$$\Lambda_{\text{MCVR}} = \sum_{k=1}^{K} \left[d_k \ln\left(\frac{\overline{P_{D,k}}}{P_{F,k}}\right) + (1-d_k) \ln\left(\frac{1-\overline{P_{D,k}}}{1-P_{F,k}}\right)\right] . \tag{12}$$

The CVR, obtained as the result of Log-Likelihood Ratio Test, is the optimal test statistics at the FC and results in the CR in the particular case where the sensors have equal local probabilities of detection and false alarm [20]. Unfortunately, the CVR cannot be used in its form as it requires knowledge of the $P_{D,k}$'s. For this reason the MCVR here proposed replaces $P_{D,k}$ with $\overline{P_{D,k}}$, via Eq. (7), for all k which are available. The computational complexity of both fusion rules (CR and MCVR) is $\mathcal{O}(K)$. Global system performances for each fusion rule are expressed in terms of *Global Probability of Detection* and *Global Probability of False Alarm* at the FC, defined respectively as $Q_D = \Pr(\Lambda \geq \tau_o | \mathcal{H}_1)$ and $Q_F = \Pr(\Lambda \geq \tau_o | \mathcal{H}_0)$. It is worth noticing that Q_D will depend on the leak position, then the same approach used in Sec. III-A for local performances is considered here, i.e.

$$\overline{Q_D} = \sum_{m=1}^{M} \varphi_m Q_{D,m} . \tag{13}$$

C. Threshold Selection

Local thresholds τ_k are hyper-parameters that ideally should be optimized based on the global performance. Such a task does not exhibit an easy solution, then sub-optimal approaches are usually considered. In this work, thresholds selection is based on the maximization of the Youden's Index (J) [58]:

$$\tau^* = \arg\max_{\tau} J(\tau) = \arg\max_{\tau} \left\{ P_D(\tau) - P_F(\tau) \right\} . \tag{14}$$

In Eq. (14), the variables τ, P_D, and P_F are replaced with τ_k, $\overline{P_{D,k}}$, and $P_{F,k}$ when tuning the sensors, while they are replaced with τ_o, $\overline{Q_D}$, and Q_F when tuning the FC.

When tuning the FC, from a practical point of view, the number of thresholds is finite and their values can be obtained as follows (due to d_k in Eqs. (10) and (12) being binary):

- *CR case* – The CR exhibits a simple behavior; the set of possible thresholds is $\{0, 1, \ldots, K\}$ as these are the possible outcomes of Λ_{CR}. The number of possible thresholds is the number of K-combinations with repetitions of 2 elements (since the local decisions are binary):
$$C_{2,K} = \binom{(2+K)-1}{K} = K+1 ; \tag{15}$$
- *MCVR case* – Being each sensor decision weighted with coefficients depending on the local performance, the number of possible thresholds is larger (unless all the coefficients happen to be equal). These thresholds can be obtained by computing all the possible outcomes of Λ_{MCVR}, given that the coefficients are known. The number of possible thresholds is the number of K-permutations with repetitions of 2 elements :
$$R_{2,K} = 2^K . \tag{16}$$

Note that the number of possible thresholds in the two cases includes also the threshold corresponding to the case in which $d_k = 0$ for all $k = 1, 2, \ldots, K$ resulting in $Q_D = Q_F = 1$.

IV. Leak Localization

Consequently to the detection of a leak, the FC provides an estimate of its position. In practical scenarios, a leakage happens at a certain (unknown) time denoted n_0 and remains in place for $n \geq n_0$ until maintenance is operated. Without loss of generality for the analysis of localization performance[2], we

[2]It is worth repeating that our focus here is to assess the performance of the localization accuracy, while the assessment of early response of the system to a leakage usually analyzed within the framework of quickest detection [59] is beyond the scope of this work.

assume $n_0 = 1$ with the leakage present all the time. In this work, four different algorithms are considered: (i) centroid-based localization, (ii) modified-centroid-based localization, (iii) MAP localization, and (iv) MMSE localization.

A. Centroid-Based Localization

This algorithm is based on the following steps:

1) Calculate the centroid of the sensors detecting a leakage at time n:
$$\boldsymbol{x}^{(\mathrm{c})}[n] = \frac{\sum_{k=1}^{K} d_k[n]\boldsymbol{s}_k}{\sum_{k=1}^{K} d_k[n]} \; ; \tag{17}$$
2) Calculate the cumulative moving average (CMA) of the centroid positions based on Eq. (18) at the top of the next page;
3) Estimate the leak position via distance minimization between the positions of the hotspots and the CMA of the centroid:
$$m_o[n] = \underset{m=1,\ldots,M}{\arg\min} \left\| \overline{\boldsymbol{x}^{(\mathrm{c})}}[n] - \boldsymbol{h}_m \right\| \; , \tag{19}$$
$$\widehat{\boldsymbol{\theta}}[n] = \boldsymbol{h}_{m_o[n]} \; . \tag{20}$$

B. Modified Centroid-Based Localization

This algorithm is proposed as the centroid-based algorithm does not allow the localization of those leakages happening in hotspots located outside the smallest convex volume inscribing all K sensors. This can be overcome through the modification of Eq. (17). The heuristic is to have, for each sensor not detecting the spill, the antipodal point ($\boldsymbol{s}_k^{(\mathrm{a})}[n]$) with respect to a point reflection with the centroid $\boldsymbol{x}^{(\mathrm{c})}[n]$ being the point of inversion. Hence, for the kth sensor such that $d_k[n] = 0$:

$$\boldsymbol{s}_k^{(\mathrm{a})}[n] = 2\boldsymbol{x}^{(\mathrm{c})}[n] - \boldsymbol{s}_k \; . \tag{21}$$

Let us define $\boldsymbol{z}$ as the centroid of all sensors present in the WSN:

$$\boldsymbol{z} = \frac{1}{K}\sum_{k=1}^{K} \boldsymbol{s}_k \; . \tag{22}$$

This operation is necessary to obtain a modified centroid that accounts for both the active sensors (via actual position) and inactive sensors (via antipodal position):

$$\begin{aligned} \boldsymbol{x}^{(\mathrm{mc})}[n] &= \frac{1}{K}\sum_{k=1}^{K}\left(d_k[n]\boldsymbol{s}_k + (1-d_k[n])\boldsymbol{s}_k^{(\mathrm{a})}[n]\right) \\ &= 2\boldsymbol{x}^{(\mathrm{c})}[n] - \boldsymbol{z} \; . \end{aligned} \tag{23}$$

The presence of the antipodal position makes it possible for the FC to localize leakages outside the sensor's perimeter. Although it is possible to perform this algorithm by substituting Eq. (17) in Step 1 of the centroid-based algorithm with Eq. (23), the next steps show a way to present the algorithm that highlights the relationship with the final result of the centroid-based algorithm:

1) Calculate $\boldsymbol{z}$ using Eq. (22) — Since this term is constant over time, this step does not need to be repeated;
2) Calculate $\boldsymbol{x}^{(\mathrm{c})}[n]$ as in Eq. (17);
3) Calculate a modified version of Eq. (18) using Eq. (24) at the top of the next page, which consists of the CMA of the modified centroid from Eq. (23);
4) Estimate the leak position via distance minimization between the positions of the hotspots and the CMA of the modified centroid:
$$m_o[n] = \underset{m=1,\ldots,M}{\arg\min} \left\| \overline{\boldsymbol{x}^{(\mathrm{mc})}}[n] - \boldsymbol{h}_m \right\| \; , \tag{25}$$
$$\widehat{\boldsymbol{\theta}}[n] = \boldsymbol{h}_{m_o[n]} \; . \tag{26}$$

C. Maximum A-Posteriori Localization

The following Bayesian estimator is proposed in order to exploit the prior knowledge of φ_m. This algorithm makes the simplification that $\Pr(\boldsymbol{\theta} = \boldsymbol{h}_m|\boldsymbol{d}[n], \mathcal{H}_1) = \Pr(\boldsymbol{\theta} = \boldsymbol{h}_m|\boldsymbol{d}[n], \widehat{\mathcal{H}} = \mathcal{H}_1)$:

1) For each hotspot, calculate of the log-likelihood of the decision vector at the nth discrete time $\boldsymbol{d}[n]$ given that the leak is located in the mth hotspot using Eq. (27) at the top of the next page;
2) For each hotspot, compute the joint probability of the decision vectors up to the current discrete time via the updating formula in Eq. (28) at the top of the next page, where we have exploited conditional independence of sensors decision both in space and time;
3) Estimate the leak position chosen among the M hotspots through joint probability maximization:
$$m_o[n] = \underset{m=1,\ldots,M}{\arg\max} \ln \Pr(\boldsymbol{d}[1], \ldots, \boldsymbol{d}[n], \boldsymbol{\theta} = \boldsymbol{h}_m, \mathcal{H}_1) \; , \tag{29}$$
$$\widehat{\boldsymbol{\theta}}[n] = \boldsymbol{h}_{m_o[n]} \; . \tag{30}$$

D. Minimum Mean Square Error Localization

Also this Bayesian estimator is proposed to exploit the knowledge of φ_m, still relying on the simplification that $\Pr(\boldsymbol{\theta} = \boldsymbol{h}_m|\boldsymbol{d}[n], \mathcal{H}_1) = \Pr(\boldsymbol{\theta} = \boldsymbol{h}_m|\boldsymbol{d}[n], \widehat{\mathcal{H}} = \mathcal{H}_1)$. For compactness, let us introduce the following definition:

$$\alpha_m[n] \triangleq \Pr\left(\boldsymbol{d}[n], \ldots, \boldsymbol{d}[1], \boldsymbol{\theta} = \boldsymbol{h}_m, \mathcal{H}_1, \right) \; . \tag{31}$$

1) For each hotspot, calculate the likelihood of the decision vector at the nth discrete time $\boldsymbol{d}[n]$ given that the leak is located at the mth hotspot where we have exploited conditional independence of sensors decision in space;
$$\begin{aligned} &\Pr(\boldsymbol{d}[n]|\boldsymbol{\theta} = \boldsymbol{h}_m, \mathcal{H}_1) \\ &= \prod_{k=1}^{K}\left(P_{D,k,m}{}^{d_k[n]}(1-P_{D,k,m})^{1-d_k[n]}\right) \; ; \end{aligned} \tag{32}$$
2) Compute the geometric mean of all the probabilities $\Pr(\boldsymbol{d}[n]|\boldsymbol{\theta} = \boldsymbol{h}_m, \mathcal{H}_1)$ with $m = 1, \ldots, M$:
$$c_n = \left(\prod_{m=1}^{M} \Pr(\boldsymbol{d}[n]|\boldsymbol{\theta} = \boldsymbol{h}_m, \mathcal{H}_1)\right)^{1/M} \; ; \tag{33}$$

$$\overline{\boldsymbol{x}^{(\mathrm{c})}}[n] = \begin{cases} \boldsymbol{x}^{(\mathrm{c})}[1], & n = 1 \\ \overline{\boldsymbol{x}^{(\mathrm{c})}}[n-1] + \frac{1}{n}\left(\boldsymbol{x}^{(\mathrm{c})}[n] - \overline{\boldsymbol{x}^{(\mathrm{c})}}[n-1]\right), & n > 1 \end{cases} \tag{18}$$

$$\overline{\boldsymbol{x}^{(\mathrm{mc})}}[n] = \begin{cases} 2\boldsymbol{x}^{(\mathrm{c})}[1] - \boldsymbol{z}, & n = 1 \\ 2\overline{\boldsymbol{x}^{(\mathrm{c})}}[n-1] + \frac{2}{n}\left(\boldsymbol{x}^{(\mathrm{c})}[n] - \overline{\boldsymbol{x}^{(\mathrm{c})}}[n-1]\right) - \boldsymbol{z}, & n > 1 \end{cases} \tag{24}$$

$$\ln \Pr(\boldsymbol{d}[n] | \boldsymbol{\theta} = \boldsymbol{h}_m, \mathcal{H}_1) = \sum_{k=1}^{K} \left(d_k[n] \ln P_{D,k,m} + (1 - d_k[n]) \ln\left(1 - P_{D,k,m}\right)\right) \tag{27}$$

$$\ln \Pr(\boldsymbol{d}[n], \ldots, \boldsymbol{d}[1], \boldsymbol{\theta} = \boldsymbol{h}_m, \mathcal{H}_1) = \begin{cases} \ln \Pr(\boldsymbol{d}[1] | \boldsymbol{\theta} = \boldsymbol{h}_m, \mathcal{H}_1) + \ln \varphi_m, & n = 1 \\ \ln \Pr(\boldsymbol{d}[n] | \boldsymbol{\theta} = \boldsymbol{h}_m, \mathcal{H}_1) + \ln \Pr(\boldsymbol{d}[n-1], \ldots, \boldsymbol{d}[1], \boldsymbol{\theta} = \boldsymbol{h}_m, \mathcal{H}_1), & n > 1 \end{cases} \tag{28}$$

3) For each hotspot, compute the scaled version of the joint probability $\alpha_m[n]$ via the updating formula in Eq. (34) at the top of the next page;
4) Calculate the expected value of the posterior probability of the leak position given the decisions vectors up to the current discrete time (proof is reported in Appendix III):

$$\begin{aligned} \boldsymbol{x}^{(\mathrm{mmse})}[n] &= \mathbb{E}\left(\boldsymbol{\theta} | \boldsymbol{d}[n], \ldots, \boldsymbol{d}[1], \mathcal{H}_1\right) \\ &= \frac{\sum_{m=1}^{M} \tilde{\alpha}_m[n] \boldsymbol{h}_m}{\sum_{m=1}^{M} \tilde{\alpha}_m[n]} ; \end{aligned} \tag{35}$$

5) Estimate the leak position via distance minimization between the positions of the hotspots and the result of Eq. (35):

$$m_o[n] = \underset{m=1,\ldots,M}{\arg\min} \left\| \boldsymbol{x}^{(\mathrm{mmse})}[n] - \boldsymbol{h}_m \right\| , \tag{36}$$

$$\widehat{\boldsymbol{\theta}}[n] = \boldsymbol{h}_{m_o[n]} . \tag{37}$$

A normalization procedure like that reported in Steps 2 and 3 is required to avoid arithmetic underflow for sufficiently large values of n. A proper normalization coefficient can be found computing a log-average of the values (by averaging their natural logarithms and then performing the exponential to return to the original scale), which is equivalent to their geometric mean. This has the benefit to properly scale all likelihoods of the observations of the sensors at each instant avoiding an unwanted underflow.

Table I compares the computational complexity of the proposed leak localization algorithms.

TABLE I: Computational complexity of the proposed leak localization algorithms

Localization Algorithm	Complexity
Centroid-Based	$\mathcal{O}(K+M)$
Modified Centroid-Based	$\mathcal{O}(K+M)$
Maximum A-Posteriori	$\mathcal{O}(KM)$
Minimum Mean Square Error	$\mathcal{O}(KM)$

V. Case Study — Goliat FPSO

The Goliat FPSO is an oil production platform located in the Norwegian Barents Sea and it is currently the world's northernmost offshore platform. Because of its location in an environmentally sensitive area, the platform is subject to strict regulations, especially regarding oil spills. The Goliat FPSO employs a SPS which relies on 8 subsea templates for a total of 22 wells (12 production wells, 7 water injectors, and 3 gas injectors). Each template is equipped with a manifold and four well slots as shown in Fig. 2. The LDS monitoring each template is a combination of internal and external sensors, although the main usage of the internal sensors is process monitoring. Regarding the external LDS, one capacitive sensor is positioned above each subsea tree, while $K = 3$ passive acoustic sensors are installed to monitor the manifold [60], [61]. It is important to mention that the installed LDS is mainly designed to carry out the detection task, not the localization task being this one less critical. $M = 20$ hotspots have been recognized after a reliability analysis on the SPS. Such components correspond to 14 valves (8 branch valves and 6 isolation valves) and 6 connectors (4 connecting production lines and 2 connecting gas lift lines). Sensors and hotspots are highlighted in Fig. 2 where it can be seen that 6 (resp. 14) hotspots being inside (resp. outside) the sensors' perimeter. According to the OREDA (Offshore and Onshore Reliability Data) Handbook, the failure rates of connectors and isolation valves (in subsea manifolds) have the same order of magnitude ($10^{-6}\,\mathrm{h}^{-1}$) giving no specific values based on the different diameters or other design specifications [62]. As a consequence, we can assume the hotspots to have the same value of f_m. In the case study, hotspots and sensors are assumed to be at the same height.

The methodologies for detection and localization described in the previous sections are applied here assuming that the sensors are part of a WSN as described in Sec. II.

In order to better analyze the results, two different cases are

$$\tilde{\alpha}_m[n] = \begin{cases} \varphi_m, & n = 0 \\ c_n^{-1} \Pr(\boldsymbol{d}[n] | \boldsymbol{\theta} = \boldsymbol{h}_m, \mathcal{H}_1) \tilde{\alpha}_m[n-1], & n > 0 \end{cases} \tag{34}$$

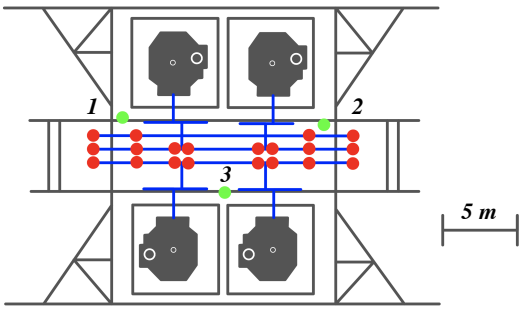

Fig. 2: Goliat's subsea template: the grey elements are the structure and the subsea trees, the blue lines constitutes the manifold, the green dots are the passive acoustic sensors, and the red dots are the hotspots

TABLE II: Parameters used to simulate a leak scenario

Parameter	Value	Note / Reference
Reference Frequency	2.5 kHz	[13]
Temperature	3.8 °C	[63]
Salinity	35 ‰	[63]
Depth	350 m	[60]
pH	8	[64]
Spreading Coefficient (k_{sc})	1.5	[65]
Reference Length (ℓ_{ref})	1 m	–
Noise Variance (σ_w^2)	1	–
φ_m	$1/M$	$f_1 = f_2 = \ldots = f_M$
Γ_{ref}	10 dB; 15 dB	–

simulated: $\Gamma_{\text{ref}} \in \{10\,\text{dB}, 15\,\text{dB}\}$.

The values of $\overline{Q_D}$ and Q_F have been computed via numerical simulation with 10^8 Monte Carlo runs equally divided between $\mathcal{H}_0$ and $\mathcal{H}_1$. The localization performances have been produced via numerical simulation with 10^4 Monte Carlo runs where the $\mathcal{H}_1$ scenario is simulated. The simulation is carried out with the FC performing both the CR and the MCVR operating at the thresholds obtained via maximization of the Youden's Index. The performances are assessed in terms of variation of the RMSE with respect to the number of instants (N) since the leakage started occurring. All the simulations have been carried out using the software MATLAB. The parameters used for the case study are found in Table II.

A. Local Detection Results

Table III shows the average SNR for each sensor in the case of $\Gamma_{\text{ref}} = 10$ dB and $\Gamma_{\text{ref}} = 15$ dB obtained via Eq. (8).

Table IV shows the tuning result after the maximization of the local Youden's Index which highlights how a higher value of Γ_k allows a higher resulting threshold τ_k^*. In this specific scenario sensor 2 has the highest value of Γ_k for both Γ_{ref}.

TABLE III: Average Sensing SNR at the different sensors

Γ_{ref}	Γ_1	Γ_2	Γ_3
10 dB	−0.63 dB	0.39 dB	−1.61 dB
15 dB	4.37 dB	5.39 dB	3.39 dB

TABLE IV: Leak Detection Performances at the sensors

Γ_{ref}	Sensor (k)	τ_k^*	$\overline{P_{D,k}}(\tau_k^*)$	$P_{F,k}(\tau_k^*)$	$J(\tau_k^*)$
10 dB	1	1.4402	0.3540	0.2301	0.1238
	2	1.5204	0.3563	0.2176	0.1388
	3	1.3189	0.3701	0.2508	0.1193
15 dB	1	1.7916	0.4230	0.1807	0.2422
	2	1.8820	0.4293	0.1701	0.2592
	3	1.6887	0.4460	0.1938	0.2522

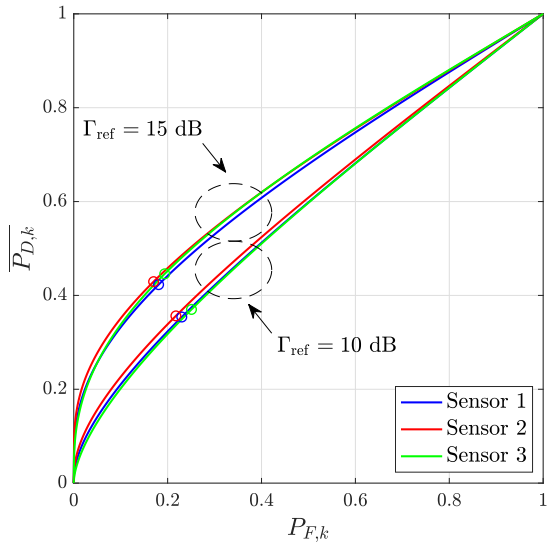

Fig. 3: Local ROC curves highlighting the operating points selected via Youden's Index maximization

The location of the operating points in the ROC space can be seen in Fig. 3 where it can be noticed that the averaging procedure in Eq. (7) provides 3 similar ROC curves, leading to similar operating points.

This behavior is not surprising as this case study shows sufficiently similar values of Γ_k. The impact of efficient sensor placement, possible through the maximization of Γ_k for each sensor, is not investigated in this work.

TABLE V: Leak Detection Performances at the FC

Γ_{ref}	Fusion Rule	τ_o^*	$\overline{Q_D}(\tau_o^*)$	$Q_F(\tau_o^*)$	$J(\tau_o^*)$
10 dB	CR	1	0.7183	0.5487	0.1696
	Clairvoyant CVR	0.0849	0.5435	0.3081	0.2354
	MCVR	0.0650	0.5823	0.3977	0.1846
15 dB	CR	2	0.4093	0.0868	0.3225
	Clairvoyant CVR	0.1411	0.6411	0.2328	0.4083
	MCVR	1.3584	0.4092	0.0869	0.3224

B. Global Detection Results

Fig. 4 shows the ROC curves of the LDS in the two cases comparing the the CR and the MCVR using the (position) Clairvoyant CVR as upper bound (enabling the use of Eq. (11)). The impact of Γ_{ref} on the global performance is apparent. The ROC curves of the two different fusion rules are largely similar, thus each operation point of the CR might be achieved also with the MCVR via appropriate threshold selection. Excluding the useless cases with $\overline{Q_D} = Q_F = 0$ and $\overline{Q_D} = Q_F = 1$, based on Eq. (15) and Eq. (16) the CR (resp. the MCVR) provides 3 (resp. 7) possible operation points, thus the large flexibility of the MCVR allows to take into account for more design needs with respect to the CR. On the other hand, the Clairvoyant CVR shows a different behavior since its points do not overlap with those generated by the two fusion rules. Note that in Fig. 4 the curves of the MCVR and the CR cross the curve of the Clairvoyant CVR in certain areas of the plot. This should not surprise as the lines are simple linking segments between points representing two consecutive thresholds and must not be interpreted as a continuous locus of possible operation points.

Table V shows the operation points from the threshold optimization procedures. Both CR and MCVR show lower values of maximum Youden's Index when compared to the Clairoyant CVR. It is interesting to notice that in the case of high SNR (e.g. $\Gamma_{\text{ref}} = 15\,\text{dB}$), the optimal operation points from the two considered fusion rules are very similar, while for lower SNR values (e.g. $\Gamma_{\text{ref}} = 10\,\text{dB}$) the optimization points are different and the one from the MCVR has no counterpart with the CR, moreover, the optimization point from the MCVR in such scenario tends to be closer (in terms of $\overline{Q_D}$ and Q_F) to the one from the Clairvoyant CVR. This shows how the MCVR, maintaining the same complexity of the CR, gives more flexibility to the LDS and may enable better results.

C. Localization Results

Fig. 5, 6, 7, and 8 show the result of the four proposed localization techniques for both fusion rules (CR and MCVR) and both reference SNR values ($\Gamma_{\text{ref}} = 10\,\text{dB}$ and $\Gamma_{\text{ref}} = 15\,\text{dB}$). In addition, the Cramér-Rao Lower Bound (CRLB) is displayed for an estimator that follows a perfect detector ($\overline{Q_D} = 1$, $Q_F = 0$). The derivation of the CRLB can be found in Appendix IV. As a consequence, such CRLB is independent of the evaluated fusion rule and only depends on the value of Γ_{ref}. Clearly, such lower bound is purely theoretical and cannot be attained as a perfect detection cannot be achieved even in the case of the (position) Clairvoyant CVR (see Fig. 4). The

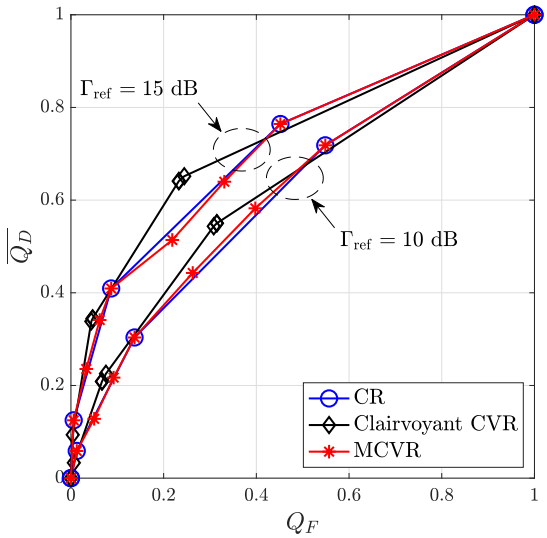

Fig. 4: Global ROC curves

different performance related to the case of a leakage located inside or outside the sensor perimeter is also highlighted. For the simulations, local and global thresholds in Table IV and Table V were considered.

Again, the figures show that even from the localization perspective, at high SNR (i.e. $\Gamma_{\text{ref}} = 15\,\text{dB}$) the corresponding localization procedures perform similarly independently of the considered fusion rule (CR or MCVR). Apparently, the centroid-based method is the least performing, as it fails in localizing leakages outside the sensor perimeter. The newly proposed modified-centroid-based method tackles this limitation through the reflection of the positions of the inactive sensors and the numerical simulations confirm the effectiveness of such approach, which does not require additional computational resources. It is worth highlighting that the centroid-based method is extremely well performing when leakages are located inside the sensor perimeter, but extremely bad-performing in the other cases.

Both the considered statistical approaches exhibit better performance than the previous heuristic ones, with a price in terms of computational complexity. More specifically, MAP and MMSE behave similarly, with the latter slightly outperforming the former when few samples are available.

The CRLB shows little variation when the target is inside the sensor perimeter compared to when it is located outside. Not surprisingly the CRLB, despite showing better performances in case $\Gamma_{\text{ref}} = 15\,\text{dB}$ for small values of N (the RMSE is around 1 meter smaller), converges to zero in both case as $N \to \infty$. This convergence is fast enough to make the difference in RMSE look imperceptible in the two cases at sufficiently high values of N.

Finally, it is worth mentioning that the trade-off between the probabilities of detection and false alarm at the detection stage is handled in this work through the Youden's Index

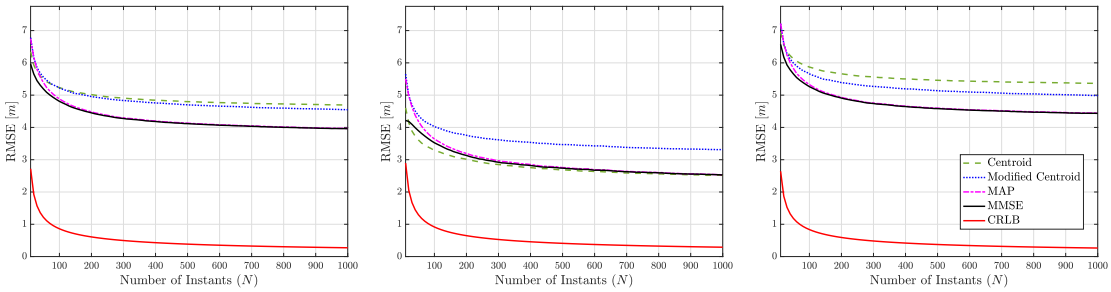

(a) All hotspots (b) Hotspots inside sensor perimeter (c) Hotspots outside sensor perimeter

Fig. 5: Localization performance with CR and $\Gamma_{\text{ref}} = 10\,\text{dB}$

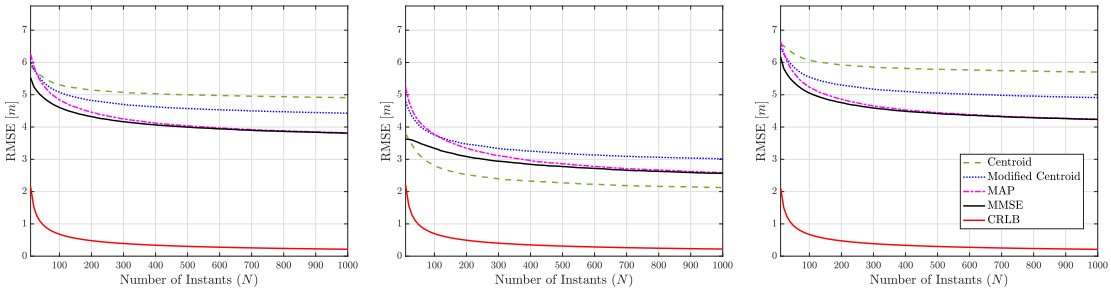

(a) All hotspots (b) Hotspots inside sensor perimeter (c) Hotspots outside sensor perimeter

Fig. 6: Localization performance with CR and $\Gamma_{\text{ref}} = 15\,\text{dB}$

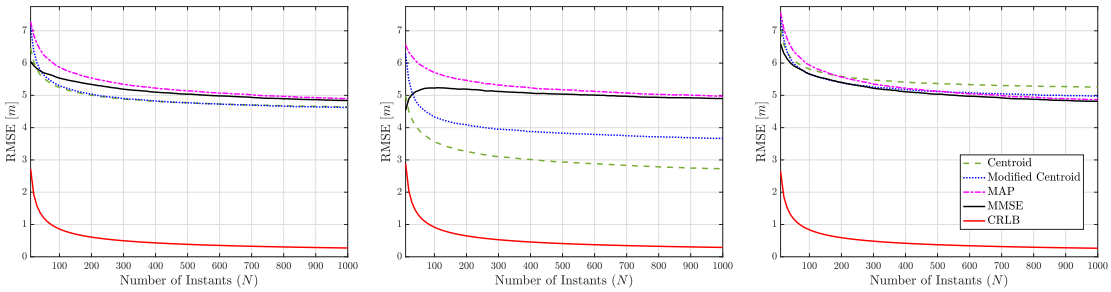

(a) All hotspots (b) Hotspots inside sensor perimeter (c) Hotspots outside sensor perimeter

Fig. 7: Localization performance with MCVR and $\Gamma_{\text{ref}} = 10\,\text{dB}$

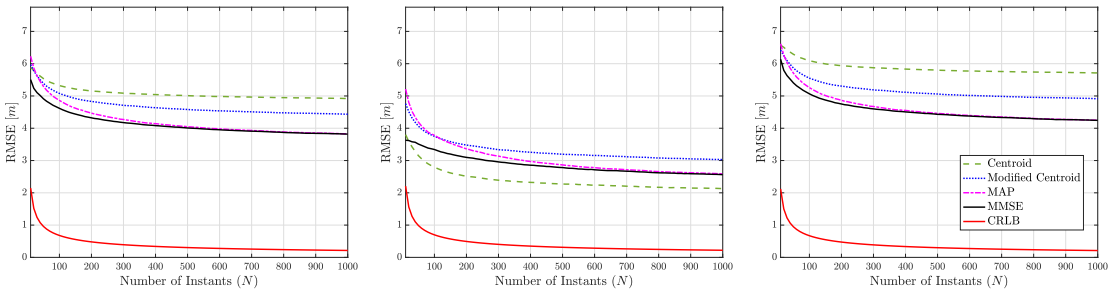

(a) All hotspots (b) Hotspots inside sensor perimeter (c) Hotspots outside sensor perimeter

Fig. 8: Localization performance with MCVR and $\Gamma_{\text{ref}} = 15\,\text{dB}$

maximization. However, from localization perspective, it is the detection probability that matters as localization performance increases with it. This must be considered when comparing performance related to different reference SNR which might correspond to different operation points of the ROC. The design of the overall parameters configuration taking into account both detection and localization performance is not considered in this work.

VI. Conclusions

This work investigated the use of WSNs for subsea oil spill detection and localization, using Goliat FPSO as a case study. Local sensors' binary decisions are collected at the FC, where CR and MCVR are considered for data fusion. ROC performances, obtained through realistic numerical simulations, showed the potential benefit of the considered approach. Two heuristic and two Bayesian estimation algorithms have been considered for localization, with the second pair exhibiting better performance but higher computational complexity.

The proposed methodologies were developed taking into account a possible integration of the LDS with the DRMF, exploiting the results of a risk analysis carried out on the SPS. The detection and localization results show the benefit of designing a LDS exploiting the knowledge of the hotspots of the SPS and their failure rates as these help us computing prior probabilities to be used in the algorithms. A key element for a performing LDS is the integration of the results of the risk analysis into the LDS design in an iterative exchange of information to increase the system capability of predicting and handling unwanted events. Thresholds selection has been based on detection performance only, while future work would include localization performance into hyperparameters optimization and exploring the impact of system design on risk management.

Appendix I
Francois & Garrison Equation

The following equation can be found in [48], [49]. This method requires that the input values are in the exact measurement units reported at the end of the Appendix.

Absorption Coefficient [dB km^{-1}]:

$$\alpha = \underbrace{\frac{A_1 P_1 f_1 f^2}{f^2 + f_1^2}}_{\substack{H_3BO_3 \\ \text{Contribution}}} + \underbrace{\frac{A_2 P_2 f_2 f^2}{f^2 + f_2^2}}_{\substack{MgSO_4 \\ \text{Contribution}}} + \underbrace{A_3 P_3 f^2}_{\substack{H_2O \\ \text{Contribution}}}$$

H_3BO_3 Contribution:

$$A_1 = \frac{8.86}{c}\, 10^{(0.78\ \mathrm{pH}-5)} \qquad \left[\frac{\text{dB}}{\text{km kHz}}\right]$$
$$P_1 = 1$$
$$f_1 = 2.8\ (S/35)^{0.5}\ 10^{[4-1245/(T+273)]} \qquad [\text{kHz}]$$

TABLE VI: Coefficients of the H_2O contribution

Temperature	$a_0 \cdot 10^4$	$a_1 \cdot 10^5$	$a_2 \cdot 10^7$	$a_3 \cdot 10^8$
$T \leq 20$ °C	4.397	-2.59	9.11	-1.50
$T > 20$ °C	3.964	-1.146	1.45	$-6.5 \cdot 10^{-2}$

$MgSO_4$ Contribution:

$$A_2 = 21.44\ \frac{S}{c}\ (1 + 0.025\ T) \qquad \left[\frac{\text{dB}}{\text{km kHz}}\right]$$
$$P_2 = 1 - 1.37 \cdot 10^{-4}\ D + 6.2 \cdot 10^{-9}\ D^2$$
$$f_2 = \frac{8.17 \cdot 10^{[8-1990/(T+273)]}}{1 + 0.0018\ (S-35)} \qquad [\text{kHz}]$$

H_2O Contribution:

$$A_3 = \sum_{m=0}^{3} a_m T^m \qquad \left[\frac{\text{dB}}{\text{km kHz}^2}\right]$$
$$P_3 = 1 - 3.83 \cdot 10^{-5}\ D + 4.9 \cdot 10^{-10}\ D^2$$

In the above-reported method f is the frequency [kHz], c is the speed of sound [m s^{-1}], S is the salinity [‰], T is the temperature [°C], and D is the depth [m]. The temperature-dependent values of the coefficients a_m $(m = 0, 1, 2, 3)$ are reported in Tab. VI.

Appendix II
Chen & Millero Equation

The following equation can be found in [54]. Table VII uses the updated coefficient present in [56] after the adoption of the International Temperature Scale of 1990. This method requires that the input values are in the exact measurement units reported at the end of the Appendix.

Speed of Sound:

$$c = C + AS + BS^{3/2} + DS^2$$
$$C = \sum_{m=0}^{3}\sum_{n=0}^{5} C_{mn} P^m T^n$$
$$A = \sum_{m=0}^{3}\sum_{n=0}^{4} A_{mn} P^m T^n$$
$$B = \sum_{m=0}^{1}\sum_{n=0}^{1} B_{mn} P^m T^n$$
$$D = D_{00} + D_{10} P$$

where c is the speed of sound [m s^{-1}], S is the salinity [‰], T is the temperature [°C], and P is the pressure [kPa]. The values of the coefficients C_{mn}, A_{mn}, B_{mn}, and D_{mn} are reported in Tab. VII.

TABLE VII: Updated coefficients of Chen & Millero Equation

Coefficient	Value	Coefficient	Value
C_{00}	1402.388	A_{01}	$-1.262 \cdot 10^{-2}$
C_{01}	5.03830	A_{02}	$7.166 \cdot 10^{-5}$
C_{02}	$-5.81090 \cdot 10^{-2}$	A_{03}	$2.008 \cdot 10^{-6}$
C_{03}	$3.3432 \cdot 10^{-4}$	A_{04}	$-3.21 \cdot 10^{-8}$
C_{04}	$-1.47797 \cdot 10^{-6}$	A_{10}	$9.4742 \cdot 10^{-5}$
C_{05}	$3.1419 \cdot 10^{-9}$	A_{11}	$-1.2583 \cdot 10^{-5}$
C_{10}	0.153563	A_{12}	$-6.4928 \cdot 10^{-8}$
C_{11}	$6.8999 \cdot 10^{-4}$	A_{13}	$1.0515 \cdot 10^{-8}$
C_{12}	$-8.1829 \cdot 10^{-6}$	A_{14}	$-2.0142 \cdot 10^{-10}$
C_{13}	$1.3632 \cdot 10^{-7}$	A_{20}	$-3.9064 \cdot 10^{-7}$
C_{14}	$-6.1260 \cdot 10^{-10}$	A_{21}	$9.1061 \cdot 10^{-9}$
C_{15}	0	A_{22}	$-1.6009 \cdot 10^{-10}$
C_{20}	$3.1260 \cdot 10^{-5}$	A_{23}	$7.994 \cdot 10^{-12}$
C_{21}	$-1.7111 \cdot 10^{-6}$	A_{30}	$1.100 \cdot 10^{-10}$
C_{22}	$2.5986 \cdot 10^{-8}$	A_{31}	$6.651 \cdot 10^{-12}$
C_{23}	$-2.5353 \cdot 10^{-10}$	A_{32}	$-3.931 \cdot 10^{-13}$
C_{24}	$1.0415 \cdot 10^{-12}$	A_{33}	0
C_{25}	0	A_{34}	0
C_{30}	$-9.7729 \cdot 10^{-9}$	A_{24}	0
C_{31}	$3.8513 \cdot 10^{-10}$	B_{00}	$-1.922 \cdot 10^{-2}$
C_{32}	$-2.3654 \cdot 10^{-12}$	B_{01}	$-4.42 \cdot 10^{-5}$
C_{33}	0	B_{10}	$7.3637 \cdot 10^{-5}$
C_{34}	0	B_{11}	$1.7950 \cdot 10^{-7}$
C_{35}	0	D_{00}	$1.727 \cdot 10^{-3}$
A_{00}	1.389	D_{10}	$-7.9836 \cdot 10^{-6}$

APPENDIX III
PROOF OF MMSE ALGORITHM

Here we show the validity of Eq. (35) exploiting the conditional independence of sensors decision in time:

$$
\begin{aligned}
&\boldsymbol{x}^{(\text{mmse})}[n] = \mathbb{E}\left(\boldsymbol{\theta}|\boldsymbol{d}[n],\dots,\boldsymbol{d}[1],\mathcal{H}_1\right)\\
&= \int p(\boldsymbol{\theta}|\boldsymbol{d}[n],\dots,\boldsymbol{d}[1],\mathcal{H}_1)\boldsymbol{\theta}\,\mathrm{d}\boldsymbol{\theta}\\
&= \int \frac{p(\boldsymbol{d}[n],\dots,\boldsymbol{d}[1]|\boldsymbol{\theta},\mathcal{H}_1)p(\boldsymbol{\theta}|\mathcal{H}_1)}{p(\boldsymbol{d}[n],\dots,\boldsymbol{d}[1]|\mathcal{H}_1)}\boldsymbol{\theta}\,\mathrm{d}\boldsymbol{\theta}\\
&= \frac{\int p(\boldsymbol{d}[n],\dots,\boldsymbol{d}[1]|\boldsymbol{\theta},\mathcal{H}_1)p(\boldsymbol{\theta}|\mathcal{H}_1)\boldsymbol{\theta}\,\mathrm{d}\boldsymbol{\theta}}{\int p(\boldsymbol{d}[n],\dots,\boldsymbol{d}[1]|\boldsymbol{\theta},\mathcal{H}_1)p(\boldsymbol{\theta}|\mathcal{H}_1)\,\mathrm{d}\boldsymbol{\theta}}\\
&= \frac{\sum_{m=1}^{M}\Pr(\boldsymbol{d}[n],\dots,\boldsymbol{d}[1]|\boldsymbol{\theta}=\boldsymbol{h}_m,\mathcal{H}_1)\Pr(\boldsymbol{\theta}=\boldsymbol{h}_m|\mathcal{H}_1)\boldsymbol{h}_m}{\sum_{m=1}^{M}\Pr(\boldsymbol{d}[n],\dots,\boldsymbol{d}[1]|\boldsymbol{\theta}=\boldsymbol{h}_m,\mathcal{H}_1)\Pr(\boldsymbol{\theta}=\boldsymbol{h}_m|\mathcal{H}_1)}\\
&= \frac{\left(\prod_{i=1}^{n}c_i^{-1}\right)\sum_{m=1}^{M}\left(\prod_{i=1}^{n}\Pr(\boldsymbol{d}[i]|\boldsymbol{\theta}=\boldsymbol{h}_m,\mathcal{H}_1)\right)\varphi_m\boldsymbol{h}_m}{\left(\prod_{i=1}^{n}c_i^{-1}\right)\sum_{m=1}^{M}\left(\prod_{i=1}^{n}\Pr(\boldsymbol{d}[i]|\boldsymbol{\theta}=\boldsymbol{h}_m,\mathcal{H}_1)\right)\varphi_m}\\
&= \frac{\sum_{m=1}^{M}c_n^{-1}\Pr(\boldsymbol{d}[n]|\boldsymbol{\theta}=\boldsymbol{h}_m,\mathcal{H}_1)\tilde{\alpha}_m[n-1]\boldsymbol{h}_m}{\sum_{m=1}^{M}c_n^{-1}\Pr(\boldsymbol{d}[n]|\boldsymbol{\theta}=\boldsymbol{h}_m,\mathcal{H}_1)\tilde{\alpha}_m[n-1]}\\
&= \frac{\sum_{m=1}^{M}\tilde{\alpha}_m[n]\boldsymbol{h}_m}{\sum_{m=1}^{M}\tilde{\alpha}_m[n]}\,,
\end{aligned}
$$

where

$$
\begin{aligned}
&p(\boldsymbol{d}[n],\dots,\boldsymbol{d}[1]|\boldsymbol{\theta},\mathcal{H}_1)\\
&= \sum_{m=1}^{M}\Pr(\boldsymbol{d}[n],\dots,\boldsymbol{d}[1]|\boldsymbol{\theta}=\boldsymbol{h}_m,\mathcal{H}_1)\delta(\boldsymbol{\theta}-\boldsymbol{h}_m)\,,
\end{aligned}
$$

and

$$
p(\boldsymbol{\theta}|\mathcal{H}_1) = \sum_{m=1}^{M}\Pr(\boldsymbol{\theta}=\boldsymbol{h}_m|\mathcal{H}_1)\delta(\boldsymbol{\theta}-\boldsymbol{h}_m)\,.
$$

APPENDIX IV
DERIVATION OF THE CRAMÉR-RAO LOWER BOUND

We derive the CRLB of an estimator $\widehat{\boldsymbol{\theta}}$ that follows a perfect detector ($\overline{Q_D}=1$, $Q_F=0$). In agreement with the case study, we consider $\boldsymbol{\theta}$, $\boldsymbol{s}_k$, $\boldsymbol{h_m} \in \mathbb{R}^2$, $\forall k = 1,\dots,K$ and $\forall\, m = 1,\dots,M$, although the procedure is analogous for the case of vectors belonging to $\mathbb{R}^3$.

The CRLB, for each component of $\widehat{\boldsymbol{\theta}} = \begin{bmatrix}\widehat{\theta}_1 & \widehat{\theta}_2\end{bmatrix}^T$, is based on the Fisher Information Matrix (FIM) $\boldsymbol{I}(\boldsymbol{\theta})$:

$$
CRLB\left(\widehat{\theta}_i\right) = \left[\boldsymbol{I}(\boldsymbol{\theta})\right]^{-1}_{ii}\,. \tag{38}
$$

The FIM is obtained exploiting its additive property for independent observations in space and time, i.e.

$$
\boldsymbol{I}(\boldsymbol{\theta}) = N\sum_{k=1}^{K}\boldsymbol{I}_k(\boldsymbol{\theta})\,, \tag{39}
$$

where $\boldsymbol{I}_k(\boldsymbol{\theta})$ is the FIM with respect to the local decisions of the kth sensor at the generic instant n, and N is the number of instants since the spill occurred (i.e. the number of performed estimations). The expression of $\boldsymbol{I}_k(\boldsymbol{\theta})$ is obtained as follows:

$$
\begin{aligned}
\boldsymbol{I}_k(\boldsymbol{\theta}) =& \mathbb{E}_{d_k[n]|\mathcal{H}_1}\left[\left(\frac{\partial \ln p(d_k[n]|\mathcal{H}_1;\boldsymbol{\theta})}{\partial\boldsymbol{\theta}}\right)\right.\\
&\left.\times\left(\frac{\partial \ln p(d_k[n]|\mathcal{H}_1;\boldsymbol{\theta})}{\partial\boldsymbol{\theta}}\right)^T\right]\,,
\end{aligned}
$$

where

$$
\begin{aligned}
\frac{\partial \ln p(d_k[n]|\mathcal{H}_1;\boldsymbol{\theta})}{\partial\boldsymbol{\theta}} =& \frac{\partial}{\partial\boldsymbol{\theta}}\ln\left({P_{D,k}}^{d_k[n]}(1-P_{D,k})^{1-d_k[n]}\right)\\
=& \frac{d_k[n]-P_{D,k}}{P_{D,k}(1-P_{D,k})}\frac{\partial P_{D,k}}{\partial\boldsymbol{\theta}}\,,
\end{aligned}
$$

and, using the definition of $P_{D,k}$ in Eq. (5),

$$
\begin{aligned}
\frac{\partial P_{D,k}}{\partial\boldsymbol{\theta}} =& p_{\mathcal{N}(0,1)}\left(\sqrt{\frac{\tau_k}{\sigma_\xi^2 g^2(u)+\sigma_w^2}}\right)\\
&\times\frac{\sigma_\xi^2\sqrt{\tau_k}}{\left[\sigma_\xi^2 g^2(u)+\sigma_w^2\right]^{3/2}}\frac{\partial\left(g^2(u)\right)}{\partial\boldsymbol{\theta}}\,,
\end{aligned}
$$

with $u = \|\boldsymbol{s}_k-\boldsymbol{\theta}\|$. Also, the chain rule provides

$$
\frac{\partial\left(g^2(u)\right)}{\partial\boldsymbol{\theta}} = \frac{\partial\left(g^2(u)\right)}{\partial u}\frac{\partial u}{\partial\boldsymbol{\theta}} = \psi(u)\frac{\boldsymbol{\theta}-\boldsymbol{s}_k}{u}
$$

where, using the definition of $g(u)$ in Eq. (2),

$$
\psi(u) = \frac{\partial\left(g^2(u)\right)}{\partial u} = -\frac{{l_{\text{ref}}}^{k_{\text{sc}}}\left(k_{\text{sc}}\,10^4+\alpha\,u\ln 10\right)}{10^{[4+\alpha(u-l_{\text{ref}})10^{-4}]}\,u^{k_{\text{sc}}+1}}\,.
$$

Combining the previous expressions, we get

$$\frac{\partial \ln p(d_k[n]|\mathcal{H}_1;\boldsymbol{\theta})}{\partial \boldsymbol{\theta}} = \frac{d_k[n]-P_{D,k}}{P_{D,k}(1-P_{D,k})} \times p_{\mathcal{N}(0,1)}\left(\sqrt{\frac{\tau_k}{\sigma_\xi^2 g^2(u)+\sigma_w^2}}\right) \times \frac{\psi(u)\sigma_\xi^2\sqrt{\tau_k}}{u\left[\sigma_\xi^2 g^2(u)+\sigma_w^2\right]^{3/2}}(\boldsymbol{\theta}-\boldsymbol{s}_k)\ ,$$

and then

$$\boldsymbol{I}_k(\boldsymbol{\theta}) = \frac{p^2_{\mathcal{N}(0,1)}\left(\sqrt{\frac{\tau_k}{\sigma_\xi^2 g^2(u)+\sigma_w^2}}\right)}{{P_{D,k}}^2(1-P_{D,k})^2} \frac{\psi^2(u)\sigma_\xi^4\tau_k}{u^2\left[\sigma_\xi^2 g^2(u)+\sigma_w^2\right]^3} \times (\boldsymbol{\theta}-\boldsymbol{s}_k)(\boldsymbol{\theta}-\boldsymbol{s}_k)^T\ , \quad (40)$$

where the expectation has been calculated with the knowledge that $d_k[n]|\mathcal{H}_1 \sim \mathcal{B}(P_{D,k})$. Finally, replacing Eq. (40) into Eq. (39), we get the CRLB via Eq. (38).

REFERENCES

[1] H. Fang and M. Duan, *Offshore Operation Facilities: Equipment and Procedures*. Elsevier Science, 2014.

[2] Y. Bai and Q. Bai, *Subsea Engineering Handbook*. Houston, TX: Elsevier, 2012.

[3] F. Pallavicini, "Developement of offshore fields," in *Encyclopaedia of Hydrocarbons Volume 1 - Exploration, Production and Transport*. Rome, Italy: Treccani, 2005, ch. 5.2, pp. 609–628.

[4] C. Mai, S. Pedersen, L. Hansen, K. L. Jepsen, and Zhenyu Yang, "Subsea infrastructure inspection: A review study," in *2016 IEEE International Conference on Underwater System Technology: Theory and Applications (USYS)*, Penang, Malaysia, 2016, pp. 71–76.

[5] N. Paltrinieri, F. Khan, P. Amyotte, and V. Cozzani, "Dynamic approach to risk management: Application to the Hoeganaes metal dust accidents," *Process Saf. Environ. Protect.*, vol. 92, no. 6, pp. 669–679, Nov. 2014.

[6] V. Villa, N. Paltrinieri, F. Khan, and V. Cozzani, "Towards dynamic risk analysis: A review of the risk assessment approach and its limitations in the chemical process industry," *Saf. Sci.*, vol. 89, pp. 77–93, Nov. 2016.

[7] T. Grøtan and N. Paltrinieri, "Dynamic risk management in the perspective of a resilient system," in *Dynamic Risk Analysis in the Chemical and Petroleum Industry*. Elsevier, 2016, pp. 245–257.

[8] N. Paltrinieri, L. Comfort, and G. Reniers, "Learning about risk: Machine learning for risk assessment," *Saf. Sci.*, vol. 118, pp. 475–486, 2019.

[9] M. A. Adegboye, W. K. Fung, and A. Karnik, "Recent advances in pipeline monitoring and oil leakage detection technologies: Principles and approaches," *Sensors*, vol. 19, no. 11, 2019.

[10] U. Baroudi, A. A. Al-Roubaiey, and A. Devendiran, "Pipeline leak detection systems and data fusion: A survey," *IEEE Access*, vol. 7, pp. 97 426–97 439, 2019.

[11] DNV-GL, "Recommended practice RP-F302 offshore leak detection," Apr. 2016.

[12] H. Fuchs and R. Riehle, "Ten years of experience with leak detection by acoustic signal analysis," *Appl. Acoust.*, vol. 33, no. 1, pp. 1–19, 1991.

[13] E. G. Eckert, J. W. Maresca, R. W. Hillger, and J. J. Yezzi, "Location of leaks in pressurized petroleum pipelines by means of passive-acoustic sensing methods," in *Leak Detection for Underground Storage Tanks*, P. Durgin and T. Young, Eds. West Conshohocken, PA: ASTM International, 1993, pp. 53–69.

[14] J. Li, C. Wang, Q. Zheng, and Z. Qian, "Leakage localization for long distance pipeline based on compressive sensing," *IEEE Sens. J.*, vol. 19, no. 16, pp. 6795–6801, 2019.

[15] M. Meribout, "A wireless sensor network-based infrastructure for real-time and online pipeline inspection," *IEEE Sens. J.*, vol. 11, no. 11, pp. 2966–2972, 2011.

[16] T. R. Sheltami, A. Bala, and E. M. Shakshuki, "Wireless sensor networks for leak detection in pipelines: a survey," *J. Ambient Intell. Humaniz. Comput.*, vol. 7, no. 3, pp. 347–356, Jun. 2016.

[17] N. Paltrinieri, G. Landucci, and P. Salvo Rossi, "An integrated approach to support the dynamic risk assessment of complex industrial accidents," *Chem. Eng. Trans.*, vol. 77, pp. 265–270, 2019.

[18] M. Bucelli, I. B. Utne, P. Salvo Rossi, and N. Paltrinieri, "A system engineering approach to subsea spill risk management," *Saf. Sci.*, vol. 123, 2020.

[19] M. R. Akhondi, A. Talevski, S. Carlsen, and S. Petersen, "Applications of wireless sensor networks in the oil, gas and resources industries," in *2010 24th IEEE International Conference on Advanced Information Networking and Applications*, Perth, Australia, 2010, pp. 941–948.

[20] P. K. Varshney, *Distributed Detection and Data Fusion*. New York, NY: Springer-Verlag, 1997.

[21] A. Shoari, G. Mateos, and A. Seyedi, "Analysis of target localization with ideal binary detectors via likelihood function smoothing," *IEEE Signal Process. Lett.*, vol. 23, no. 5, pp. 737–741, May 2016.

[22] Z. Chair and P. K. Varshney, "Optimal data fusion in multiple sensor detection systems," *IEEE Trans. Aerosp. Electron. Syst.*, vol. AES-22, no. 1, pp. 98–101, Jan. 1986.

[23] R. Niu, P. K. Varshney, and Q. Cheng, "Distributed detection in a large wireless sensor network," *Inf. Fusion*, p. 15, 2006.

[24] B. Chen, R. Jiang, T. Kasetkasem, and P. Varshney, "Channel aware decision fusion in wireless sensor networks," *IEEE Trans. Signal Process.*, vol. 52, no. 12, pp. 3454–3458, Dec. 2004.

[25] X. Wang, G. Li, and P. K. Varshney, "Distributed detection of weak signals from one-bit measurements under observation model uncertainties," *IEEE Signal Process. Lett.*, vol. 26, no. 3, pp. 415–419, Mar. 2019.

[26] D. Ciuonzo, G. Papa, G. Romano, P. Salvo Rossi, and P. Willett, "One-bit decentralized detection with a rao test for multisensor fusion," *IEEE Signal Process. Lett.*, vol. 20, no. 9, pp. 861–864, Sep. 2013.

[27] D. Ciuonzo, P. Salvo Rossi, and P. Willett, "Generalized rao test for decentralized detection of an uncooperative target," *IEEE Signal Process. Lett.*, vol. 24, no. 5, pp. 678–682, May 2017.

[28] D. Ciuonzo and P. Salvo Rossi, "Distributed detection of a non-cooperative target via generalized locally-optimum approaches," *Inf. Fusion*, vol. 36, pp. 261–274, 2017.

[29] D. Ciuonzo, G. Romano, and P. Salvo Rossi, "Channel-aware decision fusion in distributed MIMO wireless sensor networks: Decode-and-fuse vs. decode-then-fuse," *IEEE Trans. Wirel. Commun.*, vol. 11, no. 8, pp. 2976–2985, 2012.

[30] P. Salvo Rossi, D. Ciuonzo, T. Ekman, and H. Dong, "Energy detection for MIMO decision fusion in underwater sensor networks," *IEEE Sens. J.*, vol. 15, no. 3, pp. 1630–1640, 2015.

[31] P. Salvo Rossi, D. Ciuonzo, K. Kansanen, and T. Ekman, "Performance analysis of energy detection for MIMO decision fusion in wireless sensor networks over arbitrary fading channels," *IEEE Trans. Wirel. Commun.*, vol. 15, no. 11, pp. 7794–7806, 2016.

[32] A. Shoari and A. Seyedi, "Localization of an uncooperative target with binary observations," in *2010 IEEE 11th International Workshop on Signal Processing Advances in Wireless Communications (SPAWC)*, Marrakech, Morocco, Jun. 2010, pp. 1–5.

[33] J. Zhao, Q. Zhao, Z. Li, and Y. Liu, "An improved weighted centroid localization algorithm based on difference of estimated distances for wireless sensor networks," *Telecommun. Syst.*, vol. 53, no. 1, pp. 25–31, May 2013.

[34] Q. Dong and X. Xu, "A novel weighted centroid localization algorithm based on RSSI for an outdoor environment," *J. Commun*, vol. 9, no. 3, pp. 279–285, 2014.

[35] S. Durocher and D. Kirkpatrick, "The Steiner centre of a set of points: Stability, eccentricity, and applications to mobile facility locations," *Int. J. Comput. Geom. Appl.*, vol. 16, no. 04, pp. 345–371, Aug. 2006.

[36] Q. Zhou, X. Li, and Y. Xu, "Smallest enclosing circle based localization approach for wireless sensor networks," in *2009 WRI International Conference on Communications and Mobile Computing*. Kunming, Yunnan, China: IEEE, Jan. 2009, pp. 61–65.

[37] A. Vempaty, H. He, B. Chen, and P. K. Varshney, "On quantizer design for distributed bayesian estimation in sensor networks," *IEEE Trans. Signal Process.*, vol. 62, no. 20, pp. 5359–5369, Oct. 2014.

[38] A. Kose and E. Masazade, "A multiobjective optimization approach for adaptive binary quantizer design for target tracking in wireless sensor networks," in *2015 IEEE International Conference on Multisensor Fusion and Integration for Intelligent Systems (MFI)*, San Diego, CA, USA, Sep. 2015, pp. 31–36.

[39] D. Ciuonzo and P. Salvo Rossi, "Quantizer design for generalized locally optimum detectors in wireless sensor networks," *IEEE Wireless Commun. Lett.*, vol. 7, no. 2, pp. 162–165, Apr. 2018.

[40] J. Fang, Y. Liu, H. Li, and S. Li, "One-bit quantizer design for multisensor GLRT fusion," *IEEE Signal Process. Lett.*, vol. 20, no. 3, pp. 257–260, Mar. 2013.

[41] S. Kar, H. Chen, and P. K. Varshney, "Optimal identical binary quantizer design for distributed estimation," *IEEE Trans. Signal Process.*, vol. 60, no. 7, pp. 3896–3901, Jul. 2012.

[42] G. Tabella, N. Paltrinieri, V. Cozzani, and P. Salvo Rossi, "Data fusion for subsea oil spill detection through wireless sensor networks," in *2020 IEEE SENSORS*. Rotterdam, The Netherlands: IEEE, Oct. 2020.

[43] ——, "Subsea oil spill risk management based on sensor networks," *Chem. Eng. Trans.*, vol. 82, pp. 199–204, Oct. 2020.

[44] W. H. Thorp, "Analytic description of the low-frequency attenuation coefficient," *J. Acoust. Soc. Am.*, vol. 42, no. 1, pp. 270–270, 1967.

[45] M. Schulkin and H. W. Marsh, "Sound absorption in sea water," *J. Acoust. Soc. Am.*, vol. 34, no. 6, pp. 864–865, 1962.

[46] F. H. Fisher and V. P. Simmons, "Sound absorption in sea water," *J. Acoust. Soc. Am.*, vol. 62, no. 3, pp. 558–564, 1977.

[47] M. A. Ainslie and J. G. McColm, "A simplified formula for viscous and chemical absorption in sea water," *J. Acoust. Soc. Am.*, vol. 103, no. 3, pp. 1671–1672, 1998.

[48] R. E. Francois and G. R. Garrison, "Sound absorption based on ocean measurements: Part I: Pure water and magnesium sulfate contributions," *J. Acoust. Soc. Am.*, vol. 72, no. 3, pp. 896–907, 1982.

[49] ——, "Sound absorption based on ocean measurements. part II: Boric acid contribution and equation for total absorption," *J. Acoust. Soc. Am.*, vol. 72, no. 6, pp. 1879–1890, Dec. 1982.

[50] P. C. Etter, *Underwater Acoustic Modeling and Simulation*, 5th ed. CRC Press, 2018.

[51] H. Medwin, "Speed of sound in water: A simple equation for realistic parameters," *J. Acoust. Soc. Am.*, vol. 58, no. 6, pp. 1318–1319, 1975.

[52] K. V. Mackenzie, "Nine-term equation for sound speed in the oceans," *J. Acoust. Soc. Am.*, vol. 70, no. 3, pp. 807–812, 1981.

[53] V. A. Del Grosso, "New equation for the speed of sound in natural waters (with comparisons to other equations)," *J. Acoust. Soc. Am.*, vol. 56, no. 4, pp. 1084–1091, 1974.

[54] C. Chen and F. J. Millero, "Speed of sound in seawater at high pressures," *J. Acoust. Soc. Am.*, vol. 62, no. 5, pp. 1129–1135, 1977.

[55] F. J. Millero and X. Li, "Comments on "on equations for the speed of sound in seawater" [J. Acoust. Soc. Am. 93, 255–275 (1993)]," *J. Acoust. Soc. Am.*, vol. 95, no. 5, pp. 2757–2759, 1994.

[56] G. S. K. Wong and S. Zhu, "Speed of sound in seawater as a function of salinity, temperature, and pressure," *J. Acoust. Soc. Am.*, vol. 97, no. 3, pp. 1732–1736, 1995.

[57] S. Kay, *Fundamentals of Statistical Signal Processing: Detection theory*, 1st ed., ser. Prentice Hall Signal Processing Series. Upper Saddle River, NJ: Prentice-Hall PTR, 1998.

[58] W. J. Youden, "Index for rating diagnostic tests," *Cancer*, vol. 3, pp. 32–35, 1950.

[59] H. V. Poor and O. Hadjiliadis, *Quickest Detection*. Cambridge University Press, 2008.

[60] E. Bjørnbom, "Goliat – leak detection and monitoring from template to satellite," Available at https://www.norskoljeoggass.no/globalassets/dokumenter/drift/presentasjonerarrangementer/subsea-leak-detection--2011/4.-enino_n1862090_v1_eni_presentation_-_olf_seminar_-_subsea_leak_detection_-_03_november_2011.pdf (2020/12/29), 2011.

[61] E. Røsby, "Goliat development project - subsea leak detection design," Available at https://www.norskoljeoggass.no/globalassets/dokumenter/drift/presentasjonerarrangementer/subsea-leak-detection--2011/15.-goliat-development-project_subsea_leak_detection_3_nov_2011_elling-rosby.pdf (2020/12/29), 2011.

[62] SINTEF, *OREDA Offshore Reliability Data Handbook*, 4th ed. OREDA Participants, 2002.

[63] Institute of Marine Research, "Mareano," Available at http://www.mareano.no/kart (2020/09/09).

[64] A. A. Vetrov and E. A. Romankevich, *Carbon Cycle in the Russian Arctic Seas*. Springer Berlin Heidelberg, 2004.

[65] M. Stojanovic, "On the relationship between capacity and distance in an underwater acoustic communication channel," in *Proceedings of the 1st ACM international workshop on Underwater networks - WUWNet '06*. ACM Press, 2006.

Gianluca Tabella (GS'20) was born in Suzzara, Italy in 1993. He received the B.Sc. degree in chemical and biochemical engineering (with specialization in process engineering) and the M.Sc. degree in chemical and process engineering (with specialization in offshore engineering) from the University of Bologna, Italy, in 2017 and 2019, respectively. He carried out his master's thesis at the Dept. Mechanical and Industrial Engineering, Norwegian University of Science and Technology (NTNU), Norway.

Since 2020, he has been working towards the Ph.D. degree in electronics and telecommunications at the Dept. Electronic Systems, NTNU, Norway within the signal processing research group. His research interests are in distributed detection and localization for safety and risk analysis with a focus on industrial and Oil&Gas applications.

Nicola Paltrinieri received the B.Sc. degree in chemical engineering, the M.Sc. degree (*summa cum laude*) in chemical and process engineering and the Ph.D. degree in environmental, safety and chemical engineering from the University of Bologna, Italy, in 2005, 2008 and 2012, respectively. From 2012 to 2016 he was research scientist at the Dept. Safety Research, SINTEF Technology and Society (Norway) and in 2012 he held a postdoctoral position at the University of Bologna. He is Associate Professor of risk analysis at the Norwegian University of Science and Technology (NTNU), Norway, and Adjunct Professor in offshore HSE management at the University of Bologna, Italy, since 2016. His research focuses on both the method and the application of risk analysis within socio-technical systems. Regarding the former, he has investigated the concepts and techniques supporting dynamic risk analysis, from uncertainty to machine learning. Regarding the latter, he has worked on risk analysis for safety-critical emerging technologies (e.g. hydrogen technologies). Prof. Paltrinieri is chartered engineer in the British Engineering Council register and charted scientist in the British Science Council register. He serves as associate editor of the journal Safety Science. He is member of the editorial boards of the Journal of Marine Science and Engineering, Journal of Risk Research and Safety in Extreme Environments. He is member of the board of the NTNU Team Hydrogen. He is member of the board and treasurer of the Society of Risk Analysis – Europe. He serves as Norwegian delegate of the Working Party on Loss Prevention and Safety Promotion within the European Federation of Chemical Engineering. He is co-chair on Accident and Incident modelling, European Safety and Reliability Association Technical Committee. He serves as member of the scientific committees for the ESREL, Loss Prevention and CISAP conferences since 2016.

Valerio Cozzani received the M.Sc. degree (*cum laude*) and the Ph.D. degree in chemical engineering from the University of Pisa, Italy, in 1992 and 1997, respectively. From 1995 to 1996 he was Visiting Scientist at the Industrial Hazards Unit, Institute for Safety, Informatics and Systems, European Community Joint Research Centre. From 1997 to 1998 he was Research Assistant at the National Research Group on Chemical and Environmental Risk of the Italian National Research Council (CNR). From 1995 to 1996 he was Visiting Scientist at the Industrial Hazards Unit, Institute for Safety, Informatics and Systems, European Community Joint Research Centre. From 1998 to 2002 he was Lecturer at the Faculty of Engineering and member of the Dept. Chemical Engineering, University of Pisa, Italy. From 2002 to 2006 he was Associate Professor at the Faculty of Engineering and member of the Dept. Chemical Engineering, University of Bologna, Italy. Since 2006 he is Professor at the School of Engineering and member of the Dept. Civil, Chemical, Environmental and Materials Engineering, University of Bologna, Italy. At the University of Bologna he is Director of the M.Sc. in offshore engineering, leads the laboratory of industrial safety and environmental sustainability, associated to the IChemE Safety Centre, and coordinates several courses for professionals in the fields of industrial safety and design of Oil&Gas facilities. His specific research topics are: the assessment of major accidents involving dangerous substances caused by external hazard factors, cascading events and domino effects; the safety and sustainability assessment of innovative chemical processes; the safety assessment of alternative fuel systems and synthetic fuel supply chains. He chairs the ESRA Technical Committee on Chemical and Process Industry, and is the Italian Delegate in the EFCE Working Party on Loss Prevention in the Process Industry. He serves as Associate Editor for Safety Science, and as member of the Editorial Board for Elsevier publications on chemical engineering, for the Journal of Hazardous Materials and the Journal of Loss Prevention in the Process Industry. He serves as member of the scientific committees of ESREL conferences since 2008, and chairs the scientific committee of CISAP conferences since 2012.

Pierluigi Salvo Rossi (SM'11) was born in Naples, Italy, in 1977. He received the Dr.Eng. degree (*summa cum laude*) in telecommunications engineering and the Ph.D. degree in computer engineering from the University of Naples "Federico II", Italy, in 2002 and 2005, respectively. He held visiting appointments at the Dept. Electrical and Computer Engineering, Drexel University, USA; at the Dept. Electrical and Information Technology, Lund University, Sweden; at the Dept. Electronics and Telecommunications, Norwegian University of Science and Technology (NTNU), Norway; and at the Excellence Center for Wireless Sensor Networks, Uppsala University, Sweden. From 2005 to 2008, he held postdoctoral positions with the Dept. Computer Science and Systems, University of Naples "Federico II", Italy; with the Dept. Information Engineering, Second University of Naples, Italy; and with the Dept. Electronics and Telecommunications, NTNU, Norway. From 2008 to 2014, he was an Assistant Professor (tenured in 2011) in telecommunications with the Dept. Industrial and Information Engineering, Second University of Naples, Italy. From 2014 to 2016, he was an Associate Professor in signal processing with the Dept. Electronics and Telecommunications, NTNU, Norway. From 2016 to 2017, he was a Full Professor in signal processing with the Dept. Electronic Systems, NTNU, Norway. From 2017 to 2019, he was a Principal Engineer with the Dept. Advanced Analytics and Machine Learning, Kongsberg Digital AS, Norway. Since 2019, he has been a Full Professor of statistical machine learning with the Dept. Electronic Systems, NTNU, Norway, and also the Director of IoT@NTNU. Since 2021, he is also a (part-time) Research Scientist with the Department of Gas Technology, SINTEF Energy Research, Norway. His research interests fall within the areas of communication theory, data fusion, machine learning, and signal processing. He serves as an Executive Editor for the IEEE Communications Letters since 2019, an Area Editor for the IEEE Open Journal of the Communications Society since 2019, an Associate Editor for the IEEE Transactions on Signal and Information Processing over Networks since 2019, an Associate Editor for the IEEE Sensors Journal since 2021. He was an Associate Editor of the IEEE Transactions on Wireless Communications from 2015 to 2020, a Senior Editor from 2016 to 2019 and an Associate Editor from 2012 to 2016 of the IEEE Communications Letters. He was awarded as an Exemplary Senior Editor of the IEEE Communications Letters in 2018.

Paper 4

Spatio-Temporal Decision Fusion for
Quickest Fault Detection Within Industrial Plants:
The Oil and Gas Scenario

G. Tabella, D. Ciuonzo, N. Paltrinieri, and P. Salvo Rossi

presented at the *IEEE 24th International Conference on Information Fusion*,
Sun City, South Africa, Nov. 2021.

Spatio-Temporal Decision Fusion for Quickest Fault Detection Within Industrial Plants: The Oil and Gas Scenario

Gianluca Tabella*, Domenico Ciuonzo†, Nicola Paltrinieri‡, Pierluigi Salvo Rossi*§
*Dept. Electronic Systems, Norwegian University of Science and Technology, Trondheim, Norway
†Dept. Electrical Engineering and Information Technologies (DIETI), University of Naples "Federico II", Naples, Italy
‡Dept. Mechanical and Industrial Engineering, Norwegian University of Science and Technology, Trondheim, Norway
§Dept. Gas Technology, SINTEF Energy Research, Norway
Email: gianluca.tabella@ntnu.no; domenico.ciuonzo@unina.it; nicola.paltrinieri@ntnu.no; salvorossi@ieee.org

***Abstract*—In this work, we present a spatio-temporal decision fusion approach aimed at performing quickest detection of faults within an Oil and Gas subsea production system. Specifically, a sensor network collectively monitors the state of different pieces of equipment and reports the collected decisions to a fusion center. Therein, a spatial aggregation is performed and a global decision is taken. Such decisions are then aggregated in time by a post-processing center, which performs quickest detection of system fault according to a Bayesian criterion which exploits change-time statistical distributions originated by system components' datasheets. The performance of our approach is analyzed in terms of both detection- and reliability-focused metrics, with a focus on (fast & inspection-cost-limited) leak detection in a real-world oil platform located in the Barents Sea.**

***Index Terms*—data fusion, distributed detection, maintenance, monitoring, reliability, wireless sensor network.**

I. Introduction

THE last decade has seen the growth of Wireless Sensor Networks (WSNs) and their use in monitoring applications. In particular, the task of event detection and localization has received large attention, especially in relation to the design of barriers for safety-critical systems. WSNs are usually made of low-cost devices having the task of monitoring the surrounding environment. In order to lower communication and processing costs, the sensors are often designed to transmit binary decisions to a Fusion Center (FC), which has the task to collect the local decisions and formulate a global decision on whether the event of interest is occurring. When an adverse event is detected, the FC produces an alarm so that proper actions can be taken to mitigate the event's consequences.

This scenario particularly applies to the process, energy, and manufacturing industry, where the failure of a piece of equipment could compromise the safety of the workers and the environment. Indeed, this may result in high costs as well as missed revenues due to unplanned shutdowns [1].

This research is a part of BRU21 – NTNU Research and Innovation Program on Digital and Automation Solutions for the Oil and Gas Industry (www.ntnu.edu/bru21).

Event detection via WSNs for industrial applications has been an object of study and many architectures have been analyzed and proposed, lately with a focus on underwater environments [2], [3]. One of the vital issues of the industry is the detection of equipment failures that can lead to dangerous losses of containment, especially in those environments where inspections are highly costly.

Various algorithms for detection of non-cooperative targets via distributed WSNs are presented in [4], where the Generalized Likelihood Ratio Test (GLRT), the Bayesian approach, and a hybrid GLRT/Bayesian detector are used to approach the problem. In [5] the sub-optimal *Counting Rule* (CR) is extended with an ordering-based where highly-informative sensors have a higher priority in the transmission to the FC, showing the same performances as the classical CR with fewer transmissions. In [6], the CR is applied to the case of radiation detection, while in [7], [8] the same rule is employed for subsea oil spill detection. In [9], [10] the work is extended including a modified version of the *Chair-Varshney Rule* incorporating in the design of the WSN the positions and the failure rates of those items susceptible to failure.

Nevertheless, no approach has been provided that successfully incorporates information on the reliability of the monitored system in the design of the detection algorithm. Such information is often available and regards critical items whose failure is to be detected exploiting their emitted signal. Data such as positions, failure rates, and failure models constitute prior information that can be embodied in a Bayesian framework.

Accordingly, the *main contributions* of this work are summarized as follows. We propose a spatio-temporal decision fusion approach aimed at performing quickest detection of faults within a critical system. More specifically, a sensor network collectively monitors the state of different pieces of equipment and reports their decisions to a FC. Herein, a *spatial aggregation* is performed and an optimal per-sample decision is performed. Such decisions are then aggregated *in time* by a Post-Processing Center (PPC), which performs quickest detection of faulty system according to a Bayesian criterion and

exploits change-time statistical distributions driven by system components' datasheets. The separation between the FC and PPC allows for system modularity and implementation of the two components via appealing edge-cloud architectures [11]. The results of the proposed approach are analyzed focusing on a real Oil and Gas setup, namely the Goliat FPSO oil production system. Results, both in terms of (i) detection and (ii) reliability-focused metrics, highlight the appeal of the proposed approach and the additional benefit of temporal aggregation (as opposed to the sole spatial aggregation).

The rest of the manuscript is organized as follows. Sec. II describes the system model considered, whereas Sec. III introduces the proposed decision fusion approach for quickest fault detection. Our approach is then numerically validated on a real case study in Sec. IV. Finally, Sec. V ends the paper with some pointers to future directions of research.

Notation – vectors are denoted with bold letters; $(\cdot)^T$, and $\|\cdot\|$ denote transpose and Euclidean norm operators, respectively; $\hat{a}$, $\mathbb{E}\{a\}$, and $\mathbb{E}\{a|b\}$ denote an estimate of the random variable a, its expectation, and its conditional expectation given the random variable b, respectively; $\Pr(\cdot)$ and $p(\cdot)$ denote probability mass functions (pmfs) and probability density functions (pdfs), while $\Pr(\cdot|\cdot)$ and $p(\cdot|\cdot)$ their corresponding conditional counterparts; $\mathcal{N}(\mu, \sigma^2)$ denotes a Gaussian distribution with mean μ and variance σ^2; $\mathcal{Q}(\cdot)$ is the complementary cumulative distribution function (ccdf) of the standard normal distribution; $\text{Exp}(\lambda)$ denotes an exponential distribution with rate λ; $\text{Gamma}(\alpha, \beta)$ denotes a Gamma distribution with shape α and rate β; the symbol $\sim$ means "distributed as".

II. System Model

A. Failure Model

The monitored system consists of $m = 1, 2, \ldots, M$ points, with mth point located at position $\boldsymbol{h}_m$. These points are *items* (pieces of equipment at locations of interest) and their individual state at time t is described via the following variable:

$$\mathcal{H}_m(t) = \begin{cases} 0, & m\text{th item in } \textbf{active} \text{ state at time } t \\ 1, & m\text{th item in } \textbf{failed} \text{ state at time } t \end{cases}, \quad (1)$$

where *active* means that the item is working the way it was intended and no action should be taken, whereas *failed* means that the item is in a condition requiring maintenance. Moreover, we define the state variable for the *entire system*:

$$\mathcal{H}(t) = 1 - \prod_{m=1}^{M} (1 - \mathcal{H}_m(t)) = \begin{cases} 0, & \text{system in } \textbf{active} \text{ state at time } t \\ 1, & \text{system in } \textbf{failed} \text{ state at time } t \end{cases}, \quad (2)$$

meaning that the system is considered in failed state when at least one of its items is in such state and that the failures are independent. An item in failed state maintains its condition until maintenance is performed. While in failed state, the item generates a signal (any significant change in a measurable variable caused by the failed state). Once the signal is detected, an inspection is performed to assess the condition of the whole system, and maintenance is eventually performed on all items in failed state.

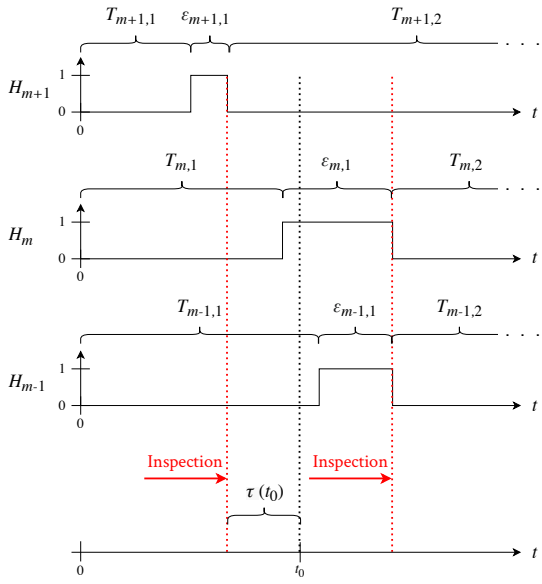

Fig. 1. Failure model (inspection and maintenance time are neglected).

The failure of the mth item is modeled as a *homogeneous Poisson process* with *failure rate* λ_m (see Fig. 1). Let us define $T_{m,j}$ as the time spent by the mth item between the $(j-1)$th and the jth failure, then $T_{m,j} \sim \text{Exp}(\lambda_m)\ \forall j \in \mathbb{N}$. In addition, we define $T^*_{m,j} \triangleq T_{m,j} + \varepsilon_{m,j}$, where $\varepsilon_{m,j}$ is the time spent before the failed state is acknowledged by an inspection. At time t, we can also define $\tau(t)$ as the amount of time since the last inspection. Because of the *memoryless property* of the homogeneous Poisson process, maintenance can be seen either as component repair or substitution. As a consequence of the failure model we can obtain its *failure function*:

$$F_m(t) = \Pr(\mathcal{H}_m(t) = 1) = 1 - e^{-\lambda_m \tau(t)}\,. \quad (3)$$

Next, we can obtain the failure function of the whole system at a given time t:

$$F(t) = \Pr(\mathcal{H}(t) = 1) = 1 - \prod_{m=1}^{M} (1 - F_m(t))\,. \quad (4)$$

Moreover, for sufficiently small λ_m's, we can simplify the model:

$$F(t) \approx \sum_{m=1}^{M} F_m(t)\,. \quad (5)$$

Such approximation implies *disjoint failures*, meaning that at any time t, *at most* one item is in failed state and will be exploited in the design of the detectors.

The exact failure rate of an item λ_m is typically *unknown*, however, estimates (average values and their variances) are usually available for categories of items. Therefore, the proposed method will treat the failure rate of each item as a random variable whose realization must be estimated within a Bayesian framework during the item lifetime.

Finally, as the system monitoring is performed at constant intervals of length Δt (except during inspection and maintenance), we generically consider the processing at nth discrete time, where $n = 1$ corresponds to the first algorithm instance since the last inspection.

B. Signal Model

When an item is in failed state, a signal is generated. Such signal is sensed by K sensors deployed in the environment. The model of the received signal $y_k[n]$ at the kth sensor during the nth discrete time is the following:

$$y_k[n] = \sum_{m=1}^{M} s_{m,k}[n] + w_k[n] \ , \tag{6}$$

where $s_{m,k}[n]$ and $w_k[n] \sim \mathcal{N}(0,\, \sigma^2_{w,k})$ represent the received signal from the mth item and the Additive White Gaussian Noise (AWGN), respectively. $s_{m,k}[n]$ and $w_k[n]$ are assumed statistically independent due to the spatial separation of the sensors. More specifically, $s_{m,k}[n]$ is assumed to have the following shape:

$$s_{m,k}[n] = \begin{cases} 0 & \text{if } \mathcal{H}_m[n] = 0 \\ \xi_m[n]\ g(\boldsymbol{x}_k, \boldsymbol{h}_m) & \text{if } \mathcal{H}_m[n] = 1 \end{cases} \ , \tag{7}$$

where $\xi_m[n] \sim \mathcal{N}(0,\, \sigma^2_{\xi,m})$ represents the emitted signal by the mth item in failed state at a reference length (ℓ_{ref}). The values of $\sigma^2_{\xi,m}$ and $\sigma^2_{w,k}$ are assumed to be *known*. Finally, $g(\boldsymbol{x}_k, \boldsymbol{h}_m)$ represents the Amplitude Attenuation Function (AAF), depending on the distance between the kth sensor position ($\boldsymbol{x}_k$) and the mth item position ($\boldsymbol{h}_m$).

It is worth noticing that the considered model can be reduced to a binary hypothesis as a consequence of the simplification introduced in Eq. (5) which excludes the possibility of more than one item to be in failed state at a given moment. Accordingly, it holds:

$$\begin{cases} \mathcal{H}[n] = 0: & y_k[n] = w_k[n] \\ \mathcal{H}[n] = 1: & y_k[n] = \xi_m[n]\ g(\boldsymbol{x}_k, \boldsymbol{h}_m) + w_k[n] \end{cases} . \tag{8}$$

Consequently, we can write the statistics of the signal:

$$\begin{cases} y_k|\mathcal{H} = 0 \ \sim \ \mathcal{N}\left(0,\, \sigma^2_{w,k}\right) \\ y_k|\mathcal{H} = 1 \ \sim \ \mathcal{N}\left(0,\, \sigma^2_{\xi,m}\, g^2(\boldsymbol{x}_k, \boldsymbol{h}_m) + \sigma^2_{w,k}\right) \end{cases} . \tag{9}$$

In both Eqs. (8) and (9), only the failure of the generic mth item can be the cause of the system being in failed state.

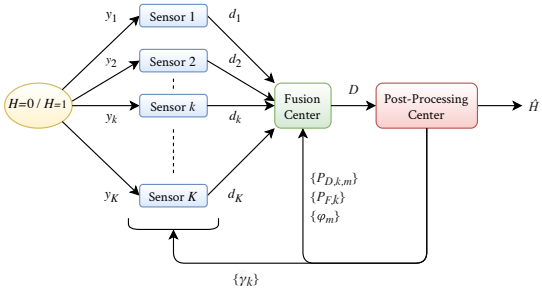

Fig. 2. Distributed Wireless Sensor Network.

C. Wireless Sensor Network Model

The proposed distributed WSN architecture (see Fig. 2) is made of K sensors, one FC, and a PPC. The sensors sense the environment at fixed time intervals of length Δt to detect whether the system is in active ($\mathcal{H}[n] = 0$) or failed ($\mathcal{H}[n] = 1$) state[1]. The kth sensor measures the signal $y_k[n]$ and individually computes a (time-dependent) decision statistic $\Lambda_{k,n}(y_k[n])$, which is then compared to a threshold $\gamma_k[n]$. The sensor takes a local decision $d_k[n] = i \in \{0, 1\}$ if $\mathcal{H}[n] = i$ is declared.

The vector of local decisions $\boldsymbol{d}[n] = \begin{bmatrix} d_1[n] & \cdots & d_K[n] \end{bmatrix}^T$ is collected and processed at the FC for a global decision $\mathcal{D}[n] = i \in \{0, 1\}$ if $\mathcal{H}[n] = i$ is declared. In addition to being spectrally efficient, as only 1-bit communication is required on the reporting channel between the sensor and the FC, such a system is highly energy-efficient when On-Off Keying (OOK) is employed for communicating the local decisions.

Both sensors and the FC perform a *Maximum Likelihood (ML) Detection* on the simplified binary hypothesis of Eq. (8), assuming no prior knowledge on the probability of the events $\mathcal{H}[n] = 0$ and $\mathcal{H}[n] = 1$, and considering every measurement statistically independent.

The PPC collects $\mathcal{D}[1], \ldots, \mathcal{D}[n]$ and integrates the knowledge of the failure model accounting for the signal model of Eq. (6) and (7), and takes a final decision $\widehat{\mathcal{H}}[n]$ through a *Maximum A-Posteriori (MAP) Detection*, with $\widehat{\mathcal{H}}[n] = 1$ triggering inspection operations. The PPC has also the task to continuously communicate to the sensors an updated value of their respective γ_k and a list of parameters necessary for the FC to perform the global detection task. Moreover, at each confirmed failure of the mth item, the PPC will generate a new estimate of λ_m for all $m = 1, \ldots, M$.

III. Proposed Reliability-Based Fusion Approach

This section describes the *three* functional blocks constituting the proposed approach. Specifically, Sec. III-A provides details for the local detection approach at each sensor, while Sec. III-B describes the fusion rule implemented at the FC,

[1]The analysis related to the sampling frequency is not considered in the present work.

implementing spatial processing. Finally, Sec. III-C describes the (a) temporal integration of FC decisions and (b) online item failure rate estimation made by the PPC.

A. Local Detection

At local and sample level, the optimal test is a Likelihood Ratio Test (LRT) associated with the binary hypothesis of Eq. (8) and based on $y_k[n]$, where the position of the failed item is marginalized by using its prior distribution. Specifically, for kth sensor at time n, it holds:

$$\Lambda_{k,n}(y_k[n]) = \frac{p(y_k[n] \,|\, \mathcal{H}[n]=1)}{p(y_k[n] \,|\, \mathcal{H}[n]=0)} \tag{10}$$
$$= \frac{\sum_{m=1}^{M} p(y_k[n]|\mathcal{H}_m[n]=1)\Pr(\mathcal{H}_m[n]=1 \,|\, \mathcal{H}[n]=1)}{p(y_k[n] \,|\, \mathcal{H}[n]=0)} ,$$

where $\Pr(\mathcal{H}_m[n]=1|\mathcal{H}[n]=1)$ is estimated exploiting the approximation in Eq. (5). Such estimate is denoted as $\varphi_m[n]$:

$$\varphi_m[n] \triangleq \Pr(\mathcal{H}_m[n]=1|\mathcal{H}[n]=1) = \frac{\Pr(\mathcal{H}_m[n]=1)}{\Pr(\mathcal{H}[n]=1)} \approx \frac{1-e^{-\widehat{\lambda}_m[n]\tau[n]}}{M-\sum_{m=1}^{M} e^{-\widehat{\lambda}_m[n]\tau[n]}} , \tag{11}$$

where $\widehat{\lambda}_m[n]$ denotes the latest available estimate of λ_m at the nth instant. Therefore, exploiting Eq. (9), we obtain the following ML Detector:

$$\Lambda_{k,n}(y_k[n]) = \sum_{m=1}^{M} \left(\varphi_m[n]\, a_{m,k}\, e^{b_{m,k}\, y_k^2[n]}\right) \underset{d_k[n]=0}{\overset{d_k[n]=1}{\gtrless}} 1 , \tag{12}$$

where

$$a_{m,k} = \sqrt{\frac{\sigma_{w,k}^2}{\sigma_{\xi,m}^2\, g^2(\boldsymbol{x}_k, \boldsymbol{h}_m) + \sigma_{w,k}^2}} , \tag{13}$$

$$b_{m,k} = \frac{1}{2}\left(\frac{1}{\sigma_{w,k}^2} - \frac{1}{\sigma_{\xi,m}^2\, g^2(\boldsymbol{x}_k, \boldsymbol{h}_m) + \sigma_{w,k}^2}\right) . \tag{14}$$

Since $\Lambda_{k,n}(y_k[n])$ in Eq. (12) is monotonically increasing in the variable $y_k^2[n]$, there exists a unique value $\gamma_k[n]$ such that:

$$\Lambda_{k,n}\left(\sqrt{\gamma_k[n]}\right) = 1 . \tag{15}$$

As a consequence, by the Karlin-Rubin Theorem, the test in Eq. (12) can be substituted with the following equivalent energy test [12]:

$$y_k^2[n] \underset{d_k[n]=0}{\overset{d_k[n]=1}{\gtrless}} \gamma_k[n] . \tag{16}$$

The task of numerically finding the value of $\gamma_k[n]$ that satisfies Eq. (15) is carried out by the PPC that continuously communicates the value of $\gamma_k[n]$ to the sensors.

For the kth sensor, the *probability of detection* ($P_{D,k,m}[n]$) when the mth item is in failed state and *probability of false alarm* ($P_{F,k}[n]$) with respect to the energy test in Eq. (16), at the nth instant, can be easily found as a consequence of Eq. (9) and are the following [13]:

$$P_{D,k,m}[n] \triangleq \Pr(d_k[n]=1|\mathcal{H}_m[n]=1) = 2\mathcal{Q}\left(\sqrt{\gamma_k[n] \Big/ \left[\sigma_{\xi,m}^2\, g^2(\boldsymbol{x}_k, \boldsymbol{h}_m) + \sigma_{w,k}^2\right]}\right) , \tag{17}$$

$$P_{F,k}[n] \triangleq \Pr(d_k[n]=1|\mathcal{H}[n]=0) = 2\mathcal{Q}\left(\sqrt{\gamma_k[n] \,/\, \sigma_{w,k}^2}\right) . \tag{18}$$

B. Fusion Center Detection

The FC, at the nth instant, receives $\boldsymbol{d}[n]$ and, similarly to all sensors, performs a ML Detection as a consequence of the LRT based on Eqs. (8) and (9) [4]:

$$\Lambda_n^{\mathrm{FC}}(\boldsymbol{d}[n]) = \frac{\Pr(\boldsymbol{d}[n] \,|\, \mathcal{H}[n]=1)}{\Pr(\boldsymbol{d}[n] \,|\, \mathcal{H}[n]=0)} = \sum_{m=1}^{M}\left\{\varphi_m[n]\prod_{k=1}^{K}\left[\left(\frac{P_{D,k,m}[n]}{P_{F,k}[n]}\right)^{d_k[n]} \times \left(\frac{1-P_{D,k,m}[n]}{1-P_{F,k}[n]}\right)^{1-d_k[n]}\right]\right\} \underset{\mathcal{D}[n]=0}{\overset{\mathcal{D}[n]=1}{\gtrless}} 1 , \tag{19}$$

where the values of $\varphi_m[n]$, $P_{D,k,m}[n]$'s, and $P_{F,k}[n]$'s are transmitted to the FC by the PPC.

Also for the FC it is possible to obtain the (FC) *probability of detection* ($Q_{D,m}[n]$) when the mth item is in failed state and the *probability of false alarm* ($Q_F[n]$) at the nth instant:

$$Q_{D,m}[n] \triangleq \Pr(\mathcal{D}[n]=1|\mathcal{H}_m[n]=1) = \sum_{\boldsymbol{d}\,:\Lambda_n^{\mathrm{FC}}(\boldsymbol{d})\geq 1}\left\{\prod_{k=1}^{K}\left[P_{D,k,m}[n]^{d_k}\left(1-P_{D,k,m}[n]\right)^{1-d_k}\right]\right\} , \tag{20}$$

$$Q_F[n] \triangleq \Pr(\mathcal{D}[n]=1|\mathcal{H}[n]=0) = \sum_{\boldsymbol{d}:\,\Lambda_n^{\mathrm{FC}}(\boldsymbol{d})\geq 1}\left\{\prod_{k=1}^{K}\left[P_{F,k}[n]^{d_k}\left(1-P_{F,k}[n]\right)^{1-d_k}\right]\right\} . \tag{21}$$

C. Post-Processing Center Elaboration

1) Post-Processing Detection: The PPC has the main task of collecting $\mathcal{D}[n]$ and establishing whether an alarm should be raised. Unlike the local and global detection, the PPC *integrates the knowledge of the failure model*. Moreover, it takes advantage of all the values of $\mathcal{D}[j]$ where $j=1,\ldots,n$ (with $j=1$ is the first algorithm instance after the last inspection) to implement an effective quickest fault detection approach. For compactness, we define the (accumulated) vector $\boldsymbol{\mathcal{D}}[n] \triangleq \left[\mathcal{D}[1] \quad \cdots \quad \mathcal{D}[n]\right]^T$. In this case, the PPC performs a test equivalent to the following MAP Detector:

$$\Lambda_n^{\mathrm{PPC}}(\boldsymbol{\mathcal{D}}[n]) \triangleq \frac{\Pr(\boldsymbol{\mathcal{D}}[n]|\mathcal{H}[n]=1)}{\Pr(\boldsymbol{\mathcal{D}}[n]|\mathcal{H}[n]=0)} \underset{\widehat{\mathcal{H}}[n]=0}{\overset{\widehat{\mathcal{H}}[n]=1}{\gtrless}} \frac{\Pr(\mathcal{H}[n]=0)}{\Pr(\mathcal{H}[n]=1)} , \tag{22}$$

which is equivalent to the following test:

$$\mathcal{R}[n] \triangleq \Pr(\mathcal{H}[n]=1|\boldsymbol{\mathcal{D}}[n]) = \sum_{m=1}^{M} \Pr(\mathcal{H}_m[n]=1|\boldsymbol{\mathcal{D}}[n]) = \sum_{m=1}^{M} \mathcal{R}_m[n] \underset{\widehat{\mathcal{H}}[n]=0}{\overset{\widehat{\mathcal{H}}[n]=1}{\gtrless}} \frac{1}{2}\,, \tag{23}$$

where we exploited Eq. (5). By looking at the test in Eq. (23), it can be recognized that our approach is *optimal from a Bayesian viewpoint* (i.e. assuming the change point is a random variable, whose pdf originates from the reliability assumptions made in Sec. II-A) and corresponds to the Shiryaev decision statistic [14] with a threshold $(1/2)$ ensuring the minimization of a uniform Bayesian risk.

In the following, we detail how the expression of $\mathcal{R}_m[n]$ (for each m) can be updated in a recursive form based on the previous value $\mathcal{R}_m[n-1]$. First, capitalizing Bayes' Theorem and the conditional (i.e. given $\mathcal{H}_m[n]=1$) independence of FC decisions' $\mathcal{D}[1],\ldots,\mathcal{D}[n]$ in time, we obtain Eq. (27) for the mth item at the bottom of the page.

The latter expression depends on (i) the FC decision likelihood at time n ($\Pr(\mathcal{D}[n]|\mathcal{H}_m[n]=1)$) and (ii) the one-step prediction of the mth fault probability ($\Pr(\mathcal{H}_m[n]=1|\boldsymbol{\mathcal{D}}[n-1])$). The former likelihood is obtained as follows:

$$\Pr(\mathcal{D}[n]\,|\,\mathcal{H}_m[n]=1) = Q_{D,m}[n]^{\mathcal{D}[n]}\,(1-Q_{D,m}[n])^{(1-\mathcal{D}[n])} \tag{24}$$

$$\Pr(\mathcal{D}[n]\,|\,\mathcal{H}_m[n]=0) = Q_{F}[n]^{\mathcal{D}[n]}\,(1-Q_{F}[n])^{(1-\mathcal{D}[n])} \tag{25}$$

Conversely, the term $\Pr(\mathcal{H}_m[n]=1|\boldsymbol{\mathcal{D}}[n-1])$ can be rewritten as Eq. (28) at the bottom of the page. Such expression is obtained leveraging: (i) the independence of $\mathcal{H}_m[n]$ from $\boldsymbol{\mathcal{D}}[n-1]$ given $\mathcal{H}_m[n-1]$, and (ii) the inability of an item to self-repair (i.e. $\Pr(\mathcal{H}_m[n]=1|\mathcal{H}_m[n-1]=1)=1$). Furthermore, in Eq. (28) the term $\Pr(\mathcal{H}_m[n]=1|\mathcal{H}_m[n-1]=0)$ can be estimated explicitly using Eq. (3):

$$\Pr(\mathcal{H}_m[n]=1|\mathcal{H}_m[n-1]=0) = 1-e^{-\widehat{\lambda}_m[n]\Delta t}\,. \tag{26}$$

Combining the previous results, we obtain Eq. (29) at the bottom of the page as the final expression for $\mathcal{R}_m[n]$. Eq. (29) has been obtained in sequential form so that the PPC, at the nth instant, needs to store only the M values of $\mathcal{R}_m[n-1]$ and the value of $\mathcal{D}[n]$, instead of the n values present in $\boldsymbol{\mathcal{D}}[n]$. Eq. (29) requires initialization: still, it can be easily demonstrated that $\mathcal{R}_m[0]=0$.

2) Failure Rate Estimation: The exact failure rate of the generic mth item is unknown, however, literature can often provide an unbiased estimate ($\lambda_{m,0}$), as well as the corresponding variance (ν_m). However, literature data is typically obtained with a finite number of experiments on items that are not necessarily equal to those present in the system (or in the same operating conditions). Therefore, each λ_m is treated herein by the PPC as a random variable.

In detail, when an alarm is raised by the PPC, the system is shut down and an inspection is carried out to verify the condition of the system. If the mth item's ith failure is acknowledged, it is possible to compute an updated estimate of λ_m using $T_{m,i}$. As $T_{m,i}$ is not directly available, the assumption here is that $T_{m,j} \approx T^*_{m,j}$, which holds if $\varepsilon_{m,j} \ll \lambda_m$ for all $j=1,\ldots,i$ (i.e. the expected item lifetime is much higher than the delay accumulated by the system to detect the fault). By defining the vector $\boldsymbol{T}_m[i] \triangleq \begin{bmatrix} T_{m,1} & \cdots & T_{m,i} \end{bmatrix}^T$, the PPC computes the following *Minimum Mean Square Error Estimator* (MMSE) for the mth item:

$$\widehat{\lambda}_{m,i} = \mathbb{E}\{\lambda_m|\boldsymbol{T}_m[i]\}\,. \tag{30}$$

In order to evaluate such expectation, the PPC needs to compute the (posterior) pdf of $\lambda_m\,|\,\boldsymbol{T}_m[i]$. Since $T_{m,j} \sim \text{Exp}(\lambda_m)$ for all $j=1,\ldots,i$, we embody the prior knowledge about the mth item lifetime via $\lambda_m \sim \text{Gamma}(\alpha_{m,0},\,\beta_{m,0})$, where $\alpha_{m,0} \triangleq (\lambda^2_{m,0}\,/\,\nu_m)$ and $\beta_{m,0} \triangleq (\lambda_{m.0}\,/\,\nu_m)$ are obtained based on the available literature values. Our choice leverages the Gamma pdf since it is known to be the *conjugate prior* of the Exponential pdf [15]. Capitalizing the advantages of using a conjugate prior, it is not difficult to show that $\lambda_m\,|\,\boldsymbol{T}_m[i] \sim \text{Gamma}(\alpha_{m,i},\,\beta_{m,i})$, where the Gamma parameters can be computed *recursively* by the PPC as $\alpha_{m,i} = (\alpha_{m,i-1}+1)$ and $\beta_{m,i} = (\beta_{m,i-1}+T_{m,i})$, respectively.

Once the (Gamma) posterior pdf of $\lambda_m\,|\,\boldsymbol{T}_m[i]$ is calculated, the corresponding MMSE estimator after ith failure is obtained by exploiting standard properties of Gamma distribution:

$$\widehat{\lambda}_{m,i} = \alpha_{m,i}\,/\,\beta_{m,i} \tag{31}$$

Clearly, at generic time n, the latest available estimate of λ_m is obtained as $\widehat{\lambda}_{m,\mathcal{S}_m} \rightarrow \widehat{\lambda}_m[n]$, assuming $\mathcal{S}_m$ failures for mth item have been reported up to time $(n-1)$.

$$\mathcal{R}_m[n] = \frac{\Pr(\mathcal{D}[n]|\mathcal{H}_m[n]=1)\,\Pr(\mathcal{H}_m[n]=1|\boldsymbol{\mathcal{D}}[n-1])}{\Pr(\mathcal{D}[n]|\mathcal{H}_m[n]=1)\,\Pr(\mathcal{H}_m[n]=1|\boldsymbol{\mathcal{D}}[n-1]) + \Pr(\mathcal{D}[n]|\mathcal{H}_m[n]=0)\,[1-\Pr(\mathcal{H}_m[n]=1|\boldsymbol{\mathcal{D}}[n-1])]} \tag{27}$$

$$\Pr(\mathcal{H}_m[n]=1|\boldsymbol{\mathcal{D}}[n-1]) = \mathcal{R}_m[n-1] + \Pr(\mathcal{H}_m[n]=1|\mathcal{H}_m[n-1]=0)(1-\mathcal{R}_m[n-1]) \tag{28}$$

$$\mathcal{R}_m[n] = \frac{\Pr(\mathcal{D}[n]|\mathcal{H}_m[n]=1)\left[1-e^{-\widehat{\lambda}_m[n]\Delta t}(1-\mathcal{R}_m[n-1])\right]}{\Pr(\mathcal{D}[n]|\mathcal{H}_m[n]=1)\left[1-e^{-\widehat{\lambda}_m[n]\Delta t}(1-\mathcal{R}_m[n-1])\right] + \Pr(\mathcal{D}[n]|\mathcal{H}_m[n]=0)\left[e^{-\widehat{\lambda}_m[n]\Delta t}(1-\mathcal{R}_m[n-1])\right]} \tag{29}$$

3) Parameters Calculation and Communication: At the beginning of a next $(n+1)$ step, the PPC updates (if needed) the estimates of the failure rates of the appropriate items to obtain $\widehat{\lambda}_m[n+1]$, and then calculates the values of $\varphi_m[n+1]$'s via Eq. (11). Next, it computes and transmits the values of $\gamma_k[n+1]$'s to the respective sensors to be used for the next energy test (see Eq. (16)). This consists of finding the $\gamma_k[n+1]$ that solves Eq. (15) for the $(n+1)$th instant for all sensors:

$$\sum_{m=1}^{M} \left(\varphi_m[n+1]\, a_{m,k}\, e^{b_{m,k}\, \gamma_k[n+1]} \right) = 1 \,. \tag{32}$$

The left-hand side of Eq. (32) is a smooth, convex, and increasing function in the variable $\gamma_k[n+1]$, therefore convergence is guaranteed from any starting point $\gamma_k[n+1]^{(0)}$ when solving it using the *Newton-Raphson method* [16]:

$$\gamma_k[n+1]^{(q+1)} \tag{33}$$
$$= \gamma_k[n+1]^{(q)} - \frac{\sum_{m=1}^{M} \left(\varphi_m[n+1]\, a_{m,k}\, e^{b_{m,k}\, \gamma_k[n+1]^{(q)}} \right) - 1}{\sum_{m=1}^{M} \left(\varphi_m[n+1]\, a_{m,k}\, b_{m,k}\, e^{b_{m,k}\, \gamma_k[n+1]^{(q)}} \right)},$$

where q denotes the iteration index.

Once obtained the thresholds, the PPC computes the values of $P_{D,k,m}[n+1]$'s and $P_{F,k}[n+1]$'s via Eqs. (17) and (18) and transmits them to the FC together with the values of $\varphi_m[n+1]$'s. This allows the FC to evaluate $\Lambda_{n+1}^{\mathrm{FC}}(\boldsymbol{d}[n+1])$ via Eq. (19). As a last step, the PPC computes the values of $Q_{D,m}[n+1]$'s and $Q_F[n+1]$ via Eqs. (20) and (21) to be used by the PPC itself in the (recursive) computation of $\Lambda_{n+1}^{\mathrm{PPC}}(\boldsymbol{\mathcal{D}}[n+1])$ via Eqs. (24) and (25). Note that Eqs. (20) and (21) can be calculated exactly with a finite number of operations since the number of possible outcomes of $\Lambda_n^{\mathrm{FC}}(\boldsymbol{d})$ is 2^K.

IV. Case Study – Goliat FPSO

The Goliat FPSO is an oil production platform located in the Barents Sea. Such platform relies on a Subsea Production System made of eight templates installed on the seabed[2]. As a consequence, oil leaks happen in deep waters making the detection even more challenging. Moreover, because of the high depths, the inspections must be performed by *remotely operated vehicles* with high costs making the reduction of false alarms of great importance [18]. On the other hand, strict environmental regulations are enforced on companies operating offshore, asking for quick detection of the spills [19]. A characteristic of oil leaks is their related acoustic signal that can be sensed via passive acoustic sensors [20], [21]. Therefore, each template has its manifold monitored by $K = 3$ *passive acoustic sensors* measuring the sound pressure as part of the leak detection system [22], [23]. An analysis recognized $M = 20$ *critical items* assumed to be at the same height as the sensors, as shown in Fig. 3. The previously described algorithm is assumed to be implemented over the system in place to verify the performance. The AAF used for this case study is the following:

$$g(\boldsymbol{x}_k, \boldsymbol{\theta}) = \sqrt{\left(\frac{\ell_{\mathrm{ref}}}{\|\boldsymbol{x}_k - \boldsymbol{\theta}\|} \right)^{k_{\mathrm{sc}}} 10^{(\ell_{\mathrm{ref}} - \|\boldsymbol{x}_k - \boldsymbol{\theta}\|)\alpha 10^{-4}}} \,, \tag{34}$$

where ℓ_{ref} and $\|\boldsymbol{s}_k - \boldsymbol{\theta}\|$ are in meters, the seawater absorption coefficient α is in [dB/km], and k_{sc} is the spreading coefficient. The value of α has been computed using *Francois & Garrison equation* [24], [25], with the underwater speed of sound obtained via the *Chen & Millero equation* [26] with parameters in Tab. I.

The proposed algorithm is compared with a WSN without the PPC, meaning that the sensors will perform the energy test in Eq. (16), and the FC, after collecting $\boldsymbol{d}[n]$, will provide the final decision on whether an oil spill is occurring at time n via Eq. (19), i.e. without exploiting the temporal dimension. It can be shown that the latter approach corresponds to a quickest oil spill detection based on the classical *Shewhart chart* [14]. However, the absence of a PPC removes the possibility to update parameters and transmit them to the sensors and the FC. Therefore, the values of φ_m's are taken as constants:

$$\varphi_m = \Pr(\mathcal{H}_m = 1 | \mathcal{H} = 1) \approx \lambda_{m,0} \Big/ \sum_{m=1}^{M} \lambda_{m,0} \,, \tag{35}$$

TABLE I
Parameters used for the simulation

Parameter	Value	Note / Reference
Ref. Frequency	2.5 kHz	[27]
Temperature	3.8 °C	[28]
Salinity	35 ‰	[28]
Depth	350 m	[22]
pH	8	[29]
k_{sc}	1.5	[30]
ℓ_{ref}	1 m	–
Simulated time	15 yr	[31]
Δt	15 min	–
$SNR_{m,k}$	10/15/20/25 dB	$\forall\, m, k$

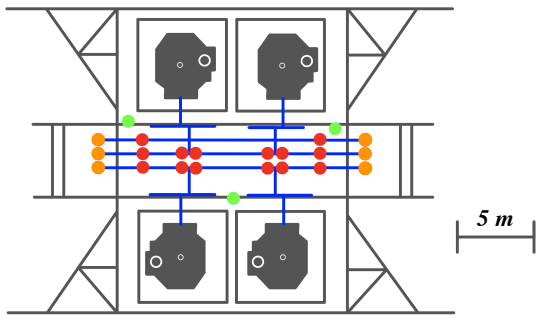

Fig. 3. Goliat's subsea template: the gray elements are the structure, the blue lines are the manifold, the green dots are the passive acoustic sensors, the red dots are the valves, and the orange dots are the connectors.

[2]For further details on subsea production systems, please see [17].

TABLE II
LITERATURE VALUES OF FAILURE RATES OF SUBSEA ITEMS

Item Category	$\lambda_{m,0}$ [yr^{-1}]	ν_m [yr^{-2}]
Valve, process isolation (manifold)	7.3000×10^{-3}	7.0715×10^{-5}
Connector (manifold)	9.5812×10^{-4}	2.4649×10^{-6}

where the literature values of the failure rates $\lambda_{m,0}$'s are used as parameter estimates. Eq. (35) was obtained exploiting the properties of a merged Poisson process. The time-independent property of the values of φ_m's also reflects on the values of γ_k's, $P_{D,k,m}$'s, and $P_{F,k}$'s which no longer need to be updated.

Numerical results have been obtained via simulations with 200 Monte Carlo runs using the software MATLAB. In detail, each run simulates the life of the Goliat FPSO (assuming negligible inspection time and not accounting for maintenance time). The simulated time, the value of Δt, and the different values of $SNR_{m,k} \triangleq \sigma^2_{\xi,m}/\sigma^2_{w,k}$ are in Tab. I. At each run, for each item, a new realization of the M Poisson processes and their corresponding failure rates is generated, where the λ_m's are originated from a Gamma distribution with moments from Tab. II which reports the literature values retrieved from *OREDA Handbook* [32].

The main results are in Tab. III where the aggregated average of the values of $\varepsilon_{m,j}$ (and the corresponding number of collected samples), the *Fault Rate* $P_1 = \Pr(\mathcal{H}[n] = 1)$, and the *False Positive Rate* $P_{10} = \Pr\left(\widehat{\mathcal{H}}[n] = 1 | \mathcal{H}[n] = 0\right)$ are displayed. Also, the *True Positive Rate* is defined as $P_{11}^{(N)} = \Pr\left(\bigcup_{j=0}^{N-1} \left\{\widehat{\mathcal{H}}[n+j] = 1\right\} | \mathcal{H}[n] = 1\right)$, where $(N-1)\Delta t$ is the allowed detection delay, with $N \geq 1$ as the number of collected samples. Fig. 4 shows the True Positive Rate as a function of N for different relevant SNR spill values. Moreover, the *Error Rate* (P_e) as a function of N is reported in Fig. 5 and is calculated as follows:

$$P_e^{(N)} = P_{10}(1 - P_1) + \left(1 - P_{11}^{(N)}\right) P_1 \,. \tag{36}$$

From Tab. III we notice the significant difference in behavior between the two architectures. When the Reliability-Based Fusion is implemented, the WSN performs a temporal integration with a consequent higher number of measurements needed by the PPC to declare the presence of a leak as it can be seen from the values of $\varepsilon_{m,j}$ which, on average, are higher when the PPC is implemented. This originates two opposing effects: on one hand, without the PPC, the WSN reaches a higher value of True Positive Rate for a given value of N as shown in Fig. 4, on the other hand, the temporal integration of the PPC allows the WSN to dramatically decrease the value of False Positive Rate of *five orders of magnitude*. It is also important to notice that Fault Rate will be higher in case the PPC is implemented as a consequence of the tendency of showing higher values of $\varepsilon_{m,j}$. Thus, it is evident the need to use the Error Rate as a metric in order to better evaluate the trade-off between quick detection (fast spill detection) and a high number of false alarms (high inspection costs).

TABLE III
SIMULATION RESULTS

	$SNR_{m,k}$ [dB]	With PPC	Without PPC
Average no. failures	–	1.5350	1.5350
Average $\varepsilon_{m,j}$ (no. samples)	10	32 hr 23 min (130.56)	5 min 46 s (1.38)
	15	11 hr 40 min (47.69)	4 min 50 s (1.32)
	20	5 hr 13 min (21.85)	2 min 59 s (1.20)
	25	2 hr 30 min (11)	4 min 3 s (1.27)
Fault Rate	10	3.8104×10^{-4}	4.0402×10^{-6}
	15	1.3918×10^{-4}	3.8596×10^{-6}
	20	6.3779×10^{-5}	3.4984×10^{-6}
	25	3.2103×10^{-5}	3.7075×10^{-6}
False Positive Rate	10	5.0405×10^{-6}	5.4641×10^{-1}
	15	4.9821×10^{-6}	4.4817×10^{-1}
	20	3.3560×10^{-6}	3.3096×10^{-1}
	25	2.1866×10^{-6}	1.4331×10^{-1}

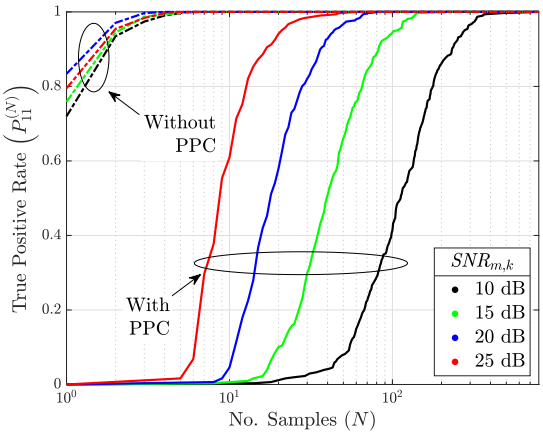

Fig. 4. True Positive Rate as a function of the number of collected samples N.

Finally, Fig. 5 shows the Error Rate versus N. In absence of PPC, the Error Rate is found to be greater than 0.1 without significant changes with N, whereas such value decreases as $SNR_{m,k}$ increases. Indeed, a fault detection mechanism not capitalizing time integration incurs in a high False Positive Rate (see Tab. III), which represents the dominating term in Eq. (36). On the contrary, when the PPC is implemented, the Error Rate starts from a value $\in [10^{-5}, 10^{-3}]$ and, as N increases, decreases by settling around a value $\in [10^{-6}, 10^{-5}]$. Such decrease in the Error Rate with N (when the PPC is present) is due to the corresponding increase of True Positive Rate made possible by the temporal integration performed by the PPC. Clearly, a higher value of $SNR_{m,k}$ lowers the Error Rate regardless of the employed architecture. Hence, using the

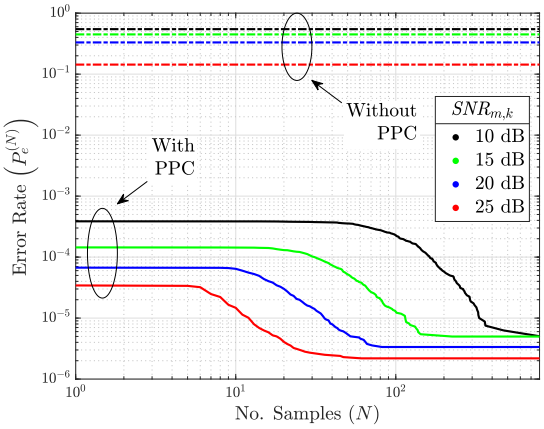

Fig. 5. Error Rate as a function of the number of collected samples N.

Error Rate as a metric, our Reliability-Based Fusion algorithm evidently outperforms the same architecture lacking the PPC.

V. Conclusions and Future Directions

In this work, we tackled quickest detection of faults within an Oil and Gas subsea production system, by means of spatio-temporal decision fusion approach. The sensor network collectively monitors the state of different pieces of equipment and reports their decisions to a FC based on individual LRTs. Herein, a spatial aggregation is performed, based on a global (per-sample) LRT and a global decision is performed. Such decisions are then aggregated in time by a PPC, which performs quickest detection of the system state according to a Bayesian criterion and exploits statistical distributions about the change time driven by datasheet reliability metrics. Results have highlighted the benefit in terms of Error Rate of a reliability-based algorithm with respect to an architecture that does not include the knowledge of the reliability features of the monitored system in its design. *Future directions* of research will include: (a) reliability-aided quickest fault detection in the presence of unknown parameters, (b) lossy reporting channels and (c) considering more complex reliability models.

References

[1] T. Sahoo, *Process Plants - Shutdown and Turnaround Management*. Boca Raton (FL), USA: Taylor & Francis Group, 2014.

[2] Y. Song, "Underwater Acoustic Sensor Networks With Cost Efficiency for Internet of Underwater Things," *IEEE Trans. Ind. Electron.*, vol. 68, no. 2, pp. 1707–1716, Feb. 2021.

[3] N. Paltrinieri, G. Landucci, and P. Salvo Rossi, "Real-Time Data for Risk Assessment in the Offshore Oil and Gas Industry," in *Proc. Int. Conf. Omae*, Trondheim, Norway, 2017.

[4] D. Ciuonzo and P. Salvo Rossi, "Distributed detection of a non-cooperative target via generalized locally-optimum approaches," *Inf. Fusion*, vol. 36, pp. 261–274, Jul. 2017.

[5] N. Sriranga, K. G. Nagananda, R. S. Blum, A. Saucan, and P. K. Varshney, "Energy-Efficient Decision Fusion for Distributed Detection in Wireless Sensor Networks," in *Proc. Int. Conf. Inf. Fusion*, Cambridge, UK, 2018, pp. 1541–1547.

[6] S. Sen, N. S. V. Rao, C. Q. Wu, M. L. Berry, K. M. Grieme, R. R. Brooks, and G. Cordone, "Performance analysis of Wald-statistic based network detection methods for radiation sources," in *Proc. Int. Conf. Inf. Fusion*, Heidelberg, Germany, 2016, pp. 820–827.

[7] G. Tabella, N. Paltrinieri, V. Cozzani, and P. Salvo Rossi, "Subsea oil spill risk management based on sensor networks," *Chem. Eng. Trans.*, vol. 82, pp. 199–204, Oct. 2020.

[8] M. Bucelli, I. B. Utne, P. Salvo Rossi, and N. Paltrinieri, "A system engineering approach to subsea spill risk management," *Saf. Sci.*, vol. 123, Mar. 2020.

[9] G. Tabella, N. Paltrinieri, V. Cozzani, and P. Salvo Rossi, "Data fusion for subsea oil spill detection through wireless sensor networks," in *Proc. IEEE Sensors*, Rotterdam, The Netherlands, 2020.

[10] ——, "Wireless sensor networks for detection and localization of subsea oil leakages," *IEEE Sens. J.*, vol. 21, no. 9, pp. 10 890–10 904, May 2021.

[11] J. Pan and J. McElhannon, "Future edge cloud and edge computing for internet of things applications," *IEEE Internet Things J.*, vol. 5, no. 1, pp. 439–449, 2017.

[12] G. Casella and R. L. Berger, *Statistical Inference*, 2nd ed. Pacific Groove (CA), USA: Thomson Learning, 2002.

[13] S. Kay, *Fundamentals of Statistical Signal Processing: Detection Theory*, 1st ed., ser. (Prentice Hall Signal Processing Series). Upper Saddle River (NJ), USA: Prentice-Hall, 1998.

[14] L. Xie, S. Zou, Y. Xie, and V. V. Veeravalli, "Sequential (quickest) change detection: Classical results and new directions," *IEEE Journal on Selected Areas in Information Theory*, 2021.

[15] M. Rausand and S. Haugen, *Risk Assessment: Theory, Methods, and Applications*, 1st ed. Hoboken (NJ), USA: John Wiley & Sons, 2011.

[16] D. Kincaid and W. Cheney, *Numerical Analysis: Mathematics of Scientific Computing*, 3rd ed. Providence (RI), USA: AMS, 2002.

[17] Y. Bai and Q. Bai, *Subsea Engineering Handbook*. Houston (TX), USA: Elsevier, 2012.

[18] C. Mai, S. Pedersen, L. Hansen, K. L. Jepsen, and Zhenyu Yang, "Subsea infrastructure inspection: A review study," in *IEEE Int. Conf. Underwater Syst. Technol., Theory Appl. (USYS)*, Penang, Malaysia, Dec. 2016, pp. 71–76.

[19] DNV-GL, "Recommended practice RP-F302 offshore leak detection," Oslo, Norway, Apr. 2016.

[20] H. V. Fuchs and R. Riehle, "Ten years of experience with leak detection by acoustic signal analysis," *Appl. Acoust.*, vol. 33, no. 1, pp. 1–19, 1991.

[21] M. A. Adegboye, W. K. Fung, and A. Karnik, "Recent advances in pipeline monitoring and oil leakage detection technologies: Principles and approaches," *Sensors*, vol. 19, no. 11, p. 2548, Jun. 2019.

[22] E. Bjørnbom, "Goliat – Leak detection and monitoring from template to satellite," 2011.

[23] E. Røsby, "Goliat development project - Subsea leak detection design," Aker Solutions, 2011.

[24] R. E. Francois and G. R. Garrison, "Sound absorption based on ocean measurements: Part I: Pure water and magnesium sulfate contributions," *J. Acoust. Soc. Am.*, vol. 72, no. 3, pp. 896–907, 1982.

[25] ——, "Sound absorption based on ocean measurements: Part II: Boric acid contribution and equation for total absorption," *J. Acoust. Soc. Am.*, vol. 72, no. 6, pp. 1879–1890, Dec. 1982.

[26] G. S. K. Wong and S. Zhu, "Speed of sound in seawater as a function of salinity, temperature, and pressure," *J. Acoust. Soc. Am.*, vol. 97, no. 3, pp. 1732–1736, Mar. 1995.

[27] E. G. Eckert, J. W. Maresca, R. W. Hillger, and J. J. Yezzi, "Location of leaks in pressurized petroleum pipelines by means of passive-acoustic sensing methods," in *Leak Detection for Underground Storage Tanks*. West Conshohocken (PA), USA: ASTM Int., 1993, pp. 53–69.

[28] Institute of Marine Research, "Mareano," 2021.

[29] A. A. Vetrov and E. A. Romankevich, *Carbon Cycle in the Russian Arctic Seas*. Berlin, Germany: Springer, 2004.

[30] M. Stojanovic, "On the relationship between capacity and distance in an underwater acoustic communication channel," in *Proc. Int. Workshop Underwater Networks (WUWNet)*, Oct. 2006, pp. 34–43.

[31] Vår Energi, "Goliat Barrier Status Panel," 2016.

[32] SINTEF, *OREDA Offshore Reliability Data Handbook*, 4th ed. OREDA Participants, 2002.

Paper 5

Bayesian Fault Detection and Localization Through Wireless Sensor Networks in Industrial Plants

G. Tabella, D. Ciuonzo, N. Paltrinieri, and P. Salvo Rossi

IEEE Internet of Things Journal, 2024. in press.

Bayesian Fault Detection and Localization Through Wireless Sensor Networks in Industrial Plants

Gianluca Tabella, *Graduate Student Member, IEEE,* Domenico Ciuonzo, *Senior Member, IEEE,* Nicola Paltrinieri, and Pierluigi Salvo Rossi, *Senior Member, IEEE*

***Abstract*—This work proposes a data fusion approach for quickest fault detection and localization within industrial plants via wireless sensor networks. Two approaches are proposed, each exploiting different network architectures. In the first approach, multiple sensors monitor a plant section and individually report their local decisions to a fusion center. The fusion center provides a global decision after spatial aggregation of the local decisions. A post-processing center subsequently processes these global decisions in time, which performs quick detection and localization. Alternatively, the fusion center directly performs a spatio-temporal aggregation directed at quickest detection, together with a possible estimation of the faulty item. Both architectures are provided with a feedback system where the network's highest hierarchical level transmits parameters to the lower levels. The two proposed approaches model the faults according to a Bayesian criterion and exploit the knowledge of the reliability model of the plant under monitoring. Moreover, adaptations of the well-known Shewhart and CUSUM charts are provided to fit the different architectures and are used for comparison purposes. Finally, the algorithms are tested via simulation on an active Oil and Gas subsea production system, and performances are provided.**

***Index Terms*—Data fusion, fault detection, Industry 4.0, localization, monitoring, quickest detection, reliability, wireless sensor network.**

I. Introduction

OVER the last decades, Wireless Sensor Networks (WSNs) have surged in growth, harnessing low-cost "green" devices for monitoring applications [2]. Fueled by the advances in sensor technology, wireless communication protocols, and the popularization of the Internet of Things (IoT) [3], this expansion has ushered in a new era of data acquisition and situation awareness. WSNs, as the sensing arm of the IoT, play a pivotal role in this paradigm, seamlessly merging the physical and digital realms through real-time data for diverse inference tasks [4].

Part of this work has been presented at the 2021 24th International Conference on Information Fusion (FUSION) [1].

G. Tabella is with the Dept. Gas Technology, SINTEF Energy Research, 7034 Trondheim, Norway, and with the Dept. Electronic Systems, NTNU Norwegian University of Science and Technology, 7034 Trondheim, Norway (e-mail: gianluca.tabella@sintef.no).

D. Ciuonzo is with the Dept. Electrical Engineering and Information Technologies, University of Naples "Federico II," 80138 Naples, Italy (e-mail: domenico.ciuonzo@unina.it)

N. Paltrinieri is with the Dept. Mechanical and Industrial Engineering, NTNU Norwegian University of Science and Technology, 7034 Trondheim, Norway (e-mail: nicola.paltrinieri@ntnu.no).

P. Salvo Rossi is with the Dept. Electronic Systems, NTNU Norwegian University of Science and Technology, 7034 Trondheim, Norway, and with the Dept. Gas Technology, SINTEF Energy Research, 7034 Trondheim, Norway (e-mail: salvorossi@ieee.org).

Specifically, there has been a considerable focus on the detection and localization of adverse events, with a particular emphasis on their application in developing safeguards for safety-critical systems. This situation holds considerable importance in sectors like the process industry, energy production, and manufacturing, where the malfunction of a single component (the event under scrutiny) could jeopardize the well-being of both employees and the environment. Consequently, this could lead to significant environmental and societal expenses, as well as substantial financial losses resulting from unexpected shutdowns [5]. For that reason, the global critical infrastructure protection market currently commands a valuation of USD 132 billion, and forecasts indicate a steady 3.4% compound annual growth rate through 2030. In this context, IoT technologies will play a dominant role [6]. In light of those reasons, the exploration of event detection using Wireless Sensor Networks (WSNs) for industrial purposes has garnered significant attention. Various architectural designs have been scrutinized and put forth, with a specific focus on underwater applications, as referenced in previous literature [7], [8].

A pivotal concern in this context revolves around identifying equipment malfunctions that could potentially result in *loss of containment*. This concern is particularly pronounced in settings where inspections come at a substantial cost, such as subsea facilities, as indicated by prior research [9], [10].

On top of that, to lower communication and processing costs (thus prolonging the WSN lifetime and reducing monitoring costs), the sensors are typically engineered to communicate 1-bit decisions to a Fusion Center (FC), which gathers such decisions and formulates a global decision regarding the presence of the event of interest (in our case a fault on the monitored plant) [11], [12]. Upon detecting a hostile event, the FC generates an alarm, enabling appropriate measures (e.g., emergency plant maintenance) to be implemented in order to mitigate the event's repercussions.

It is important to highlight that the efficacy of a system for detecting and localizing faults also depends on how well it is integrated into a risk management framework. This integration allows full exploitation of the amount of information available about the surveilled system during the design stage of the fault detection and localization system. A suitable integration can be achieved by using the *Dynamic Risk Management Framework* (DRMF), which is designed to incorporate external experiences and early warnings, thereby allowing the assimilation of unknown variables [13]–[16]. Enhanced risk awareness associated with unforeseen events enables learning and understanding, which is based on the continuous *monitoring* and *review* of

accumulated information. DRMF involves several steps, such as (i) *horizon screening*, (ii) *hazard identification*, (iii) *assessment*, and finally (iv) *decision/action*. These steps are necessary for a comprehensive evaluation of the risks connected to known potential accident scenarios. To make the DRMF an adaptive process, iterative updates are essential. In this context, the fault detection and localization system serves as a warning subsystem within a decision-support system by playing a role in actions like plant shutdown and maintenance.

In this context, **peculiar characteristics and challenges for the problem** are: (i) the finite spatial extent of the event being monitored (i.e., some sensors may be out-of-range for detecting a certain fault), (ii) the fault location is unknown (viz. it may have originated from different items of interest within the plant), (iii) each fault may be more or less probable depending on the reliability of the item responsible for it, (iv) efficient detection algorithms should be conceived to detect such events as quickly as possible (viz. minimize the permanence in a risky condition) while keeping false-alarms under control (viz. avoid unnecessary maintenance/shutdowns), (v) detection approaches should be coupled with (or better, include) localization procedures to identify the faulty item (viz. minimize the plant maintenance time/costs).

In the context of challenges (i) and (ii), various algorithms have been proposed in the literature for detecting spatially localized events at unknown locations (such as radiation releases, anomalous parameter fields, or non-cooperative targets) via distributed WSNs. Initial attempts involve the straightforward application [17], [18] or adaptations/extensions [19] (e.g., by using ordering schemes according to most informative sensors) of the sub-optimal *Counting Rule* (CR). Notably, the plain CR has recently found application in the specific domain of subsea oil spill detection [20], [21]. An alternative approach is explored in [10], [22], where a modified version of the *Chair-Varshney Rule* is devised. This rule is designed to partially incorporate critical items' locations and failure rates. Additionally, it is coupled with localization techniques to address challenge (v). Regrettably, these rules do not take into account the *limited extent* and *unknown location* of the detected phenomenon by design. This results in *diminished detection performance*.

Conversely, recent years have witnessed the emergence of a range of fusion rules designed for the explicit detection of spatially localized events with unknown locations through distributed WSNs [12], [23], [24]. To tackle this challenge, these approaches have harnessed methodologies such as the Generalized Likelihood Ratio Test (GLRT), Bayesian techniques, generalized score tests, or hybrid variations. While *primarily focused on detecting non-cooperative targets*, these algorithms can be adapted to address challenges (i), (ii), and (v). However, it is essential to note that the fusion methods mentioned are fundamentally designed in a batch fashion (or overlook temporal dependencies) and fail to target the rapid onset of faults, thus not fully addressing challenge (iv). Recent advancements in this domain have made strides in mitigating the constraints associated with batch design [25], [26]. Nevertheless, these proposals are not able to promptly detect events as they occur, which is crucial in addressing the quickest detection problem.

Furthermore, to the best of our understanding, *no approach has effectively integrated data regarding the dependability of the system being monitored when developing the detection algorithm*, i.e., challenge (iii). Vital data, encompassing the positions, failure rates, and failure models of critical items, represent valuable a-priori information that may be seamlessly substantiated within a Bayesian approach. Hence, the **main contributions** of this work are the following:

- We present two spatio-temporal sensor fusion approaches designed to carry out quickest *detection and localization* of faults within a system. To elaborate, a WSN collectively observes the status of various equipment components and communicates their decisions to *two different classes of architectures*.
- The first architecture (aligning to an edge-fog-cloud paradigm [27]) is composed of a FC which performs *spatial aggregation* and an optimal per-sample decision. These decisions are subsequently processed *over time* by a Post-Processing Center (PPC). The PPC is responsible for swiftly identifying system faults based on a Bayesian approach and takes advantage of time-varying statistical distributions influenced by the reliability data of system components. Differently, the second architecture (aligning to an edge-cloud paradigm) is composed of a FC only, which performs a joint spatio-temporal aggregation in a Bayesian quickest detection fashion. These architectures are compared with baselines represented by the Shewhart and CUSUM charts, respectively, as well as in terms of their computational complexity.
- The outcomes of the suggested methods are examined with a specific focus on a practical Oil and Gas configuration, specifically the subsea production system of the Goliat FPSO [28]. The results, encompassing both (i) detection and localization as well as (ii) metrics emphasizing reliability, underscore the attractiveness of the proposed methods and the added advantage of temporal aggregation compared to relying solely on spatial aggregation.

This study delves deeper into the application of WSNs for fault detection and localization, incorporating reliability-related item data into the same detection algorithm(s) as previously introduced in [1]. Indeed, this earlier conference work: (i) analyzed a Three-Layer architecture; (ii) provided a comparison with a Shewhart chart; (iii) reported a preliminary numerical analysis using only one threshold value; (v) focused on the detection task without providing a localization algorithm. Conversely, this work investigates and compares two relevant fusion architectures (i.e., two- vs. three-layer) to accommodate a larger spectrum of designer requirements using a wide number of detection thresholds. Secondly, additional baselines are included in the comparison (i.e., the CUSUM chart). Thirdly, the proposed design includes fault-localization capabilities.

The paper's remaining sections are arranged as follows. Sec. II provides a description of the system model considered (including failure and corresponding sensing models), whereas Sec. III presents the design of the local detectors that is common to all the architectures discussed in this work. Then, Sec. IV recalls the state-of-the-art in industrial fault identification,

whereas Secs. V and VI are devoted to introducing the considered Three-Layer and Two-Layer fusion approaches, respectively. Sec. VIII analyzes the proposed approaches' pros and cons in relation to a relevant case study concerning oil spills in a production platform and discusses the results. Finally, Sec. IX ends the paper with concluding remarks and a brief prospect of future avenues of research.

Notation – vectors are indicated with bold letters; the norm and transpose operators are represented as $\|\cdot\|$ and $[\cdot]^{\mathrm{T}}$; probability mass functions (PMFs) and probability density functions (PDFs) are denoted as $\mathbb{P}(\cdot)$ and $p(\cdot)$, respectively; conditional counterparts are represented by $\mathbb{P}(\cdot|\cdot)$ and $p(\cdot|\cdot)$; a Gaussian distribution with mean μ and variance σ^2 is labeled as $\mathcal{N}(\mu,\sigma^2)$; the complementary cumulative distribution function (CCDF) of the standard normal distribution is denoted by $\mathcal{Q}(\cdot)$; an exponential distribution with rate λ is expressed as $\mathrm{Exp}(\lambda)$; a Bernoulli distribution with parameter p is symbolized as $\mathcal{B}(p)$; a Gamma distribution with shape α and rate β is indicated by $\mathrm{Gamma}(\alpha,\beta)$; a Poisson distribution with parameter p is represented as $\mathrm{Poisson}(p)$; $G_a(z)$ expresses the probability-generating function of the discrete random variable a; $a^+ \triangleq \max\{a,0\}$ defines the positive component of the real number a; $\widehat{a}$, $\mathbb{E}(a)$, and $\mathbb{E}(a|b)$ stand for an estimate of the random variable a, its expected value, and conditional expectation given the random variable b, respectively; the big O notation is denoted by $\mathcal{O}(\cdot)$.

II. System Model

This work has the objective of *detecting* and *localizing* faults within a given set of critical items associated with an industrial plant (e.g., the subsea production system of an offshore oil platform). The failure model associated with each of these items is described and motivated in Sec. II-A. Possible faults are monitored by a group of inexpensive sensor nodes (arranged in a WSN), whose measurement model is detailed in Sec. II-B. At each instant, the sensor computes a one-bit compression based on a local detection logic, which is then reported for (time and spatial) aggregation according to the considered fusion architectures, as described in Sec. II-C.

A. Failure Model

The monitored portion of the plant is conceptualized as a system comprising M individual *items*. Each item's state at time t is represented by the following variable:

$$\mathcal{H}_m(t) = \begin{cases} 0\,, & m\text{th item is } \textbf{operational} \\ 1\,, & m\text{th item is } \textbf{faulty} \end{cases}, \tag{1}$$

where *operational* indicates that the item is functioning as intended with no immediate action required, while *faulty* signifies that the item needs maintenance. Moreover, we define the state variable at time t for the *whole system* as:

$$\mathcal{H}(t) = 1 - \prod_{m=1}^{M} (1 - \mathcal{H}_m(t)) = \begin{cases} 0\,, & \textbf{operational} \text{ system} \\ 1\,, & \textbf{faulty} \text{ system} \end{cases}, \tag{2}$$

implying *independent failures and that the system is regarded as faulty when at least one of its items is in such state (i.e., series system)*. An item retains a faulty state until maintenance is carried out. In the present work, we assume that, when an item becomes faulty, the sensors employed to monitor the system measure a signal with a different statistical distribution. Upon identifying a shift in the signal distribution, an inspection is carried out to evaluate the overall state of the system, and maintenance is subsequently executed on all items that have malfunctioned.

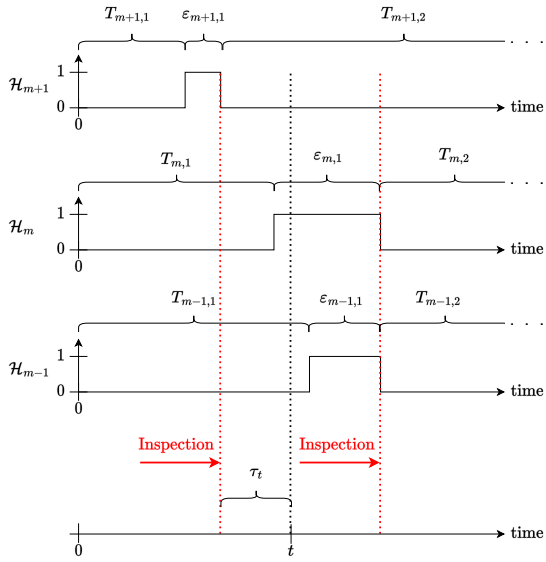

Fig. 1: Failure model (excluding inspection and maintenance durations).

The occurrence of a failure in the mth item is represented as a *homogeneous Poisson process* characterized by a *failure rate* λ_m (refer to Fig. 1).

Let us define $T_{m,j}$ as the amount of time the mth item spends in an operational state between the $(j-1)$th and the jth failures and $\mathcal{S}_m(t)$ as the number of transitions to a faulty state for the mth item at time t. It follows that $T_{m,j} \sim \mathrm{Exp}(\lambda_m)$ for all $j \in \mathbb{N}$. Furthermore, we introduce $T^*_{m,j} \triangleq T_{m,j} + \varepsilon_{m,j}$, where $\varepsilon_{m,j}$ represents the time elapsed before the failure state is detected. At time t, we define τ_t as the time elapsed since the most recent inspection. Because Poisson processes are *memoryless*, maintenance can be considered as either repair or replacement. A consequence of the failure model is the derivation of the *failure function* (or *failure probability*) for the mth item, as expressed by Eq. (3):

$$F_m(t) \triangleq \mathbb{P}(\mathcal{H}_m(t) = 1) = 1 - e^{-\lambda_m \tau_t}\,. \tag{3}$$

Subsequently, the failure function for the entire system at a given time t is determined by Eq. (4):

$$F(t) \triangleq \mathbb{P}(\mathcal{H}(t) = 1) = 1 - \prod_{m=1}^{M} (1 - F_m(t))\,. \tag{4}$$

This expression of $F(t)$ indicates independent failures. Moreover, for sufficiently small values of $\lambda_m \tau_t$ (i.e., $\lambda_m \tau_t \ll 1$), we simplify the model as:

$$F(t) \approx \sum_{m=1}^{M} F_m(t) = M - \sum_{m=1}^{M} e^{-\lambda_m \tau_t} \,. \tag{5}$$

Such approximation (henceforth called *rare events approximation*) is widely used when the items forming the monitored system have sufficiently low values of $F_m(t)$'s resulting in their products becoming negligible [29].

Furthermore, according to Eq. (5), it suggests the occurrence of *disjoint failures*. This implies that at any given time t, *at most* one item will be faulty, a characteristic that will be considered in the detectors' design. The rare event approximation allows us to define a *prior probability of item failure* for the mth item labeled as $\varphi_m(t)$:

$$\begin{aligned} \varphi_m(t) &\triangleq \mathbb{P}(\mathcal{H}_m(t) = 1 | \mathcal{H}(t) = 1) \approx \frac{\mathbb{P}(\mathcal{H}_m(t) = 1)}{\mathbb{P}(\mathcal{H}(t) = 1)} \\ &= \frac{F_m(t)}{F(t)} = \frac{1 - e^{-\lambda_m \tau_t}}{M - \sum\limits_{m=1}^{M} e^{-\lambda_m \tau_t}} \,. \end{aligned} \tag{6}$$

Such a probability can also be expressed in a time-independent fashion. In such case, we can define a *stationary prior probability of item failure* for the mth φ_m:

$$\varphi_m \triangleq \frac{\lambda_m}{\sum\limits_{m=1}^{M} \lambda_m} \,. \tag{7}$$

A detailed treatment of the mathematical modeling of the failures as Poisson processes is given in Appendix A.

Throughout the paper, the system monitoring occurs at regular time intervals of duration Δt, with the exception of inspection and maintenance periods. Therefore, in order to ease the readability of this work, we consider the nth discrete time instant, with n_0 indicating the first discrete time instant that follows the last inspection.

B. Signal Model

The expression for the received signal $y_k[n]$ at the kth sensor during the nth discrete time point is as follows:

$$y_k[n] = \sum_{m=1}^{M} s_{m,k}[n] + w_k[n] \,, \tag{8}$$

where $s_{m,k}[n]$ and $w_k[n] \sim \mathcal{N}(0, \sigma^2_{w,k})$ represent the received signal from the mth item and the Additive White Gaussian Noise (AWGN), respectively, at the kth sensor. More specifically, $s_{m,k}[n]$ is assumed to have the following shape:

$$s_{m,k}[n] \triangleq \begin{cases} 0 \,, & \text{if } \mathcal{H}_m[n] = 0 \text{ (\textbf{active} item)} \\ \xi_{m,k}[n]\, g(\boldsymbol{x}_k, \boldsymbol{h}_m) \,, & \text{if } \mathcal{H}_m[n] = 1 \text{ (\textbf{faulty} item)} \end{cases} , \tag{9}$$

where $\xi_{m,k}[n] \sim \mathcal{N}(0, \sigma^2_{\xi,m})$ represents the fluctuations in the received signal strength at the kth sensor. $\xi_{m,k}[n]$ and $w_k[n]$ are assumed statistically independent thanks to the spatial separation of the sensors with *known* values of $\sigma^2_{\xi,m}$ and $\sigma^2_{w,k}$, for all $k = 1, \ldots, K$ and $m = 1, \ldots, M$. Lastly, $g(\boldsymbol{x}_k, \boldsymbol{\theta}_m)$ denotes the attenuation function, which is a function of the distance between the location of the kth sensor ($\boldsymbol{x}_k$) and the position of the mth item ($\boldsymbol{\theta}_m$).

This model is suitable for several practical industrial settings like the acoustic signal generated by an underwater leak sensed by hydrophones [1], [10].

It is important to note that the rare event approximation introduced in Eq. (5) hinders the possibility of modeling more than one item being faulty at a given time. Thus, for any given time instance denoted as n, we can express the statistical characteristics of the measured signal as follows (see Eq. (10)):

$$\begin{cases} y_k[n] | \mathcal{H}[n] = 0 \sim \mathcal{N}\Big(0, \sigma^2_{w,k}\Big) \\ y_k[n] | \mathcal{H}_m[n] = 1 \sim \mathcal{N}\Big(0, \sigma^2_{\xi,m}\, g^2(\boldsymbol{x}_k, \boldsymbol{\theta}_m) + \sigma^2_{w,k}\Big) \end{cases} , \tag{10}$$

where it is important to state that the failure of the generic mth item caused the system to be faulty.

C. Wireless Sensor Network Models

In this work, we design **two fusion architectures**. The first uses an *edge-fog-cloud* approach where the network can be separated into three hierarchical layers with growing computational power as we approach the cloud layer, as it can be seen in Fig. 2a. In contrast, the second uses two hierarchical layers, i.e., an *edge-cloud approach*, as shown in Fig. 2b. Both architectures are proposed with an integrated feedback system that transmits updated parameters from the cloud layer to the lower layers.

The integration of an *edge-fog-cloud* architecture is particularly justified in scenarios where sensors are required to operate with minimal energy consumption. This need is exemplified in the context of underwater WSN, where the replacement of sensors is impractical, underscoring the critical importance of preserving their battery life (refer to the case study in Sec. VIII). By incorporating an underwater fog layer (FC), energy consumption during data transmission by sensors can be significantly reduced. Subsequently, this fog layer can transmit compressed information to a cloud layer (PPC) for final processing.

The proposed WSN architectures comprise a set of K sensors responsible for monitoring the area of interest at regular intervals of time Δt, aiming to identify if the system is in an operational ($\mathcal{H}[n] = 0$) or a faulty state ($\mathcal{H}[n] = 1$).[1] The generic kth sensor is tasked with capturing and assessing the signal $y_k[n]$. It does so by comparing a statistic derived from the measured signal to a threshold value that varies with time, denoted as $\gamma_k[n]$. Subsequently, the sensor reaches a local decision $d_k[n] = i$ when it declares $\mathcal{H}[n] = i$. Such a decision is then reported for further analytics. The latter choice not only offers spectral efficiency, requiring only 1-bit communication on the reporting channel linking the sensors to the fusion architecture, but it also exhibits high energy

[1] It is important to note that the present work does not delve into the analysis of the sampling frequency.

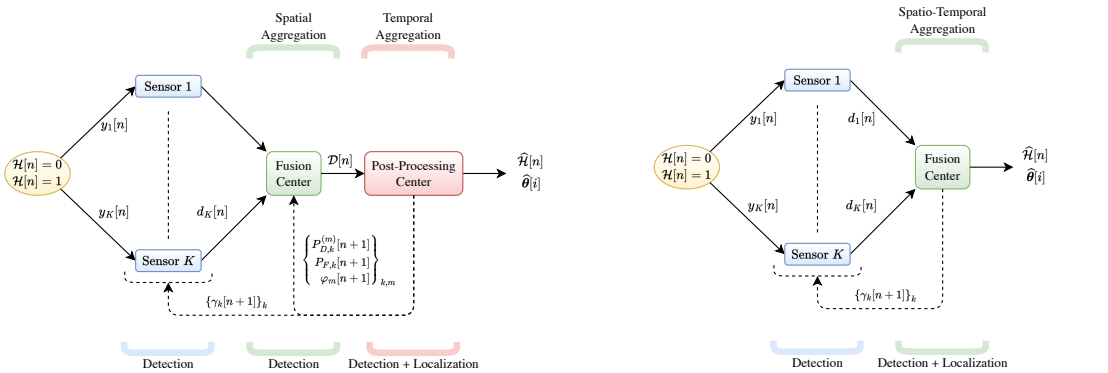

(a) Three-Layer Architecture. (b) Two-Layer Architecture.

Fig. 2: Proposed Wireless Sensor Network architectures (the dotted arrow constitutes the feedback system).

efficiency, especially when On-Off Keying (OOK) is utilized for transmitting the local decisions (see [10] for more details).

1) Three-Layer Fusion Architecture: The first WSN we propose incorporates an architecture consisting of a *fusion center* (FC) and a *post-processing center* (PPC), performing spatial and temporal aggregation, respectively. In this setup, the vector of local decisions $\boldsymbol{d}[n] = \begin{bmatrix} d_1[n] & \cdots & d_K[n] \end{bmatrix}^{\mathrm{T}}$ is gathered and processed at the FC for a global decision $\mathcal{D}[n] = i$ if $\mathcal{H}[n] = i$ is declared.

The FC performs a *Maximum Likelihood (ML) detection* based on the binary hypothesis as defined in Eq. (10), without assuming prior knowledge about the probabilities of events $\mathcal{H}[n] = 0$ and $\mathcal{H}[n] = 1$. On the other hand, the PPC collects $\boldsymbol{\mathcal{D}}[n] = \begin{bmatrix} \mathcal{D}[n_0] & \cdots & \mathcal{D}[n] \end{bmatrix}^{\mathrm{T}}$ and incorporates information from the failure model as well as the signal model defined in Eqs. (8) and (10). The PPC makes a final decision $\widehat{\mathcal{H}}[n]$ through a *Bayesian posterior detection*, with $\widehat{\mathcal{H}}[n] = 1$ triggering inspection operations.

Moreover, in the case of $\widehat{\mathcal{H}}[n] = 1$, the PPC computes the estimated position of the faulty item $\widehat{\boldsymbol{\theta}}[i] = \boldsymbol{\theta}_{\widehat{m}[i]}$, where i indicates the number of times an alarm has been raised, up to instant n. Additionally, the PPC is responsible for ongoing communication with the sensors, providing them with updated values for their individual time-dependent thresholds as well as calculating and transmitting to the FC several time-dependent parameters necessary to perform the global detection task.

This architecture is compared with an architecture lacking the PPC and the feedback system where the FC is the highest hierarchical layer. As the FC computes the final decision without temporal aggregation of the local decisions, this solution is here named *Shewhart chart* [30].

2) Two-Layer Fusion Architecture: In this second architecture, the FC collects $\boldsymbol{d}[n_0], \ldots, \boldsymbol{d}[n]$ and directly performs a *Bayesian posterior detection*, therefore incorporating the (temporal-aggregation) functions of the PPC within the FC itself. As a consequence, it becomes the FC's task to provide the estimated position of the faulty item, as well as to transmit updated local thresholds to the respective sensors.

This architecture is compared with an architecture without feedback system performing an adaptation of the *CUSUM chart* [30].

The architectures employed for executing the Shewhart and CUSUM charts can both be depicted as modifications of the architecture shown in Fig. 2b. In these variations, the feedback channel is absent, and when executing the Shewhart chart, the FC exclusively engages in spatial aggregation.

III. Local Detection

This section provides the description of the local detector as it presents the same design strategy among all the presented cases. For the sake of notation, we outline the design for systems with no feedback mechanism (as in the architecture using the Shewhart and CUSUM charts). The changes of notation necessary when using a feedback mechanism are provided at the end of the section.

The edge layer of the proposed architectures consists of the sensors individually taking local decisions. Based on the binary hypothesis in Eq. (10), the optimal test is a *Likelihood Ratio Test* (LRT) on $y_k[n]$, indicated as $\Lambda^k(y_k[n])$. Here, the unknown location of the faulty item is marginalized by employing the stationary prior probability of item failure from Eq. (7). Precisely, for the kth sensor at the nth instant, it holds:

$$\begin{aligned} \Lambda^k(y_k[n]) &\triangleq \frac{p(y_k[n]|\mathcal{H}[n]=1)}{p(y_k[n]|\mathcal{H}[n]=0)} \\ &= \frac{\sum_{m=1}^{M} \varphi_m \, p(y_k[n]|\mathcal{H}_m[n]=1)}{p(y_k[n]|\mathcal{H}[n]=0)} \, . \end{aligned} \tag{11}$$

Hence, by leveraging Eq. (10), we get the ML detector:

$$\Lambda^k(y_k[n]) = \sum_{m=1}^{M} \left(\varphi_m \, a_{m,k} \, e^{b_{m,k} \, y_k^2[n]} \right) \underset{d_k[n]=0}{\overset{d_k[n]=1}{\gtrless}} 1 \, , \tag{12}$$

where

$$a_{m,k} \triangleq \sqrt{\frac{\sigma_{w,k}^2}{\sigma_{\xi,m}^2 \, g^2(\boldsymbol{x}_k, \boldsymbol{\theta}_m) + \sigma_{w,k}^2}} \, , \tag{13}$$

$$b_{m,k} \triangleq \frac{1}{2}\left(\frac{1}{\sigma^2_{w,k}} - \frac{1}{\sigma^2_{\xi,m}\, g^2(\boldsymbol{x}_k, \boldsymbol{\theta}_m) + \sigma^2_{w,k}}\right). \quad (14)$$

Since $\Lambda^k(y_k[n])$ in Eq. (12) is monotonically increasing with $y_k^2[n]$, there exists a unique value of γ_k such that $\Lambda^k(\sqrt{\gamma_k}) = 1$. Consequently, by the Karlin-Rubin Theorem, the test in Eq. (12) is replaced with the following equivalent energy test [31], which reduces the computational complexity of the local test from $\mathcal{O}(M)$ to $\mathcal{O}(1)$:

$$y_k^2[n] \underset{d_k[n]=0}{\overset{d_k[n]=1}{\gtrless}} \gamma_k\,. \quad (15)$$

This equals to the determination of the value of γ_k that solves $\Lambda^k(\sqrt{\gamma_k}) = 1$:

$$\sum_{m=1}^{M} \left(\varphi_m\, a_{m,k}\, e^{b_{m,k}\,\gamma_k}\right) = 1\,. \quad (16)$$

The left-hand side exhibits smoothness, convexity, and increases with γ_k. Consequently, convergence is assured, starting from any initial value $\gamma_k^{(0)}$ when employing the *Newton-Raphson method* (see [32]):

$$\gamma_k^{(q+1)} = \gamma_k^{(q)} - \frac{\sum_{m=1}^{M}\left(\varphi_m\, a_{m,k}\, e^{b_{m,k}\,\gamma_k^{(q)}}\right) - 1}{\sum_{m=1}^{M}\left(\varphi_m\, a_{m,k}\, b_{m,k}\, e^{b_{m,k}\,\gamma_k^{(q)}}\right)}\,, \quad (17)$$

where q denotes the iteration index.

We express the theoretical performance of the energy test in Eq. (15), necessary when designing the higher hierarchical layer represented by the FC. Specifically, for the kth sensor, the *probability of detection* ($P_{D,k}^{(m)}$) associated with the failure of the mth item and *probability of false alarm* ($P_{F,k}$) are found from Eq. (10) as in [33]:

$$\begin{aligned} P_{D,k}^{(m)} &\triangleq \mathbb{P}(d_k[n]=1|\mathcal{H}_m[n]=1) \\ &= \mathbb{P}\big(y_k^2[n] \geq \gamma_k \big| \mathcal{H}_m[n]=1\big) \\ &= 2\mathcal{Q}\left(\sqrt{\frac{\gamma_k}{\sigma^2_{\xi,m}\, g^2(\boldsymbol{x}_k, \boldsymbol{\theta}_m) + \sigma^2_{w,k}}}\right), \end{aligned} \quad (18)$$

$$\begin{aligned} P_{F,k} &\triangleq \mathbb{P}(d_k[n]=1|\mathcal{H}[n]=0) = \mathbb{P}\big(y_k^2[n] \geq \gamma_k \big| \mathcal{H}[n]=0\big) \\ &= 2\mathcal{Q}\left(\sqrt{\frac{\gamma_k}{\sigma^2_{w,k}}}\right). \end{aligned} \quad (19)$$

In this section, we used the static prior probabilities of item failure φ_m's obtained using Eq. (7). This causes the local thresholds γ_k's to be time-independent as well. However, our two proposed systems use a feedback system allowing the sensors to be designed using the time-dependent prior probabilities of item failure $\varphi_m[n]$'s calculated via Eq. (6). Its use results in time-dependent values of $\gamma_k[n]$'s (as the values of $\varphi_m[n]$'s are used for its calculation via Eq. (17)), $P_{D,k}^{(m)}[n]$'s, and $P_{F,k}[n]$'s. Thus, the iterative procedure shown in Eq. (17) must be continuously carried out by either the PPC (in the Three-Layer WSN) or the FC (in the Two-Layer WSN), transmitting to the kth sensor the correct value of $\gamma_k[n]$.

There are no energy consumption issues associated with this, as these transmissions are sent by the highest hierarchical layer to the sensors, which only require reception without significant energy expenditure.

IV. State of Practice

This section presents two WSN architectures commonly used for detection purposes and their related localization algorithms: (i) the Shewhart chart where the FC takes per-sample decisions based on the spatial aggregation of the local decisions in that instant; (ii) the CUSUM chart where, instead, the FC aggregates the sensors' decisions in space and time.

Unlike the proposed methods, the baseline architectures shown in this section are not equipped with a feedback mechanism. Moreover, they treat the failure rates λ_m's as deterministic parameters that can be obtained via literature.

A. Shewhart Chart

In this architecture, the optimal test for the FC, at the nth instant, is to perform a LRT on the collected vector $\boldsymbol{d}[n]$ to take a global decision $\widehat{\mathcal{H}}[n]$ [24]:

$$\begin{aligned} \Lambda^{\mathrm{FC}}(\boldsymbol{d}[n]) &\triangleq \frac{\mathbb{P}(\boldsymbol{d}[n]|\mathcal{H}[n]=1)}{\mathbb{P}(\boldsymbol{d}[n]|\mathcal{H}[n]=0)} \\ &= \frac{\sum_{m=1}^{M}\varphi_m \mathbb{P}(\boldsymbol{d}[n]|\mathcal{H}_m[n]=1)}{\mathbb{P}(\boldsymbol{d}[n]|\mathcal{H}[n]=0)} \\ &= \sum_{m=1}^{M}\left(\varphi_m \prod_{k=1}^{K}\ell_{m,k}(d_k[n])\right) \underset{\widehat{\mathcal{H}}[n]=0}{\overset{\widehat{\mathcal{H}}[n]=1}{\gtrless}} \gamma^*\,, \end{aligned} \quad (20)$$

with γ^* being the decision threshold and $\ell_{m,k}(d_k[n])$ representing the likelihood ratio of a generic local decision $d_k[n]$ with respect to the failure of the mth item:

$$\begin{aligned} \ell_{m,k}(d_k[n]) &\triangleq \frac{\mathbb{P}(d_k[n]|\mathcal{H}_m[n]=1)}{\mathbb{P}(d_k[n]|\mathcal{H}[n]=0)} \\ &= \left(\frac{P_{D,k}^{(m)}}{P_{F,k}}\right)^{d_k[n]} \left(\frac{1-P_{D,k}^{(m)}}{1-P_{F,k}}\right)^{1-d_k[n]}. \end{aligned} \quad (21)$$

Similarly, for the FC, it is feasible to calculate the (FC) *probability of detection* ($Q_D^{(m)}$) associated with the failure of the mth item and the *probability of false alarm* (Q_F):[2]

$$\begin{aligned} Q_D^{(m)} &\triangleq \mathbb{P}\Big(\widehat{\mathcal{H}}[n]=1\Big|\mathcal{H}_m[n]=1\Big) \\ &= \sum_{\boldsymbol{d}:\Lambda^{\mathrm{FC}}(\boldsymbol{d})\geq\gamma^*}\prod_{k=1}^{K}\left[\left(P_{D,k}^{(m)}\right)^{d_k}\left(1-P_{D,k}^{(m)}\right)^{1-d_k}\right], \end{aligned} \quad (22)$$

$$\begin{aligned} Q_F &\triangleq \mathbb{P}\Big(\widehat{\mathcal{H}}[n]=1\Big|\mathcal{H}[n]=0\Big) \\ &= \sum_{\boldsymbol{d}:\,\Lambda^{\mathrm{FC}}(\boldsymbol{d})\geq\gamma^*}\prod_{k=1}^{K}\Big[(P_{F,k})^{d_k}(1-P_{F,k})^{1-d_k}\Big]. \end{aligned} \quad (23)$$

The derivation of $Q_D^{(m)}$ and Q_F can be found in Appendix B.

We can also express the likelihood ratio at instant n of the decision $\mathcal{D}[n]$ with respect to the mth item, which will be useful in the next sections:

$$\mathcal{L}_m(\mathcal{D}[n]) \triangleq \frac{\mathbb{P}(\mathcal{D}[n]|\mathcal{H}_m[n]=1)}{\mathbb{P}(\mathcal{D}[n]|\mathcal{H}[n]=0)}$$

[2]The following definitions imply that if $\Lambda^{\mathrm{FC}}(\boldsymbol{d}) = \gamma^*$, then $\widehat{\mathcal{H}}[n] = 1$.

$$= \left(\frac{Q_D^{(m)}}{Q_F}\right)^{\mathcal{D}[n]} \left(\frac{1-Q_D^{(m)}}{1-Q_F}\right)^{1-\mathcal{D}[n]} . \quad (24)$$

It is important to observe that Eqs. (22) and (23) can be precisely computed using a finite number of operations because the number of potential outcomes of $\Lambda^{\text{FC}}(\boldsymbol{d})$ amounts to 2^K. If $\widehat{\mathcal{H}}[n] = 1$, the FC runs a localization algorithm to identify the faulty item. For this algorithm, it is possible to use the following *Maximum A-Posteriori* (MAP) estimator:

$$\widehat{m}[i] = \underset{m=1,\ldots,M}{\arg\max} \left(\varphi_m \prod_{k=1}^{K} \ell_{m,k}(d_k[n])\right), \quad \widehat{\boldsymbol{\theta}}[i] = \boldsymbol{\theta}_{\widehat{m}[i]} , \quad (25)$$

with i indicating the number of times an alarm has been raised, up to instant n.

B. CUSUM Chart

This section describes the CUSUM algorithm to be performed by the FC upon collecting the sensors' local decisions in time.

The CUSUM procedure has the following form:

$$\max_{n_0 \le j \le n} \ln \frac{\mathbb{P}(\boldsymbol{d}[n], \ldots, \boldsymbol{d}[j] | \mathcal{H}[j] = 1)}{\mathbb{P}(\boldsymbol{d}[n], \ldots, \boldsymbol{d}[j] | \mathcal{H}[j] = 0)} \underset{\widehat{\mathcal{H}}[n]=0}{\overset{\widehat{\mathcal{H}}[n]=1}{\gtrless}} \gamma^* . \quad (26)$$

Eq. (26) implicitly estimates the instant corresponding to the system-state change via ML estimation, with the knowledge that the system does not self-repair when in a faulty state. However, Eq. (26) uses the system's state variable $\mathcal{H}[n]$, posing a problem as the only available likelihoods are with respect to the failure of the individual items, and have been explicated in Eq. (18). Due to the finite number of items M, we can use the *Generalized CUSUM* (G-CUSUM) algorithm to address this issue. The following is the G-CUSUM rule:

$$\begin{aligned}\mathcal{C}[n] &\triangleq \max_{n_0 \le j \le n} \ln \frac{\max_m \mathbb{P}(\boldsymbol{d}[n], \ldots, \boldsymbol{d}[j] | \mathcal{H}_m[j] = 1)}{\mathbb{P}(\boldsymbol{d}[n], \ldots, \boldsymbol{d}[j] | \mathcal{H}[j] = 0)} \\ &= \max_m \max_{n_0 \le j \le n} \ln \frac{\mathbb{P}(\boldsymbol{d}[n], \ldots, \boldsymbol{d}[j] | \mathcal{H}_m[j] = 1)}{\mathbb{P}(\boldsymbol{d}[n], \ldots, \boldsymbol{d}[j] | \mathcal{H}[j] = 0)} \\ &= \max_m \mathcal{C}_m[n] \underset{\widehat{\mathcal{H}}[n]=0}{\overset{\widehat{\mathcal{H}}[n]=1}{\gtrless}} \gamma^* , \end{aligned} \quad (27)$$

which is equivalent to a joint estimation (via ML) of the failure instant and the faulty item. $\mathcal{C}_m[n]$ can be expressed with a *recursive* form starting from its definition and exploiting the independence of the sensor's decision in time:

$$\begin{aligned}\mathcal{C}_m[n] &\triangleq \max_{n_0 \le j \le n} \ln \frac{\mathbb{P}(\boldsymbol{d}[n], \ldots, \boldsymbol{d}[j] | \mathcal{H}_m[j] = 1)}{\mathbb{P}(\boldsymbol{d}[n], \ldots, \boldsymbol{d}[j] | \mathcal{H}[j] = 0)} \\ &= \max_{n_0 \le j \le n} \sum_{i=j}^{n} \ln \frac{\mathbb{P}(\boldsymbol{d}[i] | \mathcal{H}_m[j] = 1)}{\mathbb{P}(\boldsymbol{d}[i] | \mathcal{H}[j] = 0)} . \end{aligned} \quad (28)$$

For $n > n_0$, we can extract the following recursive form:

$$\begin{aligned}\mathcal{C}_m[n] &= \max\left\{0, \max_{n_0 \le j \le n-1} \sum_{i=j}^{n-1} \ln \frac{\mathbb{P}(\boldsymbol{d}[i] | \mathcal{H}_m[j] = 1)}{\mathbb{P}(\boldsymbol{d}[i] | \mathcal{H}[j] = 0)}\right\} \\ &\quad + \ln \frac{\mathbb{P}(\boldsymbol{d}[n] | \mathcal{H}_m[n] = 1)}{\mathbb{P}(\boldsymbol{d}[n] | \mathcal{H}[n] = 0)} \\ &= \max\{0, \mathcal{C}_m[n-1]\} + \ln \prod_{k=1}^{K} \ell_{m,k}(d_k[n]) \\ &= (\mathcal{C}_m[n-1])^+ + \sum_{k=1}^{K} \ln \ell_{m,k}(d_k[n]) . \end{aligned} \quad (29)$$

On the other hand, when $n = n_0$, by simple application of the definition of $\mathcal{C}_m[n]$, we obtain that $\mathcal{C}_m[n_0] = \sum_{k=1}^{K} \ln \ell_{m,k}(d_k[n_0])$. This results in the following rule:

$$\mathcal{C}_m[n] = \begin{cases} \sum_{k=1}^{K} \ln(\ell_{m,k}(d_k[n_0])), & \text{if } n = n_0 \\ (\mathcal{C}_m[n-1])^+ + \sum_{k=1}^{K} \ln(\ell_{m,k}(d_k[n])), & \text{if } n > n_0 \end{cases} . \quad (30)$$

Also for the case of the CUSUM, if $\widehat{\mathcal{H}}[n] = 1$, a localization procedure is readily available. Such a procedure is the following ML estimator:

$$\widehat{m}[i] = \underset{m}{\arg\max}\, \mathcal{C}_m[n] , \quad \widehat{\boldsymbol{\theta}}[i] = \boldsymbol{\theta}_{\widehat{m}[i]} , \quad (31)$$

with i indicating the number of times an alarm has been raised, up to instant n.

V. Three-Layer Fusion Architecture

Here, we present the Three-Layer fusion architecture, which consists of an evolution of the simpler Shewhart chart. In this approach, we add the PPC layer, whose task is to filter the FC's decisions in time using a reliability-based strategy.

A. Fusion Center Detection

In our proposed Three-Layer architecture, the FC, at the nth instant, performs a ML detection, whose task is to fuse the components of $\boldsymbol{d}[n]$ into a single decision $\mathcal{D}[n]$:

$$\Lambda_n^{\text{FC}}(\boldsymbol{d}[n]) \underset{\mathcal{D}[n]=0}{\overset{\mathcal{D}[n]=1}{\gtrless}} 1 , \quad (32)$$

where $\Lambda_n^{\text{FC}}(\boldsymbol{d}[n])$ differs from the statistic in Eq. (20) due to the presence of the feedback system that allows the PPC to transmit parameters to the FC. This feedback allows Eq. (32) to exploit time-dependent parameters such as $\varphi_m[n]$'s, $P_{D,k}^{(m)}[n]$'s, $P_{F,k}[n]$'s, and $\ell_{m,k}^n(d_k[n])$. The values of these parameters are sent to the FC by the PPC.

For this case, the (FC) time-dependent *probability of detection* ($Q_D^{(m)}[n]$) associated with the failure of the mth item and the time-dependent *probability of false alarm* ($Q_F[n]$) at the nth instant can be computed. These are calculated using Eqs. (22) and (23) where the values of $\Lambda^{\text{FC}}(\boldsymbol{d})$, $P_{D,k}^{(m)}$'s, and $P_{F,k}$'s are substituted with those of $\Lambda_n^{\text{FC}}(\boldsymbol{d})$, $P_{D,k}^{(m)}[n]$'s, and $P_{F,k}[n]$'s, respectively. Consequently, the decision likelihood will also be time-dependent (indicated with $\mathcal{L}_m^n(\mathcal{D}[n])$).

B. Post-Processing Center Detection

The primary responsibility of the PPC is to receive $\mathcal{D}[n]$ and determine if an alarm should be triggered. In contrast to local and FC detection, the PPC *incorporates the understanding of the failure model* and utilizes all $\mathcal{D}[j]$ values, where $j = n_0, \ldots, n$, to enact a robust quickest fault detection strategy. For this task, the PPC acts as a Posterior Detector performing a test on $\mathbb{P}(\mathcal{H}[n] = 1|\boldsymbol{\mathcal{D}}[n])$, exploiting Eq. (5) which leads to the following test:

$$\begin{aligned}\Lambda_n^{\text{PPC}}(\boldsymbol{\mathcal{D}}[n]) &\triangleq \sum_{m=1}^{M} \mathbb{P}(\mathcal{H}_m[n] = 1|\boldsymbol{\mathcal{D}}[n]) \\ &= \sum_{m=1}^{M} \mathcal{R}_m^{\text{PPC}}[n] \underset{\widehat{\mathcal{H}}[n]=0}{\overset{\widehat{\mathcal{H}}[n]=1}{\gtrless}} \gamma^* \,, \end{aligned} \tag{33}$$

where it can be seen that our approach aligns with an *optimal Bayesian perspective* (treating the change point as a random variable whose pdf derives from the reliability model discussed in Sec. II-A). This approach corresponds to the Shiryaev decision rule [30].

The calculation of $\mathcal{R}_m^{\text{PPC}}[n]$ can be expressed recursively via Eq. (34) as shown at the bottom of the page, requiring the storage of only the M values of $\mathcal{R}_m^{\text{PPC}}[n-1]$'s and the value of $\mathcal{D}[n]$, instead of the $(n - n_0 + 1)$ values contained in $\boldsymbol{\mathcal{D}}[n]$. Its derivation is given in Appendix C. Eq. (34) uses $\widehat{\lambda}_m[n]$ since failure rates are considered random variables whose realization must be estimated. The description of this task is given below.

C. Post-Processing Center Localization

When $\widehat{\mathcal{H}}[n] = 1$, the PPC localizes the faulty item for the generic ith time by selecting the index m that maximizes the posterior probability of item failure $\mathcal{R}_m^{\text{PPC}}[n]$ resulting in the following MAP estimator:

$$\widehat{m}[i] = \arg\max_m \mathcal{R}_m^{\text{PPC}}[n] \,, \quad \widehat{\boldsymbol{\theta}}[i] = \boldsymbol{\theta}_{\widehat{m}[i]} \,, \tag{35}$$

with i indicating the number of times an alarm has been raised, up to instant n.

D. Post-Processing Center Failure Rate Estimation

The precise failure rate of the unspecified mth item often remains unknown, although literature may frequently offer an estimate (referred to here as $\lambda_{m,0}$) along with its associated variance (referred to as ν_m). Nonetheless, literature data is often derived from a limited number of experiments on items that may not be identical to those within the system (or under the same operating conditions). Consequently, the PPC treats each λ_m as a random variable in this context. This differs from the Shewhart and CUSUM charts that see the failure rates as deterministic parameters and exploit the literature values $\lambda_{m,0}$'s for their calculations.

In specific terms, when the PPC raises an alarm, the system is halted, and an inspection is conducted to assess the system's status. If the mth item's jth failure is confirmed, it becomes feasible to update the estimate of λ_m using $T_{m,j}$. Since $T_{m,j}$ is not directly accessible, the working assumption here is that $T_{m,j} \approx T_{m,j}^*$, a condition met when $\varepsilon_{m,j} \ll \lambda_m^{-1}$ (i.e., when the time delay incurred by the system in detecting the fault is significantly shorter than the mean lifetime of the item).

Utilizing the vector $\boldsymbol{T}_m[j] \triangleq \begin{bmatrix} T_{m,1} & \cdots & T_{m,j} \end{bmatrix}^{\text{T}}$, the PPC calculates the subsequent *Minimum Mean Square Error (MMSE) Estimator* for the mth item:

$$\widehat{\lambda}_{m,j} = \mathbb{E}(\lambda_m|\boldsymbol{T}_m[j]) \,. \tag{36}$$

To compute this expectation, the PPC is required to acquire the (posterior) pdf of $\lambda_m|\boldsymbol{T}_m[j]$. Given that $T_{m,j} \sim \text{Exp}(\lambda_m)$, we incorporate previous knowledge about the lifetime of the mth item by modeling $\lambda_m \sim \text{Gamma}(\alpha_{m,0}, \beta_{m,0})$. Here, $\alpha_{m,0} \triangleq (\lambda_{m,0}^2/\nu_m)$ and $\beta_{m,0} \triangleq (\lambda_{m,0}/\nu_m)$ are computed based on existing literature values. We opt for the Gamma distribution because it is the *conjugate prior* of the Exponential distribution (see [34]). Leveraging the use of a conjugate prior, it becomes apparent that $\lambda_m|\boldsymbol{T}_m[j] \sim \text{Gamma}(\alpha_{m,j}, \beta_{m,j})$, with the Gamma parameters calculated *recursively* by the PPC as $\alpha_{m,j} = (\alpha_{m,j-1} + 1)$ and $\beta_{m,j} = (\beta_{m,j-1} + T_{m,j})$. Once the parameters of the (Gamma) posterior pdf of $\lambda_m|\boldsymbol{T}_m[j]$ are determined, the corresponding MMSE estimator following the jth failure is computed using properties of the Gamma distribution:

$$\widehat{\lambda}_{m,j} = \frac{\alpha_{m,j}}{\beta_{m,j}} \,. \tag{37}$$

At any given time n, the most recent estimate of λ_m corresponds to $\widehat{\lambda}_{m,\mathcal{S}_m[n-1]}$, where $\mathcal{S}_m[n-1]$ denotes the count of failures for the mth item reported up to time $(n-1)$. For brevity, we will refer to this estimate as $\widehat{\lambda}_m[n]$.

E. Post-Processing Center Parameters Calculation and Transmission

The last step of the PPC at instant n, after updating (if needed) the estimates of the failure rates of the respective items, consists of obtaining the values of $\varphi_m[n+1]$'s via Eq. (6) exploiting $\widehat{\lambda}_m[n+1]$. Next, via Eq. (17), it computes and delivers the values of the local thresholds $\gamma_k[n+1]$'s to the respective sensors to be used for the next local detection.

Once produced the thresholds, the PPC proceeds to calculate the values of $P_{D,k}^{(m)}[n+1]$'s and $P_{F,k}[n+1]$'s via Eqs. (18) and (19) and sends them to the FC alongside the values of $\varphi_m[n+1]$'s. This allows the FC to evaluate $\Lambda_{n+1}^{\text{FC}}(\boldsymbol{d}[n+1])$ via Eq. (20).

In the final step, the PPC computes the values of $Q_D^{(m)}[n+1]$'s and $Q_F[n+1]$ using Eqs. (22) and (23) to be used by the

$$\mathcal{R}_m^{\text{PPC}}[n] \triangleq \mathbb{P}(\mathcal{H}_m[n] = 1|\boldsymbol{\mathcal{D}}[n]) = \begin{cases} \left[1 + \frac{1}{\mathcal{L}_m^{n_0}(\mathcal{D}[n_0])}\left(\frac{1}{1-e^{-\widehat{\lambda}_m[n_0]\Delta t}} - 1\right)\right]^{-1}, & \text{if } n = n_0 \\ \left[1 + \frac{1}{\mathcal{L}_m^{n}(\mathcal{D}[n])}\left(\frac{1}{1-e^{-\widehat{\lambda}_m[n]\Delta t}(1-\mathcal{R}_m^{\text{PPC}}[n-1])} - 1\right)\right]^{-1}, & \text{if } n > n_0 \end{cases} \tag{34}$$

PPC itself in the recursive computation of $\Lambda^{\text{PPC}}_{n+1}(\boldsymbol{\mathcal{D}}[n+1])$ via Eqs. (33) and (34).

VI. Two-Layer Fusion Architecture

This section presents the Two-Layer fusion approach consisting of an evolution of the Three-Layer approach. Here, the FC handles both the spatial and temporal fusion using the same reliability-based strategy as in the PPC. This method is proposed as an improvement of the CUSUM chart introduced in Sec. IV-B. In our proposed Two-Layer architecture, the FC performs three stages of operations that are analogous to those made by the PPC described in Sec. V.

A. Fusion Center Detection

The FC, upon receiving $\boldsymbol{d}[n]$, establishes whether an alarm should be raised. As with the PPC, the FC now utilizes all $\boldsymbol{d}[j]$ values, where $j = n_0, \dots, n$, to perform a test on $\mathbb{P}(\mathcal{H}[n] = 1|\boldsymbol{d}[n], \dots, \boldsymbol{d}[n_0])$:

$$\begin{aligned}\Lambda^{\text{FC}}_n(\boldsymbol{d}[n], \dots, \boldsymbol{d}[n_0]) &\triangleq \sum_{m=1}^{M} \mathbb{P}(\mathcal{H}_m[n] = 1|\boldsymbol{d}[n], \dots, \boldsymbol{d}[n_0]) \\ &= \sum_{m=1}^{M} \mathcal{R}^{\text{FC}}_m[n] \underset{\widehat{\mathcal{H}}[n]=0}{\overset{\widehat{\mathcal{H}}[n]=1}{\gtrless}} \gamma^* \,, \end{aligned} \tag{38}$$

where it is easy to see the similarity with Eq. (33). However, in this case, the FC processes the unfused local decisions.

Also here, $\mathcal{R}^{\text{FC}}_m[n]$ can be expressed recursively via Eq. (39) as shown at the bottom of the page allowing the FC, at the nth instant, to store only the M values of $\mathcal{R}^{\text{FC}}_m[n-1]$'s and the vector $\boldsymbol{d}[n]$. The proof of Eq. (39) is analogous to that given in Appendix C.

B. Fusion Center Localization

Analogously to the Three-Layer architecture, the FC can provide an estimate of the faulty item by maximizing the posterior probability of item failure to raise the ith alarm if $\widehat{\mathcal{H}}[n] = 1$, resulting in the following MAP estimator:

$$\widehat{m}[i] = \arg\max_m \mathcal{R}^{\text{FC}}_m[n] \,, \quad \widehat{\boldsymbol{\theta}}[i] = \boldsymbol{\theta}_{\widehat{m}[i]} \,, \tag{40}$$

with i indicating the number of times an alarm has been raised, up to instant n.

C. Fusion Center Failure Rate Estimation

As in the Three-Layer architecture, the FC provides an updated estimate of the failure rates λ_m's by treating them as random variables. At each time n, $\widehat{\lambda}_m[n]$ indicates the most recent estimate of λ_m obtained by time $(n-1)$.

TABLE I: Computational complexity of the architectures

Architecture	Layer	Task	Complexity
Shewhart chart	FC	Detection (including localization)	$\mathcal{O}(KM)$
G-CUSUM chart	FC	Detection (including localization)	$\mathcal{O}(KM)$
Three-Layer Fusion Architecture	FC	Detection	$\mathcal{O}(KM)$
	PPC	Detection (incl. loc.)	$\mathcal{O}(M)$
		Failure Rates Update	$\mathcal{O}(1)$ *per item*
		$\varphi_m[n+1]$'s Calculation	$\mathcal{O}(M)$
		$\gamma_k[n+1]$'s Calculation	$\mathcal{O}(KM)$ *per iter.*
		$P_{F,k}[n+1]$'s Calculation	$\mathcal{O}(K)$
		$P^{(m)}_{D,k}[n+1]$'s Calculation	$\mathcal{O}(KM)$
		$Q_F[n+1]$ Calculation	$\mathcal{O}(2^K)$
		$Q^{(m)}_D[n+1]$'s Calculation	$\mathcal{O}(2^K M)$
Two-Layer Fusion Architecture	FC	Detection (incl. loc.)	$\mathcal{O}(KM)$
		Failure Rates Update	$\mathcal{O}(1)$ *per item*
		$\varphi_m[n+1]$'s Calculation	$\mathcal{O}(M)$
		$\gamma_k[n+1]$'s Calculation	$\mathcal{O}(KM)$ *per iter.*
		$P_{F,k}[n+1]$'s Calculation	$\mathcal{O}(K)$
		$P^{(m)}_{D,k}[n+1]$'s Calculation	$\mathcal{O}(KM)$

D. Fusion Center Parameters Calculation and Transmission

In the final stage of the process, the FC proceeds to update the estimates of the failure rates and subsequently computes the values of $\varphi_m[n+1]$'s using Eq. (6). Following this, it calculates and transmits the values of $\gamma_k[n+1]$'s to the respective sensors for use in the forthcoming energy test, as per Eq. (17).

After obtaining the thresholds, the FC calculates the values of $P^{(m)}_{D,k}[n+1]$'s and $P_{F,k}[n+1]$'s based on Eqs. (18) and (19). These values play a key role in the (recursive) computation of $\Lambda^{\text{FC}}_{n+1}(\boldsymbol{d}[n+1], \dots, \boldsymbol{d}[n_0])$ using Eqs. (38) and (39).

VII. Computational Complexity

This section is focused on the computational complexity of the tasks performed in all the architectures previously outlined.

All the architectures share the same edge-layer design in which each sensor performs an energy test at each discrete instant. Specifically, we were able to lower the computational complexity of the local tests from $\mathcal{O}(M)$ to $\mathcal{O}(1)$, as previously discussed in Sec. III.

Tab. I shows the computational complexity of each architecture with a subdivision by layer (excluding the edge layer) and the task performed. We can notice that the detection techniques relying on the Shewhart and CUSUM charts do not differ in computational complexity thanks to the recursive form of the CUSUM chart shown in Eq. (30). The detection rules used by the FC in both proposed architectures hold the same complexity.

$$\mathcal{R}^{\text{FC}}_m[n] \triangleq \mathbb{P}(\mathcal{H}_m[n] = 1|\boldsymbol{d}[n], \dots, \boldsymbol{d}[n_0]) = \begin{cases} \left[1 + \left(\prod_{k=1}^{K} \ell^{n_0}_{m,k}(d_k[n_0])\right)^{-1} \left(\frac{1}{1-e^{-\lambda_m[n_0]\Delta t}} - 1\right)\right]^{-1}, & \text{if } n = n_0 \\ \left[1 + \left(\prod_{k=1}^{K} \ell^{n}_{m,k}(d_k[n])\right)^{-1} \left(\frac{1}{1-e^{-\lambda_m[n]\Delta t}(1-\mathcal{R}^{\text{FC}}_m[n-1])} - 1\right)\right]^{-1}, & \text{if } n > n_0 \end{cases} \tag{39}$$

An essential difference between the proposed and the baseline architectures is, however, the existence of the feedback system present in the proposed algorithms.

In the Three-Layer architecture, the PPC has a low-complexity detection rule, as this does not perform spatial aggregation of the local decisions. However, the feedback system requires the PPC to obtain the parameters to be transmitted to the sensors and the FC. The calculation of the thresholds $\gamma_k[n+1]$'s is an iterative procedure with a complexity of $\mathcal{O}(KM)$ *per iteration*. Other calculations such as $\varphi_m[n+1]$'s, $\gamma_k[n+1]$'s, $P_{F,k}[n+1]$'s, and $P_{D,k}^{(m)}[n+1]$'s have an overall computational complexity of $\mathcal{O}(KM)$. The highest complexity resides in the calculation of $Q_F[n+1]$'s and $Q_D^{(m)}[n+1]$'s as this is $\mathcal{O}(2^K M)$, making the Three-Layer architecture unsuitable when a high number of sensors is used.

On the other hand, the Two-Layer architecture transfers the spatial aggregation from the PPC to the FC, which now has to perform a spatio-temporal aggregation as well as the task of obtaining the parameters to be transmitted to the sensors. This, although it increases the absolute number of operations, keeps the computational complexity of the operations to be performed by the FC constant at $\mathcal{O}(KM)$, resulting in an overall reduction of complexity thanks to the removal of the operations requiring exponential time.

It is worth noticing that the localization techniques in all four architectures do not require any extra operation and, therefore, do not contribute to an increase in computational complexity. The reason is that such techniques are all based on function maximization via grid search, which has a complexity of $\mathcal{O}(KM)$ (or $\mathcal{O}(M)$ in the Three-Layer architecture). However, such maximization has already been obtained during the detection step. Therefore, in order to complete the localization task, it is simply necessary to store the index generating the highest among the function's values obtained during the detection stage.

VIII. Case Study

A. Simulation Setup

The Goliat FPSO is an offshore oil platform situated in the Norwegian Barents Sea. This platform uses a *subsea production system* composed of various templates placed on the seabed for its operations.[3] The challenging aspect of this setup is that oil leaks occur in deep waters, rendering their detection even more complex. Additionally, due to the significant depths involved, inspections necessitate the use of *remotely operated vehicles* or *autonomous underwater vehicle*, incurring high costs, thus emphasizing the need to minimize false alarms [9]. Simultaneously, offshore operations are subject to stringent environmental regulations, which demand the rapid detection of spills to minimize the dispersion of hydrocarbons [36]. Underwater oil leaks exhibit a distinctive feature in the form of acoustic signals that can be detected using passive acoustic sensors [37], [38]. In this specific setup, each template is equipped with a manifold that is under the surveillance of three passive acoustic sensors. These sensors measure sound pressure as an integral component of the leak detection system [28], [39].

[3]For further insights into subsea production systems, please refer to [35]

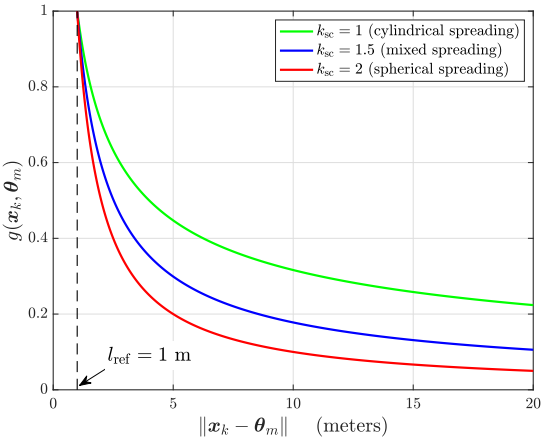

Fig. 3: Attenuation function vs. distance between sensor and faulty item.

TABLE II: Simulation input parameters

Parameter	Value	Note / Reference
Ref. Frequency	2.5 kHz	[43]
Temperature	3.8 °C	[44]
Salinity	35 ‰	[44]
Depth	350 m	[39]
pH	8	[45]
k_{sc}	1.5	[46]
l_{ref}	1 m	–
Simulated time	15 yr	[47]
Δt	15 min	–
$\sigma_{w,k}^2$	1	$\forall k$
$\text{SNR}_{m,k}$	0/5/10 dB	$\forall\, m, k$

A reliability analysis recognized $M = 20$ items of interest assumed to be positioned at the same height as the sensors, as shown in Fig. 4. The algorithms described earlier are assumed to have been integrated into the existing system to assess their performance. The attenuation function used is as follows [10]:

$$g(\boldsymbol{x}_k, \boldsymbol{\theta}_m) = \sqrt{\left(\frac{l_{\text{ref}}}{\|\boldsymbol{x}_k - \boldsymbol{\theta}_m\|}\right)^{k_{\text{sc}}} 10^{(l_{\text{ref}} - \|\boldsymbol{x}_k - \boldsymbol{\theta}_m\|)\alpha 10^{-4}}}\,, \tag{41}$$

where l_{ref} and $\|\boldsymbol{x}_k - \boldsymbol{\theta}_m\|$ are expressed in meters, α is the seawater absorption coefficient in dB/km, and k_{sc} is the dimensionless spreading coefficient. The value of α was determined using the *Francois & Garrison equation* [40], [41]. At the same time, the underwater speed of sound was calculated based on the *Chen & Millero equation* [42], utilizing the input parameters listed in Tab. II. The coefficients of these models are found in [10]. Fig. 3 shows the attenuation of the signal emitted by a faulty item with respect to its distance to a generic sensor using the parameters in Tab. II at varying values of k_{sc}.

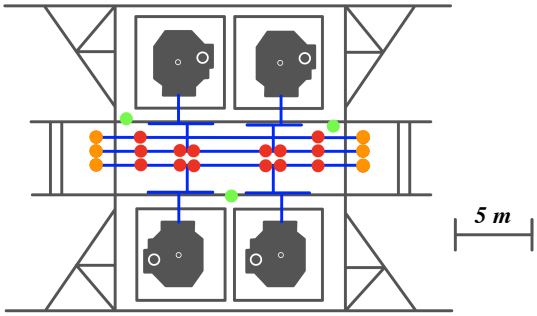

Fig. 4: Goliat's template: the structural components are represented in gray, the manifold in blue, the sensors in green, the valves in red, and the connectors in orange.

TABLE III: Literature failure rates of components in subsea manifolds

Item Category	$\lambda_{m,0}$ (in yr^{-1})	ν_m (in yr^{-2})
Valve, process isolation	7.3000×10^{-3}	7.0715×10^{-5}
Connector	9.5812×10^{-4}	2.4649×10^{-6}

The proposed Three-Layer architecture is compared with the WSN presented in Sec. IV-A. This is because the Three-Layer WSN is designed to be installed over an existing architecture where the final decision is taken by a FC via Shewhart chart by adding a PPC and a feedback system. The Two-Layer architecture is instead compared with the WSN described in Sec. IV-B performing detection via the CUSUM chart. As stated previously, the architectures used for comparison reasons lack a feedback system. The Shewhart and CUSUM charts use the stationary prior probabilities of item failure seen in Eq. (7), where the values of λ_m's are substituted by $\lambda_{m,0}$'s as the former are unknown.

The numerical results were derived via simulation consisting of 200 Monte Carlo runs using Matlab.[4] In these simulations, each run emulated the operational lifespan of the platform, neglecting inspection and maintenance times. The simulated time, the value of Δt, and the diverse $\text{SNR}_{m,k} \triangleq \sigma^2_{\xi,m}/\sigma^2_{w,k}$ values can be found in Tab. II. At each run, a new set of realizations of the M Poisson processes and their corresponding failure rates was generated, with λ_m values drawn from a Gamma distribution using central moments obtained from Tab. III, where literature values were sourced from the *OREDA Handbook* [48].

In order to summarize the main detection results, it is necessary to introduce the following metrics:

$$P_{10} \triangleq \mathbb{P}\Big(\widehat{\mathcal{H}}[n] = 1 \Big| \mathcal{H}[n] = 0\Big) \,, \tag{42}$$

$$P_1 \triangleq \mathbb{P}(\mathcal{H}[n] = 1) \,, \tag{43}$$

$$\text{ADD} \triangleq \mathbb{E}(\varepsilon_{m,j})/\Delta t \,, \tag{44}$$

[4]Each set of 200 runs was performed for various γ^* values to generate the performance curves.

where P_{10} is the *Probability of False Alarm*, P_1 is the *Probability of Faulty State*, and ADD is the *Average Detection Delay*. The localization performances are instead evaluated using the *Root Mean Square Error* (RMSE) between the estimated position of the leak and its actual location. Figs. 5, 6, and 7 show the previously introduced metrics as P_{10} varies in $[10^{-3}, 1]$, at different values of SNR (see Tab. II). Higher values (resp. lower values) of P_{10} can be obtained by decreasing (resp. increasing) the threshold γ^* in the highest architectural layer. The choice of having P_{10} to be on the abscissa in all plots is aimed at improving the readability of the results.

B. Detection Results

By looking at the plots in Figs. 5a, 6a, and 7a, it is immediately visible how ADD greatly decreases as the SNR increases regardless of the employed architecture, once P_{10} is fixed. In particular, the ADD shows a decreasing trend with respect to P_{10} as a consequence of the lowering of threshold γ^*, with $\text{ADD} \to 0$ as $P_{10} \to 1$, for all the methods. Specifically, for low values of P_{10}, the proposed Two-Layer architecture shows the lowest values of ADD among the four outlined in this work. It is worth noticing that the Shewhart chart is unable to operate at $P_{10} < 10^{-2}$ due to the lack of temporal integration in the FC. Such a limitation is overcome by using the PPC with our proposed Three-Layer architecture that shows performances equivalent to the Shewhart chart with the further benefit of being able to work at $P_{10} < 10^{-2}$. Moreover, at low SNR, the Three-Layer architecture tends to perform slightly better than the CUSUM chart, highlighting the benefits of a Bayesian approach, especially at low SNR.

These trends in the performances are also observed when evaluating P_1 representing the fraction of time that the system spends in a faulty state. Figs. 5b, 6b, and 7b show a similarity in behavior between the ADD and P_1, as we vary P_{10}. This shows the trade-off between a low P_{10} and a low P_1, which must be addressed when choosing the proper threshold γ^*. As it is desirable to work at low values of P_{10}, it is vital to select an architecture that can limit the effect of having a higher threshold on P_1. Because of the above-mentioned similarities, it is easy to see that, also in this case, the Two-Layer architecture provides the best performances by reaching the lowest values of P_1, given a fixed P_{10}.

It must be mentioned that even in the hypothetical case of $P_{10} = 1$, we will have that $P_1 > 0$ as no architecture can prevent a leak from happening but can only reduce the detection delay with the effect of minimizing P_1.

C. Localization Results

The localization results displayed in Figs. 5c, 6c, and 7c show that, for the case of the Two-Layer proposed architecture and the CUSUM chart, as we lower P_{10}, we simultaneously lower the localization RMSE causing a trade-off between localization accuracy and a quick detection. The explanation for this behavior is that raising the detection threshold has the double effect of increasing the ADD, which simultaneously means that the highest hierarchical layer has collected more inputs, therefore improving the identification of the faulty

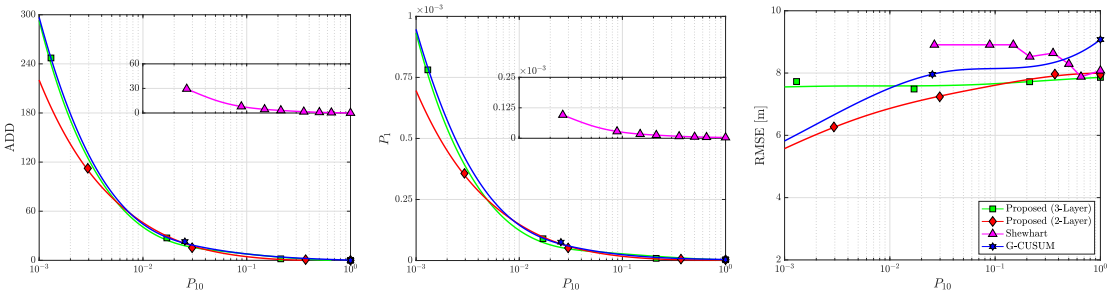

(a) P_{10} vs. ADD (b) P_{10} vs. P_1 (c) P_{10} vs. RMSE

Fig. 5: Performance curves at $\mathrm{SNR}_{m,k} = 0\,\mathrm{dB}$, $\forall m, k$.

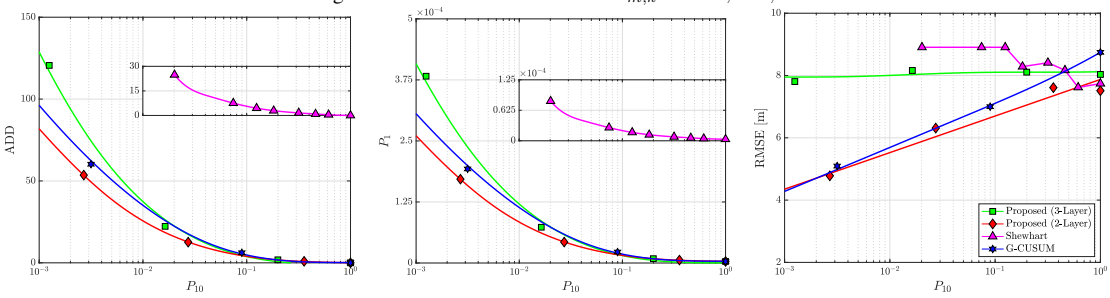

(a) P_{10} vs. ADD (b) P_{10} vs. P_1 (c) P_{10} vs. RMSE

Fig. 6: Performance curves at $\mathrm{SNR}_{m,k} = 5\,\mathrm{dB}$, $\forall m, k$.

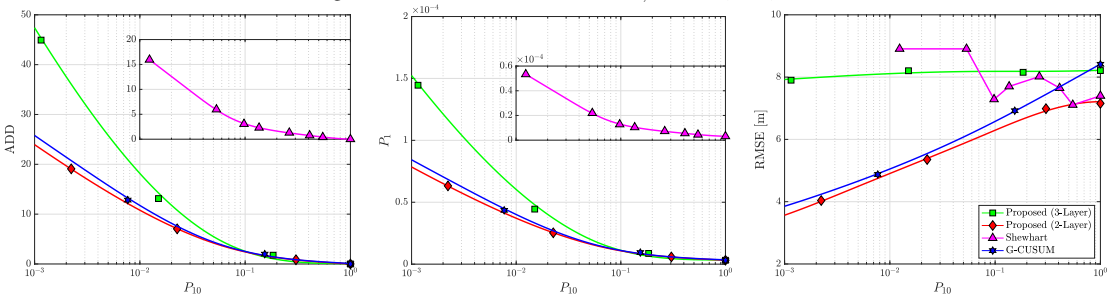

(a) P_{10} vs. ADD (b) P_{10} vs. P_1 (c) P_{10} vs. RMSE

Fig. 7: Performance curves at $\mathrm{SNR}_{m,k} = 10\,\mathrm{dB}$, $\forall m, k$.

item. This does not apply to the Shewhart chart and the Three-Layer architecture: the RMSE observed when employing the Shewhart chart does not have a monotonic behavior (as well as not being able to operate at $P_{10} < 10^{-2}$), while the Three-Layer architecture, as we lower P_{10}, has a virtually null localization improvement.

The behavior associated with the Shewhart chart is given by the nature of its localization algorithm, which produces estimates using only the last vector of local decisions as an input. Such a lack of time aggregation prevents the localization algorithm from updating its estimate as new local decisions are collected over time, which would cause the RMSE to decrease together with P_{10}, like in the case of the Two-Layer architecture and the CUSUM chart. Interestingly, we observe that in the Shewhart chart, as P_{10} decreases, the behavior of the RMSE is hard to predict. Still, in general, it tends to reach its maximum value when P_{10} reaches its minimum. In fact, for a system performing detection and localization without time aggregation, a trade-off exists between a low P_{10} and localization RMSE. The reason for this is that a lower value of P_{10} means that the threshold required to trigger an alarm must be increased with a consequent effect of triggering alarms only when a higher number of sensors sends a positive detection. However, a low threshold can compromise the ability of the system to localize the faulty item, as there is a loss of correlation between the position of the faulty item and the location of the activated sensors. This can be brought to its limit case of a system detecting a leak via Shewhart chart only when $\Lambda^{\mathrm{FC}}(\boldsymbol{d}[n]) \geq$

γ^*, with $\gamma^* = \Lambda^{\mathrm{FC}}\Big(\big[d_1[n]=1 \quad \cdots \quad d_K[n]=1\big]^{\mathrm{T}}\Big)$ (i.e., a system that triggers an alarm only when all the sensors send an alarm to the FC). In such a scenario, every alarm would be accompanied by the same localization result regardless of the position of the faulty item.

The Three-Layer architecture, as in the case of the Shewhart chart, does not provide effective results in terms of localization RMSE, confirming its main purpose of being a way to lower the probability of false alarm of the Shewhart chart. Unlike the Shewhart chart, the Three-Layer architecture performs a time aggregation in its highest hierarchical layer (the PPC), creating more stability in the behavior of the localization RMSE, as P_{10} changes. However, such time aggregation is performed on the FC's decisions over time that do not contain any spatial information regarding the sensors that contributed to such decisions. The consequence is an almost constant value of localization RMSE since the system tends to identify as faulty those items that at a generic moment show the highest value of $\widehat{\lambda}_m[n]$, regardless of the spatial location of the activated sensors since this information is unknown for the PPC.

This problem is addressed by the Two-Layer architecture and the CUSUM chart, where the FC performs both time and spatial aggregation of the sensors' local decisions over time. As in the discussion of the detection performances, we notice how the Two-Layer approach outperforms the rest of the architectures in terms of localization RMSE.

D. Final Remarks

In conclusion, the Two-Layer architecture provides the lowest values of ADD, especially at low values of P_{10}, where it guarantees a low P_1, which is a critical goal for Oil and Gas applications. On the other hand, the Three-Layer architecture has proven to be an adequate tool to upgrade an existing network performing the Shewhart chart, especially when low SNR are involved where its detection performances are comparable to those of the CUSUM chart.

As far as the localization task is concerned, it has been observed that the best-performing architectures are those where the highest hierarchical layer performs a spatio-temporal aggregation of the local decisions as in the Two-Layer architecture and the CUSUM chart. Of these two, the Two-Layer architecture is the one able to achieve the lowest RMSE.

It is crucial to emphasize that, on the detection side, the Two-Layer architecture achieves optimality in a Bayesian sense by relying on a posterior detector for decision-making. While the Three-Layer detector also attains Bayesian optimality, it is worth noting that its detection optimality is restricted by the binary nature of the input received by the PPC from the FC. In the proposed methods, the localization procedure can be deemed optimal from a Bayesian perspective, given its reliance on MAP estimation. However, at the system level, localization faces challenges due to detection errors. This is attributed to the fact that the triggering of a localization procedure is conditional to a positive decision, and this decision is based on a rule that does not prioritize the minimization of localization errors, as done in joint detection-localization procedures (see [49], [50]).

The choice of the appropriate detection threshold in the proposed architecture should be obtained via simulation based on a metric to satisfy. Possible strategies for threshold selection include: (a) selecting the threshold corresponding to the maximum value of P_{10} that is tolerated; (b) select a threshold able to guarantee a maximum value of ADD; (c) minimization of P_1; (d) the threshold is chosen using a tailored indicator that takes into consideration all the previous parameters as well as operational factors.

IX. Conclusions and Future Works

We proposed two architectures addressing the detection and localization task via WSN within industrial plants. Specifically, we proposed a Three-Layer and a Two-Layer Bayesian fusion strategy relying on reliability data for improved performances. In the Three-Layer architecture, we implement a PPC whose task is to perform quickest detection and localization via temporal aggregation of the outputs of a FC that carries out a Shewhart Chart detection rule. Such a temporal aggregation takes advantage of reliability data regarding the monitored system. On the other hand, the Two-Layer architecture directly performs quickest detection and localization at the FC via a spatio-temporal combination of the local decisions taken by the sensors capitalizing on reliability data. Both architectures are equipped with a feedback mechanism necessary for communicating updated parameters from the highest hierarchical layer to the lowest. Two baseline methods, the Shewhart and CUSUM charts, have been introduced. The case study of underwater oil spills in subsea production systems is used to test the proposed architectures, showing the improvements in terms of detection and localization accuracy when the proposed architectures are used. Specifically, the Three-Layer architecture demonstrated the advantages of being able to operate at a lower Probability of False Alarm when compared to the Shewhart chart, which was bound to be higher than 10^{-2}. Meanwhile, the Two-Layer architecture outperforms the CUSUM chart in terms of both detection and localization performance, making it the best-performing architecture among those introduced in the study. In particular, when fixing $P_{10} = 10^{-3}$, the Two-Layer architecture was able to reduce the ADD from around 10% (SNR $= 10$ dB) up to around 30% (SNR $= 0$ dB).

Future works include: (a) considering more complex failure models; (b) the reduction of complexity via more efficient techniques for the computation of $Q_D^{(m)}$ and Q_F; (c) modeling erroneous communication channels; (d) a more accurate statistical representation of the signal measured by the sensors, including possible correlations between measured samples in space and time; (e) integration of machine learning strategies for improved detection and localization performances; (f) a study on the distribution of the localization errors; (g) modeling simultaneous faults; (h) development of joint detection and localization techniques.

Appendix A
Poisson Process for Failure Modeling

With the knowledge that $\mathcal{S}_m(t) \sim \mathrm{Poisson}(\lambda_m t)$, we can obtain the failure probability for the mth item $F_m(t)$:

$$F_m(t) = \mathbb{P}(\mathcal{H}_m(t)=1) = \mathbb{P}\big(T_{m,\mathcal{S}_m(t-\tau_t)+1} \le \tau_t\big)$$

$$= 1 - e^{-\lambda_m \tau_t} \, .$$

We can now obtain $F(t)$. With the knowledge that $\mathcal{H}_m(t) \sim \mathcal{B}(F_m(t))$, we can use the probability-generating function parameterized by z of the variable $\sum_{m=1}^{M} \mathcal{H}_m(t)$:

$$G_{\sum_{m=1}^{M} \mathcal{H}_m(t)}(z) = \prod_{m=1}^{M} G_{\mathcal{H}_m(t)}(z) = \prod_{m=1}^{M} \left[1 + F_m(t)(z-1)\right].$$

Using the last result, we can obtain $\mathbb{P}\Big(\sum_{m=1}^{M} \mathcal{H}_m(t) = 1\Big)$:

$$\mathbb{P}\left(\sum_{m=1}^{M} \mathcal{H}_m(t) = 0\right) = G_{\sum_{m=1}^{M} \mathcal{H}_m(t)}(0) = \prod_{m=1}^{M} (1 - F_m(t)) \, .$$

Thus, we can finally obtain $F(t)$:

$$\begin{aligned} F(t) = \mathbb{P}(\mathcal{H}(t) = 1) &= 1 - \mathbb{P}\left(\sum_{m=1}^{M} \mathcal{H}_m(t) = 0\right) \\ &= 1 - \prod_{m=1}^{M} (1 - F_m(t)) = 1 - \prod_{m=1}^{M} e^{-\lambda_m \tau_t} \, . \end{aligned}$$

However, at low values of $\lambda_m \tau_t$'s, low detection delay, and small Δt, failures behave as disjoint events (*rare events approximation*), therefore:

$$F(t) = \mathbb{P}(\mathcal{H}(t) = 1) \approx \sum_{m=1}^{M} \mathbb{P}(\mathcal{H}_m(t) = 1) = \sum_{m=1}^{M} F_m(t) \, .$$

Thanks to the rare event approximation, we can also retrieve the value of the prior probability of item failure $\varphi_m(t)$:

$$\begin{aligned} \varphi_m(t) &\triangleq \mathbb{P}(\mathcal{H}_m(t) = 1 | \mathcal{H}(t) = 1) \\ &\approx \frac{\mathbb{P}(\mathcal{H}_m(t) = 1)}{\mathbb{P}(\mathcal{H}(t) = 1)} = \frac{F_m(t)}{F(t)} \, , \end{aligned}$$

Moreover, we can obtain the stationary prior probability of item failure by assuming the failure model as a perfect Poisson process. This is done by calculating the probability that, at a certain time t, the next fault belongs to the mth process:

$$\begin{aligned} \varphi_m &\triangleq \mathbb{P}(\mathcal{H}_m(t) = 1 | \mathcal{H}(t) = 1) \\ &= \mathbb{P}\big(T_{m,\mathcal{S}_m(t)+1} < T_{f \neq m, \mathcal{S}_{f \neq m}(t)+1}\big) = \frac{\lambda_m}{\sum_{m=1}^{M} \lambda_m} \, . \end{aligned}$$

This result is independent of t and $\mathcal{S}_m(t)$.

Appendix B
Fusion Center Performance in Three-Layer WSN

The following is the proof of the performances in Eqs. (22) and (23) of the fusion rule performed by the FC. Regarding the probability of detection associated with the failure of the mth item, we obtain:

$$\begin{aligned} Q_D^{(m)} &\triangleq \mathbb{P}\Big(\widehat{\mathcal{H}}[n] = 1 \Big| \mathcal{H}_m[n] = 1\Big) \\ &= \mathbb{P}(\Lambda^{\text{FC}}(\boldsymbol{d}[n]) \geq \gamma^* | \mathcal{H}_m[n] = 1) \\ &= \sum_{\boldsymbol{d} \colon \Lambda^{\text{FC}}(\boldsymbol{d}) \geq \gamma^*} \mathbb{P}(\boldsymbol{d} | \mathcal{H}_m[n] = 1) \\ &= \sum_{\boldsymbol{d} \colon \Lambda^{\text{FC}}(\boldsymbol{d}) \geq \gamma^*} \prod_{k=1}^{K} \mathbb{P}(d_k | \mathcal{H}_m[n] = 1) \\ &= \sum_{\boldsymbol{d} \colon \Lambda^{\text{FC}}(\boldsymbol{d}) \geq \gamma^*} \prod_{k=1}^{K} \left[\Big(P_{D,k}^{(m)}\Big)^{d_k} \Big(1 - P_{D,k}^{(m)}\Big)^{1-d_k}\right] . \end{aligned}$$

The proof exploited the independence of the local decisions. The same steps can be used to prove Q_F.

Note that, in case the WSN is provided with a feedback system (i.e., the time-dependent prior probability of item failure is used), the calculation of the values of $Q_D^{(m)}[n]$'s and $Q_F[n]$ are analogous.

Appendix C
Recursive Form of Proposed Detector

In this appendix, we detail how the expression of $\mathcal{R}_m^{\text{PPC}}[n] \triangleq \mathbb{P}(\mathcal{H}_m[n] = 1 | \boldsymbol{\mathcal{D}}[n])$ can be updated recursively as a function of $\mathcal{R}_m^{\text{PPC}}[n-1]$, for each $m = 1, \ldots, M$ and $n > n_0$.

To begin, we leverage Bayes' Theorem and the conditional independence (i.e., given $\mathcal{H}_m[n]$) of FC decisions $\mathcal{D}[1], \ldots, \mathcal{D}[n]$ over time. By doing this, we get Eq. (45) at the bottom of the next page, in which we further simplified the expression exploiting the following property:

$$\mathbb{P}(\mathcal{D}[n] | \mathcal{H}_m[n], \boldsymbol{\mathcal{D}}[n-1]) = \mathbb{P}(\mathcal{D}[n] | \mathcal{H}_m[n]) \, ,$$

which is a consequence of the uninformativeness of $\boldsymbol{\mathcal{D}}[n-1]$ when inferring $\mathcal{D}[n]$, given that $\mathcal{H}_m[n]$ is known.

Applying the definition of $\mathcal{L}_m^n(\mathcal{D}[n])$, and via algebraic manipulations, we can reformulate Eq. (45) in the following compact form:

$$\mathcal{R}_m^{\text{PPC}}[n] = \left[1 + \frac{1}{\mathcal{L}_m^n(\mathcal{D}[n])} \left(\frac{1}{\mathbb{P}(\mathcal{H}_m[n] = 1 | \boldsymbol{\mathcal{D}}[n-1])} - 1\right)\right]^{-1} .$$

Next, we need to obtain $\mathbb{P}(\mathcal{H}_m[n] = 1 | \boldsymbol{\mathcal{D}}[n-1])$. The next set of equations is defined to facilitate the derivation:

$$\mathbb{P}(\mathcal{H}_m[n] | \mathcal{H}_m[n-1], \boldsymbol{\mathcal{D}}[n-1]) = \mathbb{P}(\mathcal{H}_m[n] | \mathcal{H}_m[n-1]), \tag{46}$$

$$\mathbb{P}(\mathcal{H}_m[n] = 1 | \mathcal{H}_m[n-1] = 1) = 1 \, , \tag{47}$$

where Eq. (46) is a consequence of the uninformativeness of $\boldsymbol{\mathcal{D}}[n-1]$ when inferring $\mathcal{H}_m[n]$ given that $\mathcal{H}_m[n-1]$ is known, and Eq. (47) is the impossibility for an item to repair itself.

By applying the Law of Total Probability, we get Eq. (48) at the bottom of next the page. Eq. (48) can be reduced by applying Eq. (46) and (47). Furthermore, exploiting the definition of $\mathcal{R}_m^{\text{PPC}}[n-1]$, Eq. (48) can be written as reported in Eq. (49) at the bottom of the next page.

Moreover, via Eq. (3), it is possible to prove that $\mathcal{H}_m[n] | \mathcal{H}_m[n-1] = 0 \sim \mathcal{B}\big(1 - e^{-\lambda_m \Delta t}\big)$, leading to Eq. (50) at the bottom of the next page.

Finally, aggregating the previously obtained results, we obtain the recursive expression of $\mathcal{R}_m^{\text{PPC}}[n]$, for $n > n_0$:

$$\mathcal{R}_m^{\text{PPC}}[n] = \left[1 + \frac{1}{\mathcal{L}_m^n(\mathcal{D}[n])} \left(\frac{1}{1 - e^{-\lambda_m \Delta t}(1 - \mathcal{R}_m^{\text{PPC}}[n-1])} - 1\right)\right]^{-1} .$$

When $n = n_0$, the problem reduces to $\mathcal{R}_m^{\text{PPC}}[n_0] = \mathbb{P}(\mathcal{H}_m[n_0] = 1|\mathcal{D}[n_0])$. By applying Bayes' Theorem (as we did for the case of $n > n_0$ in Eq. (45)), and knowing that $\mathcal{H}_m[n_0] \sim \mathcal{B}\big(1 - e^{-\lambda_m \Delta t}\big)$, it becomes easy to prove the following expression:

$$\mathcal{R}_m^{\text{PPC}}[n_0] = \left[1 + \frac{1}{\mathcal{L}_m^{n_0}(\mathcal{D}[n_0])}\left(\frac{1}{1 - e^{-\lambda_m \Delta t}} - 1\right)\right]^{-1}.$$

ACKNOWLEDGMENT

This research is a part of BRU21 – NTNU Research and Innovation Program on Digital and Automation Solutions for the Oil and Gas Industry (www.ntnu.edu/bru21).

REFERENCES

[1] G. Tabella, D. Ciuonzo, N. Paltrinieri, and P. Salvo Rossi, "Spatio-temporal decision fusion for quickest fault detection within industrial plants: The oil and gas scenario," in *IEEE 24th Int. Conf. Inf. Fusion (FUSION)*, 2021.

[2] J. C. Lopez-Ardao, R. F. Rodriguez-Rubio, A. Suarez-Gonzalez, M. Rodriguez-Perez, and M. E. Sousa-Vieira, "Current trends on green wireless sensor networks," *Sensors*, vol. 21, no. 13, p. 4281, 2021.

[3] K. Rose, S. Eldridge, and L. Chapin, "The Internet of Things: An overview," *The Internet Society (ISOC)*, vol. 80, pp. 1–50, 2015.

[4] S. He, K. Shi, C. Liu, B. Guo, J. Chen, and Z. Shi, "Collaborative sensing in Internet of Things: A comprehensive survey," *IEEE Commun. Surveys Tuts.*, vol. 24, no. 3, pp. 1435–1474, 2022.

[5] T. Sahoo, *Process Plants - Shutdown and Turnaround Management*. Boca Raton (FL), USA: Taylor & Francis Group, 2014.

[6] Market Research Future, "Market Research Report," 2023.

[7] N. Paltrinieri, G. Landucci, and P. Salvo Rossi, "Real-Time Data for Risk Assessment in the Offshore Oil and Gas Industry," in *Int. Conf. Offshore Mech. Arct. Eng. (OMAE)*, 2017.

[8] Y. Song, "Underwater Acoustic Sensor Networks With Cost Efficiency for Internet of Underwater Things," *IEEE Trans. Ind. Electron.*, vol. 68, no. 2, pp. 1707–1716, 2021.

[9] C. Mai, S. Pedersen, L. Hansen, K. L. Jepsen, and Z. Yang, "Subsea infrastructure inspection: A review study," in *IEEE Int. Conf. Underw. Syst. Technol.: Theory Appl. (USYS)*, 2016, pp. 71–76.

[10] G. Tabella, N. Paltrinieri, V. Cozzani, and P. Salvo Rossi, "Wireless sensor networks for detection and localization of subsea oil leakages," *IEEE Sens. J.*, vol. 21, no. 9, pp. 10 890–10 904, 2021.

[11] M. A. Al-Jarrah, M. A. Yaseen, A. Al-Dweik, O. Dobre, and E. Alsusa, "Decision fusion for IoT-based wireless sensor networks," *IEEE Internet Things J.*, vol. 7, no. 2, pp. 1313–1326, 2019.

[12] D. Ciuonzo, P. Salvo Rossi, and P. K. Varshney, "Distributed detection in wireless sensor networks under multiplicative fading via generalized score tests," *IEEE Internet Things J.*, vol. 8, no. 11, pp. 9059–9071, 2021.

[13] N. Paltrinieri, F. Khan, P. Amyotte, and V. Cozzani, "Dynamic approach to risk management: Application to the Hoeganaes metal dust accidents," *Process Saf. Environ. Protect.*, vol. 92, no. 6, pp. 669–679, 2014.

[14] V. Villa, N. Paltrinieri, F. Khan, and V. Cozzani, "Towards dynamic risk analysis: A review of the risk assessment approach and its limitations in the chemical process industry," *Saf. Sci.*, vol. 89, pp. 77–93, 2016.

[15] T. Grøtan and N. Paltrinieri, "Dynamic risk management in the perspective of a resilient system," in *Dynamic Risk Analysis in the Chemical and Petroleum Industry*. Elsevier, 2016, pp. 245–257.

[16] N. Paltrinieri, L. Comfort, and G. Reniers, "Learning about risk: Machine learning for risk assessment," *Saf. Sci.*, vol. 118, pp. 475–486, 2019.

[17] R. Niu and P. K. Varshney, "Performance analysis of distributed detection in a random sensor field," *IEEE Trans. Signal Process.*, vol. 56, no. 1, pp. 339–349, 2007.

[18] S. Sen, N. S. V. Rao, C. Q. Wu, M. L. Berry, K. M. Grieme, R. R. Brooks, and G. Cordone, "Performance analysis of Wald-statistic based network detection methods for radiation sources," in *19th Int. Conf. Inf. Fusion (FUSION)*, 2016, pp. 820–827.

[19] N. Sriranga, K. G. Nagananda, R. S. Blum, A. Saucan, and P. K. Varshney, "Energy-efficient decision fusion for distributed detection in wireless sensor networks," in *21th Int. Conf. Inf. Fusion (FUSION)*, 2018, pp. 1541–1547.

[20] G. Tabella, N. Paltrinieri, V. Cozzani, and P. Salvo Rossi, "Subsea oil spill risk management based on sensor networks," *Chem. Eng. Trans.*, vol. 82, pp. 199–204, 2020.

[21] M. Bucelli, I. B. Utne, P. Salvo Rossi, and N. Paltrinieri, "A system engineering approach to subsea spill risk management," *Saf. Sci.*, vol. 123, 2020.

[22] G. Tabella, N. Paltrinieri, V. Cozzani, and P. Salvo Rossi, "Data fusion for subsea oil spill detection through wireless sensor networks," in *Proc. IEEE Sensors*, 2020.

[23] A. Shoari and A. Seyedi, "Detection of a non-cooperative transmitter in Rayleigh fading with binary observations," in *IEEE Mil. Commun. Conf. (MILCOM)*, 2012, pp. 1–5.

[24] D. Ciuonzo and P. Salvo Rossi, "Distributed detection of a non-cooperative target via generalized locally-optimum approaches," *Inf. Fusion*, vol. 36, pp. 261–274, 2017.

[25] L. Hu, J. Zhang, X. Wang, S. Wang, and E. Zhang, "Decentralized truncated one-sided sequential detection of a noncooperative moving target," *IEEE Signal Process. Lett.*, vol. 25, no. 10, pp. 1490–1494, 2018.

[26] X. Cheng, D. Ciuonzo, P. Salvo Rossi, X. Wang, and W. Wang, "Multi-bit & sequential decentralized detection of a noncooperative moving target through a generalized Rao test," *IEEE Trans. Signal Inf. Process. Netw.*, vol. 7, pp. 740–753, 2021.

[27] J. Pan and J. McElhannon, "Future edge cloud and edge computing for internet of things applications," *IEEE Internet Things J.*, vol. 5, no. 1, pp. 439–449, 2017.

[28] E. Røsby, "Goliat development project - Subsea leak detection design," Aker Solutions, 2011.

[29] M. Rausand and A. Høyland, *System reliability theory: models, statistical methods, and applications*, 2nd ed., ser. (Wiley series in probability and statistics). Hoboken (NJ), USA: Wiley-Interscience, 2004.

[30] L. Xie, S. Zou, Y. Xie, and V. V. Veeravalli, "Sequential (quickest) change detection: Classical results and new directions," *IEEE J. Sel. Areas Inf. Theory*, vol. 2, no. 2, pp. 494–514, 2021.

[31] G. Casella and R. L. Berger, *Statistical Inference*, 2nd ed. Pacific Grove (CA), USA: Thomson Learning, 2002.

[32] D. Kincaid and W. Cheney, *Numerical Analysis: Mathematics of Scientific Computing*, 3rd ed. Providence (RI), USA: American Mathematical Society, 2002.

[33] S. Kay, *Fundamentals of Statistical Signal Processing: Detection Theory*, ser. (Prentice Hall Signal Processing Series). Upper Saddle River (NJ), USA: Prentice-Hall, 1998.

[34] M. Rausand and S. Haugen, *Risk Assessment: Theory, Methods, and Applications*, 1st ed. Hoboken (NJ), USA: John Wiley & Sons, 2011.

$$\mathcal{R}_m^{\text{PPC}}[n] = \frac{\mathbb{P}(\mathcal{D}[n]|\mathcal{H}_m[n] = 1)\mathbb{P}(\mathcal{H}_m[n] = 1|\boldsymbol{\mathcal{D}}[n-1])}{\mathbb{P}(\mathcal{D}[n]|\mathcal{H}_m[n] = 1)\mathbb{P}(\mathcal{H}_m[n] = 1|\boldsymbol{\mathcal{D}}[n-1]) + \mathbb{P}(\mathcal{D}[n]|\mathcal{H}_m[n] = 0)[1 - \mathbb{P}(\mathcal{H}_m[n] = 1|\boldsymbol{\mathcal{D}}[n-1])]} \tag{45}$$

$$\mathbb{P}(\mathcal{H}_m[n] = 1|\boldsymbol{\mathcal{D}}[n-1]) = \sum_{i=0}^{1} \mathbb{P}(\mathcal{H}_m[n] = 1|\boldsymbol{\mathcal{D}}[n-1], \mathcal{H}_m[n-1] = i)\mathbb{P}(\mathcal{H}_m[n-1] = i) \tag{48}$$

$$\mathbb{P}(\mathcal{H}_m[n] = 1|\boldsymbol{\mathcal{D}}[n-1]) = 1 - [1 - \mathbb{P}(\mathcal{H}_m[n] = 1|\mathcal{H}_m[n-1] = 0)](1 - \mathcal{R}_m^{\text{PPC}}[n-1]) \tag{49}$$

$$\mathbb{P}(\mathcal{H}_m[n] = 1|\boldsymbol{\mathcal{D}}[n-1]) = 1 - e^{-\lambda_m \Delta t}(1 - \mathcal{R}_m^{\text{PPC}}[n-1]) \tag{50}$$

[35] Y. Bai and Q. Bai, *Subsea Engineering Handbook*. Houston (TX), USA: Elsevier, 2012.
[36] DNV-GL, "Recommended practice RP-F302 offshore leak detection," Oslo, Norway, 2016.
[37] H. V. Fuchs and R. Riehle, "Ten years of experience with leak detection by acoustic signal analysis," *Appl. Acoust.*, vol. 33, no. 1, pp. 1–19, 1991.
[38] M. A. Adegboye, W. K. Fung, and A. Karnik, "Recent advances in pipeline monitoring and oil leakage detection technologies: Principles and approaches," *Sensors*, vol. 19, no. 11, p. 2548, 2019.
[39] E. Bjørnbom, "Goliat – Leak detection and monitoring from template to satellite," 2011.
[40] R. E. Francois and G. R. Garrison, "Sound absorption based on ocean measurements: Part I: Pure water and magnesium sulfate contributions," *J. Acoust. Soc. Am.*, vol. 72, no. 3, pp. 896–907, 1982.
[41] ——, "Sound absorption based on ocean measurements: Part II: Boric acid contribution and equation for total absorption," *J. Acoust. Soc. Am.*, vol. 72, no. 6, pp. 1879–1890, 1982.
[42] G. S. K. Wong and S. Zhu, "Speed of sound in seawater as a function of salinity, temperature, and pressure," *J. Acoust. Soc. Am.*, vol. 97, no. 3, pp. 1732–1736, 1995.
[43] E. G. Eckert, J. W. Maresca, R. W. Hillger, and J. J. Yezzi, "Location of leaks in pressurized petroleum pipelines by means of passive-acoustic sensing methods," in *Leak Detection for Underground Storage Tanks*. West Conshohocken (PA), USA: ASTM Int., 1993, pp. 53–69.
[44] Institute of Marine Research, "Mareano," 2021.
[45] A. A. Vetrov and E. A. Romankevich, *Carbon Cycle in the Russian Arctic Seas*. Berlin, Germany: Springer, 2004.
[46] M. Stojanovic, "On the relationship between capacity and distance in an underwater acoustic communication channel," in *Int. Workshop Underw. Netw. (WUWNet)*, 2006, pp. 34–43.
[47] Vår Energi, "Goliat Barrier Status Panel," 2016.
[48] SINTEF, *OREDA Offshore Reliability Data Handbook*, 4th ed. OREDA Participants, 2002.
[49] A. Tajer, G. H. Jajamovich, X. Wang, and G. V. Moustakides, "Optimal joint target detection and parameter estimation by mimo radar," *IEEE J. Sel. Top. Signal Process.*, vol. 4, no. 1, pp. 127–145, 2010.
[50] G. V. Moustakides, G. H. Jajamovich, A. Tajer, and X. Wang, "Joint detection and estimation: Optimum tests and applications," *IEEE Trans. Inf. Theory*, vol. 58, no. 7, pp. 4215–4229, 2012.

Gianluca Tabella (Graduate Student Member, IEEE) was born in Suzzara, Italy, in 1993. He received the B.Sc. degree in chemical and biochemical engineering (curriculum process engineering) and the M.Sc. degree in chemical and process engineering (curriculum offshore engineering) from the University of Bologna, Italy, in 2017 and 2019, respectively. Since 2020, he has been working towards the Ph.D. degree in electronics and telecommunication at the Dept. Electronic Systems, Norwegian University of Science and Technology (NTNU), Trondheim, Norway. He is a Research Scientist at the Dept. Gas Technology, SINTEF Energy Research, Trondheim, Norway. In 2022, he was a visiting scholar at the Dept. Electrical Engineering, Columbia University, New York (NY), USA. His research interests are in distributed detection and localization, focusing on the process and energy industries.

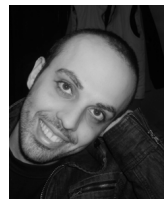

Domenico Ciuonzo (Senior Member, IEEE) received the Ph.D. degree in Electronic Engineering from the University of Campania, Italy, in 2013. He is an Assistant Professor with the University of Naples "Federico II", Naples, Italy. Since 2011, he has been holding several visiting researcher appointments. His research interests include data fusion, wireless sensor networks, the Internet of Things, and machine learning. Dr. Ciuonzo is a recipient of Best Paper Awards from the IEEE International Conference on Computer and Communication Systems in 2019 and Computer Networks in 2020, the Exceptional Service Award from IEEE Aerospace and Electronic Systems Society in 2019, and the Early-Career Technical Achievement Award from IEEE Sensors Council of sensor networks/systems in 2020. Since 2014, he has been an (Area) Editor of several IEEE journals.

Nicola Paltrinieri received the B.Sc. degree in chemical engineering, the M.Sc. degree (*summa cum laude*) in chemical and process engineering and the Ph.D. degree in environmental, safety and chemical engineering from the University of Bologna, Italy, in 2005, 2008 and 2012, respectively. From 2012 to 2016, he was Research Scientist at the Dept. Safety Research, SINTEF Technology and Society (Norway), and in 2012 he held a postdoctoral position at the University of Bologna. He has been a Professor of risk analysis at the Norwegian University of Science and Technology (NTNU), Norway, and an Adjunct Professor of offshore HSE management at the University of Bologna, Italy, since 2016. His research focuses on both the method and the application of risk analysis within socio-technical systems. Regarding the former, he has investigated the concepts and techniques supporting dynamic risk analysis, from uncertainty to machine learning. Regarding the latter, he has worked on risk analysis for safety-critical emerging technologies (e.g., hydrogen technologies). Prof. Paltrinieri is a chartered engineer in the British Engineering Council register, and a charted scientist in the British Science Council register. He is a member of the editorial boards of the journal SAFETY SCIENCE, JOURNAL OF MARINE SCIENCE AND ENGINEERING, JOURNAL OF RISK RESEARCH, and SAFETY IN EXTREME ENVIRONMENTS. He is the leader of NTNU Energy Team Hydrogen. He serves as Norwegian delegate of the Working Party on Loss Prevention and Safety Promotion within the European Federation of Chemical Engineering. He is co-chair of Accident and Incident Modeling, European Safety and Reliability Association Technical Committee. He has served as a member of the scientific committees for the ESREL, Loss Prevention, and CISAP conferences since 2016.

Pierluigi Salvo Rossi (Senior Member, IEEE) was born in Naples, Italy, in 1977. He received the Dr.Eng. degree (*summa cum laude*) in telecommunications engineering and the Ph.D. degree in computer engineering from the University of Naples "Federico II", Italy, in 2002 and 2005, respectively. He is a Full Professor and the Deputy Head with the Department of Electronic Systems, Norwegian University of Science and Technology (NTNU), Trondheim, Norway. He is also a part-time Research Scientist with the Department of Gas Technology, SINTEF Energy Research, Norway.

Previously, he worked with the University of Naples "Federico II", Italy, with the Second University of Naples, Italy, with NTNU, Norway, and with Kongsberg Digital AS, Norway. He held visiting appointments with Drexel University, USA, Lund University, Sweden, NTNU, Norway, and Uppsala University, Sweden. His research interests fall within communication theory, data fusion, machine learning, and signal processing.

Prof. Salvo Rossi was awarded as an Exemplary Senior Editor of the IEEE COMMUNICATIONS LETTERS in 2018. He is (or has been) on the Editorial Board of the IEEE OPEN JOURNAL OF THE COMMUNICATIONS SOCIETY, the IEEE TRANSACTIONS ON SIGNAL AND INFORMATION PROCESSING OVER NETWORKS, the IEEE SENSORS JOURNAL, the IEEE COMMUNICATIONS LETTERS, and the IEEE TRANSACTIONS ON WIRELESS COMMUNICATIONS.

Paper 6

Decision Fusion for Carbon Dioxide Release Detection from Pressure Relief Devices

G. Tabella, Y. Di Martino, D. Ciuonzo, N. Paltrinieri, X. Wang, and P. Salvo Rossi

presented at the *12th IEEE Sensor Array and Multichannel Signal Processing*, Trondheim, Norway, Jun. 2022, pp. 46–50.

Decision Fusion for Carbon Dioxide Release Detection from Pressure Relief Devices

Gianluca Tabella*†, Yuri Di Martino, Domenico Ciuonzo‡, Nicola Paltrinieri§, Xiaodong Wang†, and Pierluigi Salvo Rossi*¶

*Dept. Electronic Systems, Norwegian University of Science and Technology, Trondheim, Norway

†Dept. Electrical Engineering, Columbia University, New York, NY, USA

‡Dept. Electrical Engineering and Information Technologies (DIETI), University of Naples "Federico II", Naples, Italy

§Dept. Mechanical and Industrial Engineering, Norwegian University of Science and Technology, Trondheim, Norway

¶Dept. Gas Technology, SINTEF Energy Research, Norway

Email: gianluca.tabella@ntnu.no; yuri.di.martino@gmail.com; domenico.ciuonzo@unina.it; nicola.paltrinieri@ntnu.no; wangx@ee.columbia.edu; salvorossi@ieee.org

***Abstract*—This work investigates the distributed detection of carbon dioxide (CO_2) release from storage tanks caused by the opening of pressure relief devices via inexpensive sensor devices in an industrial context. A realistic model of the dispersion is put forward in this paper. Both full-precision and rate-limited setups for sensors are considered, and fusion rules capitalizing the dispersion model are derived. Simulations analyze the performance trends with relevant system parameters.**

***Index Terms*—Carbon Dioxide, Decision Fusion, Distributed Detection, Industry 4.0, Internet of Things, Wireless Sensor Networks.**

I. Introduction

The last decades have seen the growth of Wireless Sensor Networks (WSNs) due to their collective, cost-effective, and successful use in monitoring applications. In particular, the task of harmful-event discovery has received large attention in the last years. Relevant scenarios include counter-terrorism and safety in Industry 4.0. The associated inference problems are related to source localization and "early" detection [1]. In this context, most of the works only assume a Gaussian plume point source model based on diffusion/advection processes, e.g. with application to dispersion of biochemical moving sources [2], [3], localization of atmospheric pollutants [4] and release of light gases [5]. On the contrary, *carbon dioxide* (CO_2) is a (heavy) gas whose density, at atmospheric temperature and pressure, is about 1.5 larger than the air density and is present in atmosphere at average concentration ≈ 400 ppm, as of today. Nowadays, CO_2 finds several applications at domestic and industrial levels [6], [7]. Unluckily, when CO_2 is stored, it is possible that accidental releases occur with the main danger of asphyxiation. We remark that CO_2 *does not adhere* to neutral or positively-buoyant dispersion behavior.

For bulk storage, CO_2 is typically stored as liquid in insulated tanks[1] (see Fig. 1), usually equipped with systems to limit the internal pressure, namely *pressure relief devices* (PRDs). These can be safety valves, rupture disks, or their combinations. PRDs are designed in accordance to international or national standards to protect the vessel when the internal pressure exceeds the *maximum allowable working pressure* (MAWP). The causes of overpressure may be several, ranging from process upsets to external fires. In any of these cases, the PRD must release the flow rate necessary to avoid dangerous pressure build-up inside the tank. In such cases, however, the consequences of PRD activation can still be harmful to human life and accurate detection of these critical events should be performed leveraging WSNs.

To this end, Industrial IoT, with inexpensive sensors and the possibility of leveraging collective analytics to obtain improved performance, represents an enabler for this task. However, due to their stringent bandwidth and energy constraints toward close-to-perpetual lifetime of IoT devices, sensors are usually constrained to send extremely-compressed versions of their measurements to a Fusion Center (FC). For this reason, the localization of the same diffusive sources via WSNs has shifted toward the use of binary sensors [9], [10].

Accordingly, the *contributions* of this work are as follows. We model the release of CO_2 from PRDs via a more appropriate *Britter & McQuaid* (B&M) model and include unavoidable fluctuations in the concentration. The sensors measure the concentration and report only one bit to the FC, targeting an industrial IoT setup with small-battery (low-energy) sensors. Since the activated PRD is unknown, the FC is in charge of performing decision fusion by tackling a composite hypothesis testing. For the mentioned reason, a generalized likelihood ratio (GLR)-based fusion rule is devised and compared with a GLR counterpart based on full-precision measurements and the counting rule. Simulation results highlight the need for fusion rules weighting sensors' decisions according to a practical CO_2 release model.

The rest of the paper is organized as follows: Sec. II describes the considered system model, whereas Secs. III and IV introduce the proposed decision fusion approach for CO_2 release detection. Our approach is then numerically validated on a real case study in Sec. V. Sec. VI ends the paper with

This research is a part of BRU21 – NTNU Research and Innovation Program on Digital and Automation Solutions for the Oil and Gas Industry (www.ntnu.edu/bru21).

[1]Storage temperature is below ambient temperature, typically $\in [-30, -20]$°C with corresponding pressures of $\in [14.3, 19.7]$ bar [7], [8].

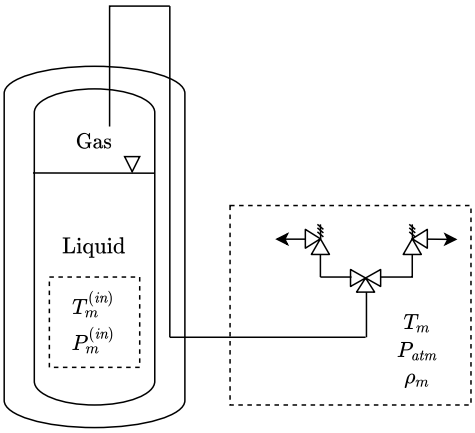

Fig. 1: Scheme of the tank and its PRD with the corresponding thermodynamic conditions.

some pointers to future directions of research.[2]

II. System Model

WSN model: The examined industrial facility consists of M vessels containing liquefied CO_2 and their respective PRDs. The plant is monitored by K concentration sensors individually assessing the absence ($\mathcal{H}_0$) or presence ($\mathcal{H}_1$) of a gas dispersion by measuring the local gas concentration y_k and reporting their local decision $d_k = i$, if $\mathcal{H}_i$ is declared as reported in Fig. 2. Binary decisions are spectrally efficient, as only 1-bit communication is required on the communication channel between the sensor and the FC, as well as being energy-efficient when OOK is employed [11], [12]. The vector of local decisions $\boldsymbol{d} = \begin{bmatrix} d_1 & \cdots & d_K \end{bmatrix}^T$ is acquired by the FC that processes it and takes a global decision $\widehat{\mathcal{H}} \in \{\mathcal{H}_0, \mathcal{H}_1\}$. As a comparative tool, the WSN is also examined in the case in which the FC acquires full-precision measurements $\boldsymbol{y} = \begin{bmatrix} y_1 & \cdots & y_K \end{bmatrix}^T$ from the sensors.

Dispersion model: The heavy gas dispersion model used herein is based on the well-known B&M for continuous release [13]–[18]. The output of the dispersion model allows the evaluation of the *average molar fraction concentration* at the kth sensor when the mth PRD is open, denoted with $c_{k,m}$. Inside the tank corresponding to the mth valve there exists a CO_2 liquid-vapor equilibrium at a certain pressure $P_m^{(in)} > P_{atm}$ and the corresponding saturation temperature $T_m^{(in)} = T_{sat}\left(P_m^{(in)}\right)$, where *atm* stands for *atmospheric* and

[2]*Notation* – Bold letters denote vectors; $(\cdot)^T$ denotes transpose; $\hat{a}$ denote an estimate of the random variable a; $\Pr(\cdot)$ and $p(\cdot)$ denote probability mass functions (pmfs) and probability density functions (pdfs), while $\Pr(\cdot|\cdot)$ and $p(\cdot|\cdot)$ their corresponding conditional counterparts; $F_a(\cdot)$ is the cumulative distribution function (cdf) of the random variable a and $F_{a|b}(\cdot)$ is its conditional counterpart given the random variable b; Gamma (α, β) denotes a Gamma distribution with shape α and rate β; $\Gamma(\cdot)$ is the Gamma function; the symbol $\sim$ (resp. $\overset{\text{approx.}}{\sim}$) means "distributed as" (resp. "approximately distributed as"); finally $\mathcal{O}(\cdot)$ denotes the big O notation.

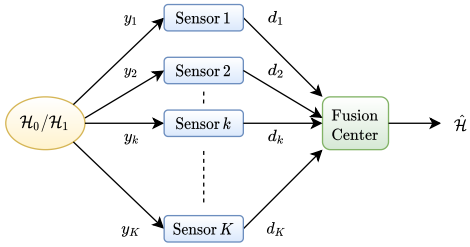

Fig. 2: Wireless Sensor Network Architecture.

sat for *saturation*. When $P_m^{(in)}$ reaches the PRD set pressure, the device opens, releasing the gas phase in atmosphere. At this point a *Joule-Thompson process* occurs with a consequent (isenthalpic) expansion and cooling of the gas[3]. At release condition, the gas will be at a temperature T_m, pressure P_{atm}, and a certain density ρ_m. T_m and ρ_m can be obtained through an appropriate equation of state (EOS) using $T_m^{(in)}$ and $P_m^{(in)}$ as inputs (see Fig. 1). As well as the previous thermodynamic properties, the B&M model requires the following parameters for its use: the atmospheric temperature (T_{atm}), the density of air at T_{atm} (ρ_{air}), the volumetric flow rate from the mth PRD ($\dot{V}_m$), the wind speed at a height of 10 m (u) and its direction (φ)[4], the mth PRD's diameter (D_m), and the concentration at release condition from the mth PRD (c_m).[5]

Signal Model: When a PRD opens, the released gas affects its value of concentration in the surrounding environment. The following equations describe the concentration (y_k) measured by kth sensor in terms in the case of normal operations ($\mathcal{H}_0$), and in the case of an open PRD ($\mathcal{H}_1$):

$$\begin{cases} \mathcal{H}_0: & y_k = w_k \\ \mathcal{H}_1: & y_k = c_{k,m} \cdot \xi_k + w_k \end{cases}, \tag{2}$$

where $w_k \sim \text{Gamma}\left(\frac{b^2}{\nu^2}, \frac{b}{\nu^2}\right)$ is the concentration present in atmosphere in normal conditions with b as its mean value and ν as its standard deviation. $c_{k,m}$ is the mean value of concentration contribution where the kth sensor is located due to the opening of the mth PRD. Finally, $\xi_k \sim \text{Gamma}\left(\omega^{-2}, \omega^{-2}\right)$ is the fluctuation around the value of $c_{k,m}$, where ω is the relative mean fluctuation [19]. Due to the spatial separation of the sensors, ξ_k's and w_k's are both assumed statistically independent. Treating $p(y_k|\mathcal{H}_1; m)$ is not trivial, being the sum of two Gamma random variables: hence, we approximate it with

[3]We neglect possible formation of liquid or solid during this transformation.

[4]Wind blowing from north: 0° (360°), east: 90°, south: 180°, west: 270°.

[5]The B&M model is meant for continuous release of heavy gases meeting the following criterion:

$$\frac{g^2 \left(\rho_m - \rho_{air}\right)^2 \dot{V}_m^{0.5}}{u^{2.5} \rho_{air}^2} \geq 3.375 \times 10^{-3}\,, \tag{1}$$

where g is the gravitational acceleration. Limitations that can affect the accuracy of the result are: the release and the calculated concentrations are assumed to be at ground level; the concentration in the plume's cross-sectional area is assumed uniform; the jet due to a high-velocity release is not modeled; obstacles are not modeled; low distances from the source cause higher errors.

a single Gamma random variable via *moment matching* [20]. The approximated signal's distribution then becomes:

$$\begin{cases} y_k|\mathcal{H}_0 \sim \text{Gamma}\left(\alpha^{(0)}, \beta^{(0)}\right) \\ y_k|\mathcal{H}_1; m \overset{\text{approx.}}{\sim} \text{Gamma}\left(\alpha_{k,m}^{(1)}, \beta_{k,m}^{(1)}\right) \end{cases}, \tag{3}$$

where $\alpha^{(0)} \triangleq \frac{b^2}{\nu^2}$, $\beta^{(0)} \triangleq \frac{b}{\nu^2}$, $\alpha_{k,m}^{(1)} \triangleq \frac{(c_{k,m}+b)^2}{\omega^2 c_{k,m}^2+\nu^2}$, and $\beta_{k,m}^{(1)} \triangleq \frac{c_{k,m}+b}{\omega^2 c_{k,m}^2+\nu^2}$.

III. Local Detection

As a consequence of Eq. (3), we can write the likelihoods of a sensor measurement as:

$$p(y_k|\mathcal{H}_i) = \frac{\beta^{(i)\alpha^{(i)}}}{\Gamma\left(\alpha^{(i)}\right)} y_k^{\alpha^{(i)}-1} e^{-\beta^{(i)} y_k}, \qquad i \in \{0,1\}. \tag{4}$$

Note that $p(y_k|\mathcal{H}_1)$, $\alpha^{(1)}$, and $\beta^{(1)}$ are always referred to as $p(y_k|\mathcal{H}_1; m)$, $\alpha_{k,m}^{(1)}$, and $\beta_{k,m}^{(1)}$, respectively. One should also keep in mind that Eq. (4), for $i = 1$, is an approximated pdf, and that such approximation will propagate throughout many of the equations in the rest of the work. At kth sensor, the log-likelihood ratio test on y_k is *uniformly most powerful* (UMP) in local sense leading to the following test:

$$\ln y_k - \left[\left(\beta_{k,m}^{(1)} - \beta^{(0)}\right) \Big/ \left(\alpha_{k,m}^{(1)} - \alpha^{(0)}\right)\right] y_k \underset{d_k=0}{\overset{d_k=1}{\gtrless}} \gamma. \tag{5}$$

Eq. (5) shows that the detector needs the values of $\alpha_{k,m}^{(1)}$ and $\beta_{k,m}^{(1)}$ to implement a UMP test. Unluckily, these values are not available for the sensors as they depend on the current wind speed and direction (which change over time), as well as the unknown parameter m. This suggests considering a (simpler) concentration level test having computational complexity $\mathcal{O}(1)$ in lieu of Eq. (5), namely:

$$y_k \underset{d_k=0}{\overset{d_k=1}{\gtrless}} \gamma. \tag{6}$$

The performance of this test is obtained thanks to the approximation carried out in Eq. (3):

$$P_{D,k}(m) \triangleq \Pr(y_k \geq \gamma|\mathcal{H}_1; m) = 1 - F_{y_k|\mathcal{H}_1;m}(\gamma), \tag{7}$$

$$P_F \triangleq \Pr(y_k \geq \gamma|\mathcal{H}_0) = 1 - F_{y_k|\mathcal{H}_0}(\gamma). \tag{8}$$

The Neyman-Pearson approach is here employed to design the threshold γ by fixing the desired value of P_F.

IV. Fusion Center

Centralized GLRT: In the case where the sensors transmit the raw measurements to the FC we exploit conditional independence $p(\boldsymbol{y}|\mathcal{H}_1; m) = \prod_{k=1}^{K} p(y_k|\mathcal{H}_1; m)$ and Eq. (4) to obtain likelihood under $\mathcal{H}_1$. Similarly, one can obtain $p(\boldsymbol{y}|\mathcal{H}_0)$ replacing $p(y_k|\mathcal{H}_1; m)$ with $p(y_k|\mathcal{H}_0)$. In such a scenario, a centralized GLRT (C-GLRT) fusion rule can be employed:

$$\begin{aligned} \Lambda_{\text{C-GLRT}} &= \ln\left[\max_{m=1,\dots,M} \frac{p(\boldsymbol{y}|\mathcal{H}_1; m)}{p(\boldsymbol{y}|\mathcal{H}_0)}\right] \\ &= \sum_{k=1}^{K} \ln\left[\frac{p(y_k|\mathcal{H}_1; \widehat{m}_{\text{C}})}{p(y_k|\mathcal{H}_0)}\right] \underset{\widehat{\mathcal{H}}=\mathcal{H}_0}{\overset{\widehat{\mathcal{H}}=\mathcal{H}_1}{\gtrless}} \overline{\gamma}, \end{aligned} \tag{9}$$

where $\widehat{m}_{\text{C}}$ is the Maximum Likelihood Estimate (MLE) of m when $\mathcal{H}_1$ holds, namely $\widehat{m}_{\text{C}} = \underset{m=1,\dots,M}{\arg\max} \sum_{k=1}^{K} \ln p(y_k|\mathcal{H}_1; m)$. This fusion rule has computational complexity $\mathcal{O}(KM)$.

Distributed GLRT: When the sensors transmit binary decisions, the corresponding likelihood is $\Pr(\boldsymbol{d}|\mathcal{H}_1; m) = \prod_{k=1}^{K} \left[P_{D,k}(m)^{d_k}(1 - P_{D,k}(m))^{1-d_k}\right]$. Similarly, one obtains $\Pr(\boldsymbol{d}|\mathcal{H}_0)$ replacing $P_{D,k}(m)$ with P_F. In this case, the FC can perform a Generalized version of the well-known Chair-Varshney Rule, or Distributed GLRT (D-GLRT):

$$\begin{aligned} \Lambda_{\text{D-GLRT}} &= \ln\left[\max_{m=1,\dots,M} \frac{\Pr(\boldsymbol{d}|\mathcal{H}_1; m)}{\Pr(\boldsymbol{d}|\mathcal{H}_0)}\right] \\ &= \sum_{k=1}^{K} \left[d_k \ln \frac{P_{D,k}(\widehat{m}_{\text{D}})}{P_F} \right. \\ &\quad \left. + (1 - d_k) \ln \frac{1 - P_{D,k}(\widehat{m}_{\text{D}})}{1 - P_F}\right] \underset{\widehat{\mathcal{H}}=\mathcal{H}_0}{\overset{\widehat{\mathcal{H}}=\mathcal{H}_1}{\gtrless}} \overline{\gamma}, \end{aligned} \tag{10}$$

where $\widehat{m}_{\text{D}}$ is the MLE of m when $\mathcal{H}_1$ holds, namely $\widehat{m}_{\text{D}} = \underset{m=1,\dots,M}{\arg\max} \sum_{k=1}^{K} \ln \Pr(d_k|\mathcal{H}_1; m)$. As before, the computational complexity is $\mathcal{O}(KM)$.

Counting Rule (CR): The well-known CR is among the simplest fusion rules, where the number of sensors detecting a dispersion is compared to a threshold:

$$\Lambda_{\text{CR}} = \sum_{k=1}^{K} d_k \underset{\widehat{\mathcal{H}}=\mathcal{H}_0}{\overset{\widehat{\mathcal{H}}=\mathcal{H}_1}{\gtrless}} \overline{\gamma}. \tag{11}$$

Unlike GLR fusion rules, the CR does not require the likelihood of $\boldsymbol{d}$ and has the lower computational complexity $\mathcal{O}(K)$.

V. Simulation Results

The results are obtained simulating a plant containing $K = 8$ sensors and $M = 2$ PRDs assumed to be identical to facilitate the discussion of the results. The geometrical configuration can be seen in Fig. 3. Because of the symmetry of the monitored area, the simulations always consider the upper PRD ($m = 1$) to be open. Simulation parameters are collected in Tab. I. From Fig. 4, it is immediately noticeable the superiority of the C-GLRT since directly transmitting $\boldsymbol{y}$ rather than $\boldsymbol{d}$ to the FC shows its benefits. However, such a network will likely show higher operating costs than a distributed network, especially in case of frequent measurements and transmissions to the FC. When considering one-bit quantization, we notice how in general the D-GLRT rule gives better performance than the CR. This highlights how a model-aware design of the FC has its benefits compared to a heuristic design (remember that the CR can be implemented with no knowledge of the signal model). It is important to remember that while the CR allows only K thresholds, the D-GLRT allows $\left(2^K - 1\right) M$ thresholds making it more versatile. It is interesting to notice the high dependency of the ROC curve with respect to the wind characteristics. Fig. 4a shows the best performances among the tested directions. This is because in

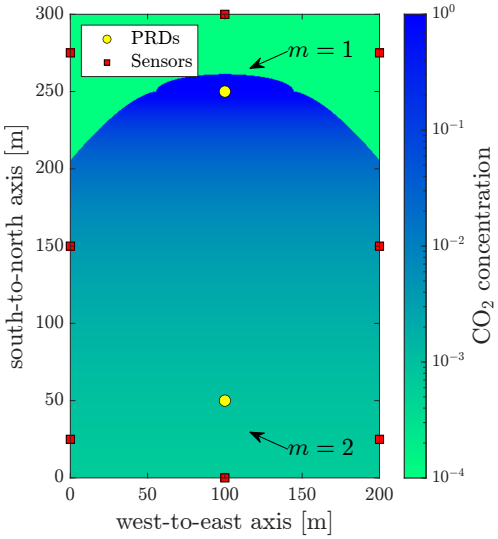

Fig. 3: (Mean) concentration map with dispersion from the upper PRD ($m = 1$) and wind blowing from north ($\varphi = 0°$).

TABLE I: Parameters used for the simulation

Parameter	Value	Note
c_m	1	$\forall m$, pure CO_2
$T_m^{(in)}$	253 K	$\forall m$, [8]
T_m	219 K	$\forall m$, *Soave-Redlich–Kwong* EOS [21]
T_{atm}	293 K	–
$P_m^{(in)}$	19.8 bar	$\forall m$
P_{atm}	1.0 bar	–
ρ_m	2.48 kg/m^3	$\forall m$, *Soave-Redlich–Kwong* EOS [21]
ρ_{air}	1.20 kg/m^3	[22]
u	1 m/s	–
$\dot{V}_m$	0.5312 m^3/s	$\forall m$
D_m	17.98 mm	$\forall m$
b	400 ppm	–
ν	200 ppm	–
ω	1	–
γ	985 ppm	from Eq. (8) with $P_F = 0.05$

such case the CO_2 plume reaches most of the sensors (see Fig. 3). In the scenarios in Figs. 4b and 4c, instead, fewer sensors notice any effect due to $\mathcal{H}_1$ being true. In these cases it is even more vital to have a FC that integrates the model. In such case, in fact, the D-GLRT weighs the different d_k's integrating the knowledge of the different c_{km}'s and the signal distribution to compute the values of the $P_{D,K}(m)$'s.

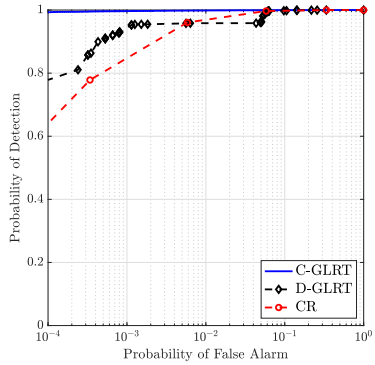

(a) Wind blowing from north ($\varphi = 0°$).

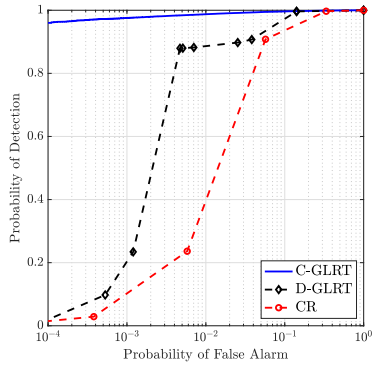

(b) Wind blowing from west ($\varphi = 270°$).

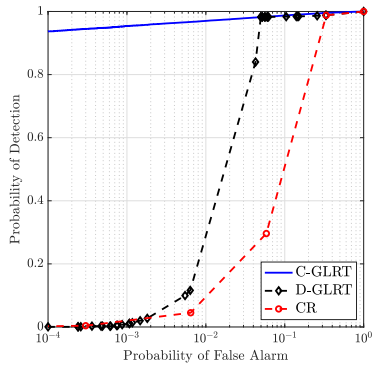

(c) Wind blowing from south ($\varphi = 180°$).

Fig. 4: ROC curves at different wind directions.

VI. Conclusions and Future Directions

In this work, we addressed the distributed detection (via a WSN) of CO_2 release from storage tanks caused by the opening of PRDs. The sensors individually monitor the facility and transmit their decisions to a FC based on individual on a concentration level test. Herein, a spatial aggregation is performed, based on GLRT and a global decision is performed. Results have highlighted the benefit in terms of ROC with respect to the well-known CR that does not include the knowledge of the dispersion model in its design. Future directions will include: (a) source localization, (b) sequential algorithms, and (c) more complex dispersion models.

REFERENCES

[1] M. Ortner and A. Nehorai, "A sequential detector for biochemical release in realistic environments," *IEEE Transactions on Signal Processing*, vol. 55, no. 8, pp. 4173–4182, 2007.

[2] T. Zhao and A. Nehorai, "Detecting and estimating biochemical dispersion of a moving source in a semi-infinite medium," *IEEE Transactions on Signal Processing*, vol. 54, no. 6, pp. 2213–2225, 2006.

[3] S. Aldalahmeh, M. Ghogho, and A. Swami, "Fast distributed detection, localization, and estimation of a diffusive target in wireless sensor networks," in *7th International Symposium on Wireless Communication Systems*. IEEE, 2010, pp. 882–886.

[4] B. Ristic, A. Gunatilaka, and R. Gailis, "Achievable accuracy in gaussian plume parameter estimation using a network of binary sensors," *Information Fusion*, vol. 25, pp. 42–48, 2015.

[5] S. Vijayakumaran, Y. Levinbook, and T. F. Wong, "Maximum likelihood localization of a diffusive point source using binary observations," *IEEE Transactions on Signal Processing*, vol. 55, no. 2, pp. 665–676, 2007.

[6] Y. Di Martino, S. E. Duque, G. Reniers, and V. Cozzani, "Making the chemical and process industries more sustainable: Innovative decision-making framework to incorporate technological and non-technological inherently safer design (ISD) opportunities," *Journal of Cleaner Production*, vol. 296, p. 126421, 2021.

[7] P. Harper, *Assessment of the major hazard potential of carbon dioxide (CO_2)*. UK: Health and Safety Executive, 2011.

[8] NIST, "Thermophysical Properties of Carbon dioxide," 2022.

[9] B. Ristic, A. Gunatilaka, and R. Gailis, "Localisation of a source of hazardous substance dispersion using binary measurements," *Atmospheric Environment*, vol. 142, pp. 114–119, 2016.

[10] D. D. Selvaratnam, I. Shames, D. V. Dimarogonas, J. H. Manton, and B. Ristic, "Co-operative estimation for source localisation using binary sensors," in *56th IEEE Annual Conference on Decision and Control (CDC)*, 2017, pp. 1572–1577.

[11] A. Shoari, G. Mateos, and A. Seyedi, "Analysis of target localization with ideal binary detectors via likelihood function smoothing," *IEEE Signal Processing Letters*, vol. 23, no. 5, pp. 737–741, 2016.

[12] G. Tabella, N. Paltrinieri, V. Cozzani, and P. Salvo Rossi, "Wireless sensor networks for detection and localization of subsea oil leakages," *IEEE Sensors Journal*, vol. 21, no. 9, pp. 10 890–10 904, 2021.

[13] R. E. Britter and J. McQuaid, *Workbook on the dispersion of dense gases*. UK: Health and Safety Executive, 1988.

[14] S. Hanna, "Britter and McQuaid (B&M) 1988 workbook nomograms for dense gas modeling applied to the Jack Rabbit II chlorine release trials," *Atmospheric Environment*, vol. 232, p. 117539, 2020.

[15] TNO, *Yellow Book – Methods for the calculation of physical effects*. The Hague, The Netherlands: The Committee for the Prevention of Disasters by Hazardous Materials, 2005.

[16] S. Mannan, *Lees' Loss Prevention in the Process Industries*, 4th ed. Oxford, UK: Butterworth-Heinemann, 2012.

[17] CCPS, *Guidelines for Consequence Analysis of Chemical Releases*, 1st ed. Hoboken, NJ, USA: John Wiley & Sons, 1999.

[18] D. A. Crowl and J. F. Louvar, *Chemical Process Safety: Fundamentals with Applications*, 4th ed. London, UK: Pearson Education, 2019.

[19] M. Cassiani, M. B. Bertagni, M. Marro, and P. Salizzoni, "Concentration fluctuations from localized atmospheric releases," *Boundary-Layer Meteorology*, vol. 177, no. 2, pp. 461–510, 2020.

[20] F. Babich and G. Lombardi, "Statistical analysis and characterization of the indoor propagation channel," *IEEE Transactions on Communications*, vol. 48, no. 3, pp. 455–464, 2000.

[21] J. M. Smith, H. C. Van Ness, M. M. Abbott, and M. T. Swihart, *Introduction to Chemical Engineering Thermodynamics*, 8th ed. New York (NY), USA: McGraw-Hill Education, 2018.

[22] Engineering ToolBox, "Air - Density, Specific Weight and Thermal Expansion Coefficient vs. Temperature and Pressure," 2022.

Paper 7

Sensor Fusion for Detection and Localization of Carbon Dioxide Releases for Industry 4.0

G. Tabella, Y. Di Martino, D. Ciuonzo, N. Paltrinieri, X. Wang, and P. Salvo Rossi

presented at the *IEEE 25th International Conference on Information Fusion*, Linköping, Sweden, Jul. 2022.

Sensor Fusion for Detection and Localization of Carbon Dioxide Releases for Industry 4.0

Gianluca Tabella*†, Yuri Di Martino, Domenico Ciuonzo‡, Nicola Paltrinieri§, Xiaodong Wang†, and Pierluigi Salvo Rossi*¶

*Dept. Electronic Systems, Norwegian University of Science and Technology, Trondheim, Norway

†Dept. Electrical Engineering, Columbia University, New York, NY, USA

‡Dept. Electrical Engineering and Information Technologies (DIETI), University of Naples "Federico II", Naples, Italy

§Dept. Mechanical and Industrial Engineering, Norwegian University of Science and Technology, Trondheim, Norway

¶Dept. Gas Technology, SINTEF Energy Research, Norway

Email: gianluca.tabella@ntnu.no; yuri.di.martino@gmail.com; domenico.ciuonzo@unina.it; nicola.paltrinieri@ntnu.no; wangx@ee.columbia.edu; salvorossi@ieee.org

***Abstract*—This work tackles the distributed detection & localization of carbon dioxide (CO_2) release from storage tanks caused by the opening of pressure relief devices via inexpensive sensor devices in an industrial context. A realistic model of the dispersion is put forward in this paper. Both full-precision and rate-limited setups for sensors are considered, and fusion rules capitalizing the dispersion model are derived. Simulations analyze the performance trends with realistic system parameters (e.g. wind direction).**

***Index Terms*—Carbon Dioxide (CO_2), Decision Fusion, Detection, Industry 4.0, Internet of Things, Localization, Wireless Sensor Networks.**

I. Introduction

The last decades have seen the growth of Wireless Sensor Networks (WSNs) due to their collective, cost-effective, and successful use in industrial & environmental monitoring applications [1]. This surge has become even more pronounced with the rise of the Internet of Things (IoT) paradigm. In particular, the discovery of *harmful events* has received large attention: relevant scenarios include (i) counter-terrorism, (ii) safety & security in Industry 4.0, and (iii) environmental protection [2].

In the above context, the associated inference problems are "early" detection of an unknown source and its precise localization [3], [4]. In this context, most of the existing works only assume a Gaussian plume point source model based on diffusion/advection processes, e.g. with application to dispersion of biochemical moving sources [5], [6], localization of atmospheric pollutants [7] and release of light gases [8]. On the contrary, *carbon dioxide* (CO_2) is a (heavy) gas whose density, at atmospheric temperature and pressure, is about 1.5 larger than the air density and is present in atmosphere at an average concentration around 400 ppm, as of today. Nowadays, CO_2 finds several applications at domestic and industrial levels [9], [10]. Unluckily, when CO_2 is stored, it is possible that accidental releases occur with the main danger of asphyxiation. Being a heavy gas, CO_2 *does not adhere* to neutral or positively-buoyant dispersion behavior.

This research is a part of BRU21 – NTNU Research and Innovation Program on Digital and Automation Solutions for the Oil and Gas Industry (www.ntnu.edu/bru21).

For bulk storage, CO_2 is typically stored as liquid in insulated tanks[1] (see Fig. 1), usually equipped with systems to limit the internal pressure, namely *pressure relief devices* (PRDs). These can be safety valves, rupture disks, or their combinations. PRDs are designed in accordance to international or national standards to protect the vessel when the internal pressure exceeds the *maximum allowable working pressure* (MAWP). The causes of overpressure may be several, ranging from process upsets to external fires. In any of these cases, the PRD must release the flow rate necessary to avoid dangerous pressure build-up inside the tank. In such cases, however, the consequences of PRD activation can still be harmful to human life and accurate detection of these critical events should be performed leveraging WSNs.

To this end, an *industrial IoT* setup with inexpensive sensors and the possibility of leveraging collective (cloud-based) analytics to obtain improved performance (and global awareness of the monitored plant), represents an enabler for this problem. However, due to their stringent bandwidth and energy constraints needed to ensure long-lasting lifetime of IoT nodes, sensors are usually constrained to send extremely-compressed versions of their measurements to a Fusion Center (FC). For such a reason, the localization of diffusive sources via WSNs has shifted toward the adoption of binary sensors [12], [13].

Accordingly, the *contributions* of this work are as follows. We model the release of CO_2 from PRDs via a set of analytical relationships desumed from the well-known *Britter & McQuaid* (B&M) empirical model, which overcomes the usual (manual) nomogram inspection. Also, our formulation accounts for the unavoidable fluctuations in the concentration. The sensors measure the concentration at their location and report only one bit to the FC, targeting an industrial IoT setup with cheap small-battery sensors. Since the activated PRD is unknown, the FC is in charge of performing decision fusion by tackling a composite hypothesis testing. For the mentioned reason, a generalized likelihood ratio (GLR)-based fusion rule

[1]Storage temperature is below ambient temperature, typically $\in [-30, -20]$°C with corresponding pressures of $\in [14.3, 19.7]$ bar [10], [11].

is devised [14] and compared with a GLR counterpart based on full-precision measurements and the Counting Rule (CR) for the *detection task*. Once a PRD opening is detected, we also address the *localization task* to infer its position accurately, with the aim of speeding up maintenance operations (and thus diminish associated costs). In such a context, the raw/one-bit Maximum Likelihood Estimator (MLE), the centroid and Center of the Minimum Enclosing Circle (CMEC) estimators are compared. Detection & localization approaches are also compared in terms of the complexity involved. Simulation results highlight the need for including a realistic CO_2 release model within the design of fusion rules in *both tasks*.

The rest of the paper is organized as follows. Sec. II describes the system model considered, whereas Sec. III and IV introduce the proposed decision fusion approach for detection, while Sec. V focuses on localization strategies. Sec. VI gives an overview of the computational complexity of the proposed algorithms. Our approach is then numerically validated on a real case study in Sec. VII. Finally, Sec. VIII ends the paper with some research prospects.

Notation – Bold letters denote vectors; $(\cdot)^T$, and $\|\cdot\|$ denote transpose and Euclidean norm operators, respectively; $\hat{a}$, $\mathbb{E}(a)$, $\mathbb{V}\text{ar}(a)$, $\mathbb{E}(a|b)$, and $\mathbb{V}\text{ar}(a|b)$ denote an estimate of the random variable a, its expectation, its variance, its conditional expectation given the random variable b and conditional variance given b, respectively; $\Pr(\cdot)$ and $p(\cdot)$ denote probability mass functions (pmfs) and probability density functions (pdfs), while $\Pr(\cdot|\cdot)$ and $p(\cdot|\cdot)$ their corresponding conditional counterparts; $F_a(\cdot)$ is the cumulative distribution function (cdf) of the random variable a and $F_{a|b}(\cdot)$ is its conditional counterpart given the random variable b; Gamma $(\alpha,\, \beta)$ denotes a Gamma distribution with shape α and rate β; $\mathcal{B}(p)$ denotes a Bernoulli distribution with parameter p; $\Gamma(\cdot)$ is the Gamma function; the symbol $\sim$ (resp. $\overset{\text{approx.}}{\sim}$) means "distributed as" (resp. "approximately distributed as"); finally $\mathcal{O}(\cdot)$ denotes the big O notation.

II. System Model

A. Wireless Sensor Network Model

The examined industrial facility consists of M vessels containing a heavy gas and their respective PRDs, where the mth PRD is located at (two-dimensional) position $\boldsymbol{h}_m = \begin{bmatrix} h_{m1} & h_{m2} \end{bmatrix}^T$. The plant is monitored by K concentration sensors with the kth sensor in position $\boldsymbol{x}_k = \begin{bmatrix} x_{k1} & x_{k2} \end{bmatrix}^T$. The K sensors individually assess the absence ($\mathcal{H}_0$) or presence ($\mathcal{H}_1$) of a gas dispersion by measuring the local gas concentration y_k and reporting their local decision $d_k = i$, if $\mathcal{H}_i$ is declared as reported in Fig. 2. Binary decisions are spectrally-efficient, as only 1-bit communication is required on the communication channel between the sensor and the FC, as well as being energy-efficient when OOK is employed [2], [15]. The vector of local decisions $\boldsymbol{d} = \begin{bmatrix} d_1 & \cdots & d_K \end{bmatrix}^T$ is acquired by the FC that processes it and takes a global decision $\widehat{\mathcal{H}} \in \{\mathcal{H}_0, \mathcal{H}_1\}$. When $\widehat{\mathcal{H}} = \mathcal{H}_1$, the FC also provides an estimate $\widehat{m} \in \{1, \ldots, M\}$ of the PRD declared as the source.

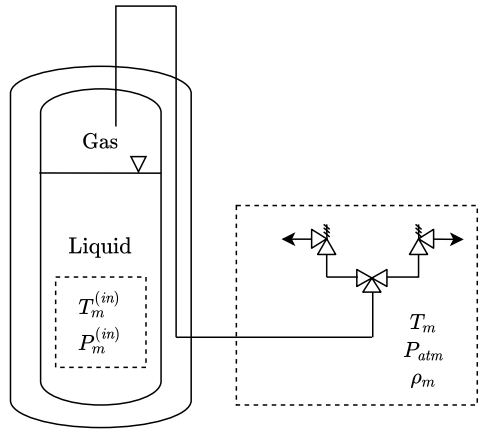

Fig. 1: Scheme of the tank and its PRD with the corresponding thermodynamic conditions.

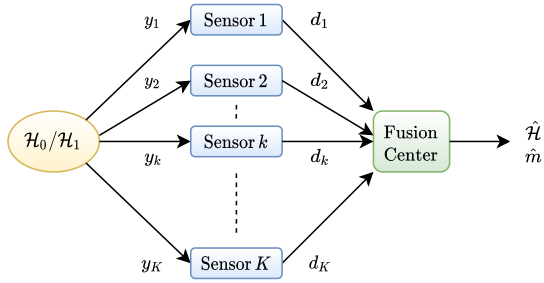

Fig. 2: Wireless Sensor Network Architecture.

As a comparative tool, the WSN is also examined in the case in which the FC acquires full-precision measurements $\boldsymbol{y} = \begin{bmatrix} y_1 & \cdots & y_K \end{bmatrix}^T$ from the sensors.

B. Dispersion Model

The heavy gas dispersion model here used is based on the well-known *Britter & McQuaid Model* (B&M) for continuous releases [16]–[21]. Such method, however, is based on the reading of a nomogram which prevents its utilization on a real-time basis by the FC. To this end, in this work we present a set of equations substituting the nomogram whose output is the value of the *average molar fraction concentration* at the kth sensor when the mth PRD is open, namely $c_{k,m}$ ($0 \leq c_{k,m} \leq 1$). More specifically, we provide the following map $\mathcal{F}$:

$$c_{k,m} = \mathcal{F}\left(\boldsymbol{x}_k, \boldsymbol{h}_m, T_m, \rho_m, c_m, \dot{V}_m, D_m, T_{atm}, \rho_{air}, u, \varphi\right), \tag{1}$$

where T_m, ρ_m, c_m, and $\dot{V}_m$ are the temperature, density, concentration, and volumetric flow rate (respectively) of CO_2 at release condition from the mth PRD, whose diameter is

denoted with D_m; T_{atm} is the atmospheric temperature; ρ_{air} is the density of air at T_{atm}; finally u and φ are the wind speed at a height of 10 meters[2] and its direction[3] (respectively). We now detail the mapping in Eq. (1) via the constituting set of relationships (and corresponding assumptions) reported in what follows.

1) Thermodynamic Properties: Inside the tank corresponding to the mth valve, there exists a CO_2 liquid-vapor equilibrium at a certain pressure $P_m^{(in)} > P_{atm}$ and the corresponding saturation temperature $T_m^{(in)} = T_{sat}\left(P_m^{(in)}\right)$. When $P_m^{(in)}$ reaches the set pressure, the device opens, releasing the gas phase in atmosphere. At this point a *Joule-Thompson process* occurs with a consequent (isenthalpic) expansion and cooling of the gas[4]. At release condition, the gas will be at temperature T_m, pressure P_{atm}, and density ρ_m. The values of T_m and ρ_m can be obtained through an appropriate equation of state (EOS) using $T_m^{(in)}$ and $P_m^{(in)}$ as inputs (see Fig. 1).

2) Applicability Criteria: The B&M model is meant for continuous release of heavy gases, so it is vital that the following criterion is met to consider the release "dense enough":

$$\frac{{g'_m}^2 \dot{V}_m^{0.5}}{u^{2.5}} \geq 3.375 \times 10^{-3} \,, \tag{2}$$

where $g'_m = g\left(\rho_m - \rho_{air}\right)/\rho_{air}$ and g is the gravitational acceleration.

Some limitations potentially affecting the accuracy of the model are:

- The release is assumed to be at ground level;
- The calculated concentrations are at ground level;
- The concentration in the cross-sectional area of the gas plume is assumed uniform;
- Jet due to a high-velocity release is not modeled;
- Obstacles are not modeled;
- Concentrations at low distances from the source have higher prediction error.

3) Change of Coordinates: All sensor positions must go through the change of coordinates represented in Fig. 3. This is because B&M centers the coordinate system at the source point with the first coordinate pointing downwind. The following rototranslation assumes that the vectors $\boldsymbol{x}_k$ and $\boldsymbol{h}_m$ are obtained from a map following the north-up standard map orientation. The following equation describes how to obtain this change when the mth PRD is open:

$$\boldsymbol{x}_k^{(m)} = \begin{bmatrix} -\sin\varphi & -\cos\varphi \\ \cos\varphi & -\sin\varphi \end{bmatrix} \left(\boldsymbol{x}_k - \boldsymbol{h}_m\right) \,, \tag{3}$$

4) Dimensionless Quantities: Two quantities relative to the mth PRD must be calculated to perform B&M:

$$L_m = \frac{\dot{V}_m g'_m}{u^3} \,, \quad \phi_m = \left(\frac{{g'_m}^2 \dot{V}_m}{u^5}\right)^{0.2} \,. \tag{4}$$

[2]If wind speed is available at a different height, several conversion methods are available [19].

[3]Wind blowing from north: 0° (360°), east: 90°, south: 180°, west: 270°.

[4]We neglect possible formation of liquid or solid during this transformation.

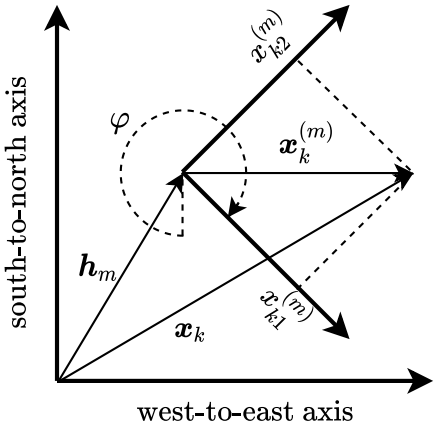

Fig. 3: Representation of the change of coordinates.

5) Concentration Ratio Calculation: The following procedure is intended to provide the concentration ratio in the whole monitored area:

$$\frac{c_{k,m}}{c_m} = \begin{cases} f_{k,m}, & x_{k1}^{(m)} > 0 \wedge \left|x_{k2}^{(m)}\right| \leq R_{W_{k,m}} \\ 1, & -x_{U_m} \leq x_{k1}^{(m)} \leq 0 \wedge \left|x_{k2}^{(m)}\right| \leq R_{U_{k,m}} \\ 0, & \text{otherwise} \end{cases} \,, \tag{5}$$

where x_{U_m} is the upwind distance, $R_{W_{k,m}}$ is the downwind radius, and $R_{U_{k,m}}$ is the upwind radius:

$$x_{U_m} = \frac{D_m}{2} + 2L_m \,, \tag{6}$$

$$R_{W_{k,m}} = R_{0_m} + 2.5 L_m^{1/3}\left(x_{k1}^{(m)}\right)^{2/3} \,, \tag{7}$$

$$R_{U_{k,m}} = R_{0_m}\sqrt{1 - \left(\frac{x_{k1}^{(m)}}{x_{U_m}}\right)^2} \,, \tag{8}$$

where $R_{0_m} = D_m + 8L_m$. Note that Eq. (8) implies an elliptical upwind dispersion. An overview of the main geometrical dimensions can be seen in Fig 4.

6) Downwind Concentration Ratio: B&M's nomogram provides a graphical way to obtain the downwind concentration ratio, $f_{k,m}$. The following procedure allows us to analytically approximate such value:

$$f_{k,m} = \begin{cases} f_{k,m}^{(1)}, & \phi_m \leq 0.2 \\ \left(\frac{5}{4} - \frac{5}{4}\phi_m\right) f_{k,m}^{(1)} + \left(\frac{5}{4}\phi_m - \frac{1}{4}\right) f_{k,m}^{(2)}, & 0.2 < \phi_m < 1 \\ f_{k,m}^{(2)}, & \phi_m \geq 1 \end{cases} \,, \tag{9}$$

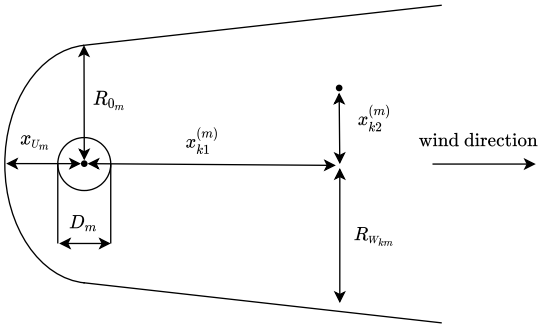

Fig. 4: Main geometrical dimensions used in B&M model.

where the functions $f_{k,m}^{(1)}$ and $f_{k,m}^{(2)}$ are defined as follows:

$$\begin{aligned} f_{k,m}^{(1)} &\triangleq 306.25 \left(x_{k1}^{(m)}\right)^{-2} \dot{V}_m u^{-1} \ , \\ f_{k,m}^{(2)} &\triangleq 401.39 \left(x_{k1}^{(m)}\right)^{-1.95} \dot{V}_m^{0.78} {g'_m}^{-0.39} \ . \end{aligned} \tag{10}$$

At low values of $x_{k1}^{(m)}$, Eq. (9) might result in $f_{k,m} > 1$, which is a wrong result generated by an excessive extrapolation from the original nomogram. Therefore, we provide the following correction to be applied to the result of Eq. (9):

$$\frac{f_{k,m}}{f_{k,m}+1} \longmapsto f_{k,m} \ . \tag{11}$$

7) Isobaric Transformation Correction: Finally, one last correction is necessary as the gas, once in contact with the atmosphere, begins a heat exchange (since $T_m < T_{atm}$) resulting in a temperature increase and expansion, therefore *decreasing* its concentration:

$$\frac{c_{k,m}}{c_{k,m} + (1 - c_{k,m})\frac{T_{atm}}{T_m}} \longmapsto c_{k,m} \ , \tag{12}$$

where T_{atm} and T_m are expressed as absolute temperatures. Eq. (12) implies an ideal gas behavior and a thermal equilibrium at any $x_{k1}^{(m)}$.

C. Signal Model

When a PRD opens, the released gas affects its value of concentration in the surrounding environment. The following equations describe the signal sensed by kth sensor in terms of concentration (y_k) in the case of normal operations (hypothesis $\mathcal{H}_0$), and in the case of an open PRD (hypothesis $\mathcal{H}_1$):

$$\begin{cases} \mathcal{H}_0 : & y_k = w_k \\ \mathcal{H}_1 : & y_k = c_{k,m} \cdot \xi_k + w_k \end{cases} \ , \tag{13}$$

where $w_k \sim \text{Gamma}\left(\frac{b^2}{\nu^2}, \frac{b}{\nu^2}\right)$ is the concentration present in the environment in normal conditions with b as its mean value and ν as its standard deviation. $c_{k,m}$ is the mean value of concentration contribution where the kth sensor is located due to the opening of the mth PRD. Finally, $\xi_k \sim \text{Gamma}\left(\omega^{-2}, \omega^{-2}\right)$ represents the fluctuation around the value of $c_{k,m}$, where ω is the relative mean fluctuation [22]. Due to the spatial separation of the sensors, it is assumed that ξ_k's and w_k's are both statistically independent. From Eq. (13), one can notice the following properties:

$$\mathbb{E}(y_k|\mathcal{H}_1; m) = c_{k,m} + b \ , \quad \mathbb{V}\text{ar}(y_k|\mathcal{H}_1; m) = \omega^2 c_{k,m}^2 + \nu^2 \ . \tag{14}$$

However, treating $p(y_k|\mathcal{H}_1; m)$ is not trivial, as it is the sum of two Gamma distributed random variables. Therefore, to simplify the the resulting algorithm, the sum of two independent Gamma random variables is approximated with a Gamma random variable with expectation (resp. variance) obtained as the sum of the expectations (resp. variances) of the two original variables (proof of validity in [23]). Consequently, during the development of the detectors, the distribution of the signal will be approximated with the following:

$$\begin{cases} y_k|\mathcal{H}_0 \sim \text{Gamma}\left(\alpha^{(0)}, \beta^{(0)}\right) \\ y_k|\mathcal{H}_1; m \overset{\text{approx.}}{\sim} \text{Gamma}\left(\alpha_{k,m}^{(1)}, \beta_{k,m}^{(1)}\right) \end{cases} \ , \tag{15}$$

where $\alpha^{(0)} \triangleq \frac{b^2}{\nu^2}$, $\beta^{(0)} \triangleq \frac{b}{\nu^2}$, $\alpha_{k,m}^{(1)} \triangleq \frac{(c_{k,m}+b)^2}{\omega^2 c_{k,m}^2 + \nu^2}$, and $\beta_{k,m}^{(1)} \triangleq \frac{c_{k,m}+b}{\omega^2 c_{k,m}^2 + \nu^2}$. Note that such approximated pdf becomes the actual pdf in case $c_{k,m} = 0$ when $\mathcal{H}_1$ is true.

III. Local Detection

As a consequence of Eq. (15), we can write the likelihoods of a sensor measurement:

$$p(y_k|\mathcal{H}_i) = \frac{{\beta^{(i)}}^{\alpha^{(i)}}}{\Gamma\left(\alpha^{(i)}\right)} y_k^{\alpha^{(i)}-1} e^{-\beta^{(i)} y_k} \ , \qquad i \in \{0, 1\} \ . \tag{16}$$

Note that $p(y_k|\mathcal{H}_1)$, $\alpha^{(1)}$, and $\beta^{(1)}$ are always referred to as $p(y_k|\mathcal{H}_1; m)$, $\alpha_{k,m}^{(1)}$, and $\beta_{k,m}^{(1)}$, respectively, to emphasize the dependency on the sensor and the source.

One should also keep in mind that Eq. (16), for $i = 1$, is an approximated pdf, and that such approximation will propagate throughout many of the equations in the rest of the work.

At a local detection level, the log-likelihood ratio test is *uniformly most powerful* (UMP) in a local sense having the following explicit expression for the test statistics:

$$\begin{aligned} \ln \frac{p(y_k|\mathcal{H}_1; m)}{p(y_k|\mathcal{H}_0)} = &\left(\alpha_{k,m}^{(1)} \ln \beta_{k,m}^{(1)} - \alpha^{(0)} \ln \beta^{(0)}\right) \\ &- \left(\ln \Gamma\left(\alpha_{k,m}^{(1)}\right) - \ln \Gamma\left(\alpha^{(0)}\right)\right) \\ &+ \left(\alpha_{k,m}^{(1)} - \alpha^{(0)}\right) \ln y_k - \left(\beta_{k,m}^{(1)} - \beta^{(0)}\right) y_k \ . \end{aligned} \tag{17}$$

The last equation shows that an equivalent test is the following:

$$\ln y_k - \frac{\beta_{k,m}^{(1)} - \beta^{(0)}}{\alpha_{k,m}^{(1)} - \alpha^{(0)}} y_k \underset{d_k=0}{\overset{d_k=1}{\gtrless}} \gamma \ . \tag{18}$$

Eq. (18) shows that in order to perform a UMP test at local level, the detector needs to know the values of $\alpha_{k,m}^{(1)}$ and $\beta_{k,m}^{(1)}$. Unfortunately, these values are not available for the sensors as

they depend on the current wind speed and direction (which change over time), as well as the unknown parameter m. This leads to the conclusion that the test in Eq. (18) can be substituted with a local concentration test[5]:

$$y_k \underset{d_k=0}{\overset{d_k=1}{\gtrless}} \gamma \,. \tag{19}$$

Thanks to the approximation carried out in Eq. (15), it is easy to obtain the performance of the concentration test:

$$P_F \triangleq \Pr(y_k \geq \gamma | \mathcal{H}_0) = 1 - F_{y_k|\mathcal{H}_0}(\gamma) \,, \tag{20}$$

$$P_{D,k}(m) \triangleq \Pr(y_k \geq \gamma | \mathcal{H}_1; m) = 1 - F_{y_k|\mathcal{H}_1;m}(\gamma) \,. \tag{21}$$

The Neyman-Pearson approach is here employed to design the threshold γ by fixing the desired value of P_F, making the choice of the threshold independent of the the unknown parameter m and the considered sensor.

IV. Fusion Center Detection

A. Input's Likelihoods

According to the typology of input received by the FC (either $\boldsymbol{d}$ or $\boldsymbol{y}$), we can define two different expressions of the likelihoods at the FC.

1) Raw measurements as input: In such case we can combine Eq. (16) and the independence of the sensor measurements in space:

$$p(\boldsymbol{y}|\mathcal{H}_1; m) = \prod_{k=1}^{K} p(y_k|\mathcal{H}_1; m) \,. \tag{22}$$

Similarly, one can obtain $p(\boldsymbol{y}|\mathcal{H}_0)$ replacing $p(y_k|\mathcal{H}_1; m)$ with $p(y_k|\mathcal{H}_0)$.

2) Binary decisions as input: When the sensors transmit binary decisions it is clear that d_k follows a (conditional) Bernoulli distribution:

$$d_k|\mathcal{H}_0 \sim \mathcal{B}(P_F) \,, \qquad d_k|\mathcal{H}_1; m \sim \mathcal{B}(P_{D,k}(m)) \,. \tag{23}$$

In this case we can exploit the independence of the sensor decisions in space:

$$\Pr(\boldsymbol{d}|\mathcal{H}_1; m) = \prod_{k=1}^{K} \left[P_{D,k}(m)^{d_k} (1 - P_{D,k}(m))^{1-d_k} \right] \,. \tag{24}$$

Similarly, one obtains $\Pr(\boldsymbol{d}|\mathcal{H}_0)$ replacing $P_{D,k}(m)$ with P_F.

B. Centralized GLRT

In the case where the sensors transmit the raw measurements to the FC, a centralized GLRT (C-GLRT) fusion rule can be employed:

$$\begin{aligned} \Lambda_{\text{C-GLRT}} &= \ln \frac{\max\limits_{m=1,\dots,M} p(\boldsymbol{y}|\mathcal{H}_1; m)}{p(\boldsymbol{y}|\mathcal{H}_0)} \\ &= \sum_{k=1}^{K} \left[\ln \frac{p(y_k|\mathcal{H}_1; \widehat{m}_{\text{C-MLE}})}{p(y_k|\mathcal{H}_0)} \right] \underset{\widehat{\mathcal{H}}=\mathcal{H}_0}{\overset{\widehat{\mathcal{H}}=\mathcal{H}_1}{\gtrless}} \overline{\gamma} \,, \end{aligned} \tag{25}$$

[5]A local test based on the locally most powerful *score test* has been obtained, however computing $P_{D,k}(m)$ and P_F in closed-form is not possible.

where $\widehat{m}_{\text{C-MLE}}$ is the Maximum Likelihood Estimate (MLE) among the possible source points conditioned to $\mathcal{H}_1$ being true:

$$\widehat{m}_{\text{C-MLE}} = \underset{m=1,\dots,M}{\arg\max} \sum_{k=1}^{K} \ln p(y_k|\mathcal{H}_1; m) \,. \tag{26}$$

C. Distributed GLRT

When the sensors send a binary decision, the FC can perform a Generalized version of the well-known Chair-Varshney Rule, here named Distributed GLRT (D-GLRT):

$$\begin{aligned} \Lambda_{\text{D-GLRT}} &= \ln \frac{\max\limits_{m=1,\dots,M} \Pr(\boldsymbol{d}|\mathcal{H}_1; m)}{\Pr(\boldsymbol{d}|\mathcal{H}_0)} \\ &= \sum_{k=1}^{K} \left[d_k \ln \frac{P_{D,k}(\widehat{m}_{\text{D-MLE}})}{P_F} \right. \\ &\quad \left. + (1 - d_k) \ln \frac{1 - P_{D,k}(\widehat{m}_{\text{D-MLE}})}{1 - P_F} \right] \underset{\widehat{\mathcal{H}}=\mathcal{H}_0}{\overset{\widehat{\mathcal{H}}=\mathcal{H}_1}{\gtrless}} \overline{\gamma} \,, \end{aligned} \tag{27}$$

where $\widehat{m}_{\text{D-MLE}}$ is the MLE among the possible source points conditioned to $\mathcal{H}_1$ being true, namely:

$$\widehat{m}_{\text{D-MLE}} = \underset{m=1,\dots,M}{\arg\max} \sum_{k=1}^{K} \ln \Pr(d_k|\mathcal{H}_1; m) \,. \tag{28}$$

D. Counting Rule

The well-known Counting Rule (CR) is among the simplest fusion rules, where the number of sensors detecting a dispersion is compared to a threshold:

$$\Lambda_{\text{CR}} = \sum_{k=1}^{K} d_k \underset{\widehat{\mathcal{H}}=\mathcal{H}_0}{\overset{\widehat{\mathcal{H}}=\mathcal{H}_1}{\gtrless}} \overline{\gamma} \,. \tag{29}$$

V. Fusion Center Localization

A. Centralized/Distributed GLRT - Maximum Likelihood Estimator

In such a case, the source identification is *automatically* incorporated in the GLRT. Therefore, once obtained that $\widehat{\mathcal{H}} = \mathcal{H}_1$, the identified source will be $\widehat{m}_{\text{C-MLE}}$ as defined in Eq. (26) for the centralized case. Analogously, for distributed GLRT, we can identify the source with $\widehat{m}_{\text{D-MLE}}$ as defined in Eq. (28).

B. Counting Rule - Heuristic Estimators

Unlike the fusion rules based on the GLRT, the CR does not require the estimation of the parameter m. Therefore, a source identification method must be developed separately. A number of heuristic methods exist that can perform such task when the sole available information is $\boldsymbol{d}$ and $\{\boldsymbol{x}_k\}_{k=1,\dots,K}$. Here we investigate the use of the Centroid Method and the Center of the Minimum Enclosing Circle (CMEC) due to their popularity, simplicity, and effectiveness [2], [15], [24].

TABLE I: Computational Complexity of the Proposed Algorithms

Algorithm	Complexity
Local Concentration Test	$\mathcal{O}(1)$
C-GLRT / D-GLRT	$\mathcal{O}(KM)$
CR + Centroid / CMEC	$\mathcal{O}(K)+\mathcal{O}(K+M)$

1) Centroid Method: The Centroid Method calculates the centroid of the sensors detecting a release:

$$\boldsymbol{x}_{\mathrm{C}} = \frac{\sum_{k=1}^{K} d_k \boldsymbol{x}_k}{\sum_{k=1}^{K} d_k} \,. \tag{30}$$

However, the position $\boldsymbol{x}_{\mathrm{C}}$ may not correspond to any of the existing PRDs. Therefore, we infer that source point is the closest to the calculated position:

$$\widehat{m}_{\mathrm{CENTROID}} = \underset{m=1,\ldots,M}{\arg\min} \, \|\boldsymbol{x}_C - \boldsymbol{h}_m\| \,. \tag{31}$$

2) CMEC Algorithm: The CMEC Algorithm calculates the center of the smallest circle enclosing all the sensors detecting a dispersion. Such point ($\boldsymbol{x}_{\mathrm{CMEC}}$) can be efficiently computed via *Megiddo Algorithm* (not reported here) [25]. Analogously to the Centroid Method, we need to employ the same final step to enforce the source position estimate to lie in the same discrete set:

$$\widehat{m}_{\mathrm{CMEC}} = \underset{m=1,\ldots,M}{\arg\min} \, \|\boldsymbol{x}_{\mathrm{CMEC}} - \boldsymbol{h}_m\| \,. \tag{32}$$

VI. Computational Complexity

Tab. I shows the computational complexity of the proposed algorithms. It is noticeable how the local detection (when employed) is obtained with a finite number of operations. Moreover, we can notice that the detection methods based on the GLRT have higher complexity than the CR ($\mathcal{O}(KM)$ against $\mathcal{O}(K)$), which has the further advantage of performing the localization algorithms only when $\widehat{\mathcal{H}} = \mathcal{H}_1$. Note that both the Centroid Method and the CMEC Algorithm have the same complexity $\mathcal{O}(K+M)$. More specifically, obtaining $\boldsymbol{x}_{\mathrm{C}}$ and $\boldsymbol{x}_{\mathrm{CMEC}}$ (using *Megiddo Algorithm*) has complexity $\mathcal{O}(K)$, while both Eqs. (31) and (32) have complexity $\mathcal{O}(M)$.

VII. Simulation Results

The results are obtained simulating $M = 9$ identical sources placed in a square grid with side equal to 200 m. Such PRDs are located in a square-shaped plant of side $L = 400$ m monitored by $K = 8$ sensors installed on the perimeter and equally spaced. Such geometrical setup is illustrated in Fig. 5 while the rest of the simulation parameters are shown in Tab. II. Because of the symmetry properties of the chosen geometrical setup, only the wind directions in the interval $\varphi \in [\varphi_0, \varphi_0 + 45°]$ with $\varphi_0 \in [0°, 360°)$ can be evaluated, all other configurations can be mapped into one of those.

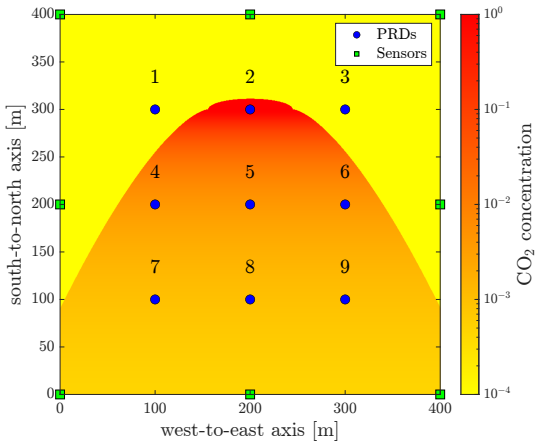

(a) Release from PRD ($m = 2$) and wind from north ($\varphi = 0°$).

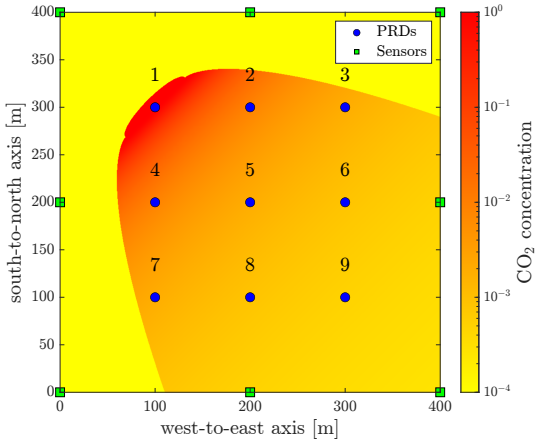

(b) Release from PRD ($m = 1$) and wind from north-west ($\varphi = 315°$).

Fig. 5: (Mean) concentration maps in a dispersion scenario.

For this reason we only considered $\varphi \in \{0°, 315°\}$. Because of the presence of $M = 9$ PRDs, the performances are averaged among all the release points, both in the detection and localization stage. From Figs. 6 and 7, it is immediately observable the superiority of the C-GLRT and its C-MLE estimator, as a consequence of directly transmitting $\boldsymbol{y}$ rather than $\boldsymbol{d}$ to the FC. However, a centralized network will likely show higher operating costs than a distributed network, especially in case of frequent measurements and transmissions to the FC. Therefore, the performance of the centralized network is solely used for benchmarking purposes. When considering one-bit quantization, we notice how the D-GLRT gives better performances than the CR in terms of detection (higher probability of detection given a fixed prob-

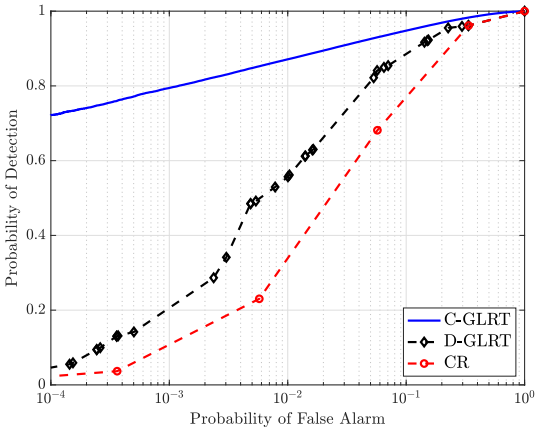

(a) Wind from north ($\varphi = 0°$).

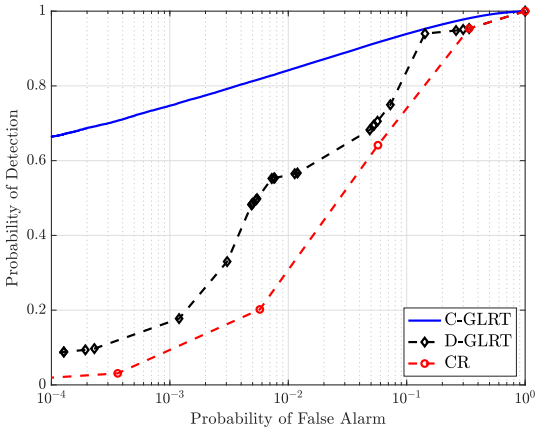

(b) Wind from north-west ($\varphi = 315°$).

Fig. 6: ROC curves at different wind directions.

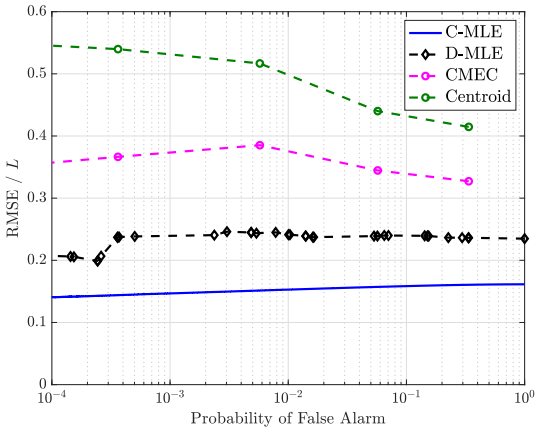

(a) Wind from north ($\varphi = 0°$).

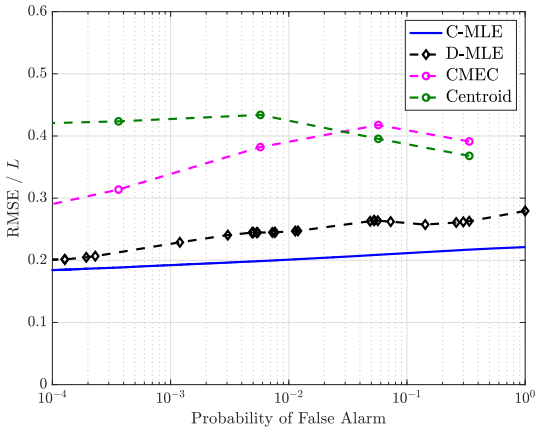

(b) Wind from north-west ($\varphi = 315°$).

Fig. 7: Localization performances at different wind directions.

ability of false alarm in the whole ROC space), highlighting how a model-aware design of the FC outperforms a heuristic design (since the CR can be used with no knowledge of the signal model). The localization performance follows a similar behavior showing how the D-MLE, in terms of *root mean square error* (RMSE), approaches the C-MLE, while the Centroid and the CMEC methods give worse results. In particular, the Centroid method gives typically the highest (i.e. worst) RMSE values. Nevertheless, an inversion of this trend can be seen in Fig. 7b: however, this holds only for values of probability of false-alarm higher than 0.057. From Fig. 7 it is evident how the 1-bit quantization makes it impossible to obtain a perfectly monotonic behavior of the RMSE as function of the probability of false alarm. On the contrary, the centralized configuration shows that lowering the detection threshold makes the system process less informative measurements, reducing the localization accuracy. While this tendency is somehow followed also by the D-MLE (some fluctuations of the RMSE are present among neighboring thresholds), a more unpredictable behavior is shown by the Centroid and CMEC methods. Ultimately, it is important to notice that while the CR allows only K thresholds, the D-GLRT allows $\left(2^K - 1\right) M$ thresholds, making it easier to tune the system to a desired false alarm rate[6], unless a randomization procedure is applied.

[6]The number of thresholds does not include those represented by the upper-right and lower-left corner points of the ROC curves.

TABLE II: Parameters used for the simulation

Parameter	Value	Note
c_m	1	$\forall m$, pure CO_2
$T_m^{(in)}$	253 K	$\forall m$, [11]
T_m	219 K	$\forall m$, *Soave-Redlich–Kwong* EOS [26]
T_{atm}	293 K	–
$P_m^{(in)}$	19.8 bar	$\forall m$
P_{atm}	1.0 bar	–
ρ_m	2.48 kg/m^3	$\forall m$, *Soave-Redlich–Kwong* EOS [26]
ρ_{air}	1.20 kg/m^3	[27]
u	1 m/s	–
$\dot{V}_m$	0.5312 m^3/s	$\forall m$
D_m	17.98 mm	$\forall m$
b	400 ppm	–
ν	200 ppm	–
ω	1	–
γ	985 ppm	from Eq. (20) with $P_F = 0.05$

VIII. Conclusions and Future Directions

In this work, we addressed the distributed detection (via a WSN) of CO_2 release from storage tanks caused by the opening of PRDs and localization of the corresponding activated PRD. The sensors individually monitor the facility and transmit their decisions to a FC based on an individual concentration level test. Herein, a spatial aggregation is carried out based on GLRT and a global decision is performed. Results have highlighted the benefit in terms of ROC with respect to the well-known CR that does not include the knowledge of the dispersion model in its design. Similar benefits have been observed for MLE-based estimators as compared to naive alternatives based on CMEC and centroid approaches. Future directions will include: (i) sequential/quickest detection setups and corresponding localization techniques, (ii) the combined adoption of quantization with censoring techniques [28], (iii) more complex dispersion models, and (iv) the use of channel-aware techniques [29].

References

[1] L. Da Xu, W. He, and S. Li, "Internet of things in industries: A survey," *IEEE Trans. Industr. Inform.*, vol. 10, no. 4, pp. 2233–2243, 2014.

[2] G. Tabella, N. Paltrinieri, V. Cozzani, and P. Salvo Rossi, "Wireless sensor networks for detection and localization of subsea oil leakages," *IEEE Sens. J.*, vol. 21, no. 9, pp. 10 890–10 904, 2021.

[3] M. Ortner and A. Nehorai, "A sequential detector for biochemical release in realistic environments," *IEEE Trans. Signal Process.*, vol. 55, no. 8, pp. 4173–4182, 2007.

[4] G. Tabella, D. Ciuonzo, N. Paltrinieri, and P. Salvo Rossi, "Spatio-temporal decision fusion for quickest fault detection within industrial plants: The oil and gas scenario," in *IEEE 24th Int. Conf. Inf. Fusion (FUSION)*, 2021.

[5] T. Zhao and A. Nehorai, "Detecting and estimating biochemical dispersion of a moving source in a semi-infinite medium," *IEEE Trans. Signal Process.*, vol. 54, no. 6, pp. 2213–2225, 2006.

[6] S. Aldalahmeh, M. Ghogho, and A. Swami, "Fast distributed detection, localization, and estimation of a diffusive target in wireless sensor networks," in *7th IEEE Int. Symp. Wirel. Commun. Syst. (ISWCS)*, 2010, pp. 882–886.

[7] B. Ristic, A. Gunatilaka, and R. Gailis, "Achievable accuracy in Gaussian plume parameter estimation using a network of binary sensors," *Inf. Fusion*, vol. 25, pp. 42–48, 2015.

[8] S. Vijayakumaran, Y. Levinbook, and T. F. Wong, "Maximum likelihood localization of a diffusive point source using binary observations," *IEEE Trans. Signal Process.*, vol. 55, no. 2, pp. 665–676, 2007.

[9] Y. Di Martino, S. E. Duque, G. Reniers, and V. Cozzani, "Making the chemical and process industries more sustainable: Innovative decision-making framework to incorporate technological and non-technological inherently safer design (ISD) opportunities," *J. Clean. Prod.*, vol. 296, p. 126421, 2021.

[10] P. Harper, *Assessment of the major hazard potential of carbon dioxide (CO_2)*. UK: Health and Safety Executive, 2011.

[11] NIST, "Thermophysical Properties of Carbon dioxide," 2022.

[12] B. Ristic, A. Gunatilaka, and R. Gailis, "Localisation of a source of hazardous substance dispersion using binary measurements," *Atmos. Environ.*, vol. 142, pp. 114–119, 2016.

[13] D. D. Selvaratnam, I. Shames, D. V. Dimarogonas, J. H. Manton, and B. Ristic, "Co-operative estimation for source localisation using binary sensors," in *56th IEEE Annu. Conf Decis Control (CDC)*, 2017, pp. 1572–1577.

[14] S. Kay, *Fundamentals of Statistical Signal Processing: Detection Theory*, 1st ed., ser. (Prentice Hall Signal Processing Series). Upper Saddle River (NJ), USA: Prentice-Hall, 1998.

[15] A. Shoari, G. Mateos, and A. Seyedi, "Analysis of target localization with ideal binary detectors via likelihood function smoothing," *IEEE Signal Process. Lett.*, vol. 23, no. 5, pp. 737–741, 2016.

[16] R. E. Britter and J. McQuaid, *Workbook on the dispersion of dense gases*. UK: Health and Safety Executive, 1988.

[17] S. Hanna, "Britter and McQuaid (B&M) 1988 workbook nomograms for dense gas modeling applied to the Jack Rabbit II chlorine release trials," *Atmos. Environ.*, vol. 232, p. 117539, 2020.

[18] TNO, *Yellow Book – Methods for the calculation of physical effects*. The Hague, The Netherlands: The Committee for the Prevention of Disasters by Hazardous Materials, 2005.

[19] S. Mannan, *Lees' Loss Prevention in the Process Industries*, 4th ed. Oxford, UK: Butterworth-Heinemann, 2012.

[20] CCPS, *Guidelines for Consequence Analysis of Chemical Releases*, 1st ed. Hoboken, NJ, USA: John Wiley & Sons, 1999.

[21] D. A. Crowl and J. F. Louvar, *Chemical Process Safety: Fundamentals with Applications*, 4th ed. London, UK: Pearson Education, 2019.

[22] M. Cassiani, M. B. Bertagni, M. Marro, and P. Salizzoni, "Concentration fluctuations from localized atmospheric releases," *Bound.-Layer Meteorol.*, vol. 177, no. 2, pp. 461–510, 2020.

[23] F. Babich and G. Lombardi, "Statistical analysis and characterization of the indoor propagation channel," *IEEE Trans. Commun.*, vol. 48, no. 3, pp. 455–464, 2000.

[24] A. Shoari and A. Seyedi, "Localization of an uncooperative target with binary observations," in *11th IEEE Int. Workshop Signal Process. Adv. Wirel. Commun. (SPAWC)*, 2010.

[25] N. Megiddo, "Linear-time algorithms for linear programming in r3 and related problems," in *23rd Annu. Symp. Found. Comput. Sci. (SFCS 1982)*, 1982, pp. 329–338.

[26] J. M. Smith, H. C. Van Ness, M. M. Abbott, and M. T. Swihart, *Introduction to Chemical Engineering Thermodynamics*, 8th ed. New York (NY), USA: McGraw-Hill Education, 2018.

[27] Engineering ToolBox, "Air - Density, Specific Weight and Thermal Expansion Coefficient vs. Temperature and Pressure," 2022.

[28] C. Rago, P. Willett, and Y. Bar-Shalom, "Censoring sensors: A low-communication-rate scheme for distributed detection," *IEEE Trans. Aerosp. Electron. Syst.*, vol. 32, no. 2, pp. 554–568, Apr 1996.

[29] M. A. Al-Jarrah, M. A. Yaseen, A. Al-Dweik, O. A. Dobre, and E. Alsusa, "Decision fusion for IoT-based wireless sensor networks," *IEEE Internet Things J.*, vol. 7, no. 2, pp. 1313–1326, 2019.

Paper 8

Time-Aware Distributed Sequential Detection of Gas Dispersion via Wireless Sensor Networks

G. Tabella, D. Ciuonzo, Y. Yilmaz, X. Wang, and P. Salvo Rossi

IEEE Transactions on Signal and Information Processing over Networks, vol. 9, pp. 721-735.

Time-Aware Distributed Sequential Detection of Gas Dispersion via Wireless Sensor Networks

Gianluca Tabella, *Graduate Student Member, IEEE,* Domenico Ciuonzo, *Senior Member, IEEE,*
Yasin Yilmaz, *Senior Member, IEEE,* Xiaodong Wang, *Fellow, IEEE,*
and Pierluigi Salvo Rossi, *Senior Member, IEEE*

***Abstract*—This work addresses the problem of detecting gas dispersions through concentration sensors with wireless transmission capabilities organized as a distributed Wireless Sensor Network (WSN). The concentration sensors in the WSN perform local sequential detection (SD) and transmit their individual decisions to the Fusion Center (FC) according to a transmission rule designed to meet the low-energy requirements of a wireless setup. The FC receives the transmissions sent by the sensors and makes a more reliable global decision by employing a SD algorithm. Two variants of the SD algorithm named *Continuous Sampling Algorithm* (CSA) and *Decision-Triggered Sampling Algorithm* (DTSA), each with its own transmission rule, are presented and compared against a fully-batch algorithm named *Batch Sampling Algorithm* (BSA). The CSA operates as a *time-aware* detector by incorporating the time of each transmission in the detection rule. The proposed framework encompasses the gas dispersion model into the FC's decision rule and leverages real-time weather measurements. The case study involves an accidental dispersion of carbon dioxide (CO_2). System performances are evaluated in terms of the receiver operating characteristic (ROC) curve as well as average decision delay and communication cost.**

***Index Terms*—Wireless Sensor Networks, Sequential Detection, Distributed Detection, Industry 4.0, Gas Dispersion.**

I. Introduction

WIRELESS SENSOR NETWORKS (WSNs) have become increasingly popular for monitoring applications in the past decade: a trend that was amplified with the emergence of the Internet of Things (IoT) paradigm [3]. One area of interest has been the detection of *harmful events*, with applications related to (i) security, counter-terrorism, and defense [4], and (ii) safety and environmental protection in Industry 4.0 [5], [6].

This research is a part of BRU21 – NTNU Research and Innovation Program on Digital and Automation Solutions for the Oil and Gas Industry (www.ntnu.edu/bru21).

Part of this work has been presented to the 2022 IEEE 12th Sensor Array and Multichannel Signal Processing Workshop (SAM) [1] and the 2022 25th International Conference on Information Fusion (FUSION) [2].

G. Tabella is with the Department of Electronic Systems, Norwegian University of Science and Technology, Trondheim, Norway (e-mail: gianluca.tabella@ntnu.no).

D. Ciuonzo is with the Department of Electrical Engineering and Information Technologies, University of Naples "Federico II," Naples, Italy (e-mail: domenico.ciuonzo@unina.it)

Y. Yilmaz is with the Department of Electrical Engineering, University of South Florida, Tampa, FL, USA (e-mail: yasiny@usf.edu)

X. Wang is with the Department of Electrical Engineering, Columbia University, New York, NY, USA (e-mail: wangx@ee.columbia.edu).

P. Salvo Rossi is with the Department of Electronic Systems, Norwegian University of Science and Technology, Trondheim, Norway, and with the Department of Gas Technology, SINTEF Energy Research, Norway (e-mail: salvorossi@ieee.org).

More specifically, WSNs are typically composed of low-cost devices monitoring the surrounding environment. Due to stringent bandwidth and/or energy constraints (e.g. to ensure the long-lasting lifetime of IoT nodes), sensors are usually required to send extremely-compressed versions of their measurements to a Fusion Center (FC) which collects and analyzes the data for a final decision. For this reason, the detection of diffusive sources in safety-critical systems via WSNs has shifted toward the adoption of binary sensors [7], [8]. In such scenarios, the FC generates an alarm if an adverse event is detected, triggering appropriate actions to mitigate the consequences. This is particularly relevant to manufacturing, energy, and process industries, where equipment malfunctions can put workers and the environment in danger, as well as result in unplanned shutdowns, high costs, and lost revenue [9].

In this context, the associated inference problems involve the *early* detection of uncooperative sources, such as the loss of containment of fluids in the process industry (in gas and/or liquid form). The detection of *heavy gases* is among the most relevant problems, as heavy gases *do not adhere* to neutral or positively-buoyant dispersion behavior and tend to spread along the ground, with the further threat of asphyxiation induced by the displacement of air, resulting in low oxygen concentrations. In these industrial scenarios, it is of utmost importance to accurately detect such critical events as quickly as possible. An additional source of complexity must be taken into account in case the gas of interest is commonly found in the atmosphere: this can sensibly decrease the detector's performance. To this end, an *industrial IoT* setup with inexpensive sensors and the possibility of exploiting real-time weather data as well as the integration of the gas dispersion model represents an enabler for this problem.

This work addresses the *sequential detection* (SD) of gas dispersion using a network of wireless concentration sensors, focusing on gases with a non-null atmospheric concentration in normal conditions. Performance evaluation is carried out on a simulated dispersion of heavy gas. More specifically, in this study, we adopt the SD framework with the aim of achieving higher accuracy and lower detection time with respect to a fully batch approach. In SD the observations are processed one at a time, and a decision is made after each observation to either declare the presence or absence of the event of interest or continue with the detection process.

A. Related Work

Several methods for gas detection have been developed assuming a Gaussian-plume point-source model based on diffusion/advection processes (not suitable for heavy gases) or direct use of Fick's laws of diffusion (not suitable for complex systems), e.g. with application to dispersion of biochemical moving sources [10], [11], atmospheric pollutants [12] and release of light gases [13]. Also, in order to deal with the vague prior, importance sampling was implemented using the progressive correction technique in [14]. The algorithm showed good performance in terms of both localization and estimation accuracy. An interesting feature of this approach is that system-level performance can be controlled by a local detection threshold. Other novel methods rely on neural networks for plume tracking [15]. However, such works neglect the detection task and directly focus on the characterization of the dispersion which is facilitated by the use of a centralized sensor network.

Nevertheless, the current literature lacks studies on the use of WSNs for the detection of gases with a non-null atmospheric concentration in normal conditions, e.g. carbon dioxide (CO_2) whose current average concentration in the atmosphere is around 400 ppm. Most of the above-mentioned studies focus on the detection of gases that are not commonly present in the atmosphere, leading to amplified signal-to-noise ratios. Some preliminary investigations have attempted to fill this gap by demonstrating that the use of a model-based algorithm implemented through a WSN can improve performances in contrast to a model-free algorithm (i.e. the implementation of a *counting rule* on the received binary decisions) [1], [2]. This study builds upon these initial inquiries by incorporating the issue of *early* detection, achieved through the implementation of a SD approach.

Event detection can be tackled with multiple approaches. Distributed detection via WSNs using *batch* decision rules is a mature area of research [16]–[20]. SD (also known as *sequential analysis* or *sequential hypothesis testing*) is a well known framework popularized by Wald with the *sequential probability ratio test* (SPRT) [21], [22]. The optimality of SPRT allows achieving faster online decisions with respect to traditional *batch* detectors requiring a fixed sample size before decisions can be made via the *likelihood ratio test* (LRT) [23]. A complete overview of SD can be found in [21], [23], [24].

SD via WSNs has been explored in the last decade, but still remains an open research topic. In [25], an architecture was proposed where both the sensors and the FC perform sequential detection with sensors communicating their respective local decisions to the FC. Such a setup was proven to have asymptotically equivalent performance to the centralized counterpart in specific conditions. A higher-performance alternative was presented later in [26], grounded on the assumption that the observed signal is a sampled version of a continuous stochastic process with continuous paths. Other works (e.g. [27]) applied the distributed SD paradigm to develop spectrum sensing schemes for cognitive radio networks exploring quantization strategies. Practical aspects such as imperfect reporting channels (between sensors and FC) and requirements for reduced energy consumption were considered in [28], [29]. Recent works have focused on alternative tests than the SPRT to be used in WSNs, as the exact knowledge of the distribution function of the signal in the alternative hypothesis is often missing. Therefore, for a composite hypothesis test suitable in WSNs, a *generalized sequential probability ratio test* (GSPRT) was studied in [30].

Truncated versions of sequential tests have been explored in order to bind the decision time that might otherwise become undesirably long. When applied to one-sided tests, they are usually referred to as *truncated one-sided* (TOS) tests. A solid overview of truncated tests can be found in [24]. This option was firstly explored for SPRT and GSPRT in [31], and recently adopted in combinations with other tests. More specifically, truncation was applied to the *repeated significance test* in [32], to the *random distortion test* in [33], and finally to a FC performing the *score test* in the context of detection of a non-cooperative moving target in [34], [35].

B. Contribution and Paper Organization

This work investigates the use of a WSN made of concentration sensors in an industrial IoT setup with inexpensive small-battery sensors for gas detection purposes. First, we introduce a fully-batch algorithm, named *Batch Sampling Algorithm* (BSA), characterized by a fixed sample size at both sensors and FC. Next, with the goal of reducing the detection time, we propose two fully sequential algorithms. In the proposed strategies, each sensor measures the local concentration and takes a local decision via SD regarding the presence or absence of a gas dispersion. A *transmission rule* is present to regulate the communication from the sensors to the FC. Next, the FC, based on the transmissions received by the sensors, performs a global decision taking advantage of updated weather measurements and the integration of the gas dispersion model in the detection rule.

The first proposed method, named *Decision-Triggered Sampling Algorithm* (DTSA), has the FC sampling the sensors' transmission only when local decisions are taken. The second proposed method, named *Continuous Sampling Algorithm* (CSA), requires the FC to continuously monitor the transmissions from the sensors (which also encodes the temporary lack of a local decision). In the CSA, at each instant, the FC updates a test statistic based on the transmission values and the time elapsed since the last sensors' decision, resulting in a *time-aware* algorithm.

This work presents *new advances* in the field of industrial monitoring as listed in the following:

- The study is based on the integration of the gas dispersion model into the design of the FC;
- The proposed methods make use of externally-available measurements from weather stations (e.g. wind measurements);
- The sequential nature of the proposed methods allows to reduce the detection time and removes the limitation imposed by a fixed number of samples needed to take a decision;

- The introduction of a transmission rule tailored for sequential binary local detectors allows for reduced energy consumption in the case of CSA.

This work further explores the use of WSNs for gas detection via the integration of the dispersion model within the detection algorithm previously presented in [1], [2]. In these earlier works, we compared the well-known model-free *counting fusion rule* with a model-aware *generalized Chair-Varshney fusion rule*, proving the benefits of such implementation. The further contribution given by this work is the extension from a single-sample detection to a SD approach.

The remainder of the paper is organized as follows: Sec. II provides a system overview, focusing on the WSN architecture and the signal model (including the gas dispersion characterizations); the batch approach is described in Sec. III; the proposed sequential algorithms are described in Sec. IV, focusing on both sensors and the FC; Sec. V discusses the performances of the local sequential detectors in terms of accuracy, and decision delay; the computational complexity and the communication costs are discussed in Sec. VI; numerical results of the considered case study are presented in Sec. VII; finally, conclusions and further works are addressed in Sec. VIII.

C. Notation

Uppercase (resp. lowercase) bold letters denote matrices (resp. column vectors); $[\cdot]^{\mathrm{T}}$ denotes the transpose operator; $\hat{a}$ is an estimate of the variable a; $\mathbb{E}(\cdot)$, $\mathbb{V}\mathrm{ar}(\cdot)$, $\mathbb{C}\mathrm{ov}(\cdot\,,\cdot)$ denote expectation, variance, and covariance; $\mathbb{P}(\cdot)$ and $p(\cdot)$ denote probability mass functions (PMFs) and probability density functions (PDFs), while $\mathbb{P}(\cdot|\cdot)$ and $p(\cdot|\cdot)$ their corresponding conditional counterparts; in particular, $\mathbb{E}_j(\cdot)$, $\mathbb{P}_j(\cdot)$ and $p_j(\cdot)$ denote the expectation, the PMF, and PDF, respectively, under the hypothesis $\mathcal{H}_j$, with $j \in \{0,1\}$; $\mathcal{L}_\theta(a) \triangleq \ln[\mathbb{P}_1(a;\theta)/\mathbb{P}_0(a)]$ is the log-likelihood ratio where the dependence on the parameter θ is highlighted; $\mathcal{U}(a,b)$ denotes a continuous uniform distribution with minimum value a and maximum value b; $\mathcal{N}(\boldsymbol{\mu},\boldsymbol{\Sigma})$ denotes a multivariate Gaussian distribution with mean $\boldsymbol{\mu}$ and covariance matrix $\boldsymbol{\Sigma}$; $\mathcal{Q}(\cdot)$ is the complementary cumulative distribution function (CCDF) of the standard normal distribution; $\delta_{a,b}$ is the Kronecker delta; finally $\mathcal{O}(\cdot)$ denotes the big O notation.

II. System Model

What follows is the overview of the distributed WSN under consideration, followed by the characterization of the signal measured by the sensors.

A. Wireless Sensor Network Model

The scenario consists of a distributed WSN comprising K static sensors and its task is to assess the *global* absence ($\mathcal{H}_0$) or presence ($\mathcal{H}_1$) of a gas leak within the monitored environment (a schematic representation is given in Fig. 1)[1].

[1]The possibility of incurring faulty sensors is not taken into account as it is outside of the scope of the present work. Fault detection and identification techniques based on data-driven philosophy could be readily incorporated in the proposed approach [36].

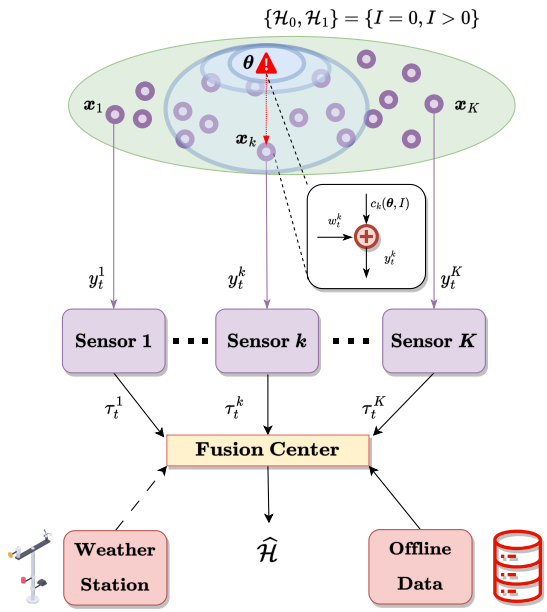

Fig. 1: Wireless Sensor Network Architecture.

Such a dispersion is characterized by its position $\boldsymbol{\theta}$ and intensity I. For the kth sensor ($k = 1, \ldots, K$), the location and the measurement of gas concentration at discrete-time $t \in \mathbb{N}^+$ are denoted by $\boldsymbol{x}_k$ and y_t^k, respectively. Each sensor computes a test statistic on the above-mentioned signal and assesses the *local* absence ($\mathcal{H}_0$) or presence ($\mathcal{H}_1$) of an anomalous excessive gas concentration. For the sake of convenience, we assumed the sensor to have the same sampling frequency and to be perfectly synchronized. In the algorithms under study, when a sensor makes a decision, it immediately starts a new detection instance until the FC takes a global decision, allowing the FC to receive multiple decisions from a single sensor. The global decision exploits the integration of real-time weather data as well as the dispersion model of the gas.

When the BSA is employed, each sensor takes a decision after a fixed number of measurements. At each instant, each sensor sends a *transmission value* $\tau_t^k = 1$ (resp. $\tau_t^k = -1$) to the FC if $\mathcal{H}_1$ is declared (resp. $\mathcal{H}_0$), or $\tau_t^k = 0$ if the sensor has not finished collecting its fixed number of samples. Specifically, when $\tau_t^k = 0$, the sensor *does not* transmit a physical communication to the FC. At a predetermined time, the FC takes a global decision $\widehat{\mathcal{H}} \in \{\mathcal{H}_0, \mathcal{H}_1\}$ computing a test statistic on the received values $\left\{\tau_t^k : |\tau_t^k| = 1\right\}_{k,t}$.

In the newly proposed methods (DTSA and CSA), both the sensors and the FC make use of SD, with the aim of reducing the decision delay obtained in the BSA.

In the DTSA, the sensors send a transmission value to the FC after completing a sequential test, i.e. not at predetermined times, unlike in the BSA. Here, at each t, the FC performs a test on $\left\{\tau_t^k : |\tau_t^k| = 1\right\}_k$ and takes a global decision.

In the CSA, each individual sensor transmits a bit $\tau_t^k = 1$

(resp. $\tau_t^k = 0$) to the FC if $\mathcal{H}_1$ is locally declared (resp. if $\mathcal{H}_0$ is locally declared or if the sensor has not reached a decision yet). In addition to being spectrally efficient, as only one bit is transmitted on the communication channel between the sensor and the FC, such a system is highly energy efficient when OOK modulation is employed for communicating the local decisions [5]. Moreover, at each t, the FC sequentially performs a *time-aware* test on the transmission values $\left\{\tau_t^k, a_t^k\right\}_k$, where a_t^k is the number of instants passed since the last decision made by the kth sensor.

In this work, we assume a perfect communication channel between sensors and FC.

B. Signal Model

The statistical model of the measured gas concentration y_t^k, depending on the corresponding hypothesis, is the following:

$$\begin{cases} \mathcal{H}_0: & y_t^k = w_t^k \\ \mathcal{H}_1: & y_t^k = c_k + w_t^k \end{cases}, \tag{1}$$

where $w_t^k \sim \mathcal{N}\left(\mu_k, \sigma_k^2\right)$ represents the gas concentration present in normal operating conditions in the surrounding of the kth sensor [37], where the values of μ_k and σ_k^2 are both *known*. The values of $\{\mu_k\}_k$ and $\left\{\sigma_k^2\right\}_k$ can be estimated by calculating the sample mean and sample variance from a set of measurements acquired in normal operating conditions ($\mathcal{H}_0$). Also, $c_k \geq 0$ is the observed excess gas concentration resulting from dispersion, here assumed constant in time since this work deals with steady-state dispersions.

In this work, we assume that the measurements collected by the same sensor $\left\{y_t^k\right\}_t$ are i.i.d., while the measurements collected by different sensors $\left\{y_t^k\right\}_k$ are independent, with distributions that vary depending on $\{c_k\}_k$. This assumption arises from Eq. (1) and the treatment of $\left\{w_t^k\right\}_{t,k}$ as i.i.d. variables. Although this treatment simplifies reality, assuming null space and time correlation in the modeling of $\left\{w_t^k\right\}_{t,k}$ can be justified by ensuring adequate spatial separation between the sensors and a sufficiently low sampling frequency. A low sampling frequency results in auto-covariance values dominated by lower-frequency components. Moreover, accurately predicting these lower-frequency components in the atmospheric fluctuation of the concentration of the gas presents significant complexities. Therefore, we chose to simplify the model by excluding them [20], [38]. Hence, the distribution of y_t^k is:

$$\begin{cases} \mathcal{H}_0: & y_t^k \sim \mathcal{N}\left(\mu_k, \sigma_k^2\right) \\ \mathcal{H}_1: & y_t^k \sim \mathcal{N}\left(\mu_k + c_k, \sigma_k^2\right) \end{cases}, \tag{2}$$

where the value of c_k is the result of a dispersion phenomenon. There is extensive literature on how to obtain the value of c_k due to its industrial safety applications. We assume:

$$c_k = \mathcal{F}(\boldsymbol{x}_k, \mathcal{A}, \mathcal{B}, \mathcal{C}), \tag{3}$$

where $\mathcal{A}$ is the set of all *unknown* variables such as the release position ($\boldsymbol{\theta}$), and the intensity (I); $\mathcal{B}$ is the set of variables whose value is *known* and constant in time, once the variables in $\mathcal{A}$ are fixed. $\mathcal{B}$ includes variables such as temperature, density, initial concentration of the release, as well as morphological properties of the area. $\mathcal{C}$ is the set of variables that can be considered independent from the variables in $\mathcal{A}$ and $\boldsymbol{x}_k$, and whose value is *known* via real-time measurement. This set includes the meteorological parameters. The values of the variables in $\mathcal{B}$ are set by exploiting the knowledge of the monitored environment, while those in $\mathcal{C}$ require real-time meteorological data. For the case of a release, the most important variables belonging to $\mathcal{A}$ are $\boldsymbol{\theta}$ and I, hence once $\boldsymbol{x}_k$, $\boldsymbol{\theta}$, and I are fixed, and the variables in $\mathcal{B}$ and $\mathcal{C}$ are available, the value of c_k can be unequivocally determined.

III. Batch Detection

This section is dedicated to the BSA which relies on fixed sample size at both sensors and FC levels for the detection task. This algorithm is designed for a FC that is able to compute c_k via the map in Eq. (3) once the unknown dispersion variables belonging to $\mathcal{A}$ have been fixed. c_k is written as $c_k(\theta, I)$ to emphasize the unknown variables. The other variables in Eq. (3) are known and constant throughout the detection procedure. Real-time weather data and, possibly, physical knowledge of the monitored area are necessary to determine the variables in $\mathcal{B}$ and $\mathcal{C}$. The considered architecture requires solving a maximization problem: we assume grid-search optimization.

Specifically, the kth sensor will take a local decision after collecting $\mathcal{T}_k$ samples, after which it restarts a new detection instance. As a consequence, each sensor is characterized by a deterministic *stopping time* corresponding to the mth decision $t_m^k = m\mathcal{T}_k$. For the model described in Eq. (1), the *likelihood ratio test* (LRT) is *uniformly most powerful*, resulting in each sensor calculating a statistic Λ_t^k with the following form[2]:

$$\Lambda_t^k \triangleq \sum_{i=1}^{t} \left(y_i^k - \mu_k\right) = \begin{cases} \lambda_1^k, & t = 1 \\ \Lambda_{(t-1)}^k + \lambda_t^k, & t > 1 \end{cases}, \tag{4}$$

where $\lambda_t^k \triangleq y_t^k - \mu_k$. This leads to the following decision rule:

$$d_m^k \triangleq \begin{cases} \mathcal{H}_1, & \text{if } \Lambda_{m\mathcal{T}_k}^k - \Lambda_{(m-1)\mathcal{T}_k}^k \geq \gamma_k \\ \mathcal{H}_0, & \text{otherwise} \end{cases}, \tag{5}$$

with γ_k as a local test threshold. The *probability of false alarm* ($\mathcal{P}_F^k$) and *detection* ($\mathcal{P}_D^k(c_k)$) of the local batch detector are the following:

$$\begin{aligned} \mathcal{P}_F^k &\triangleq \mathbb{P}_0\left(d_m^k = \mathcal{H}_1\right) = \mathbb{P}_0\left(d_1^k = \mathcal{H}_1\right) \\ &= \mathbb{P}_0\left(\Lambda_{\mathcal{T}_k}^k \geq \gamma_k\right) = \mathcal{Q}\left(\frac{\gamma_k}{\sqrt{\mathcal{T}_k \sigma_k^2}}\right), \\ \mathcal{P}_D^k(c_k) &\triangleq \mathbb{P}_1\left(d_m^k = \mathcal{H}_1\right) = \mathcal{Q}\left(\frac{\gamma_k - \mathcal{T}_k c_k}{\sqrt{\mathcal{T}_k \sigma_k^2}}\right), \end{aligned} \tag{6}$$

where we exploited the fact that $\left\{\Lambda_{m\mathcal{T}_k}^k - \Lambda_{(m-1)\mathcal{T}_k}^k\right\}_m$ are i.i.d., and therefore we chose $m = 1$.

[2]The LRT statistic can be simplified into $\sum_{i=1}^{t} y_i^k$. However, we prefer using the above-mentioned statistic to ease the comparison with the DTSA and CSA.

To prove that the above-mentioned elements are i.i.d., it is sufficient to say that, since $\left\{y_i^k\right\}_i$ are i.i.d., the same applies to the disjoint subsequences $\left\{y_{(m-1)\mathcal{T}_k+1}^k, \ldots, y_{m\mathcal{T}_k}^k\right\}_m$. This means that the set of statistics computed over these subsequences, expressed as $\left\{\sum_{i=(m-1)\mathcal{T}_k+1}^{m\mathcal{T}_k} \lambda_i^k\right\}_m$, also consist of i.i.d. elements. Finally, by applying the definition of Λ_t^k from Eq. (4), we can conclude that the elements in the sequence $\left\{\Lambda_{m\mathcal{T}_k}^k - \Lambda_{(m-1)\mathcal{T}_k}^k\right\}_m$ are i.i.d. as well.

At each instant t, the kth sensor sends a transmission value to the FC according to the following transmission rule:

$$\tau_t^k \triangleq \begin{cases} +1\,, & \text{if } \exists\, m : t = m\,\mathcal{T}_k \ \wedge\ d_m^k = \mathcal{H}_1 \\ -1\,, & \text{if } \exists\, m : t = m\,\mathcal{T}_k \ \wedge\ d_m^k = \mathcal{H}_0 \\ 0\,, & \text{otherwise} \end{cases}, \tag{7}$$

with $\tau_t^k = 0$ indicating the absence of physical communication from the sensor to FC during the sensor's fixed decision period.

At predetermined time $\mathcal{T}^*$, the FC takes a global decision employing a GLRT statistic Λ^{B} on the local decisions:

$$\widehat{\mathcal{H}} \triangleq \begin{cases} \mathcal{H}_1\,, & \text{if } \Lambda^{\text{B}} \geq \gamma^* \\ \mathcal{H}_0\,, & \text{otherwise} \end{cases}, \tag{8}$$

with γ^* as a global test threshold. Since the statistic is a function of the local decisions having known fixed decision delays, it is recommended to set $\mathcal{T}^*$ so that $\exists\, k, a \in \mathbb{N}^+ : \mathcal{T}^* = a\,\mathcal{T}_k$. In order to calculate Λ^{B}, the FC has to keep track of the transmission times t_m^k:

$$t_m^k = \inf\left\{t > t_{m-1}^k : \left|\tau_t^k\right| = 1\right\}, \quad t_0^k = 0\,. \tag{9}$$

Specifically, Λ^{B} is a statistic on the received local decisions, which translates into a test on the transmission values $\left\{\tau_t^k : \left|\tau_t^k\right| = 1\right\}_{t,k}$:

$$\begin{aligned} \Lambda^{\text{B}} &\triangleq \max_{\boldsymbol{\theta}, I}\left\{\mathcal{L}_{\boldsymbol{\theta},I}\left(\left\{\tau_t^k : \left|\tau_t^k\right| = 1\right\}_{\substack{1\leq t\leq \mathcal{T}^* \\ 1\leq k\leq K}}\right)\right\} \\ &= \max_{\boldsymbol{\theta}, I}\left\{\sum_{k=1}^{K}\sum_{m=1}^{\mathcal{M}_{\mathcal{T}^*}^k} \mathcal{L}_{\boldsymbol{\theta},I}\left(\tau_{t_m^k}^k\right)\right\}, \end{aligned} \tag{10}$$

where $\mathcal{M}_{\mathcal{T}^*}^k \triangleq \sum_{t=1}^{\mathcal{T}^*}\left|\tau_t^k\right|$ is the number of local decisions taken by the kth sensor up to time $\mathcal{T}^*$. In particular, $\mathcal{L}_{\boldsymbol{\theta},I}\left(\tau_{t_m^k}^k\right)$ has the following form:

$$\mathcal{L}_{\boldsymbol{\theta},I}\left(\tau_{t_m^k}^k\right) = \begin{cases} \ln\frac{\mathcal{P}_D^k(c_k(\theta,I))}{\mathcal{P}_F^k}\,, & \text{if } \tau_{t_m^k}^k = +1 \\ \ln\frac{1-\mathcal{P}_D^k(c_k(\theta,I))}{1-\mathcal{P}_F^k}\,, & \text{if } \tau_{t_m^k}^k = -1 \end{cases}. \tag{11}$$

IV. Sequential Detection

In this section, we explore the CSA and DTSA. First, we examine the SD algorithm at a sensor level shared by both architectures. Next, we outline the algorithm at the FC level in the two different methods.

A. Local Sequential Detection

Each sensor performs SD on the hypotheses in Eq. (1). Eq. (2) highlights that the test has to be *one-sided* since $\{\mathcal{H}_0, \mathcal{H}_1\}$ correspond to $\{c_k = 0, c_k \geq 0\}$, respectively. For this task, we compute the GSPRT statistic, where the parameter c_k in the log-likelihood ratio is replaced with its maximum likelihood estimate $\widehat{c}_{k,t} \triangleq \frac{1}{t}\sum_{i=1}^{t} y_i^k - \mu_k$. This results in the same statistic Λ_t^k already introduced in Eq. (4).

The GSPRT, analogously to the *generalized likelihood ratio test*, is asymptotically non-negative for one-sided hypothesis testing problems, thus the use of a negative threshold is unfeasible. To overcome this issue, we resort to a TOS test by establishing the maximum amount of time $\mathcal{T}_k$ between two consecutive local decisions that the kth sensor can take in order to declare $\mathcal{H}_1$, otherwise, $\mathcal{H}_0$ is declared. Denoting γ_k as a positive local threshold and the time at which the sensor takes the mth decision with t_m^k, the mth stopping time is defined as the following:

$$\begin{aligned} t_m^k &\triangleq \min\left\{\inf\left\{t > t_{m-1}^k : \Lambda_t^k - \Lambda_{t_{m-1}^k}^k \geq \gamma_k\right\}, t_{m-1}^k + \mathcal{T}_k\right\} \\ &= \min\left\{\inf\left\{t > t_{m-1}^k : \sum_{i=t_{m-1}^k+1}^{t} \lambda_i^k \geq \gamma_k\right\}, t_{m-1}^k + \mathcal{T}_k\right\}, \end{aligned} \tag{12}$$

with $t_0^k = 0$ and $\Lambda_0^k = 0$. Next, the decision rule is as follows:

$$d_m^k \triangleq \begin{cases} \mathcal{H}_1\,, & \text{if } \Lambda_{t_m^k}^k - \Lambda_{t_{m-1}^k}^k \geq \gamma_k \\ \mathcal{H}_0\,, & \text{otherwise} \end{cases}. \tag{13}$$

Remarks – In the process of deriving the local detector, we employ the Karlin-Rubin theorem to reduce the test statistic (via monotonic transformations) before substituting c_k with its MLE. This reduction is achieved by exploiting the non-negative nature of c_k.

B. Fusion Center Sequential Detection

Here we describe the two FC detection methods for gas dispersion: (i) DTSA, a SD algorithm with the FC performing a test statistic solely based on the received local decisions (the knowledge of the sampling period is not required); (ii) CSA, a novel *time-aware* SD algorithm with the FC performing a test statistic on those instants where the sensors take decisions as well as on those instants where the sensors have not reached a decision yet (the knowledge of the sampling period for each sensor is required). As in the BSA, both methods rely on the ability to calculate the values of c_k via the map in Eq. (3).

1) Decision-Triggered Sampling Algorithm (DTSA): This algorithm consists of the FC sequentially updating a test statistic when a local decision is taken. Similarly to the BSA, the transmission rule encodes the detection status of the sensors:

$$\tau_t^k \triangleq \begin{cases} +1\,, & \text{if } \exists\, m : t = t_m^k \ \wedge\ d_m^k = \mathcal{H}_1 \\ -1\,, & \text{if } \exists\, m : t = t_m^k \ \wedge\ d_m^k = \mathcal{H}_0 \\ 0\,, & \text{otherwise} \end{cases}, \tag{14}$$

where $\tau_t^k = 0$ indicates the absence of a physical transmission from the sensor to FC. This transmission rule translates into a test statistic performed on those transmission values that are decision-triggered $\left\{\tau_t^k : \left|\tau_t^k\right| = 1\right\}_{t,k}$. Similarly to the design of the local detectors, the presence of the unknown parameters $\boldsymbol{\theta}$ and I in the hypothesis $\mathcal{H}_1$ requires the use of a GSPRT statistic here denoted by Λ_t^{D}. Likewise, we use a time limit $\mathcal{T}^*$ at which, if the FC has not declared $\mathcal{H}_1$ yet, $\mathcal{H}_0$ is automatically reported, leading to the following stopping rule and decision rule:

$$t^* \triangleq \min\{\inf\{t : \Lambda_t^{\mathrm{D}} \geq \gamma^*\}, \mathcal{T}^*\}\,, \tag{15}$$

$$\widehat{\mathcal{H}} \triangleq \begin{cases} \mathcal{H}_1\,, & \text{if } \Lambda_{t^*}^{\mathrm{D}} \geq \gamma^* \\ \mathcal{H}_0\,, & \text{otherwise} \end{cases}. \tag{16}$$

At each t, in order to calculate Λ_t^{D}, the FC needs to recover the stopping times t_m^k (using Eq. (9)), as well as (recursively) calculate the number of local decisions taken by the kth sensor up to time t, for all k:

$$\mathcal{M}_t^k = \mathcal{M}_{t-1}^k + \left|\tau_t^k\right|\,, \quad \mathcal{M}_0^k = 0\,. \tag{17}$$

The next step consists of the FC computing the GSPRT statistic Λ_t^{D}:

$$\begin{aligned}\Lambda_t^{\mathrm{D}} &\triangleq \max_{\boldsymbol{\theta},I}\left\{\mathcal{L}_{\boldsymbol{\theta},I}\left(\left\{\tau_i^k : \left|\tau_i^k\right| = 1\right\}_{\substack{1\leq i\leq t\\ 1\leq k\leq K}}\right)\right\} \\ &= \max_{\boldsymbol{\theta},I}\left\{\sum_{k=1}^{K}\sum_{m=1}^{\mathcal{M}_t^k}\mathcal{L}_{\boldsymbol{\theta},I}\left(\tau_{t_m^k}^k\right)\right\}, \end{aligned} \tag{18}$$

where again we exploited the independence of the local decisions in time and space. The term $\mathcal{L}_{\boldsymbol{\theta},I}\left(\tau_{t_m^k}^k\right)$ can be obtained using the *overall local performances* of the sensors:

$$\mathcal{L}_{\boldsymbol{\theta},I}\left(\tau_{t_m^k}^k\right) = \begin{cases} \ln\frac{\mathcal{P}_D^k(c_k(\theta,I))}{\mathcal{P}_F^k}\,, & \text{if } \tau_{t_m^k}^k = +1 \\ \ln\frac{\mathcal{P}_M^k(c_k(\theta,I))}{\mathcal{P}_C^k}\,, & \text{if } \tau_{t_m^k}^k = -1 \end{cases}, \tag{19}$$

with $\mathcal{P}_D^k$, $\mathcal{P}_F^k$, $\mathcal{P}_M^k$, and $\mathcal{P}_C^k$ representing the *overall probability of detection*, *false alarm*, *miss detection*, and *correct rejection*, respectively, of a sequential detector. These metrics are discussed in Sec. V.

2) Continuous Sampling Algorithm (CSA): In this configuration, the kth sensor transmits a message to the FC only when $\mathcal{H}_1$ is declared, so we can state the following transmission rule at each t:

$$\tau_t^k \triangleq \begin{cases} 1\,, & \text{if } \exists\, m : t = t_m^k \,\wedge\, d_m^k = \mathcal{H}_1 \\ 0\,, & \text{otherwise} \end{cases}, \tag{20}$$

where τ_t^k is the *transmission value*, with $\tau_t^k = 0$ indicating the absence of a physical transmission from the sensor to FC.

Meanwhile, the FC sequentially updates a statistic using the received transmission values $\left\{\tau_t^k\right\}_{k,t}$. The knowledge of the sampling period of each sensor allows such a continuous sampling although $\tau_t^k = 0$ does not constitute a physical transmission. The reason behind the use of the same transmission value $\tau_t^k = 0$ to represent the absence of a decision and a negative decision lies in the deterministic nature of the time taken by a sensor to declare $\mathcal{H}_0$ (equal to $\mathcal{T}_k$) which allows to unequivocally distinguish the two cases. Similarly to the previously proposed architecture, we employ a truncated GSPRT, whose statistic is indicated with Λ_t^{C} with a time limit $\mathcal{T}^*$, leading to the following stopping rule and decision rule:

$$\begin{aligned} t^* &\triangleq \min\{\inf\{t : \Lambda_t^{\mathrm{C}} \geq \gamma^*\}, \mathcal{T}^*\}\,, \\ \widehat{\mathcal{H}} &\triangleq \begin{cases} \mathcal{H}_1\,, & \text{if } \Lambda_{t^*}^{\mathrm{C}} \geq \gamma^* \\ \mathcal{H}_0\,, & \text{otherwise} \end{cases}. \end{aligned} \tag{21}$$

At each t, the calculation of Λ_t^{C} requires the FC to sequentially deduce, for each sensor, whether the received transmission value τ_t^k corresponds to a local decision or not, and retrieve the current delay a_t^k:

$$t_m^k = \min\left\{\inf\left\{t > t_{m-1}^k : \tau_t^k = 1\right\}, t_{m-1}^k + \mathcal{T}_k\right\}\,, \tag{22}$$

$$\mathcal{M}_t^k = \begin{cases} \mathcal{M}_{t-1}^k + 1\,, & \text{if } t = t_{\mathcal{M}_{t-1}^k}^k + 1 \\ \mathcal{M}_{t-1}^k\,, & \text{otherwise} \end{cases}, \tag{23}$$

$$a_t^k = \begin{cases} 1\,, & \text{if } t = t_{\mathcal{M}_{t-1}^k}^k + 1 \\ a_{t-1}^k + 1\,, & \text{otherwise} \end{cases}, \tag{24}$$

where $\mathcal{M}_t^k$ now counts the number of local decisions taken by the kth sensor at time t *including* the one that is currently being taken, with $t_0^k = 0$ and $\mathcal{M}_0^k = 0$. The next step consists of the FC computing the GSPRT statistic Λ_t^{C}:

$$\begin{aligned}\Lambda_t^{\mathrm{C}} &\triangleq \max_{\boldsymbol{\theta},I}\left\{\mathcal{L}_{\boldsymbol{\theta},I}\left(\left\{\tau_i^k\right\}_{\substack{1\leq i\leq t\\ 1\leq k\leq K}}\right)\right\} \\ &= \max_{\boldsymbol{\theta},I}\left\{\sum_{k=1}^{K}\sum_{m=1}^{\mathcal{M}_t^k}\mathcal{L}_{\boldsymbol{\theta},I}\left(\tau_{\min\{t,t_m^k\}}^k, a_{\min\{t,t_m^k\}}^k\right)\right\}, \end{aligned} \tag{25}$$

where we exploited the independence of the local decisions in time and space. The generic value of $\mathcal{L}_{\boldsymbol{\theta},I}\left(\tau_t^k, a_t^k\right)$ can be expressed using the *instant local performances* of the sensors:

$$\mathcal{L}_{\boldsymbol{\theta},I}\left(\tau_t^k, a_t^k\right) = \begin{cases} \ln\frac{\mathcal{P}_D^{(k,a_t^k)}(c_k(\theta,I))}{\mathcal{P}_F^{(k,a_t^k)}}\,, & \text{if } \tau_t^k = 1 \\ \ln\frac{\mathcal{P}_M^{(k,a_t^k)}(c_k(\theta,I))}{\mathcal{P}_C^{(k,a_t^k)}}\,, & \text{if } \tau_t^k = 0 \end{cases}, \tag{26}$$

with $\mathcal{P}_D^{(k,i)}$, $\mathcal{P}_F^{(k,i)}$, $\mathcal{P}_M^{(k,i)}$, and $\mathcal{P}_C^{(k,i)}$ representing the *instant probability of detection*, *false alarm*, *miss detection*, and *correct rejection*, respectively (see Sec. V).

V. Analysis of Local Sequential Detection

The assessment of the local performances of sequential detectors is now reported. First, we assess the *instant* and *overall performances*. Next, we analyze the local decision delays. In the rest of the work, to ease the comparison between the presented architectures, we will assume that the deadlines $\mathcal{T}_k$'s (resp. $\mathcal{T}^*$) used in the DTSA and CSA are set to have the same values of the sample sizes at sensor level (resp. FC level) used in the BSA.

A. Instant Local Performances

We analyze the local performances at the kth sensor in terms of *instant probability of false alarm* $\mathcal{P}_F^{(k,i)}$ and *instant probability of detection* $\mathcal{P}_D^{(k,i)}(c_k)$ for the generic mth decision with respect to each time instant $\{t_{m-1}^k + i\}_{i=1}^{\mathcal{T}_k}$:

$$\begin{aligned}\mathcal{P}_F^{(k,i)} &\triangleq \mathbb{P}_0\big(d_m^k = \mathcal{H}_1, t_m^k - t_{m-1}^k = i\big)\\ &= \mathbb{P}_0\Big(\big\{\Lambda_t^k < \gamma_k\big\}_{t<i}, \Lambda_i^k \geq \gamma_k\Big)\,,\\ \mathcal{P}_D^{(k,i)}(c_k) &\triangleq \mathbb{P}_1\Big(\big\{\Lambda_t^k < \gamma_k\big\}_{t<i}, \Lambda_i^k \geq \gamma_k; c_k\Big)\,, \end{aligned} \tag{27}$$

where, analogously to Eq. (6), we exploited the fact that $\left\{\Lambda_t^k - \Lambda_{t_{m-1}^k}^k\right\}_m$ are i.i.d. for any $t \in [t_{m-1}+1, t_{m-1}+i]$, and therefore we chose $m = 1$.

By examining Eqs. (2) and (4), we have:

$$\begin{cases}\mathcal{H}_0: & \Lambda_i^k \sim \mathcal{N}\big(0, i\sigma_k^2\big)\\ \mathcal{H}_1: & \Lambda_i^k \sim \mathcal{N}\big(ic_k, i\sigma_k^2\big)\end{cases}. \tag{28}$$

Therefore Eq. (27) is obtained via computing the CDF of a multivariate Gaussian random variable in the form of $\mathbb{P}_j\big(\boldsymbol{z}_i^k \leq \mathbf{0}\big)$, with $\boldsymbol{z}_i^k \overset{\mathcal{H}_j}{\sim} \mathcal{N}\Big(\boldsymbol{\mu}_{\boldsymbol{z}_i^k}^j, \boldsymbol{\Sigma}_{\boldsymbol{z}_i^k}\Big)$, where:

$$\boldsymbol{z}_i^k \triangleq \begin{bmatrix}\Lambda_1^k - \gamma_k\\ \vdots\\ \Lambda_{i-1}^k - \gamma_k\\ -\Lambda_i^k + \gamma_k\end{bmatrix},\ \boldsymbol{\mu}_{\boldsymbol{z}_i^k}^0 \triangleq \begin{bmatrix}-\gamma_k\\ \vdots\\ -\gamma_k\\ \gamma_k\end{bmatrix},\ \boldsymbol{\mu}_{\boldsymbol{z}_i^k}^1 \triangleq \begin{bmatrix}c_k - \gamma_k\\ \vdots\\ (i-1)c_k - \gamma_k\\ -ic_k + \gamma_k\end{bmatrix},$$

$$\boldsymbol{\Sigma}_{\boldsymbol{z}_i^k} \triangleq \begin{bmatrix}\sigma_k^2 & \sigma_k^2 & \cdots & \sigma_k^2 & -\sigma_k^2\\ \sigma_k^2 & 2\sigma_k^2 & \cdots & 2\sigma_k^2 & -2\sigma_k^2\\ \vdots & \vdots & \ddots & \vdots & \vdots\\ \sigma_k^2 & 2\sigma_k^2 & \cdots & (i-1)\sigma_k^2 & -(i-1)\sigma_k^2\\ -\sigma_k^2 & -2\sigma_k^2 & \cdots & -(i-1)\sigma_k^2 & i\sigma_k^2\end{bmatrix}. \tag{29}$$

Moreover, computing the *instant probability of correct rejection* ($\mathcal{P}_C^{(k,i)}$) and the *instant probability of miss detection* ($\mathcal{P}_M^{(k,i)}(c_k)$) is needed for the CSA:

$$\mathcal{P}_C^{(k,i)} \triangleq 1 - \sum_{j=1}^{i} \mathcal{P}_F^{(k,j)}\,, \quad \mathcal{P}_M^{(k,i)}(c_k) \triangleq 1 - \sum_{j=1}^{i} \mathcal{P}_D^{(k,j)}(c_k)\,. \tag{30}$$

Hence, the values of $\mathcal{P}_C^{(k,i)}$ and $\mathcal{P}_M^{(k,i)}$ are obtained from previously calculated probabilities. However, such probabilities are computed via numerical methods (being CDFs of multivariate Gaussian random variables). Unless the approximation error is sufficiently low, we might experience (mainly for high values of i) an accumulation of errors in the final result, especially undesirable when leading to negative values in Eq. (30). For this reason, we also include the direct calculation of $\mathcal{P}_C^{(k,i)}$ and $\mathcal{P}_M^{(k,i)}(c_k)$ which are defined as:

$$\begin{aligned}\mathcal{P}_C^{(k,i)} &\triangleq \mathbb{P}_0\Big(\big\{\Lambda_t^k < \gamma_k\big\}_{t\leq i}\Big)\,,\\ \mathcal{P}_M^{(k,i)}(c_k) &\triangleq \mathbb{P}_1\Big(\big\{\Lambda_t^k < \gamma_k\big\}_{t\leq i}; c_k\Big)\,.\end{aligned} \tag{31}$$

These can be obtained computing $\mathbb{P}_j\big(\boldsymbol{v}_i^k \leq \mathbf{0}\big)$, with $\boldsymbol{v}_i^k \overset{\mathcal{H}_j}{\sim} \mathcal{N}\Big(\boldsymbol{\mu}_{\boldsymbol{v}_i^k}^j, \boldsymbol{\Sigma}_{\boldsymbol{v}_i^k}\Big)$. Specifically:

$$\boldsymbol{v}_i^k \triangleq \begin{bmatrix}\Lambda_1^k - \gamma_k\\ \vdots\\ \Lambda_i^k - \gamma_k\end{bmatrix},\ \boldsymbol{\mu}_{\boldsymbol{v}_i^k}^0 \triangleq \begin{bmatrix}-\gamma_k\\ \vdots\\ -\gamma_k\end{bmatrix},\ \boldsymbol{\mu}_{\boldsymbol{v}_i^k}^1 \triangleq \begin{bmatrix}c_k - \gamma_k\\ \vdots\\ (i-1)c_k - \gamma_k\\ ic_k - \gamma_k\end{bmatrix},$$

$$\boldsymbol{\Sigma}_{\boldsymbol{v}_i^k} \triangleq \begin{bmatrix}\sigma_k^2 & \sigma_k^2 & \sigma_k^2 & \cdots & \sigma_k^2\\ \sigma_k^2 & 2\sigma_k^2 & 2\sigma_k^2 & \cdots & 2\sigma_k^2\\ \sigma_k^2 & 2\sigma_k^2 & 3\sigma_k^2 & \cdots & 3\sigma_k^2\\ \vdots & \vdots & \vdots & \ddots & \vdots\\ \sigma_k^2 & 2\sigma_k^2 & 3\sigma_k^2 & \cdots & i\sigma_k^2\end{bmatrix}. \tag{32}$$

$\boldsymbol{\Sigma}_{\boldsymbol{z}_i^k}$ and $\boldsymbol{\Sigma}_{\boldsymbol{v}_i^k}$ are derived in Appendix A.

B. Overall Local Performances

The *overall probabilities of false alarm* ($\mathcal{P}_F^k$) and *detection* ($\mathcal{P}_D^k(c_k)$) at the kth sensor for the mth decision are:

$$\begin{aligned}\mathcal{P}_F^k &\triangleq \mathbb{P}_0\big(d_m^k = \mathcal{H}_1\big) = \sum_{i=1}^{\mathcal{T}_k} \mathcal{P}_F^{(k,i)}\,,\\ \mathcal{P}_D^k(c_k) &\triangleq \mathbb{P}_1\big(d_m^k = \mathcal{H}_1; c_k\big) = \sum_{i=1}^{\mathcal{T}_k} \mathcal{P}_D^{(k,i)}(c_k)\,.\end{aligned} \tag{33}$$

The results in Eq. (30) do not relate to local decisions except for $i = \mathcal{T}_k$, in such case, the overall probabilities of correct rejection ($\mathcal{P}_C^k$) and miss detection ($\mathcal{P}_M^k(c_k)$) are readily given:

$$\mathcal{P}_C^k \triangleq \mathcal{P}_C^{(k,\mathcal{T}_k)}\,, \quad \mathcal{P}_M^k(c_k) \triangleq \mathcal{P}_M^{(k,\mathcal{T}_k)}(c_k)\,. \tag{34}$$

C. Local Decision Delays

With the local detection algorithm being sequential, one can evaluate the average time taken to reach a decision. We use $\mathcal{D}_{1j}^k$ to represent the expected time taken by the kth sensor to declare $\mathcal{H}_1$ when $\mathcal{H}_j$ is true, while $\mathcal{D}_{0X}^k$ refers to the declaration of $\mathcal{H}_0$ independently of the true hypothesis:

$$\begin{aligned}\mathcal{D}_{10}^k &\triangleq \mathbb{E}_0\big(t_m^k - t_{m-1}^k \big| d_m^k = \mathcal{H}_1\big)\\ &= \sum_{i=1}^{\mathcal{T}_k} i\,\mathbb{P}_0\big(t_1^k = i \big| d_1^k = \mathcal{H}_1\big) = \frac{1}{\mathcal{P}_F^k}\sum_{i=1}^{\mathcal{T}_k} i\,\mathcal{P}_F^{(k,i)}\,,\\ \mathcal{D}_{11}^k(c_k) &\triangleq \frac{1}{\mathcal{P}_D^k(c_k)}\sum_{i=1}^{\mathcal{T}_k} i\,\mathcal{P}_D^{(k,i)}(c_k)\,,\\ \mathcal{D}_{0X}^k &\triangleq \mathbb{E}\big(t_m^k - t_{m-1}^k \big| d_m^k = \mathcal{H}_0\big) = \mathcal{T}_k\,.\end{aligned} \tag{35}$$

In particular, given $d_m^k = \mathcal{H}_0$, then $\mathcal{D}_{0X}^k = \mathcal{T}_k$ *almost surely*. Moreover, it is possible to express the expected time $\mathcal{D}_{Xj}^k$ taken by the kth sensor to take any decision when $\mathcal{H}_j$ is true:

$$\begin{aligned}\mathcal{D}_{X0}^k &\triangleq \mathbb{E}_0\big(t_m^k - t_{m-1}^k\big) = \sum_{i=1}^{\mathcal{T}_k} i\,\mathbb{P}_0\big(t_1^k = i\big)\\ &= \mathcal{D}_{10}^k\mathcal{P}_F^k + \mathcal{T}_k\mathcal{P}_C^k = \mathcal{T}_k - \sum_{i=1}^{\mathcal{T}_k}(\mathcal{T}_k - i)\mathcal{P}_F^{(k,i)}\,,\\ \mathcal{D}_{X1}^k(c_k) &\triangleq \mathcal{D}_{11}^k(c_k)\mathcal{P}_D^k(c_k) + \mathcal{T}_k\mathcal{P}_M^k(c_k)\\ &= \mathcal{T}_k - \sum_{i=1}^{\mathcal{T}_k}(\mathcal{T}_k - i)\mathcal{P}_D^{(k,i)}(c_k)\,.\end{aligned} \tag{36}$$

These expressions explicitly show that the local decision delay of the kth sensor, in the case of sequential detection, is always upper-bounded by $\mathcal{T}_k$.

VI. Computational Complexity

This section assesses the computational complexity and the communication costs associated with the online FC detection algorithm in the case of the BSA, DTSA, and CSA.

A. Offline Preparation

In the three algorithms, the main task of the FC is to sum the observations' log-likelihood ratios and find the maximum with respect to the unknown parameters. Since the online computation of log-likelihood ratios becomes computationally intensive as the grids get *finer*, we assume an offline stage preceding the online detection where the log-likelihood ratios are pre-computed for each grid point and uploaded to the FC. The variables in $\mathcal{C}$ are known (thanks to the use of real-time weather data) but vary with time, thus a grid of possible values for those variables is required as well.

Such an offline data preparation has the benefit of reducing the real-time computational toll on the FC, but it suffers from the mismatch between the measured meteorological data and its closest value on the grid. However, such a difference can be arbitrarily reduced using a finer grid for the variables in $\mathcal{C}$ during the offline data computation.

B. Computation Complexity

The three different algorithms contain instructions for the FC on when and how the decision statistic must be updated. Given an instant where the FC is required to update the statistic, we have the same computational complexity $\mathcal{O}(K \cdot |\text{grid}(\boldsymbol{\theta})| \cdot |\text{grid}(I)|)$ across the three algorithms. The main computational difference lies in the rate at which these updates must be carried out which varies according to the employed algorithm. Let us assume that our network consists of a single sensor ($K = 1$): the BSA calculates the statistic only once after $\mathcal{T}^*$ instants (because of its batch nature); the DTSA, instead, has a mean update period of $\mathcal{D}^1_{X1}(c_k)$ when $\mathcal{H}_1$ is true (resp. $\mathcal{D}^1_{X0}$ when $\mathcal{H}_0$ is true) with $\mathcal{T}_1$ as an upper bound (see Eq. (36)), while the CSA has an update period equal to 1. We conclude by saying that: $1 \leq \mathcal{D}^1_{X1} \leq \mathcal{D}^1_{X0} \leq \mathcal{T}^*$, which shows the higher rate of update of the CSA, followed by the DTSA, both bounded by the BSA. Variations of the CSA might be proposed where the update of the statistic is carried out with a period higher than 1 and lower or equal than $\mathcal{T}_1$ as long as no local positive decision is taken (if the update period is equal to $\mathcal{T}_1$ the update frequency would collide with that of the DTSA). These observations can be extended to networks having $K > 1$.

C. Communication Costs

Each architecture is configured with a distinct combination of decision rule and transmission rule at the sensor level, resulting in a different *average transmission period* (ATP) between physical communications from *each sensor* to the FC. The subsequent results show the average transmission periods for each of the shown architectures:

$$\begin{aligned}\text{ATP}_{\text{CSA}} &\triangleq \mathbb{E}\left(t_b^k - t_a^k \middle| \sum_{t=t_a^k}^{t_b^k} \tau_t^k = 2\right) \\ &= \begin{cases} \mathcal{D}^k_{X0}/\mathcal{P}^k_F\,, & \text{if } \mathcal{H}_0 \text{ is true} \\ \mathcal{D}^k_{X1}(c_k)/\mathcal{P}^k_D(c_k)\,, & \text{if } \mathcal{H}_1 \text{ is true} \end{cases}, \qquad (37) \\ \text{ATP}_{\text{DTSA}} &\triangleq \mathbb{E}\big(t_m^k - t_{m-1}^k\big) \\ &= \begin{cases} \mathcal{D}^k_{X0}\,, & \text{if } \mathcal{H}_0 \text{ is true} \\ \mathcal{D}^k_{X1}(c_k)\,, & \text{if } \mathcal{H}_1 \text{ is true} \end{cases}, \qquad (38) \\ \text{ATP}_{\text{BSA}} &\triangleq t_m^k - t_{m-1}^k = \mathcal{T}_k\,, \quad \textit{almost surely}\,. \qquad (39)\end{aligned}$$

The derivation of ATP_{CSA} is reported in Appendix B.

We can immediately observe that $\text{ATP}_{\text{CSA}} \geq \text{ATP}_{\text{DTSA}}$. This is a direct consequence of the absence of physical communication when a sensor decides $\mathcal{H}_0$ in the CSA architecture. We can further notice, using Eq. (36), that $\text{ATP}_{\text{BSA}} \geq \text{ATP}_{\text{DTSA}}$. A comparison between ATP_{CSA} and ATP_{BSA} is less trivial and will be discussed via the case study in Sec. VII.

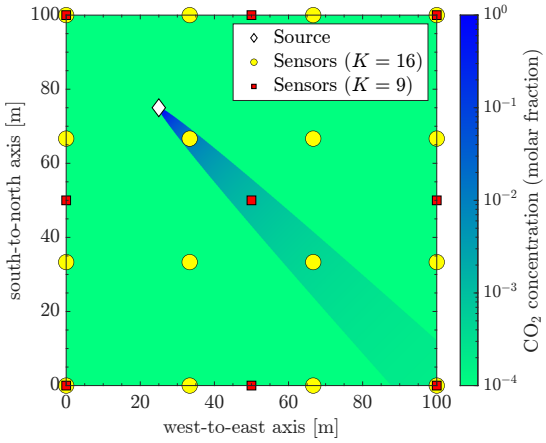

(a) Low intensity: $I = 0.05\,\text{m}^3/\text{s}$ (maximum value)

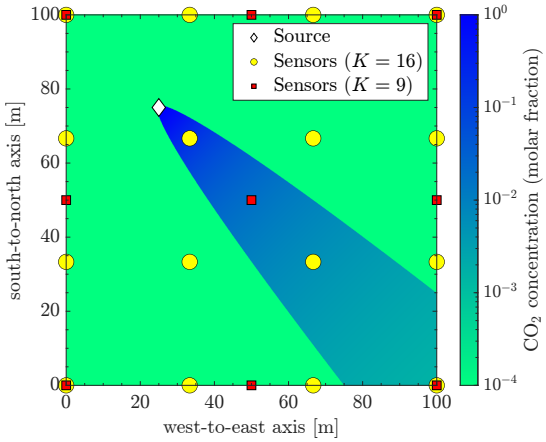

(b) High intensity: $I = 0.5\,\text{m}^3/\text{s}$ (maximum value)

Fig. 2: (Mean) concentration maps in a dispersion scenario at different intensities with $\boldsymbol{\theta} = [25\,\text{m}\ \ 75\,\text{m}]^{\text{T}}$, $\varphi = 315°$, $D = 0.1\,\text{m}$, and $u = 5\,\text{m/s}$.

VII. Results

The considered scenario simulates the dispersion of *saturated* carbon dioxide (CO_2), a heavy gas whose density, at

atmospheric temperature and pressure, is about 1.5 times larger than the air density. Heavy gases need specialized models that can predict their behavior like the well-known *Britter & McQuaid* (B&M) model for continuous releases [39]–[41]. The B&M model is based on the manual reading of a chart which prevents its use by the FC, thus a set of analytical relationships described in [2] is employed to convert it into a set of equations. The B&M's output, with respect to the kth sensor, is c_k. The variables belonging to the sets $\mathcal{A}$, $\mathcal{B}$, and $\mathcal{C}$, for the B&M model are the following:

$$\mathcal{A} = \{\boldsymbol{\theta}, I, D\},\ \mathcal{B} = \{T, \rho, c_0\},\ \mathcal{C} = \{T_{\text{atm}}, \rho_{\text{air}}, u, \varphi\}, \quad (40)$$

where T, ρ, c_0, and I are the temperature, density, concentration, and intensity of the gas at release condition; D is the release diameter; T_{atm} is the atmospheric temperature; ρ_{air} is the density of air at T_{atm}; finally u and φ are the wind speed at the height of 10 meters[3] and its direction[4]. D is a parameter that, like $\boldsymbol{\theta}$ and I, should be estimated as it is unknown. However, its contribution to the value of c_k is negligible for small values of D (which is the case for accidental dispersion), allowing us to assume it as known and equal to zero reducing the computational complexity of the algorithms.

Here, we assume that both the dispersion model and the signal model in Sec. II are accurate so that possible differences between the assumptions and the actual phenomenon can be neglected. The evaluation of the consequences of a non-negligible mismatch is outside the scope of this work.

The results are obtained via simulation of a monitored square area with sides of 100 meters with equally-spaced sensors, as shown in Fig. 2. The simulated settings refer to combinations of network size $K \in \{9, 16\}$ each with *low intensity* and *high intensity* dispersions. The corresponding four combinations allow an exhaustive comparison of the proposed algorithms. The results of each combination have been computed via numerical simulation with 10^5 Monte Carlo runs equally divided between $\mathcal{H}_0$ and $\mathcal{H}_1$ via MATLAB software. At each run, parameters such as wind direction (φ), wind speed (u), dispersion position ($\boldsymbol{\theta}$), intensity (I), and dispersion diameter (D) are generated according to a uniform distribution in a predetermined realistic range of values. The remaining parameters are kept constant across all the runs. The values or the distribution boundaries of the parameters are shown in Tab. I, while the specifications of the parameter grids necessary for the offline preparation of data are reported in Tab. II. In the present study, the selection of the threshold of a detector (γ_k) is done by fixing $\mathcal{P}_F^k$ and $\mathcal{T}_k$. For a batch local detector, this is done via inversion of Eq. (6). For the sequential case, this can be achieved via common root-finding methods applied to Eqs. (27) and (33).

Fig. 3 shows the ROC *surfaces* of the kth sensor in the case of a batch detector (Fig. 3a) and a sequential detector (Figs. 3b and 3c). These plots are obtained using the relations introduced in Sec. V. It is immediate to notice how the probability of detection strongly depends on c_k, for a fixed probability of false alarm. In terms of *area under the curve* (AUC), as $c_k \to 0$, we have $\text{AUC} \to 0.5$ (random detector), while as $c_k \to \infty$, $\text{AUC} \to 1$ (perfect detector), regardless of the used approach[5]. Furthermore, the figure highlights the decision delays in the two different approaches as the probability of false alarm and c_k change. Fig. 3a shows a constant decision delay equal to $\mathcal{T}_k$, while the remaining surfaces highlight the changes in $\mathcal{D}_{11}^k$ and $\mathcal{D}_{X1}^k$. In particular, when $\mathcal{P}_F^k \to 1$, we have $\left(\mathcal{D}_{11}^k, \mathcal{D}_{X1}^k\right) \to (1, 1)$, while when $\mathcal{P}_F^k \to 0$, we obtain $\left(\mathcal{D}_{11}^k, \mathcal{D}_{X1}^k\right) \to (\mathcal{T}_k, \mathcal{T}_k)$ thanks to the truncation that prevents the delays to diverge to infinity. Finally, in the sequential case, the plots show how the delays tend to lower from $\mathcal{T}_k$ to 1 at a faster rate with respect to $\mathcal{P}_F^k$ as c_k increases.

The comparison between a batch and a sequential detector can be facilitated using Fig. 4. In particular, Fig. 4a displays three sets of ROC curves at different values of c_k showing the negligible difference in performance between the two approaches. Meanwhile, Fig. 4b shows that once $\mathcal{P}_F^k$ has been fixed, the value of $\mathcal{T}_k$ required to achieve a desired value of $\mathcal{P}_D^k$ is similar in the case of batch and the sequential approach. Hence we can say that the differences in terms of detection accuracy between the batch approach and the sequential approach are negligible. The main advantage of a sequential approach can be seen in Fig. 4c where the decision delay $\mathcal{D}_{X1}^k$ is always smaller than $\mathcal{T}_k$ with this

TABLE I: Parameters used for the simulations

Parameter	Value / Distribution	Notes
θ_1 and θ_2	$\mathcal{U}(0, 100)$ m	uniform in monitored area
c_0	1	molar vapor fraction ($1 = 10^6$ ppm)
$T^{(\text{op})}$	253 K	[43]
$P^{(\text{op})}$	19.8 bar	saturation pressure at $T^{(\text{op})}$
T	219 K	*Soave-Redlich–Kwong* EOS [44]
P_{atm}	1.01 bar	–
ρ	2.48 kg/m^3	*Soave-Redlich–Kwong* EOS [44]
T_{atm}	293 K	–
ρ_{air}	1.20 kg/m^3	–
u	$\mathcal{U}(0, 10)$ m/s	–
φ	$\mathcal{U}(0, 2\pi)$	–
I	$\mathcal{U}(0, 0.05)$ m^3/s	low intensity dispersion
I	$\mathcal{U}(0.4, 0.5)$ m^3/s	high intensity dispersion
D	$\mathcal{U}(0, 0.2)$ m	–
μ_k	400 ppm	$\forall k$
σ_k	200 ppm	$\forall k$
$\mathcal{T}_k$	4	$\forall k$
$\mathcal{P}_F^k$	0.05	$\forall k$
γ_k	693 ppm	$\forall k$, DTSA and CSA
γ_k	658 ppm	$\forall k$, BSA

TABLE II: Parameters used for grid construction

Parameter	Grid Limits	Grid Interval
θ_1 and θ_2	$[0, 100]$ m	1 m
I (low intensity)	$[0, 0.05]$ m^3/s	$1/60$ m^3/s
I (medium intensity)	$(0.05, 0.4)$ m^3/s	$60/7$ m^3/s
I (high intensity)	$[0.4, 0.5]$ m^3/s	$1/30$ m^3/s
u	$[0.5, 10]$ m/s	0.5 m/s
φ	$[0, 2\pi)$	$\pi/8$

[3]If wind speed is available at a different height, several conversion methods are available [42].

[4]Wind blowing from north: 0° (360°), east: 90°, south: 180°, west: 270°.

[5]We remind that, for a generic detector, $\text{AUC} \triangleq \int_0^1 \mathcal{P}_D(\mathcal{P}_F)\, \mathrm{d}\mathcal{P}_F$, where $\mathcal{P}_F$ and $\mathcal{P}_D$ are the probability of false alarm and detection, respectively.

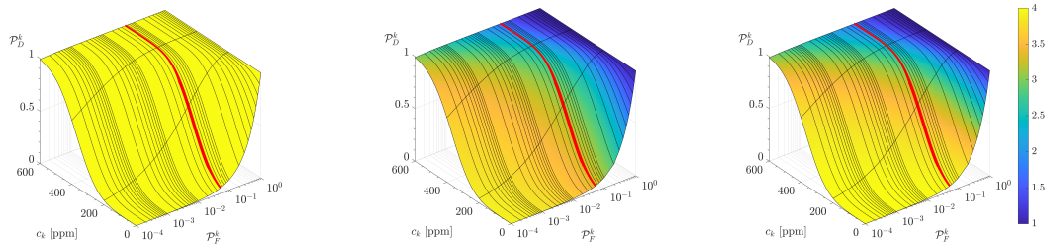

(a) Batch detector (colorbar shows $\mathcal{T}_k$) (b) Sequential detector (colorbar shows $\mathcal{D}_{11}^k$) (c) Sequential detector (colorbar shows $\mathcal{D}_{X1}^k$)

Fig. 3: ROC surfaces of local detectors using batch and sequential approach (red line indicates performances at $\mathcal{P}_F^k = 0.05$).

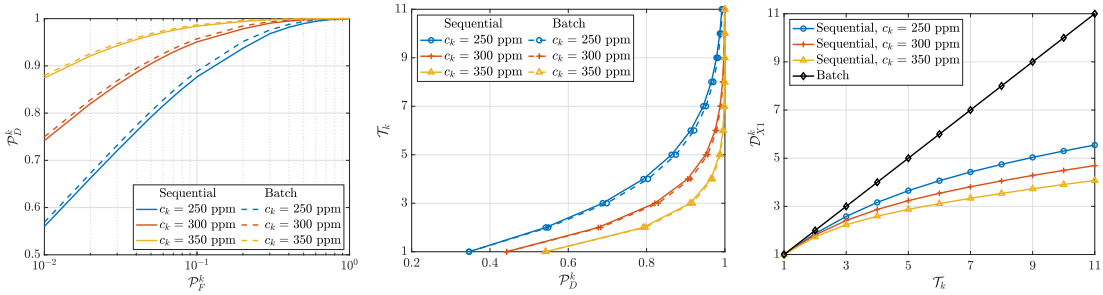

(a) ROC curves of the sensors (b) $\mathcal{P}_D^k$ vs. $\mathcal{T}_k$, with $\mathcal{P}_F^k = 0.05$ (c) $\mathcal{T}_k$ vs. $\mathcal{D}_{X1}^k$, with $\mathcal{P}_F^k = 0.05$

Fig. 4: Detection performances of the sensor.

difference increasing as we allow higher values of $\mathcal{T}_k$. This highlights that, once the probability of false alarm has been fixed, a sensor can perform detection with a smaller decision delay when a sequential approach is used rather than a batch approach at virtually the same probability of detection.

Fig. 5 shows the values of the ATP using the different architectures once the probability of occurrence of the dispersion $\mathcal{P}_1 \triangleq \mathbb{P}(\mathcal{H}_1)$ is marginalized, making it easier to compare ATP_{CSA} and ATP_{BSA}. This is because it is fair to assume that such an event happens with low frequency, with the desirable reduction communication in the WSN when $\mathcal{H}_1$ does not occur. We can notice that ATP_{CSA} and ATP_{DTSA} increase as $\mathcal{P}_1$ decreases. However, while ATP_{DTSA} is upper-bounded by ATP_{BSA} (as discussed in Sec. VI), the behavior of ATP_{CSA} relative to ATP_{BSA} varies according to both $\mathcal{P}_1$ and c_k. In the limit case of $\mathcal{P}_1 = 1$ (resp. $\mathcal{P}_1 = 0$), we can see the values of the ATP's in the hypothesis $\mathcal{H}_1$ (resp. $\mathcal{H}_0$): in $\mathcal{H}_1$, ATP_{CSA} tends to increase for lower values of c_k eventually leading to values greater than ATP_{BSA}; in $\mathcal{H}_0$, ATP_{CSA} is sensibly higher than ATP_{BSA}, regardless of c_k. Thus, ATP_{CSA} shows an improvement in the reduction of communication costs when the assumption of low $\mathcal{P}_1$ holds.

Next, we discuss the performances of the FC for each of the four configurations mentioned above in terms of *global probability of false alarm* $\mathcal{P}_F^* \triangleq \mathbb{P}_0\left(\widehat{\mathcal{H}} = \mathcal{H}_1\right)$, *global probability of detection* $\mathcal{P}_D^* \triangleq \mathbb{P}_1\left(\widehat{\mathcal{H}} = \mathcal{H}_1\right)$, and *global decision delay* (in $\mathcal{H}_1$) defined as $\mathcal{D}_{X1}^* \triangleq \mathbb{E}_1(t^*)$ for the CSA and DTSA, and equal to $\mathcal{D}_{X1}^* \triangleq \mathcal{T}^*$ for the BSA. The results are reported at increasing values of $\mathcal{T}^*$ for comparison purposes.

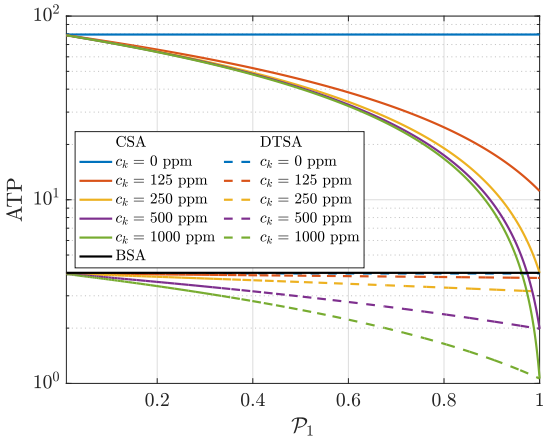

Fig. 5: Average Transmission Period vs. Probability of Occurrence.

Figs. 6 and 7 illustrate the ROC curves and the curves where $\mathcal{D}_{X1}$ is shown as function of $\mathcal{P}_F^*$. Different points of the curve are obtained by applying different values of global threshold

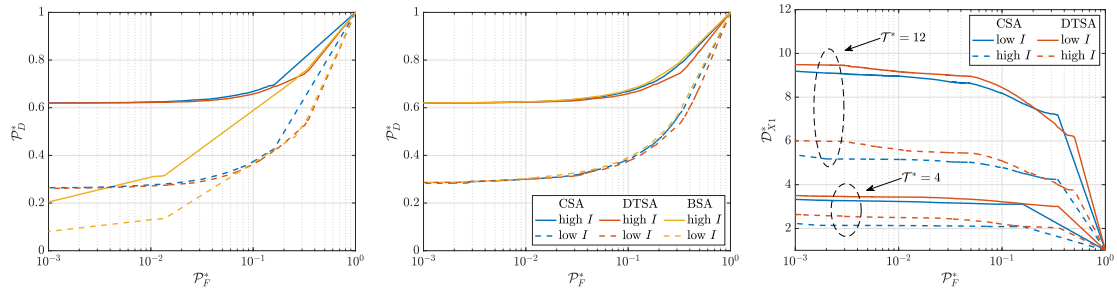

(a) ROC curves, $\mathcal{T}^* = 4$, $K = 9$ (b) ROC curves, $\mathcal{T}^* = 12$, $K = 9$ (c) Decision delay curves, $K = 9$

Fig. 6: ROC curves and decision delay curves, $K = 9$.

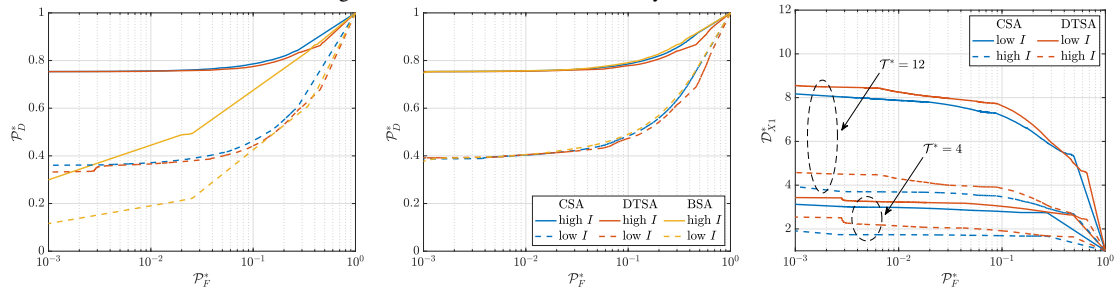

(a) ROC curves, $\mathcal{T}^* = 4$, $K = 16$ (b) ROC curves, $\mathcal{T}^* = 12$, $K = 16$ (c) Decision delay curves, $K = 16$

Fig. 7: ROC curves and decision delay curves, $K = 16$.

TABLE III: AUC in the simulated configurations

K	Method	$\mathcal{T}^* = 4$ low I	$\mathcal{T}^* = 4$ high I	$\mathcal{T}^* = 8$ low I	$\mathcal{T}^* = 8$ high I	$\mathcal{T}^* = 12$ low I	$\mathcal{T}^* = 12$ high I
9	CSA	**0.6556**	**0.8173**	0.6672	**0.8252**	0.6754	0.8313
	DTSA	0.6509	0.8121	0.6593	0.8169	0.6654	0.8208
	BSA	0.6307	0.7710	**0.6686**	0.8251	**0.6781**	**0.8343**
16	CSA	**0.7183**	**0.8878**	**0.7343**	**0.8945**	0.7428	0.8988
	DTSA	0.7047	0.8786	0.7157	0.8822	0.7221	0.8848
	BSA	0.6724	0.8294	0.7320	0.8911	**0.7444**	**0.9010**

TABLE IV: AUC($\mathcal{D}_{X1}^*$) in the simulated configurations

K	Method	$\mathcal{T}^* = 4$ low I	$\mathcal{T}^* = 4$ high I	$\mathcal{T}^* = 8$ low I	$\mathcal{T}^* = 8$ high I	$\mathcal{T}^* = 12$ low I	$\mathcal{T}^* = 12$ high I
9	CSA	**2.2263**	**1.6320**	**3.8154**	**2.4724**	**5.3837**	**3.2943**
	DTSA	2.4062	1.7448	3.9661	2.5883	5.5021	3.4148
	BSA	4	4	8	8	12	12
16	CSA	**2.1243**	**1.4326**	**3.4569**	**1.9629**	**4.7146**	**2.4609**
	DTSA	2.3249	1.5427	3.6606	2.0990	4.9415	2.6321
	BSA	4	4	8	8	12	12

γ^* to the FC's detection rule. The plots report results for $\mathcal{T}^* \in \{4, 12\}$ (as these are multiples of $\mathcal{T}_k$)[6]. The corresponding values of AUC are reported in Tab. III (with the intermediate scenario with $\mathcal{T}^* = 8$ also present). Analogously to the AUC of the ROC curve, we define $\mathrm{AUC}(\mathcal{D}_{X1}^*) \triangleq \int_0^1 \mathcal{D}_{X1}^*(\mathcal{P}_F^*)\, \mathrm{d}\mathcal{P}_F^*$ to facilitate the discussion of Figs. 6c and 7c. This metric is the mean value of $\mathcal{D}_{X1}^*$ over the domain of $\mathcal{P}_F^*$ and its values are reported in Tab. IV.

The ROC curves show that increasing the number of sensors improves $\mathcal{P}_D^*$, irrespective of the algorithm used. There are two reasons for this: Firstly, a larger number of sensors provides more information to the FC, enabling better discrimination between hypotheses. Secondly, since gas dispersions are anisotropic, having more sensors increases the chances of more sensors being in contact with the gas plume, resulting in a greater number of sensors experiencing $c_k > 0$, which enables non-random local detections. Another noticeable behavior is the higher value of $\mathcal{P}_D^*$ when the intensity I increases. This is because increasing I (fixing the other parameters) results in a higher c_k for those sensors already in the gas plume, as well as more sensors experiencing $c_k > 0$ (see Fig. 2 for a visual description of the effect of an increase of I). Such behavior of $\mathcal{P}_D^*$ with respect to K and I are numerically confirmed by an increase of AUC.

Using Tab. III, one can notice an increase in the AUC as higher values of $\mathcal{T}^*$ are used. Moreover, at $\mathcal{T}^* = 4$, the reported values show $\mathrm{AUC}_{\mathrm{CSA}} > \mathrm{AUC}_{\mathrm{DTSA}} > \mathrm{AUC}_{\mathrm{BSA}}$, with the difference in AUC (averaged among the four configurations) between the CSA and BSA, being 0.0439. This changes at $\mathcal{T}^* = 12$, showing a convergence trend in the AUC, with the BSA having the highest values. Nevertheless, the average difference in AUC between the CSA and BSA is equal to -0.0024, making this difference negligible.

Further analysis of the results showed the reason behind

[6]Higher values of $\mathcal{T}^*$ are not reported as they did not show any significant changes in the ROC curves and in the respective values of AUC.

the negligible differences in performance obtained by all the architectures as higher values of $\mathcal{T}^*$ are used. This lies in the anisotropic behavior of gas dispersions. In the simulated scenarios, a non-negligible number of Monte Carlo runs resulted in none of the sensors experiencing $c_k > 0$. In such a scenario all the sensors (and so the FC) acts as a random detector regardless of the current value of $\mathcal{T}^*$.

Unlike the previous discussion, the benefits in terms of $\mathcal{D}^*_{X1}$, as K and I increase, are only experienced by the CSA and the DTSA and are shown in Figs. 6c and 7c. This means that while, on one hand, we reach converging values of AUC by increasing $\mathcal{T}^*$, on the other hand, we are further amplifying the difference in $\mathrm{AUC}(\mathcal{D}^*_{X1})$ in favor of the sequential algorithms, and in particular the CSA. Tab. IV clearly shows that $\mathrm{AUC}(\mathcal{D}^*_{X1})_{\mathrm{CSA}} > \mathrm{AUC}(\mathcal{D}^*_{X1})_{\mathrm{DTSA}} > \mathrm{AUC}(\mathcal{D}^*_{X1})_{\mathrm{BSA}}$, for all configurations and values of $\mathcal{T}^*$. This is because, in the CSA and DTSA, $\mathcal{D}^*_{X1}$ grows slower than $\mathcal{T}^*$, unlike in the BSA where the growth is identical.

Both Figs. 6 and 7 show how the selection of the threshold γ^* affects performances. It can be seen how lowering γ^* simultaneously results in a higher $\mathcal{P}^*_D$ and lower $\mathcal{D}^*_{X1}$, with the drawback of an increased value of $\mathcal{P}^*_F$. Nevertheless, the curves show how both the CSA and DTSA are able to have lower $\mathcal{P}^*_F$ maintaining a steady level of $\mathcal{P}^*_D$ and $\mathcal{D}^*_{X1}$. This is especially visible at low values of $\mathcal{T}^*$.

The appropriate value of γ^* can be found via simulation after selecting a metric to satisfy. Possible strategies include: (a) given a fixed number of sensors, the threshold is chosen by satisfying a desired maximum $\mathcal{P}^*_F$; (b) given a fixed number of sensors, the threshold is chosen so that a minimum value of $\mathcal{P}^*_D$ is achieved given a value of I; (c) the threshold is selected by minimizing the *Bayes Risk*; (d) the threshold is chosen, together with the number of sensors, so that both $\mathcal{P}^*_F$ and $\mathcal{P}^*_D$ satisfy the desired requirements, given a value of I.

To conclude, the two proposed algorithms present the following differences in terms of performance and complexity:

- The CSA shows superior performances with respect to the DTSA both in terms of detection accuracy and decision delay;
- The CSA shows a great advantage in terms of communication costs, while the DTSA requires more frequent transmissions from the sensors to the FC;
- The DTSA requires less computations since the FC needs to update the detection statistic only when a decision is taken by the sensors. The CSA, on the other hand, requires the FC to update the detection statistic at each instant.

Thus, because of its high performance, the CSA is particularly suitable for highly safety-critical applications like hazardous gas detection. The DTSA, still maintaining high performances, shows a lower degree of accuracy and higher delay with respect to the CSA as well as higher communication costs. However, the DTSA's lower requirement in terms of computations performed by the FC makes it a desirable solution as long as a higher number of sensors is employed.

VIII. Conclusions and Future Directions

We proposed two sequential algorithms addressing the task of distributed gas detection in WSNs, named CSA and DTSA. The setup consists of sensors taking binary decisions via SD and transmitting them to a FC which takes a final decision benefiting from the integration of meteorological data and the dispersion model. The proposed methods constitute fully sequential alternatives to the traditional batch approach (BSA), with the further innovation introduced by the CSA of a time-aware sequential fusion. This enabled a significant improvement in terms of detection accuracy and delay, especially desired in such a time-critical application. System performance was also assessed in terms of communication costs showing how a time-aware algorithm as the CSA greatly reduces transmissions from sensors to the FC. The case study of CO_2 dispersion confirmed the validity of the proposed architectures.

Future works include (a) the reduction of complexity via more efficient strategies for the searching of $(\boldsymbol{\theta}, I)$, including the estimation of possible variations of I over time; (b) modeling erroneous communication channels; (c) use of Bayesian methods to improve detection and parameter estimation; (d) more accurate statistical characterization of the signal measured by the sensors including possible correlations between measurements in space and time; (e) development of algorithms accounting for imperfect knowledge of the dispersion model; (f) use of more comprehensive dispersion models, or direct use of computational fluid dynamics software; (g) integration of machine learning strategies for improved detection performances.

Appendix A
Covariance Matrices

The following is the derivation of the matrices $\boldsymbol{\Sigma}_{\boldsymbol{z}_i^k}$ and $\boldsymbol{\Sigma}_{\boldsymbol{v}_i^k}$, for any $k = 1, \dots, K$ and $i = 1, \dots, \mathcal{T}_k$. The element of the matrix $\boldsymbol{\Sigma}_{\boldsymbol{v}_i^k}$ located in the rth row and sth column is defined as the following:

$$\left[\boldsymbol{\Sigma}_{\boldsymbol{v}_i^k}\right]_{r,s} \triangleq \mathbb{C}\mathrm{ov}\big(\Lambda_r^k - \gamma_k, \Lambda_s^k - \gamma_k\big) = \mathbb{C}\mathrm{ov}\big(\Lambda_r^k, \Lambda_s^k\big) \ .$$

When $r = s \leq i$, we have that:

$$\left[\boldsymbol{\Sigma}_{\boldsymbol{v}_i^k}\right]_{r,s} = \mathbb{V}\mathrm{ar}\big(\Lambda_s^k\big) = s\sigma_k^2 = r\sigma_k^2 \ .$$

On the other hand, when $r < s \leq i$:

$$\begin{aligned}
\left[\boldsymbol{\Sigma}_{\boldsymbol{v}_i^k}\right]_{r,s} &= \mathbb{C}\mathrm{ov}\left(\Lambda_r^k, \Lambda_r^k + \sum_{j=r+1}^{s} \lambda_j^k\right) \\
&= \mathbb{E}\left(\Lambda_r^k\left(\Lambda_r^k + \sum_{j=r+1}^{s} \lambda_j^k\right)\right) - \mathbb{E}\big(\Lambda_r^k\big)\mathbb{E}\left(\Lambda_r^k + \sum_{j=r+1}^{s} \lambda_j^k\right) \\
&= \mathbb{E}\Big(\big(\Lambda_r^k\big)^2\Big) - \mathbb{E}^2\big(\Lambda_r^k\big) = \mathbb{V}\mathrm{ar}\big(\Lambda_r^k\big) = r\sigma_k^2 \ .
\end{aligned}$$

Analogously, when $s < r \leq i$, $\left[\boldsymbol{\Sigma}_{\boldsymbol{v}_i^k}\right]_{r,s} = s\sigma_k^2$. Hence, it is easy to obtain the following:

$$\left[\boldsymbol{\Sigma}_{\boldsymbol{v}_i^k}\right]_{r,s} = \min\{r, s\} \cdot \sigma_k^2 \ , \quad \forall\, r \leq i, s \leq i \ .$$

For the case of $\mathbf{\Sigma}_{\boldsymbol{z}_i^k}$, the previous holds as long as $r < i$ and $s < i$. In fact, when $r < s = i$:

$$\begin{aligned}
\left[\mathbf{\Sigma}_{\boldsymbol{v}_i^k}\right]_{r,s} &\triangleq \mathbb{C}\mathrm{ov}\big(\Lambda_r^k - \gamma_k, -\Lambda_s^k + \gamma_k\big) = \mathbb{C}\mathrm{ov}\big(\Lambda_r^k, -\Lambda_i^k\big) \\
&= \mathbb{C}\mathrm{ov}\left(\Lambda_r^k, -\Lambda_r^k - \sum_{j=r+1}^{i} \lambda_j^k\right) \\
&= \mathbb{E}\left(-\Lambda_r^k\left(\Lambda_r^k + \sum_{j=r+1}^{i} \lambda_j^k\right)\right) \\
&\quad - \mathbb{E}\big(\Lambda_r^k\big)\mathbb{E}\left(-\Lambda_r^k - \sum_{j=r+1}^{i} \lambda_j^k\right) \\
&= -\mathbb{E}\Big(\big(\Lambda_r^k\big)^2\Big) + \mathbb{E}^2\big(\Lambda_r^k\big) = -\mathbb{V}\mathrm{ar}\big(\Lambda_r^k\big) = -r\sigma_k^2 \,.
\end{aligned}$$

Similarly, when $s < r = i$, $\left[\mathbf{\Sigma}_{\boldsymbol{v}_i^k}\right]_{r,s} = -s\sigma_k^2$. Lastly, when $r = s = i$, we have:

$$\begin{aligned}
\left[\mathbf{\Sigma}_{\boldsymbol{z}_i^k}\right]_{r,s} &\triangleq \mathbb{C}\mathrm{ov}\big(-\Lambda_r^k + \gamma_k, -\Lambda_s^k + \gamma_k\big) = \mathbb{V}\mathrm{ar}\big(-\Lambda_i^k\big) \\
&= \mathbb{V}\mathrm{ar}\big(\Lambda_i^k\big) = i\sigma_k^2 \,.
\end{aligned}$$

These four cases form the following rule:

$$\begin{aligned}
\left[\mathbf{\Sigma}_{\boldsymbol{z}_i^k}\right]_{r,s} &= \begin{cases} \min\{r,s\}\cdot\sigma_k^2\,, & \text{if } r < i \text{ and } s < i \\ -r\sigma_k^2\,, & \text{if } r < s = i \\ -s\sigma_k^2\,, & \text{if } s < r = i \\ i\sigma_k^2\,, & \text{if } r = s = i \end{cases} \\
&= \sigma_k^2 \min\{r,s\}\big[1 + 2\delta_{i,\max\{r,s\}}\big(\delta_{i,\min\{r,s\}} - 1\big)\big] \,.
\end{aligned}$$

APPENDIX B
AVERAGE TRANSMISSION PERIOD IN THE CSA

We here report the derivation of the $\mathrm{ATP}_{\mathrm{CSA}}$ reported in Eq. (37). We show the proof for the case where $\mathcal{H}_0$ is true:

$$\begin{aligned}
&\mathbb{E}_0\left(t_b^k - t_a^k \middle| \sum_{t=t_a^k}^{t_b^k} \tau_t^k = 2\right) = \mathbb{E}_0\left(t_i^k \middle| \sum_{t=1}^{t_i^k} \tau_t^k = 1\right) \\
&= \sum_{i=1}^{\infty} \mathbb{E}_0\left(t_i^k \middle| \sum_{t=1}^{t_i^k} \tau_t^k = 1\right) \mathbb{P}_0\left(\sum_{t=1}^{t_i^k} \tau_t^k = 1\right) \\
&= \sum_{i=1}^{\infty} \big[(i-1)\mathbb{E}_0\big(t_1^k \big| d_1^k = \mathcal{H}_0\big) + \mathbb{E}_0\big(t_1^k \big| d_i^k = \mathcal{H}_1\big)\big] \\
&\quad \times \mathbb{P}_0\big(d_1^k = \mathcal{H}_1\big)\big[1 - \mathbb{P}_0\big(d_i^k = \mathcal{H}_1\big)\big]^{i-1} \\
&= \sum_{i=1}^{\infty} \big[(i-1)\mathcal{T}_k + \mathcal{D}_{10}^k\big]\mathcal{P}_F^k\big(1 - \mathcal{P}_F^k\big)^{i-1} \\
&= \mathcal{P}_F^k \sum_{i=0}^{\infty} \big(i\,\mathcal{T}_k + \mathcal{D}_{10}^k\big)\big(1 - \mathcal{P}_F^k\big)^i \\
&= \mathcal{P}_F^k\left(\mathcal{T}_k \sum_{i=0}^{\infty} i\big(1 - \mathcal{P}_F^k\big)^i + \mathcal{D}_{10}^k \sum_{i=0}^{\infty} \big(1 - \mathcal{P}_F^k\big)^i\right) \\
&= \mathcal{P}_F^k\left(\mathcal{T}_k \frac{1 - \mathcal{P}_F^k}{\big(\mathcal{P}_F^k\big)^2} + \frac{\mathcal{D}_{10}^k}{\mathcal{P}_F^k}\right) = \frac{\mathcal{T}_k(1 - \mathcal{P}_F^k) + \mathcal{P}_F^k\mathcal{D}_{10}^k}{\mathcal{P}_F^k} \\
&= \frac{\mathcal{D}_{X0}^k}{\mathcal{P}_F^k} \,.
\end{aligned}$$

Similarly, we obtain $\mathcal{D}_{X1}^k(c_k)/\mathcal{P}_D^k(c_k)$ when $\mathcal{H}_1$ is true.

REFERENCES

[1] G. Tabella, Y. Di Martino, D. Ciuonzo, N. Paltrinieri, X. Wang, and P. Salvo Rossi, "Decision fusion for carbon dioxide release detection from pressure relief devices," in *IEEE 12th IEEE Sens. Array Multichannel Signal Process. Workshop (SAM)*, 2022, pp. 46–50.

[2] ——, "Sensor fusion for detection and localization of carbon dioxide releases for Industry 4.0," in *IEEE 25th Int. Conf. Inf. Fusion (FUSION)*, 2022.

[3] S. Al-Sarawi, M. Anbar, R. Abdullah, and A. B. Al Hawari, "Internet of Things market analysis forecasts, 2020–2030," in *4th World Conf. on Smart Trends in Syst., Security and Sustainability (WorldS4)*, 2020.

[4] R. Abielmona, R. Falcon, N. Zincir-Heywood, and H. A. Abbass, Eds., *Recent Adv. in Comp. Intelligence in Defense and Security*, ser. (Studies in Computational Intelligence). Cham, Switzerland: Springer, 2016.

[5] G. Tabella, N. Paltrinieri, V. Cozzani, and P. Salvo Rossi, "Wireless sensor networks for detection and localization of subsea oil leakages," *IEEE Sens. J.*, vol. 21, no. 9, pp. 10 890–10 904, 2021.

[6] G. Tabella, D. Ciuonzo, N. Paltrinieri, and P. Salvo Rossi, "Spatio-temporal decision fusion for quickest fault detection within industrial plants: The oil and gas scenario," in *IEEE 24th Int. Conf. Inf. Fusion (FUSION)*, 2021.

[7] B. Ristic, A. Gunatilaka, and R. Gailis, "Localisation of a source of hazardous substance dispersion using binary measurements," *Atmos. Environ.*, vol. 142, pp. 114–119, 2016.

[8] D. D. Selvaratnam, I. Shames, D. V. Dimarogonas, J. H. Manton, and B. Ristic, "Co-operative estimation for source localisation using binary sensors," in *56th IEEE Annu. Conf. Decis. Control (CDC)*, 2017, pp. 1572–1577.

[9] T. Sahoo, *Process Plants - Shutdown and Turnaround Management*. Boca Raton (FL), USA: Taylor & Francis Group, 2014.

[10] T. Zhao and A. Nehorai, "Detecting and estimating biochemical dispersion of a moving source in a semi-infinite medium," *IEEE Trans. Signal Process.*, vol. 54, no. 6, pp. 2213–2225, 2006.

[11] S. Aldalahmeh, M. Ghogho, and A. Swami, "Fast distributed detection, localization, and estimation of a diffusive target in wireless sensor networks," in *7th IEEE Int. Symp. Wirel. Commun. Syst.*, 2010, pp. 882–886.

[12] B. Ristic, A. Gunatilaka, and R. Gailis, "Achievable accuracy in Gaussian plume parameter estimation using a network of binary sensors," *Inf. Fusion*, vol. 25, pp. 42–48, 2015.

[13] S. Vijayakumaran, Y. Levinbook, and T. F. Wong, "Maximum likelihood localization of a diffusive point source using binary observations," *IEEE Trans. Signal Process.*, vol. 55, no. 2, pp. 665–676, 2007.

[14] A. Gunatilaka, B. Ristic, A. Skvortsov, and M. Morelande, "Parameter estimation of a continuous chemical plume source," in *11th IEEE Int. Conf. Inf. Fusion (FUSION)*, 2008, pp. 1–8.

[15] J. Shi, W. Xie, J. Li, X. Zhang, X. Huang, A. S. Usmani, F. Khan, and G. Chen, "Real-time plume tracking using transfer learning approach," *Comput Chem Eng*, vol. 172, p. 108172, 2023.

[16] R. R. Tenney and N. R. Sandell, "Detection with distributed sensors," *IEEE Trans. Aerosp. Electron. Syst.*, vol. AES-17, no. 4, pp. 501–510, 1981.

[17] I. Akyildiz, W. Su, Y. Sankarasubramaniam, and E. Cayirci, "A survey on sensor networks," *IEEE Commun. Mag.*, vol. 40, no. 8, pp. 102–114, 2002.

[18] J.-F. Chamberland and V. Veeravalli, "Decentralized detection in sensor networks," *IEEE Trans. Signal Process.*, vol. 51, no. 2, pp. 407–416, 2003.

[19] B. Chen, L. Tong, and P. Varshney, "Channel-aware distributed detection in wireless sensor networks," *IEEE Signal Process. Mag.*, vol. 23, no. 4, pp. 16–26, 2006.

[20] D. Ciuonzo and P. Salvo Rossi, "Distributed detection of a non-cooperative target via generalized locally-optimum approaches," *Inf. Fusion*, vol. 36, pp. 261–274, 2017.

[21] A. Wald, *Sequential Analysis*, ser. (Wiley publication in mathematical statistics). New York (NY), USA: J. Wiley & sons, Incorporated, 1947.

[22] A. Wald and J. Wolfowitz, "Optimum character of the sequential probability ratio test," *Ann. Math. Statist.*, vol. 19, no. 3, pp. 326–339, 1948.

[23] H. Poor, *An Introduction to Signal Detection and Estimation*, 2nd ed., ser. (Springer Texts in Electrical Engineering). New York (NY), USA: Springer, 2013.
[24] D. Siegmund, *Sequential Analysis: Tests and Confidence Intervals*, ser. (Springer Series in Statistics). New York (NY), USA: Springer, 1985.
[25] Y. Mei, "Asymptotic optimality theory for decentralized sequential hypothesis testing in sensor networks," *IEEE Trans. Inf. Theory*, vol. 54, no. 5, pp. 2072–2089, 2008.
[26] G. Fellouris and G. V. Moustakides, "Decentralized sequential hypothesis testing using asynchronous communication," *IEEE Trans. Inf. Theory*, vol. 57, no. 1, pp. 534–548, 2011.
[27] Y. Yilmaz, G. V. Moustakides, and X. Wang, "Cooperative sequential spectrum sensing based on level-triggered sampling," *IEEE Trans. Signal Process.*, vol. 60, no. 9, pp. 4509–4524, 2012.
[28] ——, "Channel-aware decentralized detection via level-triggered sampling," *IEEE Trans. Signal Process.*, vol. 61, no. 2, pp. 300–315, 2013.
[29] Y. Yilmaz and X. Wang, "Sequential distributed detection in energy-constrained wireless sensor networks," *IEEE Trans. Signal Process.*, vol. 62, no. 12, pp. 3180–3193, 2014.
[30] S. Li, X. Li, X. Wang, and J. Liu, "Decentralized sequential composite hypothesis test based on one-bit communication," *IEEE Trans. Inf. Theory*, vol. 63, no. 6, pp. 3405–3424, 2017.
[31] S. Tantaratana and H. Poor, "Asymptotic efficiencies of truncated sequential tests," *IEEE Trans. Inf. Theory*, vol. 28, no. 6, pp. 911–923, 1982.
[32] M. Guerriero, V. Pozdnyakov, J. Glaz, and P. Willett, "A repeated significance test with applications to sequential detection in sensor networks," *IEEE Trans. Signal Process.*, vol. 58, no. 7, pp. 3426–3435, 2010.
[33] P. Khanduri, D. Pastor, V. Sharma, and P. K. Varshney, "Truncated sequential non-parametric hypothesis testing based on random distortion testing," *IEEE Trans. Signal Process.*, vol. 67, no. 15, pp. 4027–4042, 2019.
[34] L. Hu, J. Zhang, X. Wang, S. Wang, and E. Zhang, "Decentralized truncated one-sided sequential detection of a noncooperative moving target," *IEEE Signal Process. Lett.*, vol. 25, no. 10, pp. 1490–1494, 2018.
[35] X. Cheng, D. Ciuonzo, P. Salvo Rossi, X. Wang, and W. Wang, "Multi-bit & sequential decentralized detection of a noncooperative moving target through a generalized Rao test," *IEEE Trans. Signal Inf. Process. Netw.*, vol. 7, pp. 740–753, 2021.
[36] H. Darvishi, D. Ciuonzo, and P. Salvo Rossi, "A machine-learning architecture for sensor fault detection, isolation, and accommodation in digital twins," *IEEE Sens. J.*, vol. 23, no. 3, pp. 2522–2538, 2023.
[37] Y. Liu, Z. Pang, M. Karlsson, and S. Gong, "Anomaly detection based on machine learning in iot-based vertical plant wall for indoor climate control," *Build. Environ.*, vol. 183, p. 107212, 2020.
[38] A. D'Costa, V. Ramachandran, and A. M. Sayeed, "Distributed classification of gaussian space-time sources in wireless sensor networks," *IEEE J. Sel. Areas Commun.*, vol. 22, no. 6, pp. 1026–1036, 2004.
[39] R. E. Britter and J. McQuaid, *Workbook on the dispersion of dense gases*. UK: Health and Safety Executive, 1988.
[40] TNO, *Yellow Book – Methods for the calculation of physical effects*. The Hague, The Netherlands: The Committee for the Prevention of Disasters by Hazardous Materials, 2005.
[41] D. A. Crowl and J. F. Louvar, *Chemical Process Safety: Fundamentals with Applications*, 4th ed. London, UK: Pearson Education, 2019.
[42] S. Mannan, *Lees' Loss Prevention in the Process Industries*, 4th ed. Oxford, UK: Butterworth-Heinemann, 2012.
[43] NIST, "Thermophysical Properties of Carbon dioxide," 2023.
[44] J. M. Smith, H. C. Van Ness, M. M. Abbott, and M. T. Swihart, *Introduction to Chemical Engineering Thermodynamics*, 8th ed. New York (NY), USA: McGraw-Hill Education, 2018.

Gianluca Tabella (GS'20) was born in Suzzara, Italy, in 1993. He received the B.Sc. degree in chemical and biochemical engineering (with specialization in process engineering) and the M.Sc. degree in chemical and process engineering (with specialization in offshore engineering) from the University of Bologna, Italy, in 2017 and 2019, respectively. Since 2020, he has been working towards the Ph.D. degree in electronics and telecommunication at the Department of Electronic Systems, NTNU Norwegian University of Science and Technology, Trondheim, Norway. He was a visiting scholar at Columbia University, New York, NY, USA, in 2022. His research interests are in distributed detection and localization with a focus on industrial and Oil&Gas applications.

Domenico Ciuonzo (S'11-M'14-SM'16) is a Tenure-track Assistant Professor at University of Naples "Federico II". He holds a Ph.D. degree from the University of Campania "L. Vanvitelli", Italy. Since 2011, he has been holding several visiting researcher appointments (NATO CMRE, UConn, NTNU, CTTC). He is the recipient of two Best Paper awards (IEEE ICCCS 2019 and Elsevier Computer Networks 2020), the 2019 Exceptional Service award from IEEE AESS, the 2020 Early-Career Technical Achievement award from IEEE SENSORS COUNCIL for sensor networks/systems and the 2021 Early-Career Award from IEEE AESS for contributions to decentralized inference and sensor fusion in networked sensor systems. His research interests include data fusion, statistical signal processing, wireless sensor networks, the IoT, and machine learning.

Yasin Yilmaz (S'11-M'14-SM'20) received the Ph.D. degree in electrical engineering from Columbia University, New York, NY, USA, in 2014. He is currently an Associate Professor of electrical engineering with the University of South Florida, Tampa, FL, USA. His research interests include machine learning, statistical signal processing, and their applications to computer vision, cybersecurity, biomedical systems, energy systems, transportation systems, and communication systems.

Xiaodong Wang (S'98-M'98-SM'04-F'08) received the Ph.D. degree in Electrical Engineering from Princeton University. He is a Professor of Electrical Engineering at Columbia University in New York. Dr. Wang's research interests fall in the general areas of computing, signal processing and communications, and has published extensively in these areas. Among his publications is a book entitled *Wireless Communication Systems: Advanced Techniques for Signal Reception*, published by Prentice Hall in 2003. His current research interests include wireless communications, statistical signal processing, and genomic signal processing. Dr. Wang received the 1999 NSF CAREER Award, the 2001 IEEE Communications Society and Information Theory Society Joint Paper Award, and the 2011 IEEE Communication Society Award for Outstanding Paper on New Communication Topics. He has served as an Associate Editor for the IEEE TRANSACTIONS ON COMMUNICATIONS, the IEEE TRANSACTIONS ON WIRELESS COMMUNICATIONS, the IEEE TRANSACTIONS ON SIGNAL PROCESSING, and the IEEE TRANSACTIONS ON INFORMATION THEORY. He is a Fellow of the IEEE and listed as an ISI Highly-cited Author.

Pierluigi Salvo Rossi (SM'11) was born in Naples, Italy, in 1977. He received the Dr.Eng. degree (*summa cum laude*) in telecommunications engineering and the Ph.D. degree in computer engineering from the University of Naples "Federico II", Italy, in 2002 and 2005, respectively. He is currently a Full Professor and the Deputy Head with the Department of Electronic Systems, Norwegian University of Science and Technology (NTNU), Trondheim, Norway. He is also a part-time Research Scientist with the Department of Gas Technology, SINTEF Energy Research, Norway.

Previously, he worked with the University of Naples "Federico II", Italy, with the Second University of Naples, Italy, with NTNU, Norway, and with Kongsberg Digital AS, Norway. He held visiting appointments with Drexel University, USA, with Lund University, Sweden, with NTNU, Norway, and with Uppsala University, Sweden.

His research interests fall within the areas of communication theory, data fusion, machine learning, and signal processing. Prof. Salvo Rossi was awarded as an Exemplary Senior Editor of the IEEE COMMUNICATIONS LETTERS in 2018. He is (or was) in the Editorial Board of the IEEE SENSORS JOURNAL, the IEEE OPEN JOURNAL OF THE COMMUNICATIONS SOCIETY, the IEEE TRANSACTIONS ON SIGNAL AND INFORMATION PROCESSING OVER NETWORKS, the IEEE COMMUNICATIONS LETTERS and the IEEE TRANSACTIONS ON WIRELESS COMMUNICATIONS.

ISBN 978-82-326-7762-7 (printed ver.)
ISBN 978-82-326-7761-0 (electronic ver.)
ISSN 1503-8181 (printed ver.)
ISSN 2703-8084 (online ver.)

NTNU
Norwegian University of
Science and Technology